Development of a dermatological workstation with calibrated acquisition and management of color images for the follow-up of patients with an increased risk of skin cancer

Ontwikkeling van een dermatologisch werkstation met gekalibreerde opname en beheer van kleurenbeelden voor het opvolgen van patiënten met een verhoogd risico van huidkanker

Yves Vander Haeghen

Promotoren: Prof. dr. I. Lemahieu
Prof. dr. J. M. Naeyaert

Proefschrift ingediend tot het behalen van de graad van
Doctor in de Toegepaste Wetenschappen

Vakgroep Elektronica en Informatiesystemen
Voorzitter: Prof. dr. ir. J. Van Campenhout
Faculteit Toegepaste Wetenschappen
Academiejaar 2000–2001

UNIVERSITEIT
GENT

Acknowledgements

This book is the conclusion of several years of research. It would never have been possible without the implicit and explicit aid of many people.

First and foremost, I would like to sincerely thank my promoters prof. dr. Ignace Lemahieu and prof. dr. Jean-Marie Naeyaert. Prof. dr. Ignace Lemahieu was the one who first offered me a job on the subject of PET imaging at the university, way back in 1994. A few years later, prof. dr. Jean-Marie Naeyaert from the dermatology department of the university hospital was trying to establish cooperation with the department of applied sciences for a project regarding digital imaging of the skin. The two hooked up, and I found myself with an interesting doctoral subject. Their continued support on all fronts was and still is crucial. I would also like to thank the head of the ELIS department prof. dr. Jan Van Campenhout for the given opportunity, and for never shying away from asking questions.

Most of the research detailed in this work has been performed at the dermatology department of the university hospital of Ghent, and I would hereby like to thank all of its personnel for the pleasant working environment. Special thanks go to dr. Lieve Brochez, dr. Evelien Verhaeghe and dr. Katrien Vossaert who were a big help during the development of the patient and image database of the dermatological workstation. Together with dr. Jo Lambert and dr. Garnet Vancoillie they also evaluated the skin lesion segmentation algorithms, for which again many thanks. I am also grateful for the way all these people were always ready to answer sometimes silly questions about the dermatological aspects of things.

I would also like to thank all my colleagues of the MEDISIP-ELIS department, particularly dr. ir. Peter De Neve and ir. Koen Denecker. They were, together with prof. dr. ir. Wilfried Philips of TELIN, responsible for some discussions on the finer points of colorimetry, the scientific field central to this work. Moreover, ir. Koen Denecker was always eager to help with some of the more technical Tex, Postscript and PDF problems encountered during the realization of this book and related articles. Extra thanks also go to prof. dr. ir. Wilfried Philips for

the critical review of some of my papers and congress abstracts, as these publications formed the backbone of what was to become this book.

I also gratefully acknowledge the work of Rita Breems of MEDISIP and Liliane Calle and secretarial coworkers of the dermatology department who were always ready to take over some of my beloved administrative paperwork.

The supportive acknowledgments from some people outside the university, Jean-Pierre Van De Capelle and Joel Maelfeyt from Barco and Jean-Michel Lagarde from Pierre Fabre, were very motivating and primordial in strengthening the idea that I was on the right track. Many warm thanks for this, you had no idea how much that meant to me!

My special appreciation goes to dr. ir. Erik Sundermann, who was a colleague during my PET research years. Ironically, he went to work for a private company on color-related issues after I was about two years into the dermatological project. This meant he quickly became the ideal discussion partner on the subject of colorimetry (preferably over a snooker table after work). Besides discussion and divertissement, he was also one of the main proof readers of my articles and particularly this work. His comments were to greatly influence its structure and readability.

Finally, I have to thank my girlfriend Sylvie for her continued moral support (she certainly did a better job than I did during her phd), my parents (for the good food) and family, and my friends with whom it was possible to escape from it all once in a while.

Yves Vander Haeghen
Gent, 10 september 2000

Contents

Part I

Original English Text

Chapter 1

Introduction

Traditional (color) photography has been used in medicine almost since it was invented. Its role was mainly that of a visual record and thus rather qualitative, except for some simple geometric mensurations that could be derived from the images. However, in many instances color conveys important diagnostic information, and this is especially so in case of images of the skin. Imaging the skin in a reproducible manner is, however, not easy for a number of reasons. This brings us to our main endeavor: to build a color imaging system that can be used to acquire reproducible images of the skin, and on which diagnostically meaningful measurements can be performed.

At the start of chapter 2 the medical context of this work, i.e. the field of dermatology, will be introduced. Next, some of our motivations will become clearer when the problems regarding some types of skin cancers are discussed. Current diagnostic methods for skin cancer and imaging practices will also be reviewed, and the chapter will end with some general design goals for the color imaging system.

In chapter 3 the phenomenon of human vision and color will be explained, and the concepts from the domain of colorimetry necessary to the understanding of subsequent chapters will be detailed.

Chapter 4 is dedicated to the discussion of all the components that will make up the color imaging system, as well as how they are assembled and how they work together.

Once the imaging system is assembled it must be operated, and this is the subject of chapter 5. In the course of this chapter we will explain how the imaging system can be calibrated in order to provide reproducible color imaging, as well as how to perform the actual acquisition of an image. Next, the precision and accuracy of colorimetric measurements derived from acquired images will be experimentally evaluated and thoroughly discussed.

In order to be of any use in a clinical setting, the imaging system must be easy to use and provide a pleasant and practical working environment to the dermatologist, and this is explored in chapter 6. On a basic level the imaging system will be extended with a patient and image database and an application to manage that database, as well as with some tools to properly view the acquired images. Moreover, the colorimetric framework enables the development of human vision based image processing, and to demonstrate this a simple skin lesion segmentation algorithm will be proposed and tested.

Chapter 7 will be devoted to a reiteration of the main conclusions, a summation of personal contributions, as well as any publications resulting from this work. Finally, some general resolutions will bring the final chapter to a close.

Chapter 2

Context and goals

In this chapter the medical context of this work will be introduced by providing some background information on the field of dermatology. This branch of medicine is preoccupied with the skin, and we are especially interested in a deadly form of skin cancer known as melanoma. The possible benefits of digital color imaging in the fight against melanoma will be summed up, and prior work on its use in dermatology will be reviewed. This will then lead to a formulation of the general goals for the development of a dermatological workstation.

2.1 Dermatology

As mentioned in the introduction to this chapter, dermatology is the branch of medicine preoccupied with the skin. Although digital imaging may be of general benefit in this branch, this work is primarily concerned with the improvement of the early detection of a deadly form of skin cancer known as melanoma. Therefore, after a general introduction on the skin, we will elaborate on melanoma and some clinically similar melanocytic and non-melanocytic lesions, and the way they are currently diagnosed. Most of the background information and figures on dermatology are taken from [1], unless otherwise specified.

2.1.1 The skin

The skin is a large organ that covers almost the whole body, making up about 16 % of the body weight. It has many functions, the most important of which is the protection of the body from noxious external factors.

It is quite thin and consists of several distinct layers: the *epidermis*, the *dermis* and the *subcutis* (see fig. 2.1).

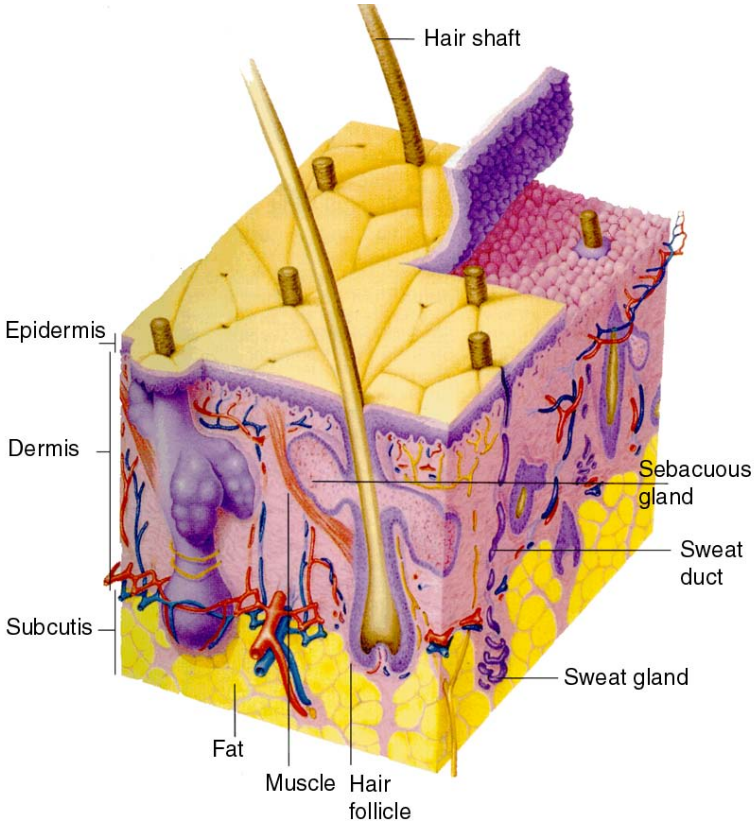

Figure 2.1: The three main layers of the skin: the epidermis, the dermis and the subcutis.

The epidermis

The epidermis is the outer skin layer, and is about 100 μm in most places. It consists of four sublayers: the stratum corneum or horny layer, the stratum granulosum or granular cell layer, the stratum spinosum or the prickle cell layer and the stratum basale or basal cell layer. These sublayers can be seen in fig. 2.2 and represent the different stages of maturation of the main cells of the epidermis called *keratinocytes*. Keratinocytes start out as undifferentiated basal cells in the basal layer.

Half of these migrate upwards, and end up in the horny layer as dead thick cells called corneocytes, where they are eventually shed. During this migration they produce polypeptides called keratins which create a sort of matrix that is used to bind them together. This explains the strength and flexibility of the horny layer, which forms the main barrier of the skin against outside agents and prevents fluids from the body of leaking out.

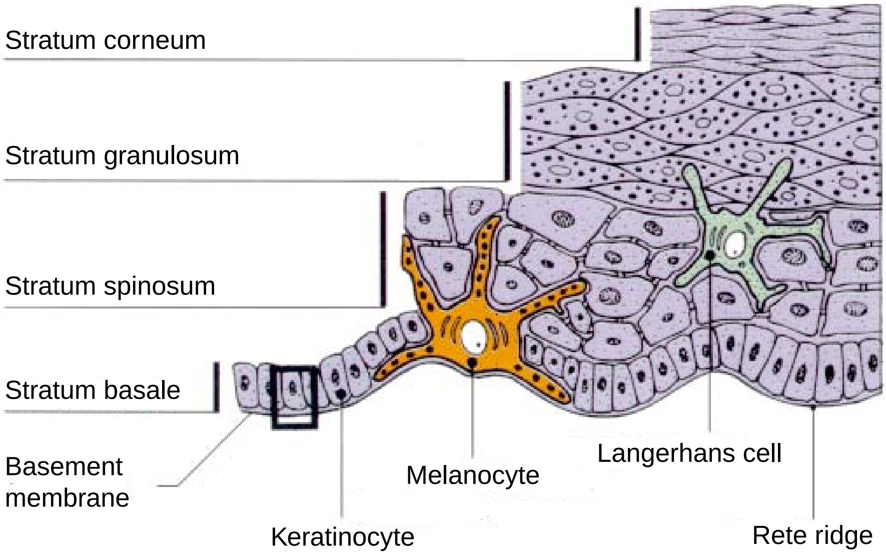

Figure 2.2: The structure of the epidermis.

Other important cells in the epidermis are the *melanocytes* which form about $5 - 10$ % of the basal cell population. These cells synthesize a pigment called *melanin* inside specialized organelles called *melanosomes.* There are two sorts of melanin: yellow or red phaemelanin and brown-black eumelanin. Natural melanin is usually made up of a mixture of these two sorts. Melanin is packaged in granules and is transferred to neighboring keratinocytes. It eventually ends up evenly distributed in the horny layer where, besides giving skin its color, it reduces the amount of ultraviolet (UV) radiation entering the skin by absorbing it. Racial variations in pigmentation are due to the number and size of melanosomes, not to the number of melanocytes.

The dermis

The dermis is a tough connective tissue matrix containing some specialized structures which are located immediately below the epidermis. It varies in thickness from about 600 μm to 3 mm. It has two sublayers: the thin papillary dermis in contact with the basal cell layer, and the reticular dermis. About 70 % of the dermis is made up of collagen, a structural protein synthesized by fibroblasts. The dermis also contains immunologically active cells like macrophages and lymphocytes. It also contains structures like sweat glands, hair follicles and blood vessels.

The subcutis

The subcutis consists of loose connective tissue and fat, which can be up to 3 cm thick on the abdomen.

2.1.2 Melanocytic naevi

A naevus is a benign proliferation of one or more of the normal constituents cells of the skin. Specifically, in the case of a *melanocytic naevus* or mole, it is a proliferation of melanocytic naevus cells derived from melanocytes. Although naevi may be present at birth (congenital naevi), most develop during childhood or adolescence. These latter types include the junctional naevus, the intradermal naevus, the compound naevus (see fig. 2.3), the Spitz naevus, the blue naevus, the halo naevus and the atypical or dysplastic naevus. On the average, a caucasoid has between about 10 and 30 melanocytic naevi.

Figure 2.3: A compound melanocytic naevus.

The reason why these types of skin lesions are mentioned here is that there is an increased risk for malignant change in some congenital and in atypical naevi, i.e. they may be precursor lesions to melanoma, which will be discussed in the next paragraph. Occurrence of the latter naevi also indicates an increased risk of developing a melanoma *elsewhere on the skin*. Moreover, the differential diagnosis between melanocytic naevi and the early stages of melanoma is sometimes very difficult. Unless there is concern for malignancy or an increased risk of malignant change, there is no *need* to remove melanocytic naevi. Sometimes though, excision may still be done for cosmetic reasons, or because of repeated inflammation.

2.1.3 Melanoma

Melanoma is a malignant tumor of the skin and sometimes mucus membranes, more precisely of the melanocytes in the epidermis, see fig. 2.4. It is the most lethal malignant skin tumor. The main types of melanoma are the superficial spreading melanoma, the lentigo maligna melanoma, the acral lentiginous melanoma and the nodular melanoma. The superficial spreading melanoma is the more common form, and has a prediliction for the lower legs of women and the back of males. The lentigo melanoma arises in sun-damaged skin, often on the face of elderly people with a long-standing outdoor occupation. The acral lentiginous melanoma affects soles, palms and nail beds, and has poor survival figures because it is often diagnosed late. The nodular melanoma is usually found on the trunk, and it may grow rapidly and ulcerate.

Figure 2.4: A nodular melanoma.

How does it evolve?

A large portion of melanoma spend a long time (months to years) in a benign stage of tumor progression called the plaque or 'radial growth phase'. This name stems from the fact that at this time the tumor is a plaque on the skin that expands along the radii of an imperfect circle. Melanoma in this stage are confined to the epidermis and are generally curable by simple surgery or excision. The next stage in tumor progression, also called the 'vertical growth phase', results in an invasion of the dermis. In this stage the melanoma may also lead to metastases, i.e. secondary tumors in other organs.

Rising incidence

The incidence of melanoma has risen spectacularly in white populations worldwide the last decades. This was first observed in the 1930's in the U.S.A. and in the 1940's in Denmark. As an example, in the U.S.A. the lifetime risk of developing melanoma has increased from 1/1500 in 1935 to 1/87 in 1996, and it is expected to rise further. At the moment melanoma represents around 1.2 percent of all new cancers worldwide, with annually some 70000 new cases. The mortality due to melanoma has known a similar albeit more moderate increase, as is shown in fig. 2.5 for Belgium, [2].

One way of trying to diminish these growing figures is by prevention campaigns, based on the accepted relationship between sun exposure and the development of melanoma. This is called primary prevention. Although as a result awareness of the problem of skin cancer is bigger now, there are few indications that both rises in incidence and mortality are artefactual and a result of better registration or detection of this type of cancer, [3].

Early diagnosis is everything

The mortality rate of melanoma has risen less sharply than its incidence, which means that the per-case mortality rate has actually decreased. As the therapy of melanoma has changed little over time since the beginning of the rise of the incidence (melanoma metastases generally show little or no response to chemo- or radiation therapy), some other factors must be at work to explain this phenomenon.

The average tumor thickness appears to have decreased over time due to the earlier detection of the (thinner) lesions as a result of increased awareness of skin cancer. Together with the correlation between the melanoma thickness and the prognosis or survival rate (see table 2.1) this leads to the conclusion that *early detection is the single most important factor in the decrease of the per-case mortality rate of melanoma once it is present.*

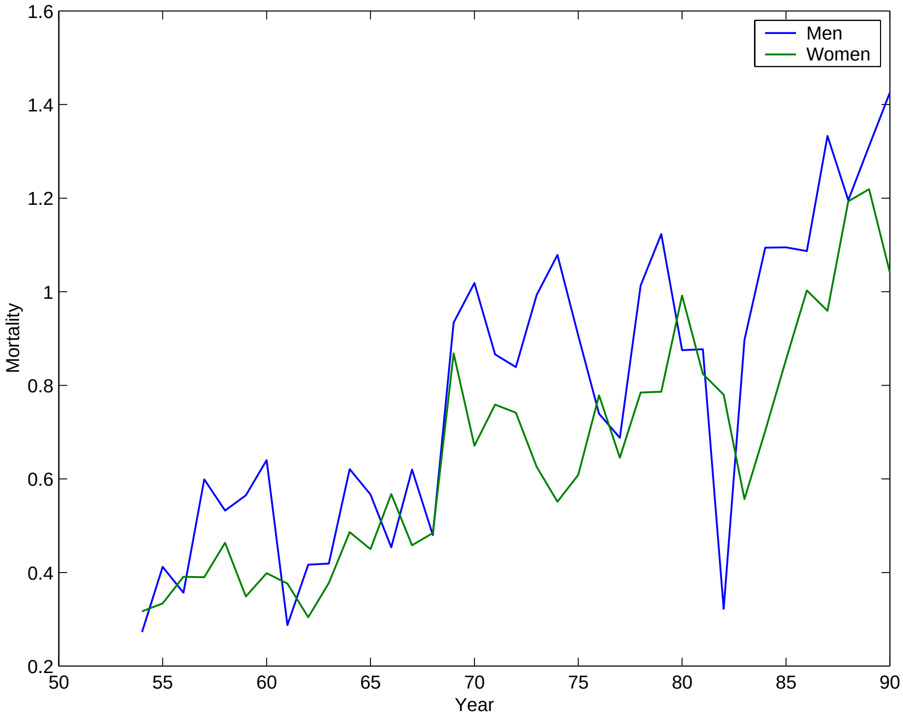

Figure 2.5: The world-standardized mortality rates per 100.000 for men and women in Belgium since the 1950's.

Breslow thickness	Survival %
$\leq$ 0.76 mm	98
0.76 - 1.69 mm	86
1.70 - 3.60 mm	69
$\geq$ 3.60 mm	33

Table 2.1: Five year prognosis for melanoma in function of the Breslow thickness.

About half of the melanoma arise in a precursor lesion, generally an atypical naevus or a congenital naevus. Occurrence of these lesions in a person indicates an increased risk for developing melanoma, although if it arises it will not necessarily be in that precursor lesion. Some of the main risk factors are listed in table 2.2. Taking this into account the importance of the follow-up of such increased-risk patients becomes clear. It allows well-targeted counselling about sun exposure and protection, i.e. primary prevention, and periodic screening to attempt early detection and diagnosis, i.e. secondary prevention.

Risk factor	**Relative risk**
Atypical naevi with family history of melanoma	100 - 400
Multiple (≥ 100) melanocytic naevi	30
Congenital naevus (≥ 1.5 cm diameter)	20
Previous melanoma	9
Red hair and blue eyes, burn in sun and tan poorly	2

Table 2.2: The major risk factors for the development of melanoma.

2.1.4 Other malignant skin tumors

Non-melanoma malignant skin tumors are amongst the most common of cancers, especially in light-skinned races (incidence 230 per 100000 per year in the USA for caucasoids). Of these, basal cell carcinoma is the commonest. It arises from the keratinocytes in the epidermis, but very rarely metastasizes. Occurrence of basal cell carcinoma is linked to prolonged UV exposure, amongst others. They can be pigmented, in which case they may be hard to differentiate from compound naevi and melanoma. Another type of cancer of the keratinocytes which is usually easy to differentiate from melanoma is squamous cell carcinoma. This type of cancer may occasionally lead to metastases. Although correct differential diagnose is of course very important in order to provide the correct treatment, incorrect diagnose will still usually lead to excision. In that sense they do not pose the same kind of problem as the melanoma which can be misdiagnosed as a melanocytic naevus which is a benign lesion which generally does not need to be excised.

2.1.5 Diagnostic tools for skin lesions

As mentioned in the previous sections, discrimination between melanoma and other, both melanocytic and non-melanocytic skin lesions, is sometimes very difficult. This is especially true for the early stages of melanoma, and diagnosing at this vitally important stage requires a lot of experience. This has led to the introduction of the *clinical ABCD rule* [4], which states that a lesion is suspicious if it is **a**symmetrical in shape, it has an irregular **b**order, contains different

colors or has a **d**iameter larger than 6 mm. This rule is used during clinical, i.e. visual, examination and is also useful for the general public when performing a self-examination. Despite this, several investigations [5, 6] confirm that the clinical diagnostic accuracy of pigmented skin lesions lies between 60% to 80% for melanoma, if the examination is done by experienced dermatologists! Obviously the result is lower for non-dermatologists and general practitioners (GP), simply due to the fact that they are only sporadically confronted with melanoma: a GP, for instance, will statistically only see a melanoma in his patients once about every 10 years or so.

In order to try to increase the clinical diagnostic accuracy the *dermatoscope* and later on the *dermatoscopic ABCD rule* [7] were developed, amongst others (see table 2.3). The dermatoscope, see fig. 2.6, is a small hand held device used to look at skin lesions under a tenfold magnification. It has a light source and a glass plate which is pressed gently onto the lesion after a few drops of water or oil have been applied to it. The resulting thin film of liquid eliminates surface reflection due to the refractive-index mismatch between skin and air, making the horny layer somewhat transparent so that underlying structures become visible. Dermatoscopy is also known as ‘epiluminiscence microscopy’ (ELM) or ‘skin surface microscopy’.

Figure 2.6: The dermatoscope, a hand held device allowing closer examination of pigmented lesions.

The dermatoscopic ABCD rule is semi-quantitative and results in a single score which indicates a risk that the inspected lesion is a melanoma. This score is known as the *final dermatoscopic score* (FDS), and a value above 5.45 indicates a melanoma while a value under 4.75 indicates a benign lesion. For FDS scores between those two values early melanoma cannot be excluded, and excision is thus generally also performed. Diagnostic accuracy is about 90 % [7]. It is used by dermatologists specialized in pigmented skin lesions. It could also be useful for other dermatologists and GPs, but requires training for proper use. Even with training, consistent application of the dermatoscopic rule remains difficult, and is probably subject to a non-negligible intra- and inter-observer variability.

Criterion	**Score**	**Weight**	**Range**
Asymmetry: number of perpendicular axes which result in asymmetrical structures or colors	0 - 2	1.3	0.0 - 2.6
Border: number of octants with abrupt cutoff in pigmented network	0 - 8	0.1	0.0 - 0.8
Colors: number of colors present out of white, red, light and dark brown, blue-gray and black	1 - 6	0.5	0.5 - 3.0
Different structures: number of structures present out of network, homogeneous areas, dots, globules and streaks	1 - 5	0.5	0.5 - 2.5
Final dermatoscopic score			1.0 - 8.9

Table 2.3: The dermatoscopic ABCD rule [8]. For an exact definition of the structures, see [9].

As dermatoscopy and the dermatoscopic ABCD rule are probably a good starting point for a dermatological workstation based on digital imaging when it comes to extracting useful information, it may be useful to review the rules in table 2.3 a bit more thoroughly using the examples of the original articles [8, 7], see figs. 2.7 to 2.10. It will also immediately become clear that consistent and reproducible application of these rules is not easy!

Concerning the follow-up of patients with an increased risk of developing melanoma, no special tools exist that also take into account the *evolution* of the features of suspect skin lesions. Basically, the methods described above are applied and the results recorded each time the patients visits, usually together with a photograph for qualitative comparison.

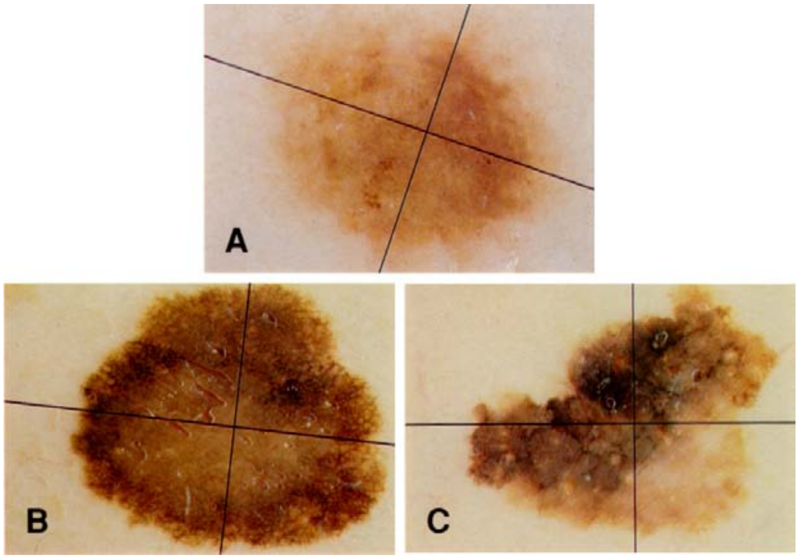

Figure 2.7: Example of the **A**symmetry score for melanocytic lesions. Lesion A: no asymmetry on any axe → $A = 0$. Lesion B: Asymmetry on one axe → $A = 1$. Lesion C: Asymmetry on two perpendicular axes → $A = 2$.

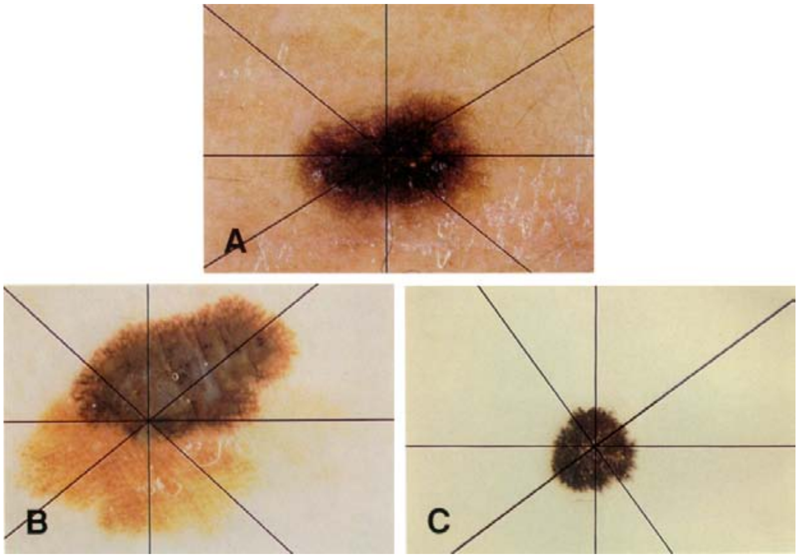

Figure 2.8: Example of the **B**order score for melanocytic lesions. Lesion A: no abrupt cutoff of pigment pattern in any of the eight segments → $B = 0$. Lesion B: abrupt cutoff of pigment pattern in four out of eight segments → $B = 4$. Lesion C: abrupt cutoff of pigment pattern in all eight segments → $B = 8$.

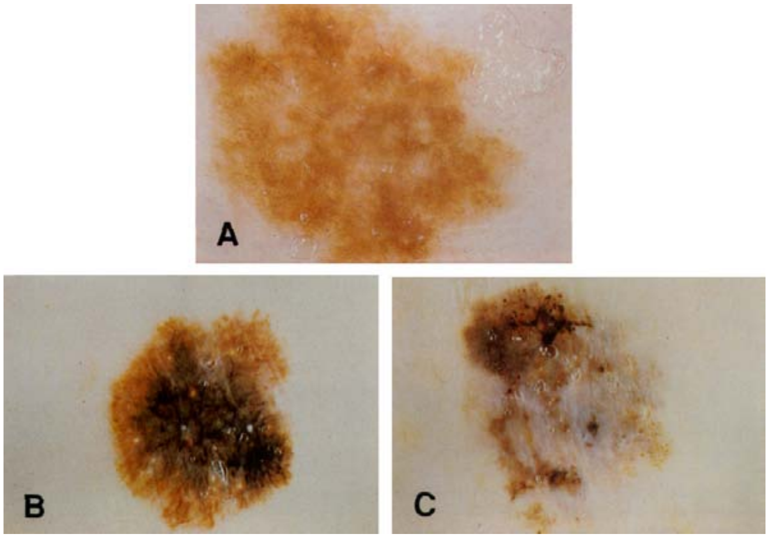

Figure 2.9: Example of the **C**olor score for melanocytic lesions. Lesion A: two colors, namely light and dark brown → $C = 2$. Lesion B: four colors, namely light and dark brown, blue-gray and black → $C = 4$. Lesion C: six colors, namely white, light and dark brown, blue-gray, red and black → $C = 6$.

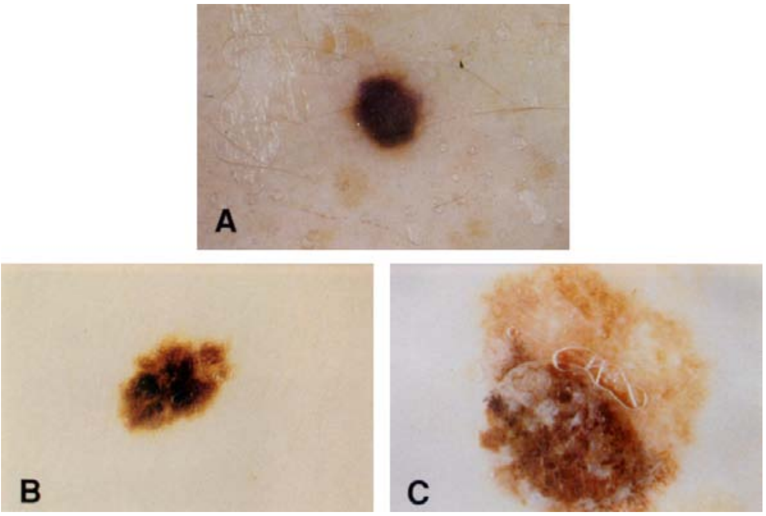

Figure 2.10: Example of the **D**ifferent structural components score for melanocytic lesions. Lesion A: one component, namely homogeneous areas → $D = 1$. Lesion B: three components, namely homogeneous areas, pigment networks and streaks → $D = 3$. Lesion C: five components, namely homogeneous areas, pigment network, streaks, dots and globules → $D = 5$. For an exact definition of the structural components, see [9]

2.2 Imaging in dermatology

By now it is clear that visual information is primordial in dermatology. One recent study, [10], stated that because of the limited ability of people to recall the appearance of a skin lesion, especially over long intervals, 'Photographic records may be the most effective aid for the detection of changes at longer intervals'. Consequently it is not surprising that imaging has been in intensive use for many years in this field, mostly using traditional photography. Digital color imaging in dermatology has been tried as early as 1990 [11], and has many potential benefits over its traditional counterpart.

2.2.1 Traditional photography

Up to about ten years ago imaging in dermatology was almost exclusively done using traditional photography, mostly slides. Their main use is for qualitative comparison or monitoring of a lesion when the patient returns at a later date, and as a visual record in a patient's case history. Due to the limitations of traditional photography, mainly variations in film, development and lighting, it is not easy nor practical to perform any sort of reproducible *measurements* on these images besides maybe some simple geometrical properties, e.g. the lesion area. To address some of these problems digitization of slides was tried by 1987 [12]. Although such a setup allows digital processing and the extraction of more complex features like shape, color and texture from the images, see also [13], it cannot compensate for the reproducibility problems associated with traditional photography.

2.2.2 Digital imaging

The use of digital color imaging in dermatology has been investigated several times since 1990 [11, 14, 15, 16, 17], and the last few years some commercial imaging systems, mainly for melanocytic lesions, have also appeared. All these systems represent a vast improvement over traditional photography on subjects like dependability (the result can be viewed instantly and reacquired if the quality is not satisfactory), cost, storage, retrieval, and image analysis possibilities. Traditional photography still has an edge when it comes to image resolution, but this will become less and less of a problem with the availability of cameras with ever higher image resolutions.

The problem with the approach of the imaging systems mentioned above at the time of writing lies in their lack of standardization regarding color. Although some of these systems undoubtedly use some kind of calibration in order to ensure reproducibility of the imaging process, none of them is able to measure color *accurately*, i.e. produce color measurements from the images that can be compared with and confirmed by a standard color measuring device like a spectrophotometer (SPM). It can be argued that it may be better to leave this kind of measurement to such standard color measuring devices, and concentrate on reproducibility alone. Unfortunately, several problems arise here. Firstly, these color measuring devices usually measure average color properties over a fixed area, which is not very useful for certain types of irregularly shaped skin lesions. Secondly, the use of images made by an imaging system without color standardization is in essence restricted to the system or type of system that created it. This severely limits the use of such systems for telemedicine or similar distributed applications. Indeed, one can easily imagine scenarios whereby a dermatologist with an imaging system from vendor X sends on image to a colleague for a second opinion, only to find out the images look completely different when seen on that colleague's imaging system from vendor Y. Most probably any of the image tools on the recipient imaging system will also be completely useless or give erroneous results. We may therefore state that any algorithm developed for such a system that is based on color, suffers from limited applicability and cannot be cross-validated. The lack of standardization also denies those systems a proper color difference metric which can be very useful for human vision based image processing, e.g. when segmenting a skin lesion from the surrounding normal skin or measuring color changes of a lesion over time. It has to be said that [15, 17] make use of such a color difference metric, but as far as can be made out this was based on a generic RGB to CIE $L^*a^*b^*$ color space transform. However, it is very unlikely that the RGB source color space of their imaging system is the same as the one for which the transform mentioned above was meant. This could have been addressed by an extra transform of the source color space, but this is mentioned nowhere.

The problem of standardization of color in medicine is in truth a general problem, with limited support for color spaces in e.g. communication and messaging standards like **D**igital **I**maging and **Co**mmunications in **M**edicine (DICOM) version 3.0 and **H**ealth **L**evel 7 (HL-7) [18].

Some of the commercial systems were demonstrated at the department of dermatology of the Ghent university hospital, and although they are compact and ergonomic systems, the dermatologists were generally not impressed with the image quality. Furthermore, because of the many possible uses of such a system within the department, i.e. clinical routine as well as research, some of the image management applications delivered with those systems seemed restrictive.

2.3 General goals

We can now formulate some general goals for the development of a dermatological workstation. Such a workstation will not only comprise an imaging system, but also extra software tools or applications for the management and processing of the acquired images.

- High quality of acquired images: high resolution and absence of artifacts, noise, geometrical deformation, etc...
- Good precision (reproducibility) of image acquisition so that images can be compared, both qualitatively, i.e. visually, and quantitatively, i.e. through measured properties.
- Use of standardized color description linked to colorimetry. This also allows assessment of accuracy of color measurements made by the workstation compared to a standard color measuring device like a spectrophotometer. It will also allow realistic display and give the possibility of meaningful exchange of images.
- Possibility of acquiring both clinical and dermatoscopic images.
- Advanced management of images and patient data, tailored for the needs of the dermatology department of the university hospital.
- Tools for the extraction of diagnostically meaningful quantitative data from the acquired images. Once enough data on a range of different types of skin lesions has been accumulated, classification of images may also be attempted.

Chapter 3

Color

Visual aspects of the skin are primordial in dermatology, and thus great care has to be taken when acquiring, handling and storing this information. The topics discussed in this and the next chapter will help us achieve this. They are not meant to be a complete overview of the subject matter of color or color imaging, but are chosen for their relevance to later chapters in this work. For a more in-depth discussion or related topics the reader is referred to [19, 20, 21, 22, 23].

3.1 A few definitions

Color itself is not a physical phenomenon, but rather the subjective interpretation by a human observer of a physical phenomenon, namely electromagnetic energy in the visible spectrum. It is therefore important to define those two terms properly:

Visual stimulus *'A visual stimulus is visible light that is about to be measured or to enter the eye of an observer.'*

Color *'Color is the interpretation by the eyes, the optic nerve and the brain of a visual stimulus. Consequently, color always implies a human observer, real or simulated.'*

The relationship between those two concepts is illustrated in fig. 3.1.

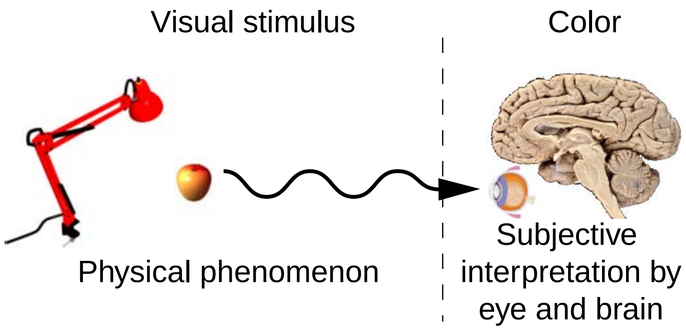

Figure 3.1: Color as the perception of a visual stimulus by a human observer.

3.2 Describing visual stimuli

Without a visual stimulus there is no color to be observed, so let us spend a few words on describing visual stimuli.

A visual stimulus is nothing else than electromagnetic energy in the visible spectrum, i.e. with wavelengths between about 340 and 780 nm, and its composition can be described by a spectrum (spectral radiance or spectral irradiance). Measuring these spectral properties is the field of radiometry, and it provides a very detailed and complete description. Unfortunately, this approach requires sophisticated equipment, is usually slow and generates a lot of unfamiliar data. For some applications it is definitely 'overkill'.

A more compact description of visual stimuli is obtained by measuring devices which are not spectral, but based on just a few, usually broadband, sensors. Such sensors integrate the spectrum of the stimulus based on their spectral sensitivity in order to produce one response per sensor. If these spectral sensitivities are unrelated to the human visual system (HVS) this approach is called *densitometric* and the resulting measurements are not easily correlated with color as defined in section 3.1. If on the other hand, the sensors have spectral sensitivities related to the human visual system, then the device is termed *colorimetric*. In that case the resulting measurements can be used to numerically describe color and color difference. It is clear that densitometric and colorimetric descriptions can be computed from radiometric data, but not the other way around. By definition, it is also impossible to *exactly* transform densitometric into colorimetric data or vice versa. See also fig. 3.2 for an overview.

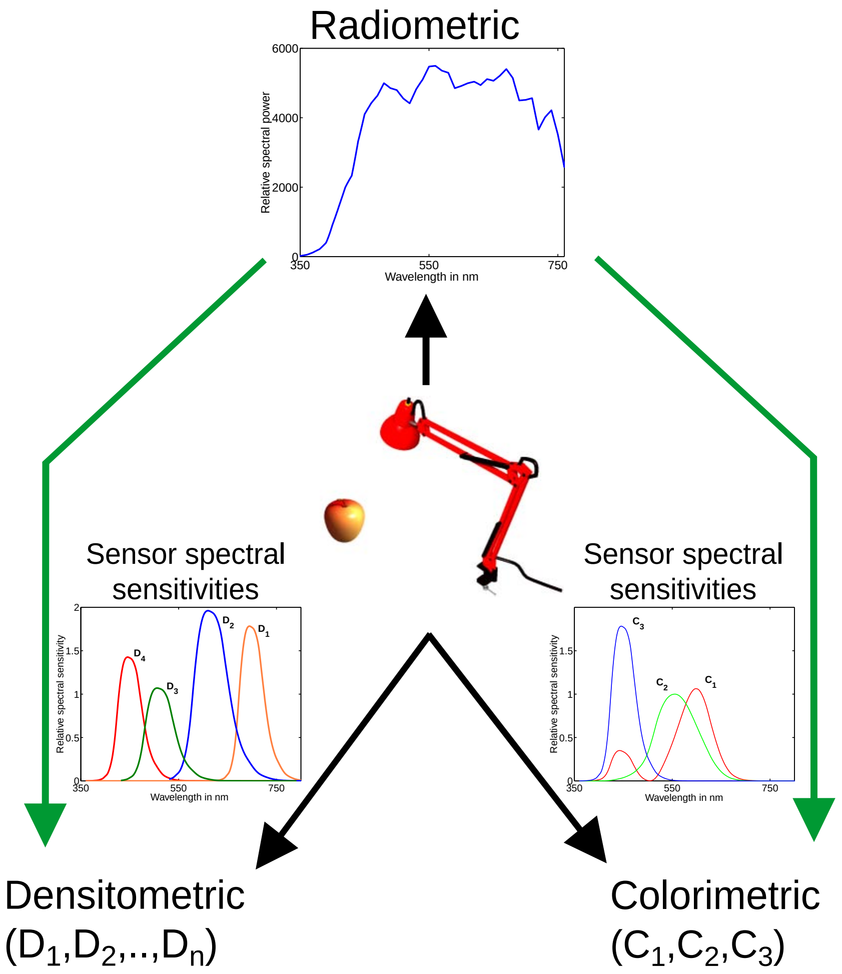

Figure 3.2: The different descriptions of visual information.

3.3 Colorimetry

Over the years several attempts at describing visual stimuli radiometrically using essentially non-spectral devices have been undertaken. This multi-spectral imaging, where a set of visual stimuli describing a whole scene is measured as in [24, 25, 26, 27], is very promising. However, these methods are experimental and generally still unwieldy in the context of clinical dermatology. Moreover, the processing of such spectral images is a field that is still relatively new and uncharted. Consequently, we move our attention to colorimetry as the next best thing. Most of the concepts and methods presented in this section are all defined by the ‘Commision International de l’Eclairage’ or CIE, an international standardizing body in the field of color science.

3.3.1 Definition

Colorimetry is the field of science which numerically describes color and differences between colors. This numerical description must be a continuous function of the radiometric properties of the visual stimulus at the origin of the color under study.

3.3.2 Generation of visual stimuli

The generation of a visual stimulus always starts with a light source, which can be described by its spectral radiant power distribution. If this light source behaves as a black body radiator and follows Planck’s law, then it is possible to describe this spectral distribution using one parameter called the color temperature. However, this is rarely the case and for this reason a quantity called correlated color temperature (CCT) has been introduced. It is defined as the color temperature of a black body radiator that has the same color as the light source under study (the fact that two different visual stimuli may result in the same color is called metamerism, and will be explained later).

An illuminant is an abstraction of a typical light source, and is defined by a radiant spectral power distribution. The CIE has proposed several such illuminants, see also fig. 3.3.

- CIE Illuminant A represents a black body radiator at 2856 K and simulates incandescent lighting;

- CIE Illuminant C is a filtered version of illuminant A and is used as a daylight simulator. Its CCT is 6774 K;

- CIE Illuminant D65 and D50 are daylight simulations statistically defined based upon measurements of real daylight. They have a CCT of 6504 K and 5003 K respectively. D65 is commonly used in colorimetry, while D50 is often used in photography and arts

- CIE F Illuminants represent various types of fluorescent lighting. The spectral characteristics of these sources are very different from those of a black body radiator.

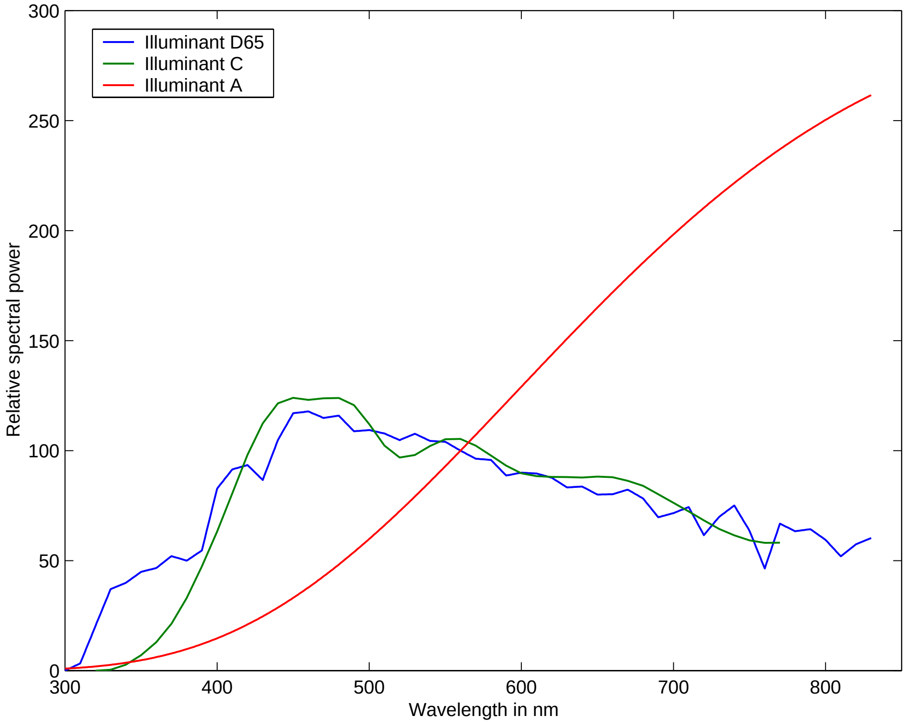

Figure 3.3: Relative radiant spectral radiant power distribution of several CIE illuminants.

The light of a light source can either hit the eye of an observer directly, or be reflected from or transmitted through an object first. In that case the radiant spectral power distribution of the visual stimulus becomes the product of the radiant spectral power distribution of the light source with the spectral reflectance or transmittance of the object, see fig. 3.4.

3.3.3 The human visual system

Colorimetry is tied to the perception of visual stimuli, mainly by the eye and brain which we will now discuss briefly.

The structure of the eye has been investigated thoroughly. As illustrated in fig. 3.5, it is an approximately spherical organ. Light enters through the transparent cornea in front of the eye, and proceeds to the biconvex lens. The shape of the lens can be altered by small muscles in order to provide a sharp image of an object in the fovea of the retina.

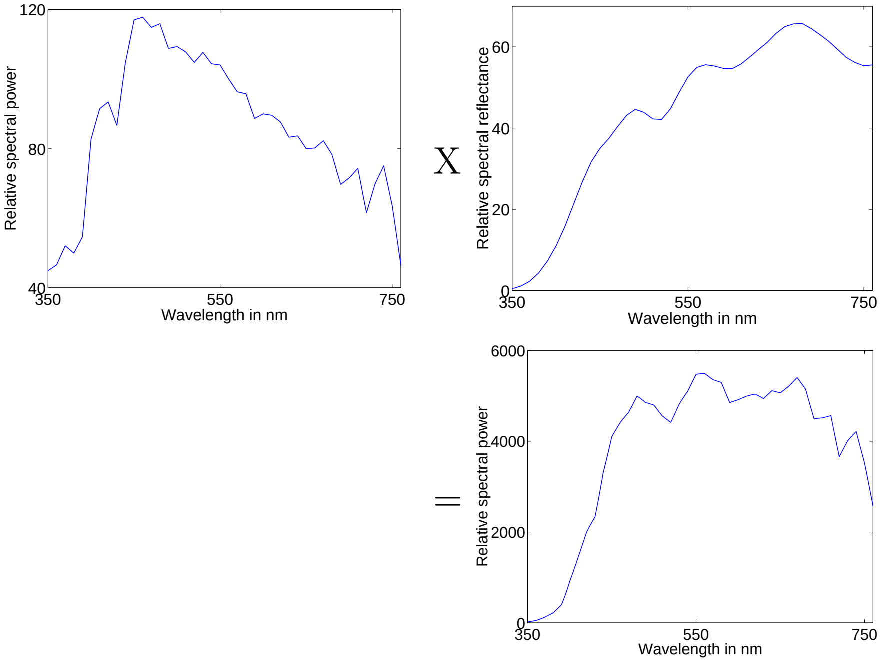

Figure 3.4: Spectral radiant power distribution of a visual stimulus as the product of the spectral radiant power distribution of the light source and the spectral reflectance or transmittance of an object.

The retina has several types of photoreceptor cells called rods and cones. The rods are responsible for low-light or scotopic vision, while the cones come into play under normal light conditions or photopic vision, and are responsible for color vision. There are three types of cones called L, M, and S, which have their maximal spectral sensitivity in the long-, middle and short-wavelength region of the visible spectrum respectively, see fig. 3.6. Behind the rods and cones there are several synaptic layers in the retina, see fig. 3.7. These contain several types of cells which interconnect rods and cones over certain areas, and whose precise function is not well understood. The final layer of ganglion cells is connected to the primary visual cortex in the brain using two pathways; one which is more color sensitive and one which is more contrast sensitive.

The brain plays a role in several visual phenomena, like adaptation to colors and lighting conditions, and memory effects to name but a few. However, no allowance has been made in CIE colorimetry for most of those effects. That is why colorimetry is not a complete description of human color vision.

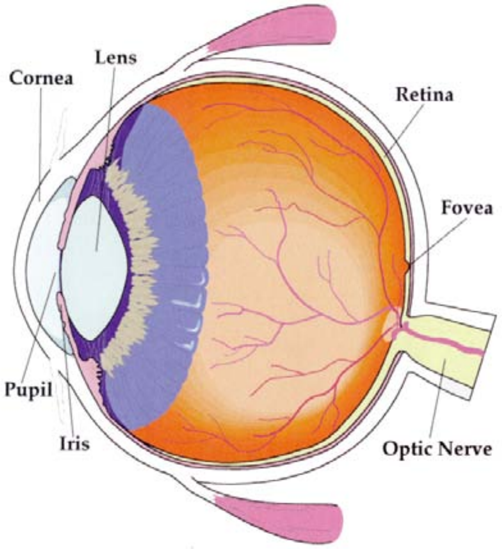

Figure 3.5: The eye. Taken from [21].

3.3.4 Color vision

Several color vision theories have been proposed which explain some visual phenomena and shed some light on certain aspects of the HVS.

The trichromatic theory of vision was based on work by Young, Maxwell and Helmholtz in the 19th century, and is build on the idea that the eye contains three types of cones sensitive in the red-orange, green and blue-violet region of the visible spectrum. The signals generated by these cones are directly fed into the brain where an appropriate 'color sensation' is generated. This theory has long been predominant, but fails to explain some simple visual phenomena like the fact that the combination of red and green stimuli forms a semantically new color 'called yellow', while the combination of green and blue does not and results in what is perceived as a mixture of two semantic colors: green-blue. It also cannot explain the absence of a hue like reddish-green.

The appearance of visual stimuli or color is appropriately described by the opponent-colors theory developed by Hering in the last century. It is based on the generation of bipolar signals depending on wavelength. It successfully explains the reasons for the existence of hues like yellow, red-yellow, yellow-green, green-blue and blue-red. It also explains the absence of hues like reddish-green and yellowish-blue.

Neither of the previous theories was successful in explaining some

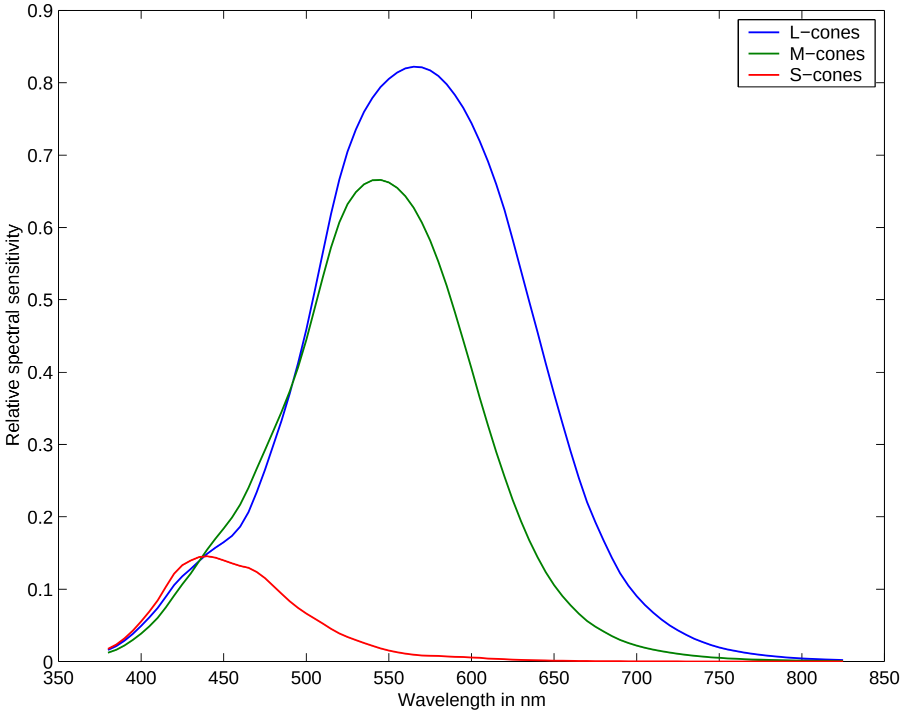

Figure 3.6: The relative spectral responses of the L-, M- and S-cones.

important visual phenomena, until they were combined in the zone theory. Here, vision is divided in zones or stages: a photochemical stage, a chemical stage and a final stage. In the photochemical stage three signals are generated by three types of cones, conform with the trichromatic theory. In the chemical stage two bipolar chromatic signals and one achromatic signal are generated by combining the three signals of the first stage, this time conforming with the opponent-color theory. The coding in the final stage is as yet undefined. See fig. 3.8 for an example of a color vision model based on zone theory.

3.3.5 Color-matching experiments

The trichromatic principle states that almost any color can be reproduced by the combination of three suitably chosen fixed colors called primary stimuli. This principle forms the basis of color-matching experiments used to derive the CIE colorimetric system in 1931. During these experiments an observer was asked to visually match an unknown

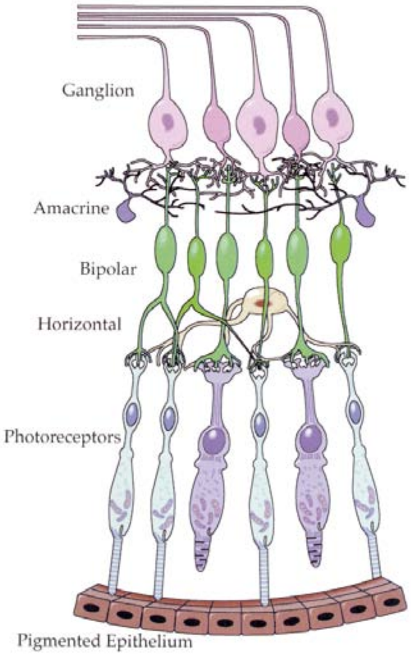

Figure 3.7: The structure of the retina. Taken from [21].

visual stimulus with a second stimulus that is a combination of varying amounts of the three primary stimuli or primaries under the observers control (see fig. 3.9). The primary stimuli were red, green and blue monochromatic visual stimuli, at 700.0 nm, 546.1 nm and 435.6 nm respectively, hence the name *RGB*. The matching areas took up 2° of the visual field.

The color-matching experiment can be described by:

$$\mathbf{Q} \equiv R_Q\mathbf{R} + G_Q\mathbf{G} + B_Q\mathbf{B}, \tag{3.1}$$

with $\mathbf{Q}$ a visual stimulus, and $\mathbf{R}$, $\mathbf{G}$ and $\mathbf{B}$ the fixed primary stimuli. (R_Q, G_Q, B_Q) is called the tristimulus value of $\mathbf{Q}$. The $\equiv$ symbol is used to indicate that the equality of the left- and right-hand terms is not physical or radiometric, but perceptual or colorimetric.

A direct result of the trichromatic principle is that two or more radiometrically completely different visual stimuli may result in the same color, and these are called *metameric stimuli*. This again underlines the fact that it is impossible to recover radiometric properties, e.g. spectral distributions, from colorimetric tristimulus values.

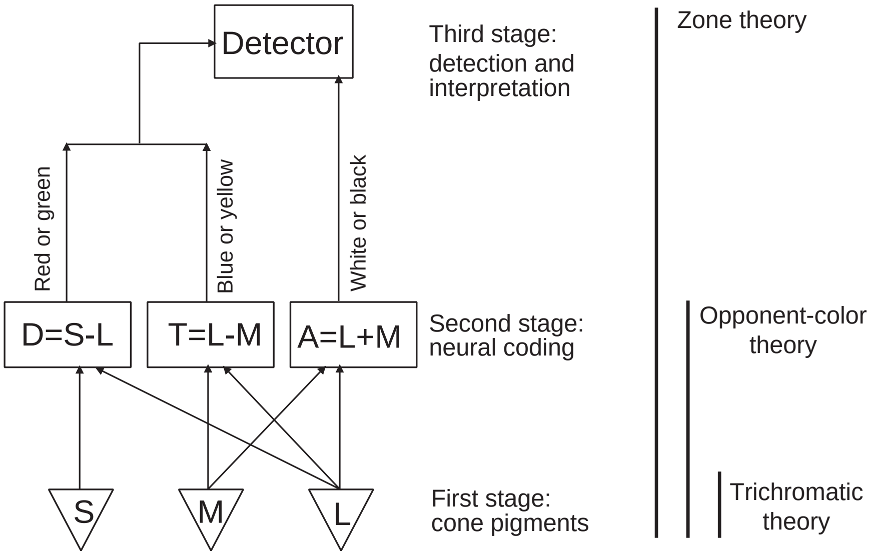

Figure 3.8: Example of a color vision model based on the zone theory. This model also nicely illustrates how the the zone theory is an extension of the opponent-colors which is in its turn an extension of the trichromatic theory. Taken from [20].

Equation (3.1) defines the tristimulus value for any color with respect to a set of primary stimuli, but is not very practical as it means setting up a color-matching experiment for each new visual stimulus. In order to solve this problem and capture all the characteristics of the HVS in a convenient representation, color-matching experiments were performed for monochromatic visual stimuli over the whole visible spectrum:

$$\mathbf{E}_\lambda \equiv R_\lambda \mathbf{R} + G_\lambda \mathbf{G} + B_\lambda \mathbf{B}, \quad \text{with } \lambda \in [360nm - 830nm], \tag{3.2}$$

with $\mathbf{E}_\lambda$ a unit radiant power monochromatic visual stimulus of wavelength λ (a stimulus with $\mathbf{E}_\lambda = 1$ over the visible spectrum is called the *equal-energy stimulus* and notated as $\mathbf{E}$). $(R_\lambda, G_\lambda, B_\lambda)$ are called spectral tristimulus values. This operation was averaged over a group of observers and resulted in the $\overline{r}(\lambda)$, $\overline{g}(\lambda)$ and $\overline{b}(\lambda)$ color-matching functions which define the 2° standard colorimetric observer, see fig. 3.10. The primary stimuli $\mathbf{R}, \mathbf{G}$ and $\mathbf{B}$ have respective power ratios of about $72.1 : 1.4 : 1$. This ensures that the equal-energy stimulus $\mathbf{E}$ is matched by equal amounts of the primary stimuli, i.e. $R_E = G_E = B_E$. This

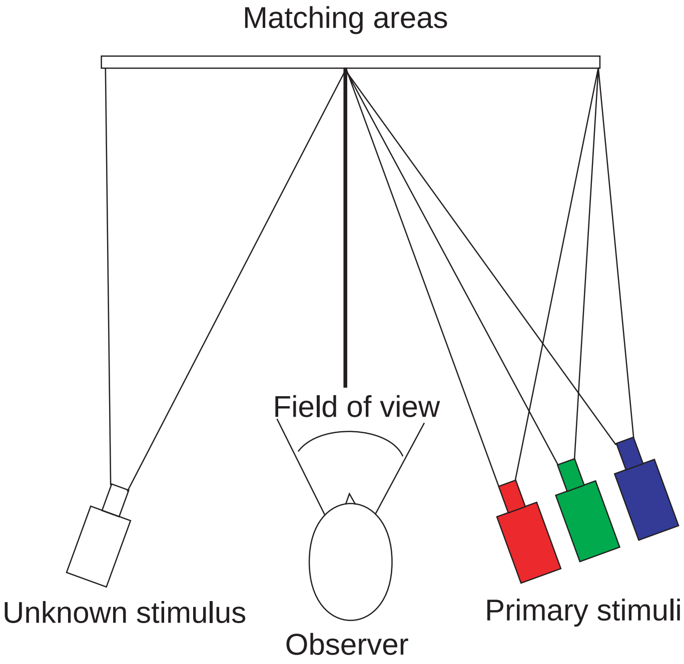

Figure 3.9: Setup of a color-matching experiment whereby an observer tries to match an unknown visual stimulus to a mixture of three primary stimuli.

is a kind of normalisation and is the same thing as requiring that the area under the three color-matching functions is the same. The result of this is that $\overline{r}(\lambda_R)$, $\overline{g}(\lambda_G)$ and $\overline{b}(\lambda_B)$ are all different from each other. The fact that no absolute radiant power requirements have to be met for the primary stimuli explains the apparent power mismatch at the wavelengths of these primaries on fig. 3.10. Based on $\overline{b}(\lambda_B) \sim 0.3$ one would therefore assume that the ratio between the radiant power of the blue primary stimulus and the unit radiant power monochromatic stimuli was about 1/0.3.

In 1964 these experiments were repeated for a larger field of view and primary stimuli at 645.2 nm, 525.3 nm and 444.4 nm respectively, resulting in the $\overline{r}_{10}(\lambda)$, $\overline{g}_{10}(\lambda)$ and $\overline{b}_{10}(\lambda)$ color-matching functions of the 10° standard colorimetric observer. This time the primary stimuli are of unit radiant power so that $\overline{r}_{10}(\lambda_R) = \overline{g}_{10}(\lambda_G) = \overline{b}_{10}(\lambda_B) = 1$.

There are two peculiar characteristics in the figures 3.10 and 3.11: firstly, there are parts of the color-matching functions which are negative, and secondly, the maxima of the color-matching functions are not located at the wavelengths of the primary stimuli.

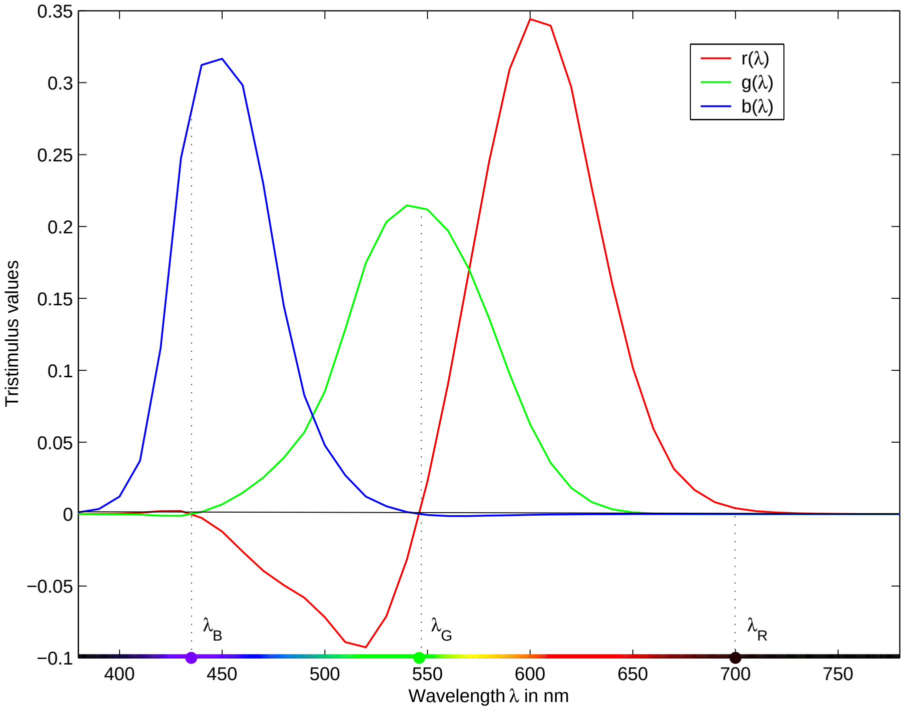

Figure 3.10: The $\overline{r}(\lambda)$, $\overline{g}(\lambda)$ and $\overline{b}(\lambda)$ color-matching functions of the 2° standard colorimetric observer, and the wavelengths λ_R, λ_G and λ_B of the corresponding primary stimuli. The primary stimuli have radiant power ratios 72.1 : 1.4 : 1 so that the equal-energy stimulus **E** has equal tristimulus component values.

The reason for the first characteristic is that it was impossible to obtain a color match for all the monochromatic visual stimuli using a purely additive mixture of the primary stimuli. Indeed, for some stimuli it was necessary to add one of the primary stimuli to the unknown stimulus in order to obtain a match. For the red primary stimulus this is equivalent to rewriting eq. (3.1) as:

$$\mathbf{Q} + R_Q\mathbf{R} \equiv G_Q\mathbf{G} + B_Q\mathbf{B}, \tag{3.3}$$

or, equivalently, to allow a negative value for R_Q in eq. (3.1).

The second characteristic is due to the fact that the luminous efficiency of the eye is not the same for all wavelengths, as shown in fig. 3.12. This curve forms the basis of the field of photometry[1] and is used

---

[1] Photometry was developed prior to colorimetry and is concerned with brightness,

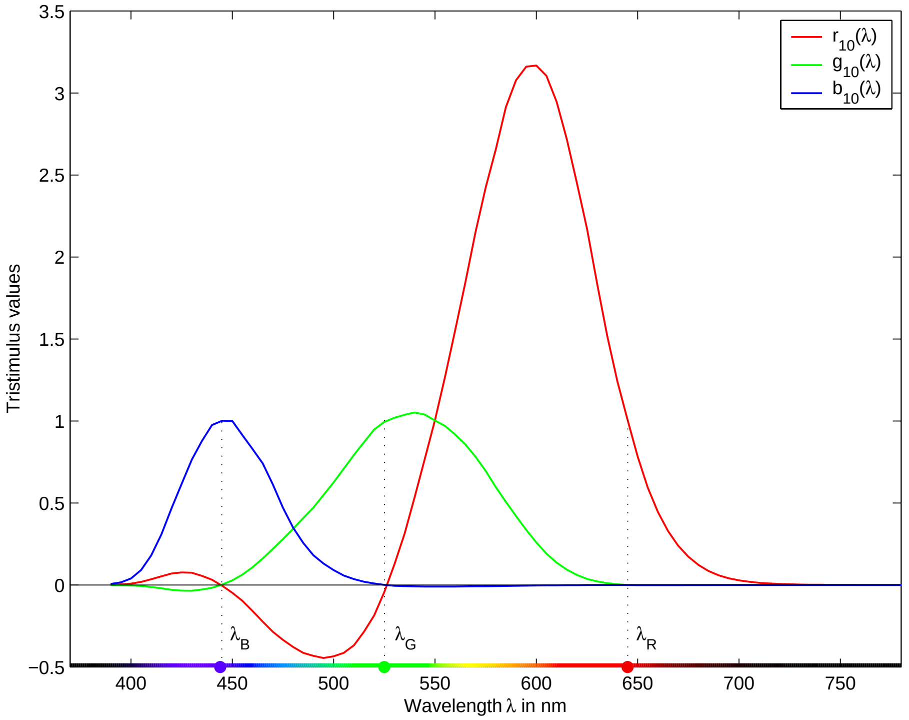

Figure 3.11: The $\overline{r}_{10}(\lambda)$, $\overline{g}_{10}(\lambda)$ and $\overline{b}_{10}(\lambda)$ color-matching functions of the 2° standard colorimetric observer, and the wavelengths λ_R, λ_G and λ_B of the corresponding primary stimuli. The primary stimuli are of unit radiant power so that $\overline{r}_{10}(\lambda_R) = \overline{g}_{10}(\lambda_G) = \overline{b}_{10}(\lambda_B) = 1$.

to compute quantities like the *luminance*[2] from the radiometrical properties of an object. The direct result is that the red primary stimulus **R**, which has a fixed wavelength and is located in a region with very low luminous efficiency, must be turned on more and more in order to obtain a color-match with a monochromatic stimulus moving from λ_R to slightly shorter wavelengths because this stimulus is perceived to be more and more luminous compared to itself. Of course, if the monochromatic stimulus moves too far away from λ_R, the green primary stimulus **G** takes over as the dominant stimulus in the color-match and the above no longer holds. This explains the high peak in the $\overline{r}(\lambda)$ color-matching

---

i.e. the way in which objects seem to emit light as observed by humans. It is based on brightness-matching experiments similar in setup to the color-matching experiments.

[2] The luminance is defined as the integral of the radiance of an object times the luminous efficiency function over the visible spectrum

function located on the left of λ_R. This effect is also present in the $\overline{g}(\lambda)$ and $\overline{b}(\lambda)$ color matching functions, albeit far less pronounced.

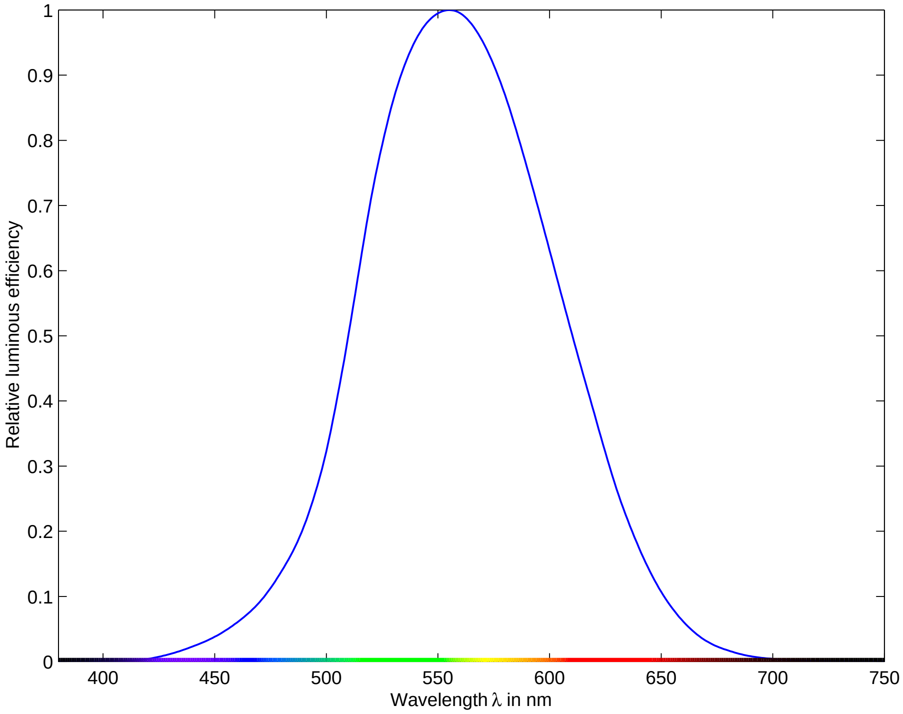

Figure 3.12: The relative luminous efficiency of the human visual system in function of the wavelength.

A visual stimulus $\mathbf{Q}$ can be described radiometrically by its spectral power distribution $Q(\lambda)$. This means $\mathbf{Q}$ can be interpreted as the summation of unit power monochromatic stimuli $\mathbf{E}(\lambda)$, each with strength $Q(\lambda)$, i.e. as:

$$\mathbf{Q} = \int Q(\lambda)\mathbf{E}(\lambda)d\lambda. \tag{3.4}$$

By replacing these unit power monochromatic stimuli by the appropriate amount of primary stimuli according to eq. (3.2) we get (the equality is now no longer physical but only perceptual):

$$\mathbf{Q} \equiv \int Q(\lambda)(\overline{r}(\lambda)\mathbf{R} + \overline{g}(\lambda)\mathbf{G} + \overline{b}(\lambda)\mathbf{B})d\lambda. \tag{3.5}$$

By comparing this equation with eq. (3.1) we get a useful expression for the CIE RGB tristimulus values of $\mathbf{Q}$:

$$\begin{aligned} R_Q &= \int Q(\lambda)\overline{r}(\lambda)d\lambda, \\ G_Q &= \int Q(\lambda)\overline{g}(\lambda)d\lambda, \\ B_Q &= \int Q(\lambda)\overline{b}(\lambda)d\lambda. \end{aligned} \tag{3.6}$$

3.3.6 The CIE XYZ tristimulus space

The determination of CIE RGB tristimulus values as defined in eq. (3.6) posed two problems back in 1931, both due to the negative portions of the color-matching functions (see fig. 3.10). The first one was of a computational nature, but is no longer relevant. The second is that it made the development of a colorimetric measuring device awkward. Indeed, eq. (3.6) meant that it was possible to measure tristimulus values directly using three sensors with spectral sensitivities equal to the color-matching functions $\overline{r}(\lambda)$, $\overline{g}(\lambda)$ and $\overline{b}(\lambda)$. Unfortunately, designing a sensor with a negative spectral sensitivity at certain wavelengths is not easy.

This prompted the CIE to develop a new tristimulus space called CIE XYZ based on new primary stimuli $\mathbf{X}$, $\mathbf{Y}$ and $\mathbf{Z}$ so that the corresponding $\overline{x}(\lambda)$, $\overline{y}(\lambda)$ and $\overline{z}(\lambda)$ color-matching functions would be all-positive. Because equation (3.1) must also hold for primary stimuli and stimuli are additive, it is clear that XYZ tristimulus values (X_Q, Y_Q, Z_Q) of any stimulus $\mathbf{Q}$ and RGB tristimulus values (R_Q, G_Q, B_Q) are related by a linear transform.

With the additional constraint that the Y component be equal to the (photometric) luminance, which is the same as demanding that $\overline{y}(\lambda)$ color-matching function is equal to the luminous efficiency function, the the color-matching functions seen in fig. 3.13 were obtained.

The (X_Q, Y_Q, Z_Q) tristimulus value of a visual stimulus $\mathbf{Q}$ can thus be written as:

$$\begin{aligned} X_Q =& k \int Q(\lambda)\overline{x}(\lambda)d\lambda, \\ Y_Q =& k \int Q(\lambda)\overline{y}(\lambda)d\lambda, \\ Z_Q =& k \int Q(\lambda)\overline{z}(\lambda)d\lambda. \end{aligned} \tag{3.7}$$

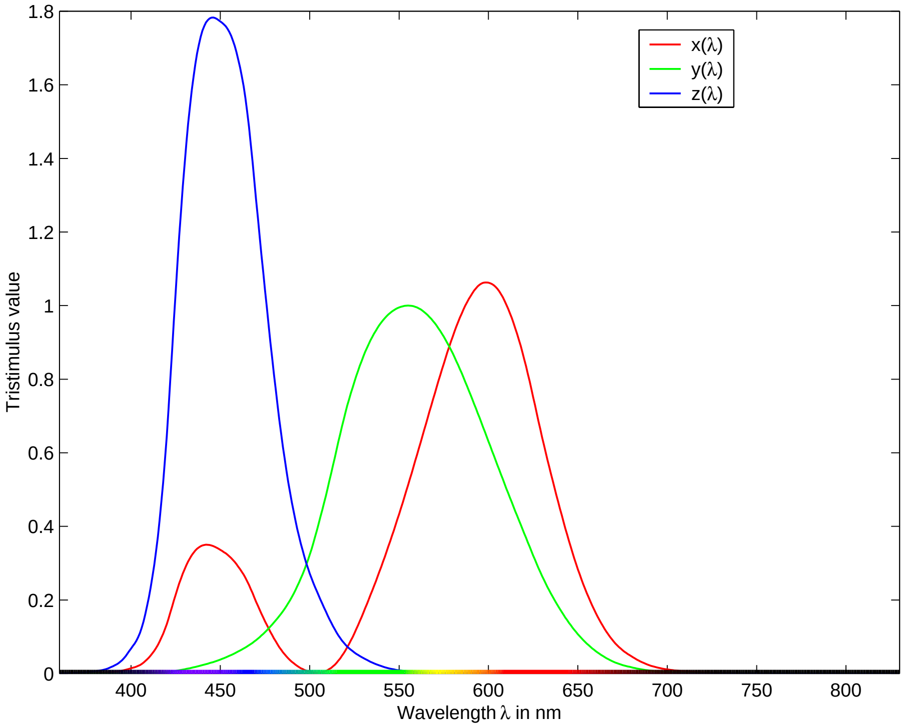

Figure 3.13: The $\overline{x}(\lambda)$, $\overline{y}(\lambda)$ and $\overline{z}(\lambda)$ color-matching functions of the 2° standard colorimetric observer.

k is a normalization constant generally chosen so that a perfectly white diffuse reflector has luminance $Y = 100$. It is possible to exceed this value when specular, i.e. mirror-like, reflection is present.

It has to be noted that the primary stimuli **X**, **Y** and **Z** are imaginary and not physically realisable. In order to explain this we now introduce chromaticity coordinates (x, y, z) defined as follows:

$$\begin{aligned} x =& \frac{X}{X+Y+Z}, \\ y =& \frac{Y}{X+Y+Z}, \\ z =& \frac{Z}{X+Y+Z}. \end{aligned} \tag{3.8}$$

It is clear that $x + y + z = 1$, and that this projective transform compresses 3-dimensional information into 2 dimensions. For this reason the Y tristimulus value is usually used in conjunction with the two chromaticity coordinates x and y in the CIE xyY space, allowing the inversion of the projective transform in eq. (3.8):

$$
\begin{aligned}
X =& \frac{xY}{y}, \\
Z =& \frac{(1.0 - x - y)Y}{y}.
\end{aligned}
\tag{3.9}
$$

Chromaticity coordinates represent color independently of its 'intensity', i.e. two visual stimuli will have the same chromaticity coordinates if their spectral distributions have the same shape, even if they have different total power. Another property of chromaticity coordinates is that all the colors obtained by mixing two visual stimuli will have chromaticity coordinates lying on a straight line between the chromaticity coordinates of these stimuli. This can be extended to all *additive mixtures* of three visual stimuli with non-collinear chromaticity coordinates: they must all lie in a triangle spanned by the chromaticity coordinates of the three stimuli. All these colors together are known as the *gamut* of the color space defined by those primary stimuli. We can take this reasoning even further and apply it to the monochromatic stimuli making up any visual stimulus, see eq. (3.4): any visual stimulus has chromaticity coordinates that lie inside the convex region described by the chromaticity coordinates of the monochromatic stimuli, i.e. the color-matching functions. This convex region is thus the gamut of the HVS, and the line between the red and blue primary stimuli is called the purple line. We can easily see on fig. 3.14 that the primary stimuli $\mathbf{X}$, $\mathbf{Y}$ and $\mathbf{Z}$ all lie outside the gamut of the HVS, which is why they are called imaginary primary stimuli. Also notice how the triangle formed by the RGB primaries $\mathbf{R}$, $\mathbf{G}$ and $\mathbf{B}$ does not span the whole gamut of the HVS, which is why, as explained in the section 3.3.5, some visual stimuli have negative components in their CIE RGB tristimulus value.

3.3.7 Color matching precision and just noticeable color differences

All CIE color spaces were derived using color-matching experiments, and this raises the question of the precision of this procedure. Clearly, the ability of the HVS to notice small color differences will be the main factor here. This ability was first investigated in 1942 by MacAdam [20] using a setup not unlike the color-matching experiments themselves. Indeed, the observer was again asked to match a variable visual stimulus under

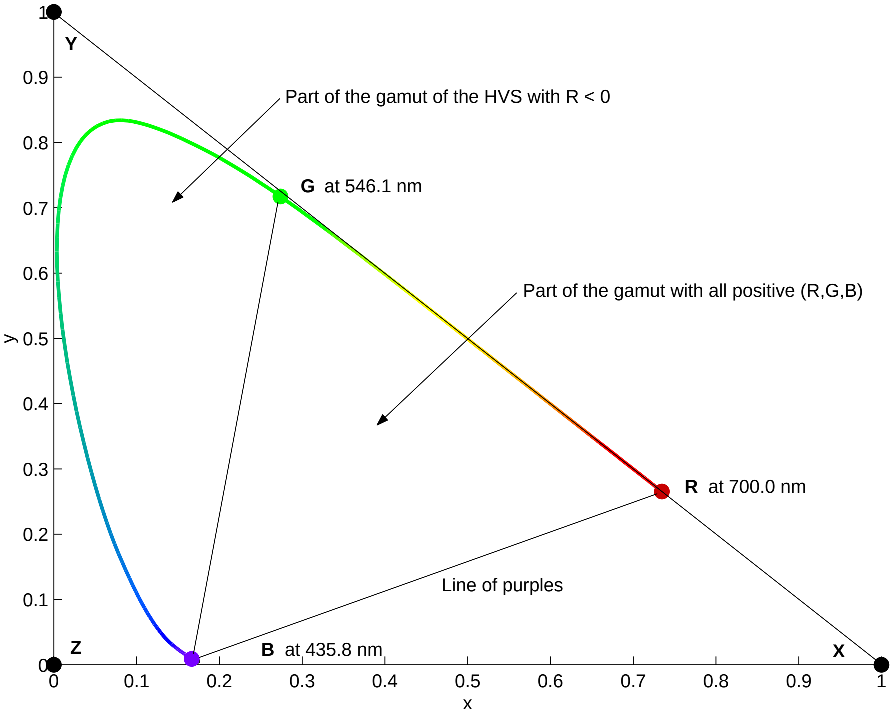

Figure 3.14: Chromaticity diagram showing the gamut of the HVS bounded by the locus of the chromaticity coordinates of the monochromatic stimuli and the so-called purple line. Also shown are the imaginary **X**, **Y** and **Z** and the **R**, **G** and **B** primary stimuli.

his control with a fixed visual stimulus. Both stimuli were mixtures of three primary stimuli. But instead of adjusting the variable stimulus by changing its mixture of primary stimuli, the observer could only turn one control knob which changed the variable stimulus on a straight line in a chromaticity diagram. This line intersected the chromaticity of the fixed stimulus. The experiment was repeated several times, resulting in sets of distances (one set per line) in the chromaticity diagram between the fixed stimulus and the variable stimulus. The premise, based on prior experiments, was that the standard deviation of a set of distances was proportional to the standard deviation of color matching on that line. Moreover, the just noticeable color difference (JND) was found to be equal to about three times this standard deviation. The standard deviation of each line was set out symmetrically as a distance from the fixed stimulus on that line, and was found to approximately lie on an ellipse (see fig. 3.15). The ellipse obtained by setting out three times the standard deviations is called the discrimination ellipse and represents the chromaticities of points with a just noticeable color difference from the center point (more precisely chromaticity difference since the experiments took place under constant luminance). This procedure was repeated for 25 different fixed stimuli, resulting in the so-called MacAdam ellipses in fig. 3.16. Although strictly speaking the conclusions of these experiments are only valid for color matches and not for color differences, they show that color matching precision and the just noticeable color difference varied strongly over the gamut of the HVS in a chromaticity diagram. Work by Wright and Wyszecki [20] on actual color differences showed that similar conclusions could be drawn for color differences in general.

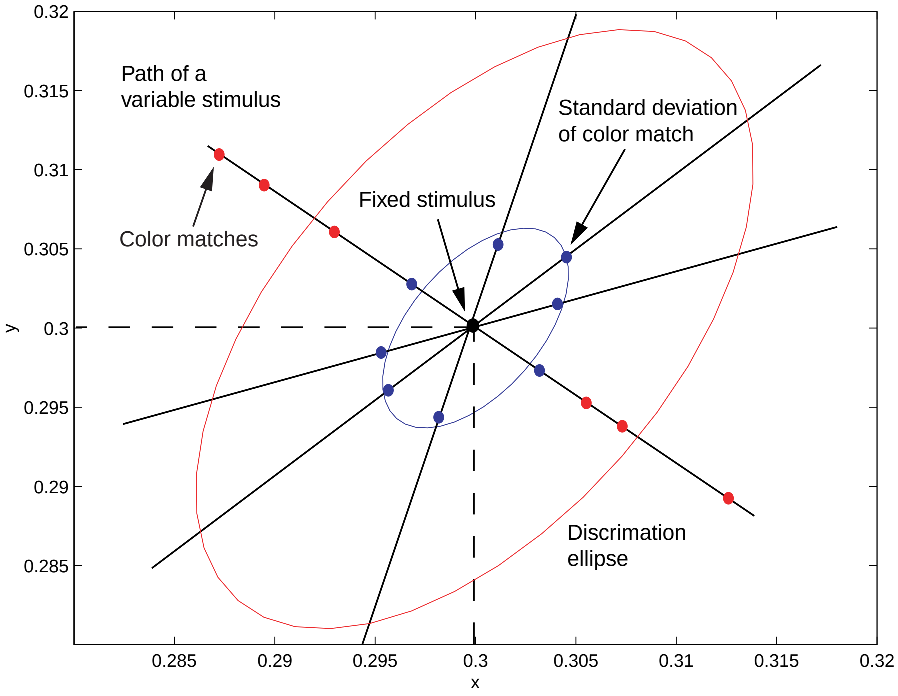

Figure 3.15: Derivation of a MacAdam ellipse from color matching around a fixed stimulus and on straight lines in the chromaticity diagram.

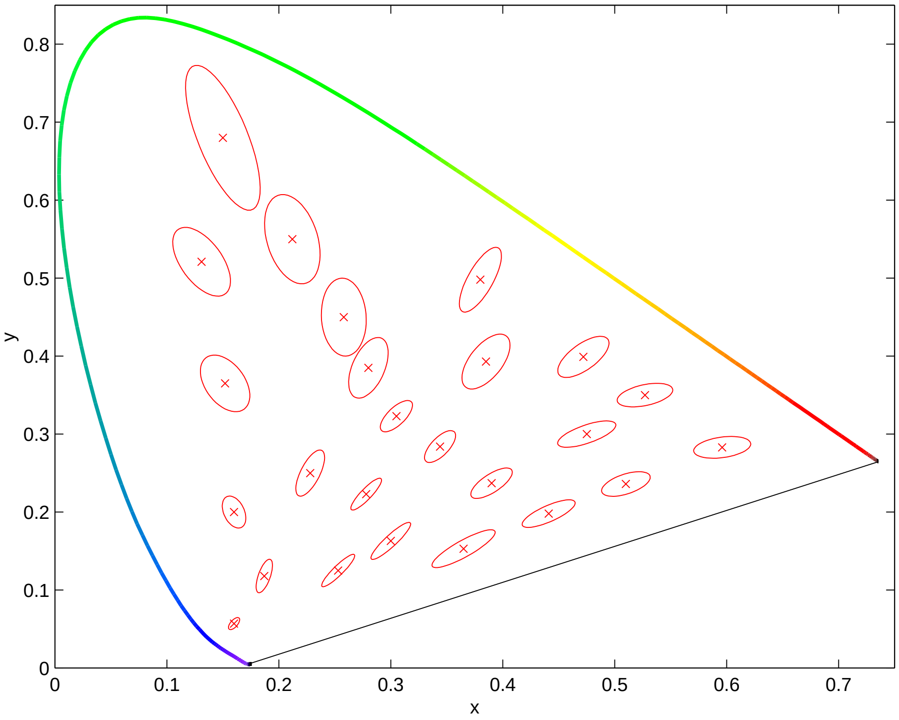

Figure 3.16: MacAdam color matching precision ellipses in a chromaticity diagram. Ellipses are drawn 10 times larger than in reality.

3.3.8 The CIE L*a*b* color space

As mentioned in the previous section, the CIE XYZ space is fine for describing color but inadequate for describing color differences because these differences will strongly depend on where they are located in the XYZ color space. As a result the CIE proposed two so-called perceptually uniform color spaces in 1976: CIE $L^*u^*v^*$ and CIE $L^*a^*b^*$. In those spaces the Euclidean distance between two stimuli is proportional to their perceived color difference, or, in other words, in these spaces the MacAdam ellipses of fig. 3.16 become circles with constant radius. Over the years CIE $L^*a^*b^*$ has rightfully gained importance over CIE

$L^*u^*v^*$, and its values (L^*, a^*, b^*) are defined as:

$$\begin{aligned} L^* =& 116 f(Y/Y_w) - 16, \\ a^* =& 500(f(X/X_w) - f(Y/Y_w)), \\ b^* =& 200(f(Y/Y_w) - f(Z/Z_w)), \\ f(t) =& \begin{cases} 7.787t + \frac{16}{116} & \text{if } t < 0.008856, \\ t^{1/3} & \text{if } 0.008856 \leq t \leq 1. \end{cases} \end{aligned} \tag{3.10}$$

The L^* is called lightness, and is a measure for which an objects seems to emit light. The a^* is a measure of redness-greenness, and b^* is a measure of yellowness-blueness. The tristimulus (X_w, Y_w, Z_w) is that of the reference white in the visual field, and is used to model a visual phenomenon called chromatic adaptation. This phenomenon is a sort of individual gain control of the L-, M- and S-cones of the eye and their pathways, as laid down by von Kries. It allows an observer to compensate for a surplus of long- or short-wavelength light, so that e.g. a white paper remains white under yellow incandescent as well as under bluish fluorescent lighting. Because the adaptation is performed on the XYZ stimuli instead of the cone responses this is sometimes termed 'wrong von Kries transform' [21]. Also notice how the L^*, a^* and b^* in eq. (3.10) are similar to some vision models based on the zone theory: formation of one achromatic and two chromatic responses based on differences between cone-like signals.

The perceptual color difference ΔE^*_{ab} between two colors (L^*_1, a^*_1, b^*_1) and (L^*_2, a^*_2, b^*_2) is given by:

$$\begin{aligned} \Delta L^* =& L^*_1 - L^*_2, \\ \Delta a^* =& a^*_1 - a^*_2, \\ \Delta b^* =& b^*_1 - b^*_2, \\ \Delta E^*_{ab} =& \sqrt{(\Delta L^*)^2 + (\Delta a^*)^2 + (\Delta b^*)^2}. \end{aligned} \tag{3.11}$$

To put ΔE^*_{ab} values into perspective we can say that the JND between two colors is $\Delta E^*_{ab} = 1$. In practice such a small color difference is only visible to a very skilled observer, and usually errors below $\Delta E^*_{ab} = 3$ go unnoticed by a casual observer. Errors of $\Delta E^*_{ab} \geq 5$ are clearly visible.

The goal of obtaining a perceptually uniform color space was not completely achieved with CIE $L^*a^*b^*$, and recently several modifications and extensions have been proposed, most notably by the CIE in 1994 with their CIE94 color difference equation noted as ΔE^*_{94}.

3.3.9 Colorimetric measuring devices

There are two main types of colorimetric measuring devices: those performing spectral measurements, i.e. spectrophotometers (SPM) and spectroradiometers, and those based on tristimulus measurements, i.e. colorimeters. Both types of devices make average measurements over a fixed area, i.e. they perform spot measurements, and are thus usually not suitable for measuring skin lesions which may have very irregular shapes and contain several distinct ‘subregions’. We will restrict ourselves to colorimetric measurements of objects which are only reflecting and not emitting light.

The colorimeter is the simpler device, and is based on sensors with spectral sensitivities proportional to the $\overline{x}(\lambda)$, $\overline{y}(\lambda)$ and $\overline{z}(\lambda)$ color-matching functions. This means the sensor responses are proportional to the (X, Y, Z) tristimulus values of the object under study. The light source used to illuminate the objects is usually close to a CIE illuminant, as it is not possible to predict the tristimulus values under another light source than the one used for the measurement due to possible metameric effects.

The SPM is a spectral device consisting of many narrow bandwidth sensors distributed over the visual spectrum. It usually doesn’t measure absolute radiometric quantities (this is left to the very similar spectroradiometer), but instead produces a relative spectral distribution which can easily be converted numerically to tristimulus values using the $\overline{x}(\lambda)$, $\overline{y}(\lambda)$ and $\overline{z}(\lambda)$ color-matching functions. Because this relative spectrum is the product of the spectrum of the used light source with the spectral reflectance of the object, see fig. 3.17, it is easy to compensate for this and predict the spectrum and tristimulus values of the object under any light source with known spectral distribution (SPMs usually come with the spectra of several CIE illuminants stored internally). SPMs are generally more precise and more accurate than colorimeters, and we will use them as reference devices when evaluating other ways of measuring colorimetric properties.

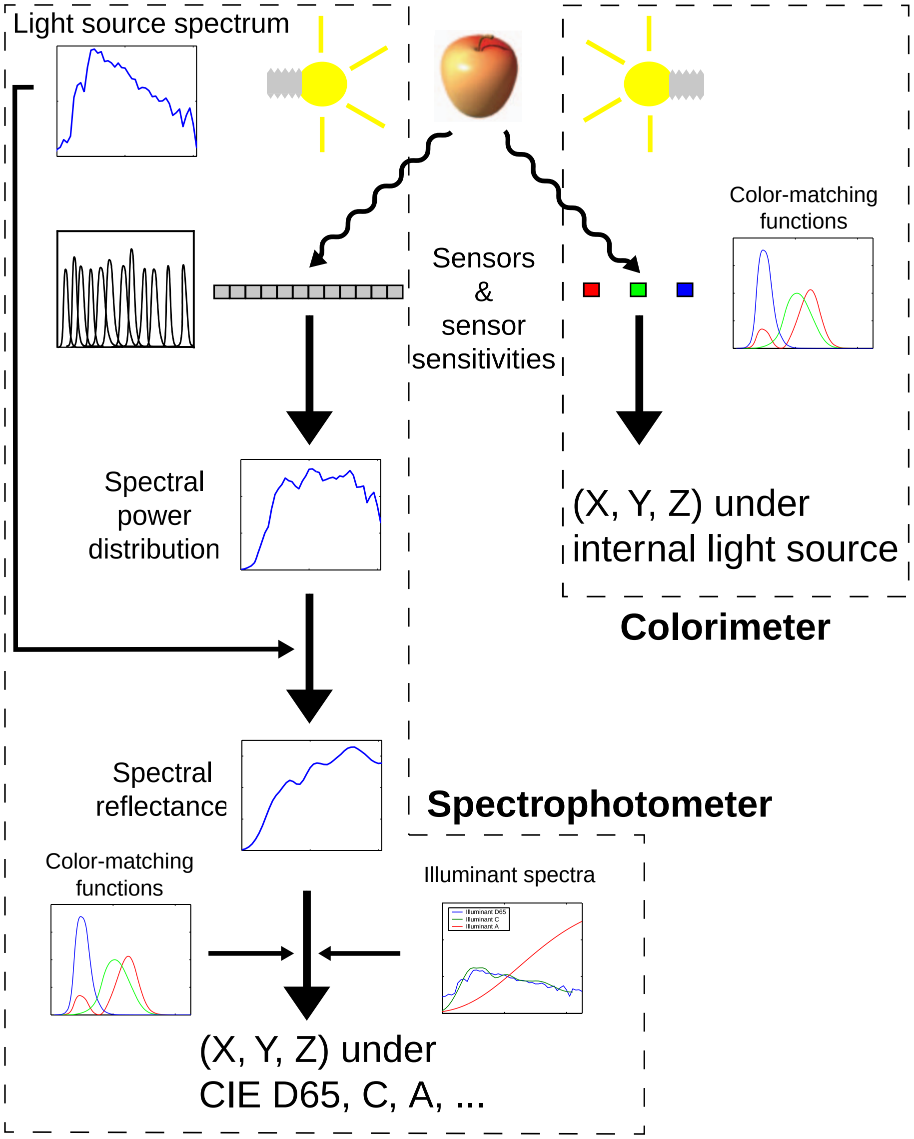

Figure 3.17: Schematic view of the operation of a spectrophotometer (left) and a colorimeter (right)

Chapter 4

Building the imaging system

In the previous chapter we have given ourselves the means of describing and measuring visual stimuli properly. Images can be seen as collections of such measurements, and we now move on to the acquisition, processing and reproduction of such images by an imaging system, keeping the general goals set out in chapter 1 in mind. Each of these tasks can more or less be identified with a distinct set of hardware and software components, i.e. a subsystem, of the imaging system. In this chapter emphasis will be on the operation of the individual acquisition, processing and reproduction subsystems, deferring review of the operation and use of the imaging system as a whole to chapter 5. The software tools and applications which, together with the imaging system, make up the dermatological workstation will be reviewed in chapter 6.

4.1 The computer and the software

A personal computer (PC) with a 150 MHz pentium processor, 80 MBytes of internal memory and running Microsoft Windows NT 4.0 forms the core not only of the imaging system, but of the whole dermatological workstation. Besides forming the main part of the image processing subsystem, it is also responsible for most of the communication between the imaging system subsystems, and allows control of the acquisition and reproduction subsystems using software modules. Another module sits on top of these and so doing controls the imaging system as a whole. Any application on the dermatological workstation that wants to access the imaging system must go through this last module.

Most of the software was developed using Microsoft Visual Basic (VB). This high-level language allows fast modular software development and easy graphical user interface (GUI) building, [28, 29, 30, 31]. For time critical routines the C language [32] was used to develop libraries that are called from VB.

4.2 Color image reproduction

Online viewing and comparison of images of skin lesions will be one of the main functions of the dermatological workstation. Consequently, we will concentrate ourselves on display devices for the imaging system and disregard other reproduction devices like color printers for the moment.

There are two main types of display devices in use today: conventional cathode ray tube based displays (CRT), and flat panel displays based on technologies like thin film transistors (TFT), liquid crystals (LCD), plasma technology, etc. .... Although flat panel displays are becoming more widespread due to their low power consumption and small size, they remain expensive compared to CRT displays. They also generally exhibit lower resolution, lower contrast, smaller viewing angle and a limited color gamut, for the moment at least. As a result a CRT display device was chosen for the imaging system.

4.2.1 Additive and subtractive color reproduction

A CRT color display reproduces colors by *additively* mixing suitable amounts of light originating from a red, green and blue light emitting phosphor (see fig. 4.1 (a)). There is also another way of reproducing color called *subtractive color reproduction*. Here light is absorbed rather than emitted, and this is the way dyes or inks reproduce color. Subtractive color reproduction requires external light for viewing, and the results will greatly vary according to that external light. Fig. 4.1, (b), shows how the widely used cyan, magenta and yellow primary stimuli are mixed to produce other colors.

4.2.2 CRT display primary stimuli and RGB space

The red, green and blue phosphors of the CRT can be seen as the primary stimuli of a RGB tristimulus color space, just as the monochromatic red, green and blue primary stimuli of the CIE RGB tristimulus space. However, because we are working with a purely additive device, negative tristimulus value components are impossible here. This results in a reduced and triangular gamut in the CIE xy chromaticity diagram,

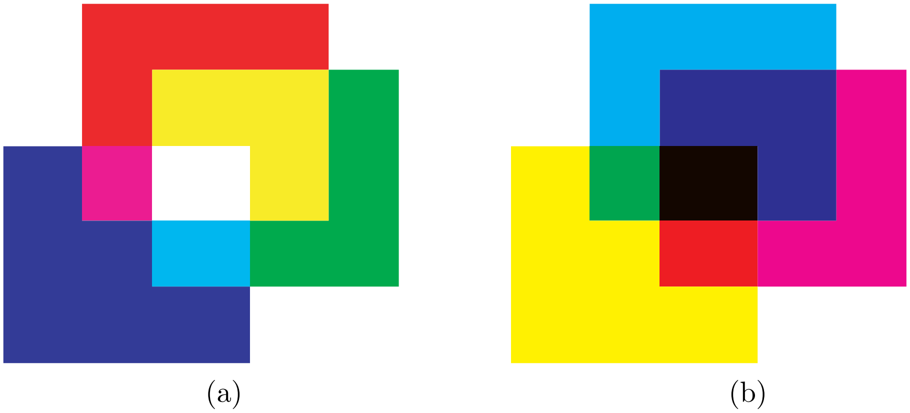

Figure 4.1: Additive and subtractive color reproduction

spanned by the chromaticity coordinates of the primary stimuli, see fig. 4.2. Another important point of the RGB space is obtained by combining the primary stimuli at maximum intensity, and is known as the *white point*. It is characterized by its chromaticity coordinates or by its CCT. The obtained RGB color space will be specific to the CRT or similar additive device under study, and is therefore termed 'device-dependent'. Clearly, it is impossible to accurately reproduce an image defined in a certain RGB space if the primary stimuli and white point of that space are unknown.

4.2.3 CRT display gamma

The red, green and blue light-emitting phosphors of the CRT are excited by three electron guns. These are driven by control signals which, in case of a computer monitor, are generated from digital RGB values in the computer memory using digital-to-analog converters (DAC), see fig. 4.3. The problem with this setup is that the amount of light or, more precisely, the luminance Y emanating from the screen of a CRT is not a linear function of the control voltage V applied to the electron guns. Instead it can be modeled by a power law:

$$Y = kV^{\gamma}, \tag{4.1}$$

with γ known as the *display gamma*, see fig. 4.4. Typical values for display gamma are between 2 and 3, e.g. 2.2 for NTSC and 2.8 for PAL and SECAM television.

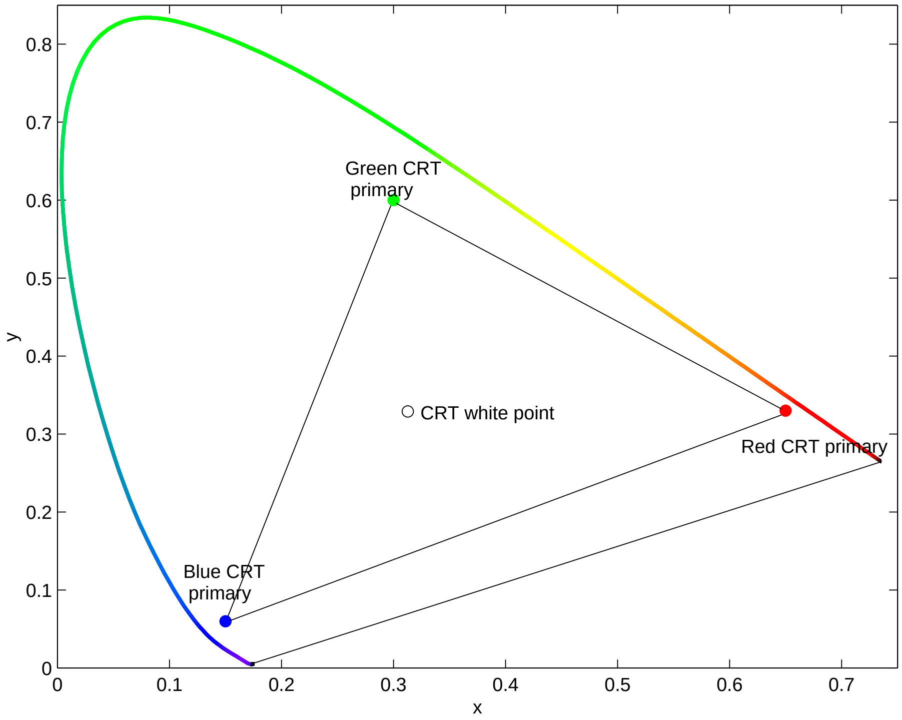

Figure 4.2: The gamut of a CRT display in a chromaticity diagram, based on the given red, green and blue primary stimuli.

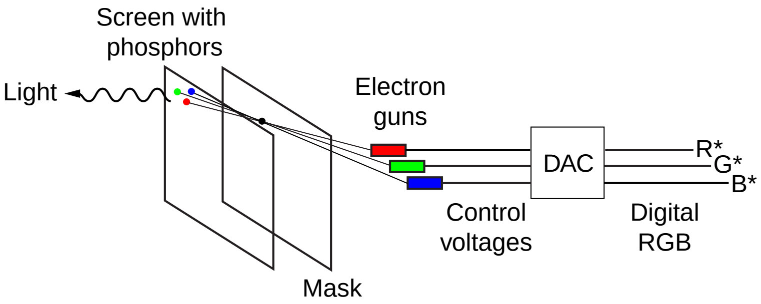

Figure 4.3: Operation principle of a CRT display of a computer.

This non-linearity has to be compensated when driving a CRT by applying what is known as the *gamma correction*. For N-bit digital linear-light RGB tristimulus component values $P = R, G, B$ the transformation to gamma-corrected $R^*G^*B^*$ component values $P^* = R^*, G^*, B^*$

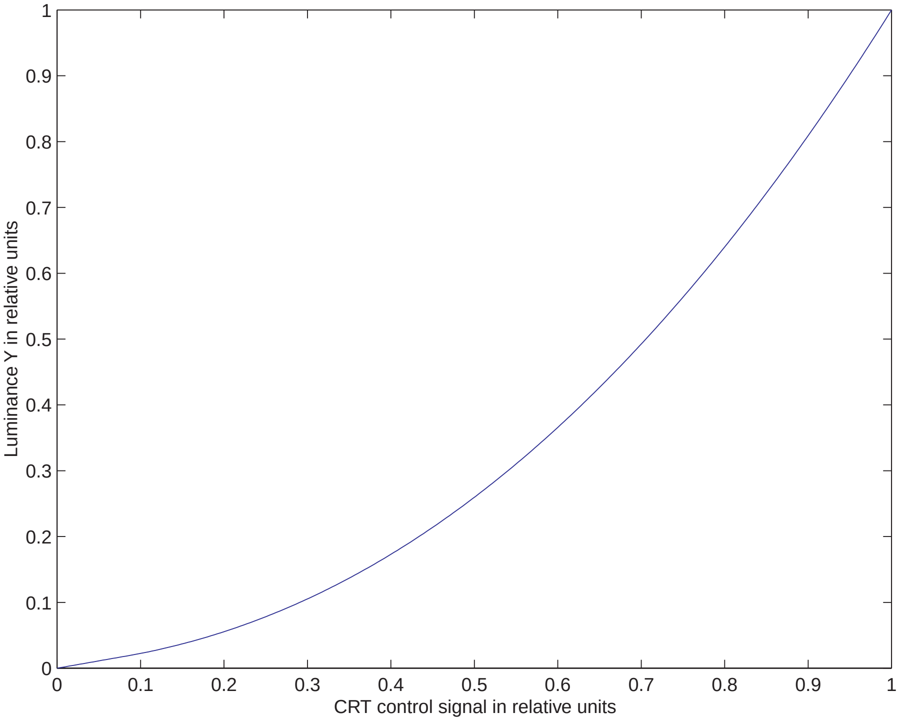

Figure 4.4: Relation between display luminance and control signal voltage.

takes on the following general form:

$$P^* = (2^N - 1)(\frac{P}{2^N - 1})^{\frac{1}{\gamma}}. \tag{4.2}$$

This is also illustrated in fig. 4.5 for 8-bit values.

At first sight this phenomenon seems to complicate matters unnecessarily, but instead gamma correction turns out to have some important benefits. Indeed, due to an extraordinary coincidence the non-linear behavior of a CRT, eq. (4.1), and the non-linear behavior of human vision as described by the cube root function used in the CIE $L^*a^*b^*$ space, eq. (3.10), are almost each others inverse. The result is that gamma-corrected digital or analog signals are perceptually much more uniform than their linear-light counterparts, and thus exhibit a more 'compact' representation of color. This has important repercussions when transforming RGB components to a representation with a limited resolution. This is called quantization, and examples of such operations are the digitization of analog RGB signals by an analog-to-digital converter (ADC),

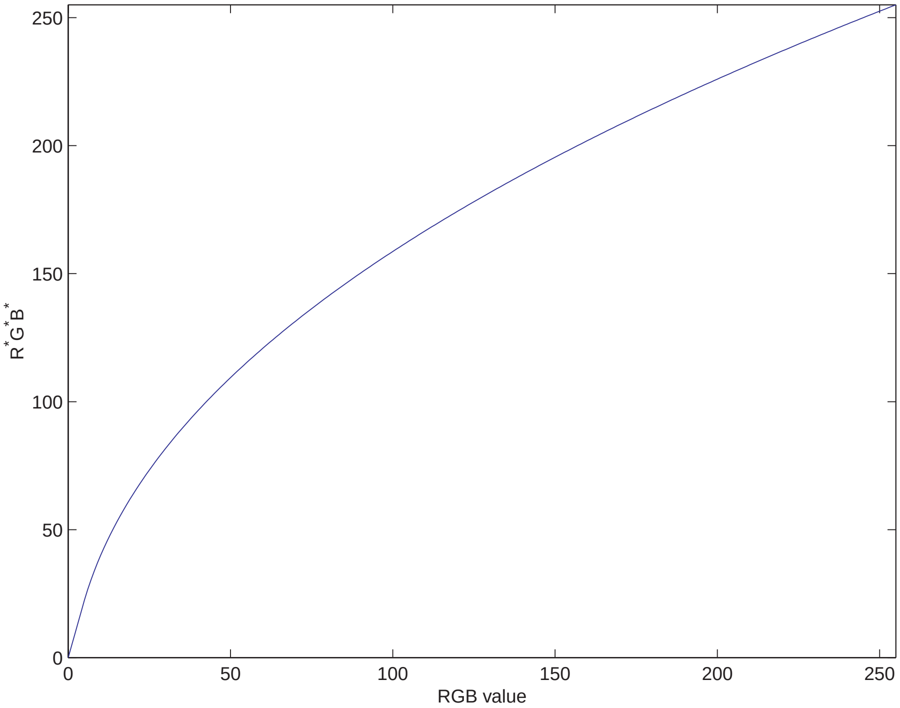

Figure 4.5: Gamma correction of 8-bit digital RGB to $R^*G^*B^*$ component values.

or the conversion on a computer of RGB tristimulus components from a high-precision floating point numeric representation to e.g. an 8-bit per component integer representation to diminish the memory footprint of an image. To demonstrate this error due to quantization the perceptual color differences in a typical RGB color space were computed between all possible tristimulus values (R, G, B) and $(R+\Delta Q, G+\Delta Q, B+\Delta Q)$, where ΔQ is half a quantization step. The same was done in the associated $R^*G^*B^*$ color space ($\gamma = 2.2$). To make the effect more clearly visible and limit the number of computations a quantization to a 5 bits was performed, and the results in ΔE^*_{ab} units can be seen in fig. 4.6. The actual location of the quantization errors in the color space can be deduced from fig. 4.7. Although this figure is limited to the errors in the planes through the axes, further investigations confirm that the highest errors are concentrated around the origin and the axes, and these areas represent the darker colors.

Fig. 4.8 shows the effect this may have on a real image. Notice how,

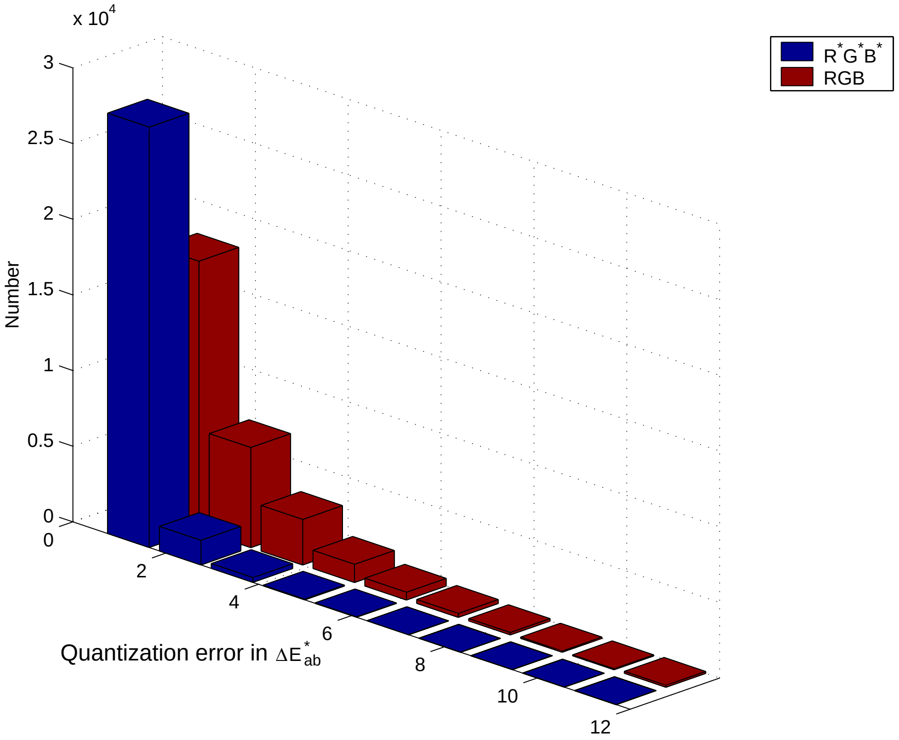

Figure 4.6: Histogram of ΔE^*_{ab} errors due to 5-bit per color component quantization for a typical RGB and associated $R^*G^*B^*$ color space ($\gamma = 2.2$). The average color differences were $\langle \Delta E^*_{ab} \rangle = 2.0$, with $\Delta E^*_{ab} \leq 23.0$ in RGB, and $\langle \Delta E^*_{ab} \rangle = 1.5$, with $\Delta E^*_{ab} \leq 6.6$ in $R^*G^*B^*$ respectively.

as predicted by fig. 4.7, the problem is worst for the darker colors and results in more clearly visible 'banding' in the dark blue portions of the sky on the left and in the dark zones underneath the wing on the right.

For digital RGB tristimulus values one can compute that 12 to 14 bits resolution per color component are needed to avoid visual artifacts, while 8 to 9 bit suffice for $R^*G^*B^*$ values. The same sort of reasoning goes for analog signals, where gamma-corrected signals need less bandwidth than linear-light signals. This fact is eagerly exploited in video encoding and broadcasting, and is also the reason why gamma correction is traditionally done at the source, e.g. in a camera, rather than in the display device.

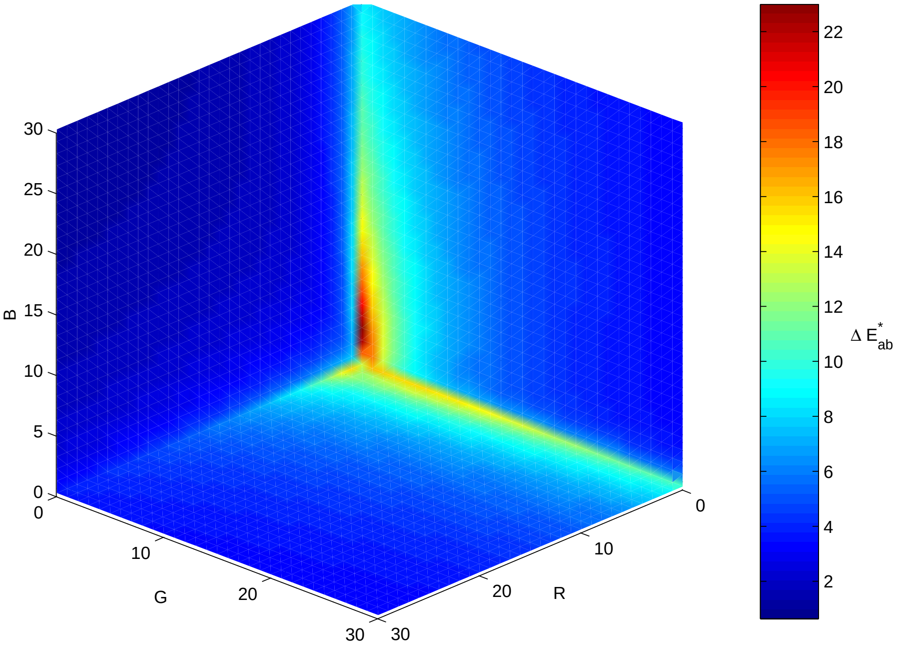

Figure 4.7: Distribution of ΔE^*_{ab} errors due to 5-bit per color component quantization for a typical RGB color space in the 3 planes containing the axes.

4.2.4 The sRGB color space

The $sRGB$ color space is a standardized RGB color space with well-defined primary stimuli, white point (CIE D65) and gamma correction [33]. It is based on the ITU-R BT.709 standard for high-definition television (HDTV). These two standards are supposedly compatible, and it seems the terms $sRGB$ and ITU-R BT.709 are sometimes used interchangeably. In any case, the reference primaries in $sRGB$ and ITU-R BT.709 are the same and are representative for many modern computer monitors, provided the white point is properly set at 6500K and not at 9300K as is more usual (see table 4.1). All of this means encoding images in this color space will ensure reasonable viewing accuracy over a wide range of monitors. The gamut of the sRGB color space, see fig. 4.9, is smaller than that of the HVS.

CIE XYZ and $sRGB$ color spaces are related by a linear transform. Using a column vector notation for the respective tristimulus values

Figure 4.8: Effect of quantization to 5 bit in $R^*G^*B^*$ (top) and RGB color space (bottom). Notice the restricted number of colors in the dark blue regions of the sky, and underneath the wing, leading to an increased banding in the bottom image.

	Red	**Green**	**Blue**	**White point**
x	0.640	0.300	0.150	0.3127
y	0.330	0.600	0.060	0.3291
z	0.030	0.100	0.790	0.3583

Table 4.1: Chromaticities of *sRGB* primary stimuli and white point.

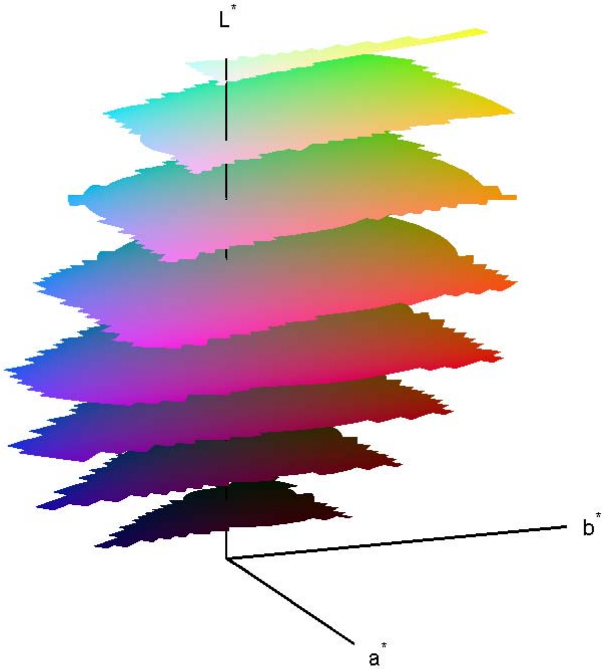

Figure 4.9: The gamut of the *sRGB* color space in the CIE $L^*a^*b^*$ color space.

$(\mathcal{R}, \mathcal{G}, \mathcal{B})$ and (X, Y, Z), this can be written as:

$$\begin{aligned}\begin{pmatrix} X \\ Y \\ Z \end{pmatrix} =& \Phi_{sRGB \rightarrow XYZ} \begin{pmatrix} \mathcal{R} \\ \mathcal{G} \\ \mathcal{B} \end{pmatrix} \\ =& 100 \begin{pmatrix} 0.412453 & 0.357580 & 0.180432 \\ 0.212671 & 0.715160 & 0.072169 \\ 0.019334 & 0.119193 & 0.950227 \end{pmatrix} \begin{pmatrix} \mathcal{R} \\ \mathcal{G} \\ \mathcal{B} \end{pmatrix}, \end{aligned} \tag{4.3}$$

and

$$\begin{aligned}\begin{pmatrix}\mathcal{R}\\ \mathcal{G}\\ \mathcal{B}\end{pmatrix} &=\Phi_{XYZ\rightarrow sRGB}\begin{pmatrix}X\\ Y\\ Z\end{pmatrix}\\ &=\Phi^{-1}_{sRGB\rightarrow XYZ}\begin{pmatrix}X\\ Y\\ Z\end{pmatrix}\\ &=1/100\begin{pmatrix}3.240479 & -1.537150 & -0.498535\\ -0.969256 & 1.875992 & 0.041556\\ 0.055648 & -0.204043 & 1.057311\end{pmatrix}\begin{pmatrix}X\\ Y\\ Z\end{pmatrix}. \end{aligned} \tag{4.4}$$

The *sRGB* component values are comprised between 0 and 1, while for the XYZ components $Y = 100$ represents a perfect white diffuser.

The ITU-R BT.709 gamma correction function for $\mathcal{P} = \mathcal{R}, \mathcal{G}, \mathcal{B} \in [0,1]$ resulting in values $\mathcal{P}^* = \mathcal{R}^*, \mathcal{G}^*, \mathcal{B}^* \in [0,1]$ is defined as:

$$\mathcal{P}^*_{ITU} = \Gamma_{ITU}(\mathcal{P}) = \begin{cases} 4.5\mathcal{P} & 0 \leq \mathcal{P} \leq 0.018 \\ 1.099(\mathcal{P})^{0.45} - 0.099 & 0.018 < \mathcal{P} \leq 1.0. \end{cases} \tag{4.5}$$

The inverse gamma correction is easily deduced as:

$$\mathcal{P}_{ITU} = \Gamma^{-1}_{ITU}(\mathcal{P}^*) = \begin{cases} \mathcal{P}^*/4.5 & 0 \leq \mathcal{P}^* \leq 0.081 \\ \Big((\mathcal{P}^* + 0.099)/1.099\Big)^{(1/0.45)} & 0.081 < \mathcal{P}^* \leq 1.0. \end{cases} \tag{4.6}$$

Eq. (4.5) is similar to the NTSC gamma correction of $\gamma = 2.2$, and incorporates a correction for the dim viewing surroundings of a television screen. When performing gamma correction at the source, e.g. a camera, a factor of $\frac{1}{\gamma} = 0.45$ is generally used. The gamma correction defined for the *sRGB* values $\mathcal{P} = \mathcal{R}, \mathcal{G}, \mathcal{B}$ in [33] is actually slightly different:

$$\mathcal{P}^*_{sRGB} = \Gamma_{sRGB}(\mathcal{P}) = \begin{cases} 12.92\mathcal{P} & 0 \leq \mathcal{P} \leq 0.00304 \\ 1.055(\mathcal{P})^{(1/2.4)} - 0.055 & 0.00304 < \mathcal{P} \leq 1.0. \end{cases} \tag{4.7}$$

We have, however, always used eq. (4.5) and (4.6) on both *sRGB* and *RGB* tristimulus component values, and will henceforth drop the subscript ‘ITU’. This is not so important as long as the correct inverse gamma correction is applied.

When representing $sR^*G^*B^*$ tristimulus component values by 8 bits the average quantization error is $\langle \Delta E^*_{ab} \rangle = 0.18$ with $\Delta E^*_{ab} \leq 0.93$.

4.3 Color image acquisition

The color image acquisition of the imaging system will be performed by a charge coupled device (CCD) camera, and digitized by a so-called frame grabber. The idea is to set up these two devices so that full use is made of their dynamic range, and so that reproducible images are obtained. This requires precise knowledge and control of the properties of these two devices. In order to achieve this we first need to understand their operation.

4.3.1 The CCD camera

A CCD camera is a complex device, and we will only go into its general operating principles (see [23] for more details). This will eventually help us when constructing a model for the acquisition process in the next chapter.

The camera is also equipped with a zoom lens and an annular light source, and consequently we will also briefly dwell on these subjects.

General CCD operation and architecture

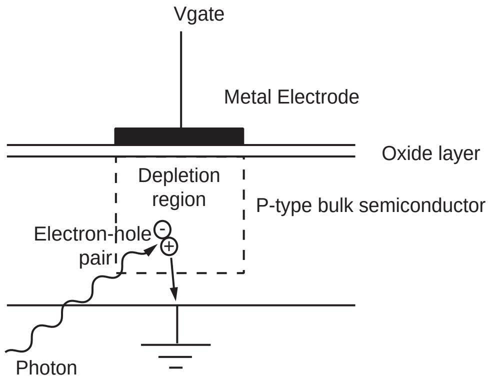

Figure 4.10: MOS capacitor trapping the electron of an electron-hole pair

The building block of the CCD is usually a metal-oxide-semiconductor (MOS) capacitor or gate. When the correct gate voltage is applied such a gate can act as a photon detector by trapping negative charges in its depletion zone while allowing positive charges to drain away. These charges arise from electron-hole pairs created by photons interacting with the bulk semi-conductor (see fig. 4.10).

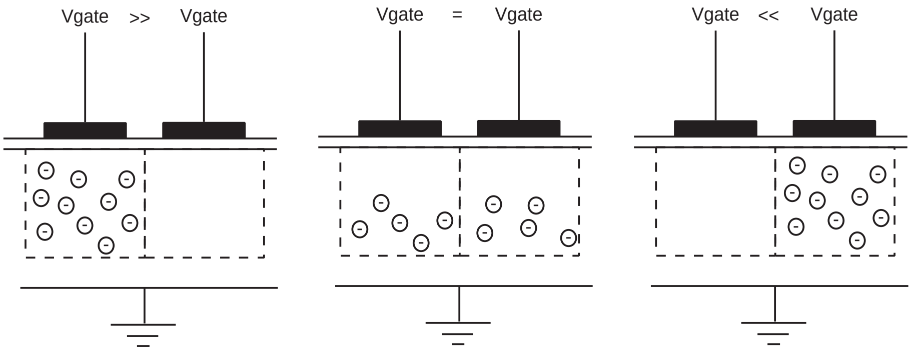

Figure 4.11: MOS capacitor transferring accumulated charge to neighboring capacitor

For imaging purposes gates are generally arranged in an n by m array. The charge accumulated under one gate can be transferred to a neighboring gate along a row by suitably adjusting the voltages of the gates, see fig. 4.11. Used repeatedly, this conveyor-belt type mechanism can be used to transport charges to a sensing device, see fig. 4.12. Notice that this requires at least 2 gates per pixel, and reduces the area of the pixel which is photosensitive.

The problem with this setup is that the transfer of charge takes time, and during this time the photosensitive gates keep on accumulating electrons. This results in a *smeared* image in the direction of the charge transport of the CCD array. This effect can be minimized by the use of an external shutter, or by the use of an interline array (also sometimes called electronic shuttering). In that case, each row of photosensitive gates has a shielded row of vertical transfer gates besides it to which accumulated charges are transferred, see fig. 4.13. Because this can be done very quickly smear is minimized. The disadvantage with this system is the smaller area available for the photosensitive gates, although there are again possible solutions for this.

Finally, at the end of each column the charges are transformed to voltages using a floating capacitance and a source-follower amplifier. This signal can then be further amplified to useful voltages using off-chip amplifiers.

In case of CCD color cameras, at least three different signals must be acquired by the trichromatic principle. There are two ways to achieve this: by using one CCD array covered with three different color filters called a color filter array, or by using three CCD arrays each covered

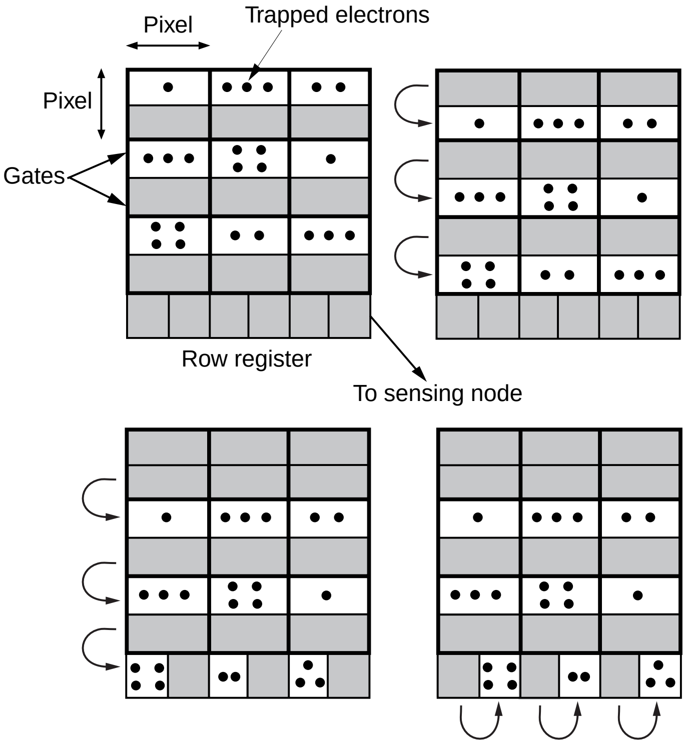

Figure 4.12: Illustration of charge transfers in a 3 by 3 array with 2 gates per pixel.

with one filter. A camera using this last setup is called a 3 CCD camera.

A color filter array consists of three filters laid out in a banded or mosaic pattern over the CCD array, see fig. 4.14. Typical filters would be red, green and blue, or their complementary colors yellow, cyan and magenta. These last filters are often preferred because they have a higher transmittance. The number of photogates assigned to each color filter is not necessarily the same, with green typically getting the most. This is necessary because the HVS is most sensitive to that color. Even so, the net result is a decreased image resolution, and possible color artifacts due to the misalignement of the pixels assigned to the different filters. This is most visible along sharp edges in the image.

The more expensive 3 CCD array setup typically uses a prism to split the incoming light into three beams going onto three filters and corresponding CCD arrays, see fig. 4.15. It doesn't suffer from the same drawbacks as the single CCD design, and thus exhibits high resolution

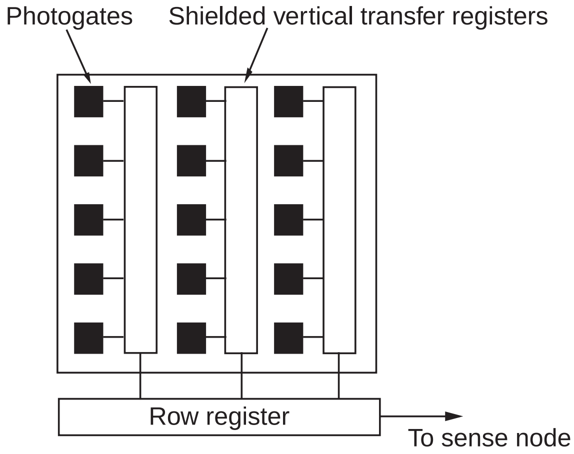

Figure 4.13: Interline array. Accumulated charge is quickly transferred to the shielded vertical registers to minimize smear during transfer to the row register.

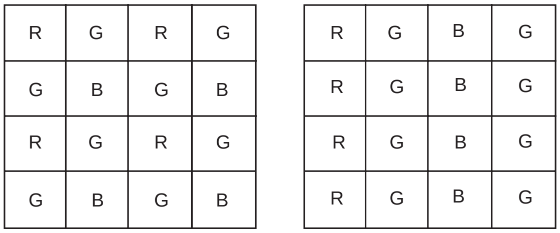

R	G	R	G
G	B	G	B
R	G	R	G
G	B	G	B

R	G	B	G
R	G	B	G
R	G	B	G
R	G	B	G

Figure 4.14: Mosaic and stripe designs for 1-chip color arrays.

and less artifacts.

Two important phenomena still deserve some explanation: dark current and blooming. Dark current is the current that flows when no light is incident upon the CCD array. It is highly dependent on the operating temperature because it is caused by thermally generated electrons. The effect of the dark current can be reduced by so-called ‘dark pixels’. These are shielded pixels at the edge of the CCD array which provide a reference dark current which can be subtracted from signals coming from unshielded pixels. Blooming is a sort of saturation effect: when a photogate is exposed to a strong light it can ‘overflow’ into neighboring gates in the same column. This can be solutioned by an anti-blooming drain, which again reduces the area for the photosensitive gate. The anti-blooming drain may distort the output of a gate for high light in-

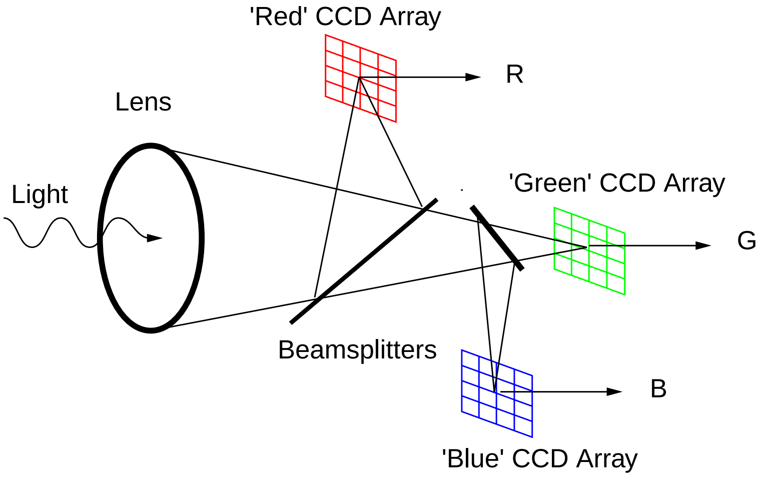

Figure 4.15: 3-chip CCD setup.

tensities, resulting in non-linear operation. Both these phenomena will have to be taken into account in our model of the imaging system.

General CCD camera operation

Besides the CCD array, a CCD camera usually contains some image processing electronics, gamma correction circuitry and video encoding circuitry, see fig. 4.16. Digital cameras also contain ADCs which transform the CCD array output into the digital domain where all subsequent processing is performed. One can then read this digital signal, or it can be converted back to an analog signal using DACs, and encoded using some video standard.

The image processing electronics can be used for several purposes, e.g. to alter the effective primary stimuli by transforming incoming color signals to a new set of color signals. This is a linear transformation that can be represented by a 3 by 3 matrix, and is called ‘matrixing’. Another possible use is automatic white balance, whereby the intensities of the primary stimuli are adapted so that a white object appears white irrespective of the lighting. This is somewhat similar to chromatic adaptation in human vision and allows compensation for e.g. the yellow hue of indoor tungsten lighting. Lastly, the image processing block is also used to try to remove all kind of artifacts like color aliasing due to the design of the CCD array(s), and image softening due to the degradation by the camera point spread function.

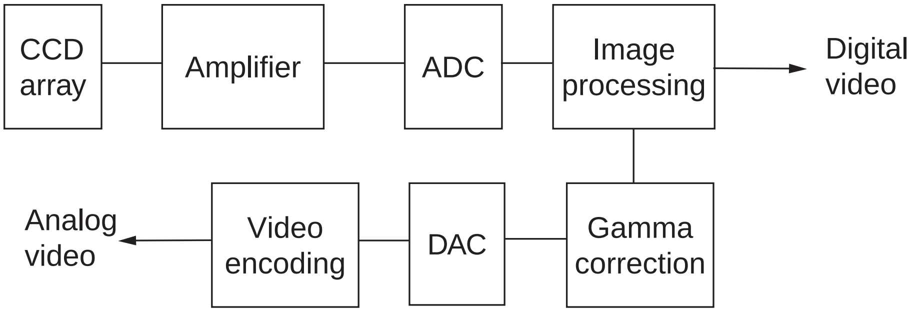

Figure 4.16: General block diagram of a CCD camera. Not all blocks need be present, e.g. the ADC and DAC in a purely analog camera, and the order of the blocks may also vary.

The gamma correction circuitry is normally only used when driving a CRT directly, and can generally be turned on or off. However, bear in mind, that as stated in section 4.2.3, when digitizing video signals the resolution requirements are lower for gamma-corrected signals than for linear-light signals!

Video encoding is quite a jungle, with lots of terminology from broadcast television used as part of camera specifications. There are three color broadcast standards worldwide: NTSC, PAL and SECAM. NTSC comes from the 'National Televisions Systems Committee' in the USA, and is used in North America, Central America and Japan. PAL or 'Phase Alteration Line system' is used in Europe and China, while SECAM for 'Sequentiel Colour Avec Mémoire' is used in France and Russia and former Soviet countries. These standards define video timing, i.e. frame rate, lines per frame, active lines, line time, scanning frequency and bandwidth. Based upon electrical bandwidth considerations it is then possible to define the number of (analog) pixels per line. This leads to two numbers, one when the nominal bandwidth is used, and one when the total allocated bandwidth is used. This last bandwidth normally includes room for the transmission of sound, and is thus an upper limit. See table 4.2 for an overview.

Usually, a 4:3 aspect ratio between vertical and horizontal pixels is used because this simplifies internal image processing circuitry, and this leads to 646 horizontal pixels for NTSC and 766 horizontal pixels for PAL and SECAM.

So far, we have discussed the timing of video signals, and not the content. In composite video, chrominance (color), luminance and synchronization information is encoded in a single signal. Broadcast NTSC,

Video Standard	**Frame Rate (Hz)**	**Active Lines**	**Analog pixels per line**
NTSC	29.97	485	440-625
PAL	25	575	569-827
SECAM	25	575	620-827

Table 4.2: Some figures for NTSC, PAL and SECAM video standards.

PAL and SECAM are composite signals. It is also possible to transmit RGB or their complementary colors using three signals, and this is known as component analog video (CAV). The timing scheme of CAV signals can be one of the broadcast standards discussed above. By using CAV, crosstalk between color channels is avoided, and the result is an image of higher quality. With color channel we mean the data pathway, both in hard- and software, of a color triplet component.

CCD camera specifications and control

Finally, we can introduce the camera chosen for the imaging system: the JVC KY-F55B[1]. It is a 3 CCD camera, with $\frac{1}{3}$ inch interline arrays with 440000 effective pixels arranged in an 580 by 760 array. It uses a prism and color filters to separate incoming light into red, green and blue components. It has a signal to noise ratio of 58 dB, and outputs PAL composite video at 750 lines or RGB CAV at 580 lines. It is equipped with gamma correction circuitry with $\frac{1}{\gamma} = 0.45$, which is consistent with the *sRGB* specifications. The black level of the camera can be set, allowing adjustment of the offset or zero-level of the three color channels. Similarly, the gains of the red and blue color channels of the camera can be used to alter the white or color balance of the camera in order to adjust to changing lighting conditions (the green gain is fixed in this camera). This can be done manually or automatically. The camera also comes with an automatic electronic shutter (EEI) and an automatic level control (ALC). The EEI and ALC usually operate together to enlarge the dynamic range of the camera by adjusting operation according to lighting conditions. At low light ALC circuitry increases the electronic gain stepwise from 0 dB to +18dB, while in high light conditions the electronic shutter will operate and decrease the amount of light incident on the CCD arrays. It is clear that, in view of our goal of having precise

---

[1] JVC: Victor Company of Japan, limited

knowledge and control over the camera parameters so that reproducibility is ensured, we have to disable any automatic operation and take full control of the camera from the PC. This is possible using the serial link capability of the camera which allows control of all its properties, see table 4.3 for relevant parameters and their meaning.

Communication software for the camera was only available from JVC as an application and not as a library callable from custom made applications. Luckily, we obtained the actual communication protocols, which made it possible to develop our own camera communication module in VB. The gamma correction is always turned on here, but this may become superfluous when higher digitization resolutions are available. Other relevant camera properties are hard coded and set during initial communication between the camera and PC. Fixed camera properties and their corresponding values are indicated by bold text in table 4.3.

Lighting and camera accessories

Because it is the intention of taking close-up images of the skin, the camera is equipped with a Pentax[2] zoom lens with a special macro front piece. The field of view (FOV) in the focal plane is 1.6 cm by 1.2 cm, which results in a spatial resolution of about 47.5 pixels per mm.

Although it is possible to compensate for spatially inhomogeneous and time varying lighting, it is much better to avoid these problems. Proper lighting is therefore crucial in acquiring high-quality and reproducible images. In order to obtain a spatially homogeneous light field a Schott[3] continuous annular light diffuser is fitted around the lens. This diffuser also ensures that the angle of the incident light on the focal plane is different from 90 degrees, thereby avoiding or at least diminishing specular, i.e. mirror-type, reflections. The diffuser is connected to a Schott KL1500 150 Watt halogen light source using a 2 m optical fiber. This source operates continuously (as opposed to a flash type operation) but at high frequency so that no light intensity variations are apparent, even at 30 frames per second. The light source has an intensity setting which allows its CCT to be varied. This setting is to remain fixed at about 2800 K. An extra blue filter in the light path then changes the color temperature from 2800 K to 6500 K, which makes it a very rough simulation of a CIE D65 illuminant and the white point of the *sRGB*

---

[2] Pentax Benelux B.V., Weiveldlaan 3-5, 1930 Zaventem, Belgium.

[3] Shott Glaswerke, Hagenauer strasze 38, D-65203 Wiesbaden.

Property	**Mode**	**Values**	**Meaning**
CONTOUR	**ON**	N.A.	Contour correction algorithm
	OFF	N.A.	
WHITE BALANCE	**MANUAL**	N.A.	Manual adjustment of white balance
	PRESET	N.A.	Fixed user defined white balance
	AUTO1	N.A.	Fixed white balance using an image of white
	AUTO2	N.A.	Fixed white balance using an image of white
	FAW	N.A.	Automatic and continuous white balance adjustment
GAIN	**0dB**	N.A.	Fixed electronic gain of 0 dB
	+6dB	N.A.	Fixed electronic gain of +6dB
	+9dB	N.A.	Fixed electronic gain of +9dB
	+12dB	N.A.	Fixed electronic gain of +12dB
	+18dB	N.A.	Fixed electronic gain of +18dB
	ALC+EEI	N.A.	Automatic electronic gain and shutter control
	ALC	N.A.	Automatic electronic gain control
GAMMA	**ON**	N.A.	Gamma correction
	OFF	N.A.	
MANUAL PAINT	RED	0-255	Red channel gain manual setting
	BLUE	0-255	Blue channel gain manual setting
MASTER BLACK	N.A.	0-255	Color channel offset setting

Table 4.3: Relevant properties of the JVC camera for the imaging system. Bold text in the first and second column indicates properties and values that remain fixed during operation.

color space.

The penetration of stray light in the lens must of course be avoided, and so a black cardboard cylinder with a glass front plate is fixed to the annular diffuser. The glass front plate makes sure the skin lesion is in the focal plane of the lens, and can be used for dermatoscopic imaging by applying some oil onto it before pressing it down on the skin lesion. This diminishes the refraction index mismatch at the glass-skin interface, and has the effect of making the stratum corneum somewhat transparent, thereby exposing some diagnostically relevant deeper structures. Calibration of the imaging system for dermatoscopy would be difficult and time consuming, and so will not be attempted. Rather, it is hoped that if the same oil is used in the same quantities calibration for clinical imaging is sufficient to ensure accurate and reproducible dermatoscopic imaging.

The glass front plate which comes into contact with the patient can be easily be cleaned and desinfected. This is important not only for medical reasons, but also avoids visual artefacts. Ideally this plate should be equipped with some kind of pressure measuring device, as it is known that skin color may vary strongly with applied pressure. Finally, to make handling easier the camera is equipped with a pistol grip with a trigger. The trigger is connected to the frame grabber and controls image acquisition. See fig. 4.17 for a schematical drawing of the camera assembly.

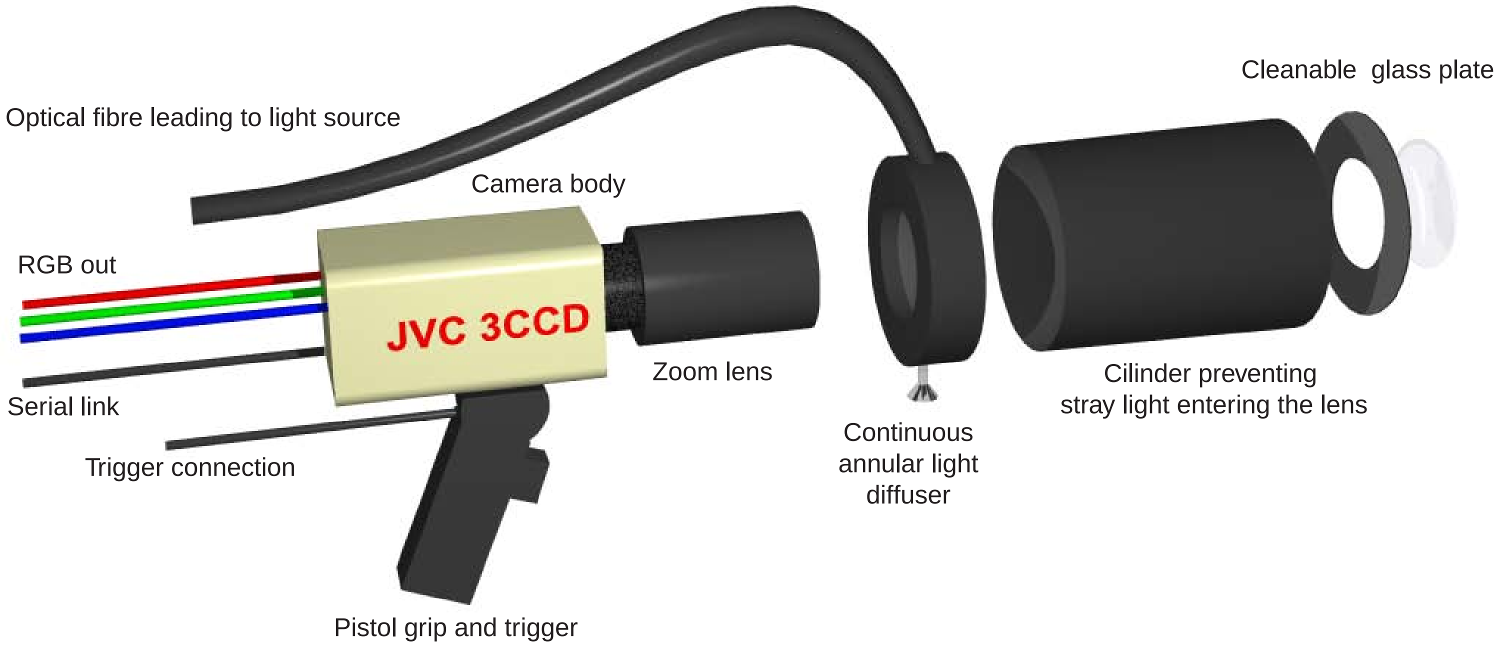

Figure 4.17: Schematical drawing of the camera and its accessories. All components are drawn approximately to scale.

4.3.2 The frame grabber

The frame grabber is responsible for digitizing the video signals sent to it by the camera, and for transferring the resulting digital pixels to the memory of the computer host. Basically, it consists of a video decoder section coupled with ADC's, a processing and control unit and on-board memory for buffering the acquired images, see fig. 4.18. Transfer of these images to the computer memory is done using the ISA, EISA, PCI or, more recently, AGP bus of the computer host. Some frame grabbers also double as display adaptors, allowing them to acquire images directly into video memory. This avoids unnecessary transfers over the host memory bus. The FlashPoint 128 Integral Technologies[4] frame grabber used in our imaging system is of this type. It accepts both PAL and NTSC video standards, and composite video, S-video and RGB CAV input types. The maximal resolution of the acquired images is 570 by 760 pixels for PAL signals. It is equipped with 4 MByte of fast on-board memory to be shared between video acquisition and display, and transfers acquired images to the host computer using the PCI bus. It can digitize and display pixels at several depths, e.g. 24 bit (8 bits for red, 8 bits for green and 8 bits for blue) or 16 bit (5 bits for red, 6 bits for green and 5 bits for blue). The settable properties which are relevant here are the contrast and the brightness, which are respectively a gain and an offset control, see table 4.4. Some of its useful extras are: input and output triggers, a serial port and a fused power output for the camera. The input trigger is connected to the switch on the pistol grip of the camera allowing easy control of acquisition. The serial port of the board is not used to communicate with the camera because the serial port of the

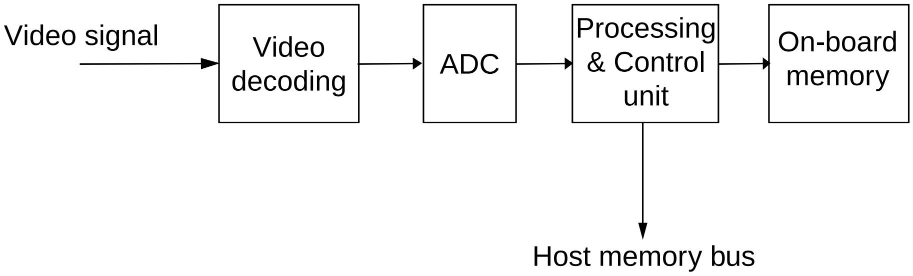

Figure 4.18: General block diagram of a frame grabber for analog video.

---

[4] Integral Technologies, Inc. 9855 Crosspoint Blvd., Suite 140. Indianapolis, IN 46256 USA.

computer was easier to program. We also preferred to use the power source that came with the camera.

Property	**Values**	**Meaning**
VIDEO STANDARD	**PAL** NTSC	The video standard
VIDEO TYPE	**RGB** COMPOSITE S-VIDEO	The type of video signal
VIDEO RECTANGLE	**570 by 760** ...	The size of the acquisition rectangle
BRIGHTNESS	0-63	The gain setting
CONTRAST	0-63	The offset setting

Table 4.4: Relevant properties of the frame grabber of the imaging system. Bold text in the first and second column indicates properties and values that remain fixed during operation.

The frame grabber software module controls the frame grabber and allows image acquisition. It is written in VB and C using a software development toolkit (FlashPoint SDK version 3.0) from the frame grabber manufacturer. It includes methods for setting the frame grabber properties, for reading the state of the camera trigger, for acquiring images and for displaying live images from the camera. It also permits the acquisition of only the central portion of the camera image, and this is used extensively when adjusting camera and frame grabber settings during calibration and image acquisition. Finally, acquired images can be sent to the Windows clipboard were they can be read by other modules for further processing and storage. It has to be noted that because the frame grabber uses video memory for acquisition, an acquired image can be very easily corrupted, e.g. by an overlapping popup window. For this reason acquisition is actually performed in a portion of the video memory that is not used for display, and then copied to the part of the memory that is used for display so that the user can see it. This does, however, limit the display resolution of the frame grabber.

4.4 Color image processing

Within the context of the imaging system, color image processing is restricted to operations on images that are necessary to calibrate and operate the imaging system. These are fairly low-level operations like the computation of spatial pixel averages and arithmetic operations on the individual pixel values like a linear or higher-order transform. These routines belong in the imaging system software module, as will become apparent in the next section.

4.5 Putting it all together

The assembly of subsystems into the complete color imaging system is depicted schematically in fig. 4.19. The figure also shows the imaging system software module that represents the imaging system as a whole and contains the software interface by which an application can gain access to the imaging system. Consequently this module contains all the routines pertaining to the operation and calibration of the imaging system, and these routines in turn depend heavily on the color image processing routines mentioned in the previous section. The calibration and operation of the imaging system will be the main subject of the next chapter.

Any further extensions of the imaging system towards a fully operational dermatological workstation, e.g. image and patient management, high-level image operations (segmentation, feature extraction, classification), etc. ..., are contained in the workstation modules. These workstation extensions will be discussed in chapter 6.

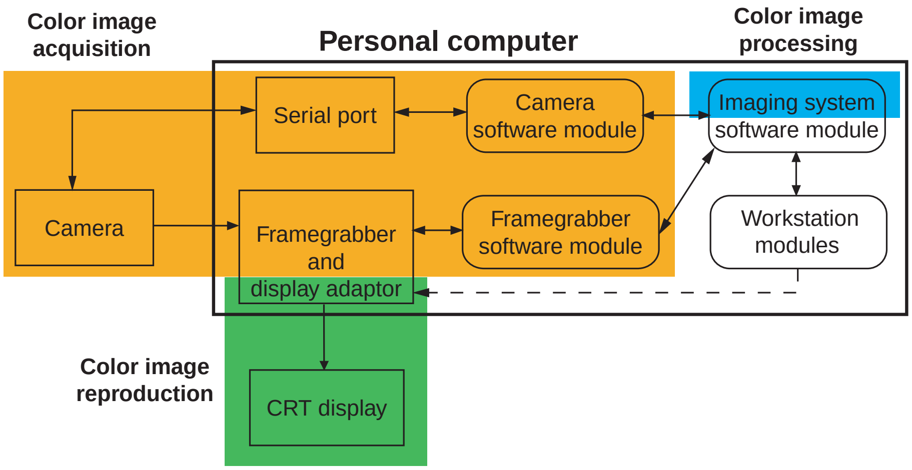

Figure 4.19: Schematical drawing of the complete imaging system.

Physically, the whole imaging system fits in a cabinet that can easily be wheeled to a patient if necessary (see fig. 4.20).

Figure 4.20: The imaging system cabinet

Chapter 5

Operation of the imaging system

Now the imaging system is properly assembled and the necessary software modules for the control of its subsystems are in place, the development of the high-level functions representing the operation and use of the imaging system as a whole can be attempted. This consists of two operations: the calibration, which needs to be performed only periodically and which ensures proper operation of the imaging system, and of course the image acquisition itself. This is followed by experiments in which, amongst others, we try to determine the accuracy and the reproducibility of the imaging system. These experimental results will be discussed in depth, and the chapter will end with some conclusions.

5.1 Calibration

As mentioned in chapter 1, most of the imaging in dermatology was and still is performed using traditional photography. The problem with this approach is the difficulty of obtaining reproducible images and performing quantitative measurements. Moreover, the exact meaning of any measurements concerning color properties is hard to determine unless the relationship with e.g. the CIE colorimetric color spaces is known.

Digital imaging on its own does not solve these problems, [34, 35]. Indeed, most or all digital imaging systems are not colorimetric and still suffer from a non-reproducible device-dependent color representation, usually RGB. Basically, each digital imaging system has its own time-varying RGB color space, depending, amongst other, on the spectral sensitivities of its imaging sensors, its settings, the temperature, etc. ... Calibration, thus, addresses two distinct problems: firstly obtaining a constant response from the imaging system by determining 'optimal' settings and adjusting them on the fly if necessary. Secondly, determining the relationship between the device-dependent RGB color space of the imaging system, and some device-independent color space, e.g. CIE XYZ, making meaningful and accurate colorimetric measurements and exchange of images possible. To our knowledge, all imaging systems developed for use in dermatology, see also the discussion in 2.2.2, fail to address this second issue. This denies these systems a framework for further human vision based image processing and meaningful exchange of images due to the lack of a proper definition of the data in the images. As a result any methods or algorithms developed for these systems, be it for image segmentation, image feature extraction or image classification, have limited scope and cannot easily be cross-validated.

The whole problem of imaging system calibration has already been covered extensively in the imaging literature, [36, 37, 35, 38, 39, 40, 41, 42]. In this work, however, emphasis is placed firmly on the development of a simple and quick calibration procedure of a specific imaging system built for a well-defined task. We will also move beyond the methods described in the literature.

Before introducing a model of the imaging system and moving on to the actual calibration procedure it is necessary to say a few words about the color spaces that play a role in the imaging system, and how they are related.

5.1.1 The color spaces of the imaging system

As mentioned earlier, calibration includes determining the relationship between the device-dependent RGB source color space, and some well-defined device-independent target color space. The choice of this calibration target color space will partly define the properties of the imaging system. We also have to choose the color space that will be used internally when storing images in memory. We call this the 'native' color space of the imaging system, and generally all computations involving calibrated images will start with pixel color triplets in that native color space.

The choice of the native color space is governed by several constraints not directly related to image acquisition, mainly small memory requirements and fast loading from file and fast display of images. This rules out the CIE XYZ color space because of its large memory footprint as a linear-light color space, and the need for transformations for display. CIE $L^*a^*b^*$ triplet values can be stored more compactly, but still need 32 bits or more per pixel due to an extended and oddly shaped gamut that makes inefficient use of a cartesian grid. Moreover, CIE $L^*a^*b^*$ values cannot be displayed without a time-consuming non-linear transformation. The $sR^*G^*B^*$ color space, on the other hand, is much better suited for our purpose. It is the natural color space of CRT monitors so that $sR^*G^*B^*$ images can be displayed without any extra computations. With 24 bits needed per pixel is also has a substantially smaller memory footprint than CIE XYZ or CIE $L^*a^*b^*$ images. For the same reason this color space can also be used to directly store images in many popular file formats, and again can be readily displayed by any graphical application that can read the file format used. This is called output rendering.

One disadvantage of the $sR^*G^*B^*$ color space is its restricted gamut, see fig. 4.9, but this problem will only occur with vivid, saturated colors, and these are not common when imaging the human skin. Another disadvantage is the need for more computations when trying to compute perceptual color differences. For this reason, operations like spatial averaging are generally performed in $sR^*G^*B^*$, and only the result is transformed to CIE $L^*a^*b^*$. This is adequate for the simple color image processing needed to operate the imaging system, but not for more complex human vision based image processing like skin lesion segmentation. To address this problem without needing large amounts of memory, a 32-bit encoding scheme is used to compute and temporarily store $L^*a^*b^*$ images in memory. Taking the range of $L^*a^*b^*$ components into account, L^* is stored using 10 bits, while both a^* and b^* are stored using 11 bits. This leads to a maximal quantization error of $\Delta E^*_{ab} = 0.08$.

The most obvious choice for the calibration target color space is CIE XYZ. However, with the choice of $sR^*G^*B^*$ as the native color space of our imaging system we might as well transform the source color space to $sRGB$ and avoid the extra transformation. It has to be noted that the $R^*G^*B^*$ and $sR^*G^*B^*$ may be superior to their linear-light counterparts as source and target calibration color spaces, depending on the mathematical method used to determine the relationship between those spaces. This is due to their greater perceptual uniformity, and we will come back to this later.

Fig. 5.1 gives an overview of the main imaging system color spaces, and illustrates some of the advantages of using a standardized color space for the exchange of images and as a framework for image processing. Table 5.1 gives some information on the numeric formats used to represent pixel values in the different imaging system color spaces.

Color space	**Component value**	$\mathbf{\Delta E^*_{ab}}$	**Use**
$R^*G^*B^*$	$\{0, \ldots, 255\}$	≈ 0.18	24-bit temporary image storage
RGB	$[0, 1]$	≈ 0	During computations No image storage
$sR^*G^*B^*$	$\{0, \ldots, 255\}$	0.18 ≤ 0.93	24-bit image storage
$sRGB$	$[0, 1]$	≈ 0	During computations No image storage
CIE XYZ	$[0, +\infty[$	≈ 0	During computations No image storage
CIE $L^*a^*b^*$	$L^* \in [0, 100]$ $a^* \in [-100, 100]$ $b^* \in [-100, 100]$	≈ 0	During computations No image storage
CIE $L^*a^*b^*$ (storage)	$L^* \in \{0, \ldots, 1023\}$ $a^* \in \{0, \ldots, 2047\}$ $b^* \in \{0, \ldots, 2047\}$	$= 0.08$	32-bit temporary image storage

Table 5.1: Numerical formats, quantization errors and uses of the color spaces of the imaging system.

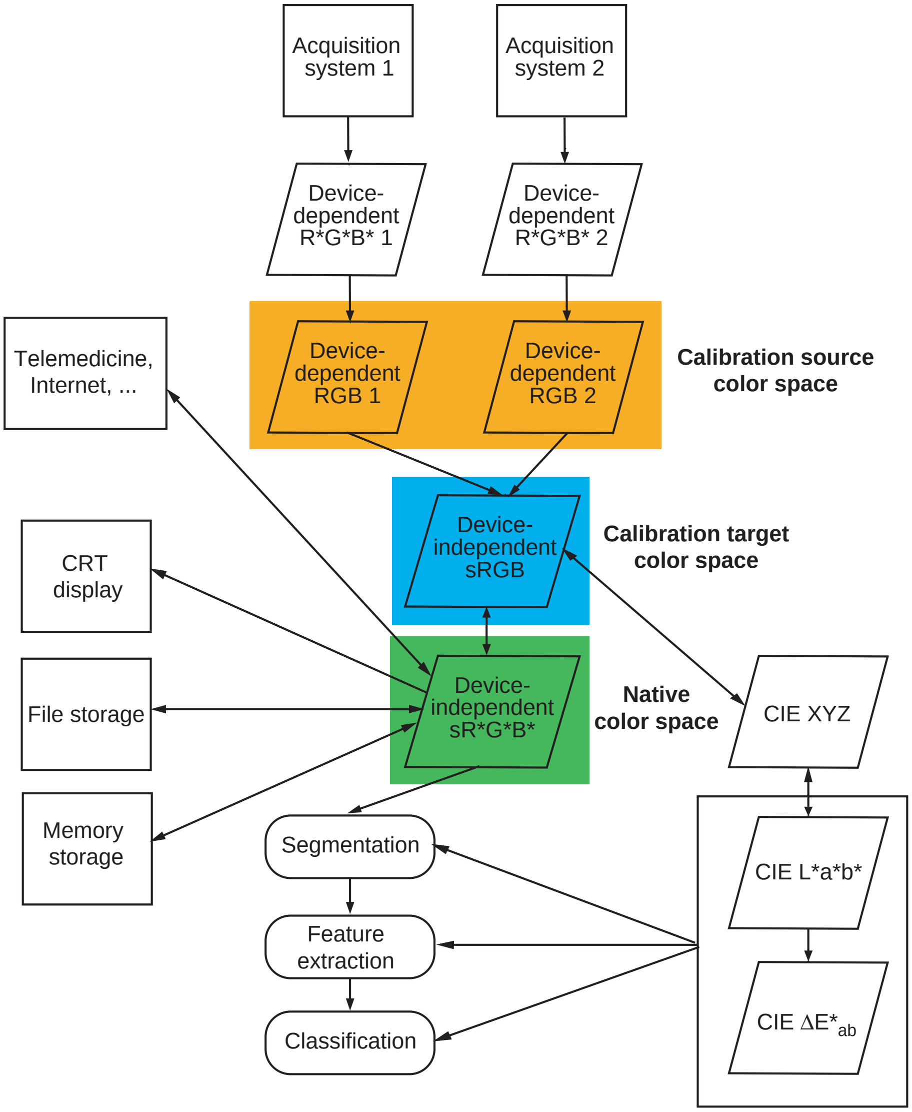

Figure 5.1: Overview of the color spaces of the imaging system. A rectangle represents a device, real or virtual, accepting or generating images. A parallelogram is a certain representation of that image and a rounded rectangle a specific operation on an image. Arrows represent the flow of images, including transformation between different image representations, i.e. parallelograms, if necessary. This figure also illustrates how images can be exchanged using $sRGB$, how CIE ΔE^*_{ab} color differences can be used for human vision based image processing and classification, and how these operations remain meaningful on images from diverse origins if the transform to $sRGB$ is known.

5.1.2 The imaging system model

In order to obtain a constant response from the imaging system we need to determine 'optimal' settings, and adjust them on the fly if necessary. To achieve this the simple mathematical model for the imaging system depicted in fig. 5.2 will be used. Most noise sources are assumed to be very small compared to the signals and are disregarded. The model may not be rigorously correct but describes the behavior of the imaging system well, and will lead to a useful calibration procedure. The model is kept simple by taking the type and number of parameters of the imaging system that can be set into account, e.g. if an offset parameter cannot be set for each color channel separately then the unknown property that this offset corrects for is also supposed to be color channel independent even if this is not necessarily the case in reality. In what follows the symbol $P = R, G, B$ and $\mathcal{P} = \mathcal{R}, \mathcal{G}, \mathcal{B}$ will be used to indicate both a tristimulus value component and a color channel when used as a subscript, in the RGB and the $sRGB$ color space respectively.

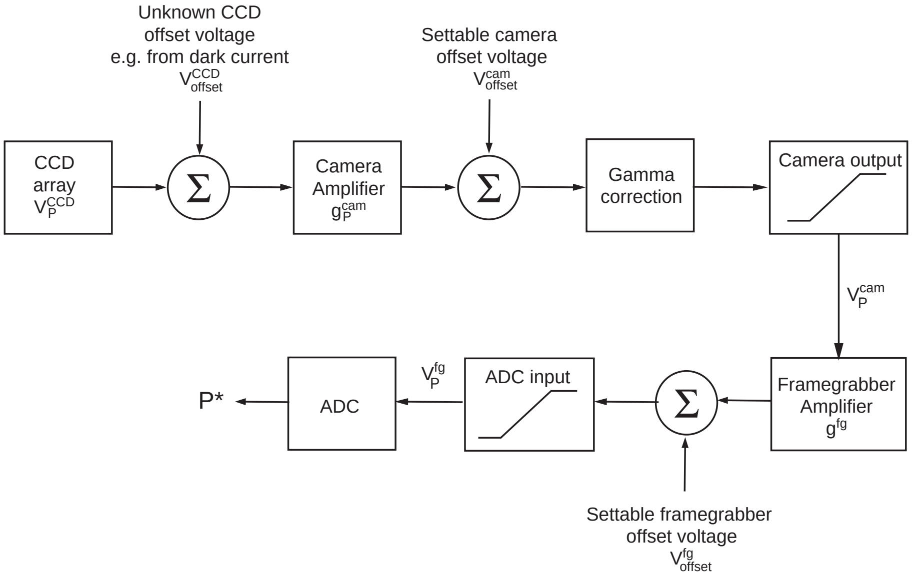

Figure 5.2: The imaging system model for one color channel $P = R, G, B$.

The CCD camera output voltage V_P^{cam} for a certain pixel and component $P = R, G, B$ can be written as:

$$V_P^{cam} = \Psi_0^{V_{\max}^{cam}} \left(\Gamma(V_{offset}^{cam} + g_P^{cam}(V_P^{CCD} + V_{offset}^{CCD}))\right), \tag{5.1}$$

with V^{cam}_{offset} the settable camera offset voltage, and V^{CCD}_{P} a voltage proportional to the light incident on the element corresponding with the pixel in CCD array of color channel P. V^{CCD}_{offset} is an unknown offset voltage resulting from, amongst others, the very temperature sensitive CCD dark current. g^{cam}_{P} is a variable color channel dependent gain. In our case the gain for the green channel is always 1, which is why the green channel will be used in determining color channel independent parameters. The function $\Psi_0^{V^{cam}_{\max}}$ represents the clipping that occurs when a voltage is out of range:

$$\Psi_0^{V_{\max}}(V) = \begin{cases} 0 & \text{if } V < 0 \\ V & \text{if } 0 \le V \le V_{\max} \\ V_{\max} & \text{if } V > V_{\max}. \end{cases} \tag{5.2}$$

The function Γ is the gamma correction as defined in eq. (4.5). The voltage inside the frame grabber before the ADC V^{fg}_{P}, the 8-bit digitized $R^*G^*B^*$ value P^* and the RGB value P may thus be written as:

$$\begin{aligned} V^{fg}_{P} =& \Psi_0^{V^{fg}_{\max}}(V^{fg}_{offset} + g^{fg} V^{cam}_{P}) \\ P^* =& \Re\left(255\frac{V^{fg}_{P}}{V^{fg}_{\max}}\right),\ P^* \in \{0, \ldots, 255\} \\ P =& \Gamma^{-1}(\frac{P^*}{255}),\ P \in [0, 1], \end{aligned} \tag{5.3}$$

with V^{fg}_{offset} again a settable offset voltage, g^{fg} the variable but color channel independent frame grabber gain and $\Re$ the integer rounding operator.

The camera parameters V^{cam}_{offset} and g^{cam}_{P} correspond with the 'MASTER BLACK' and 'MANUAL PAINT' properties of the camera in table 4.3 respectively, and possible settings are $\in \{0, \ldots, 255\}$. The frame grabber parameters V^{fg}_{offset} and g^{fg} correspond with the properties 'BRIGHTNESS' and 'CONTRAST' in table 4.4 respectively, and here possible settings are $\in \{0, \ldots, 63\}$. It is assumed that the relationship between these settings and the actual gains and offset voltages, is linear.

5.1.3 The RGB to sRGB transform

One of the possible methods to determine the relationship between the RGB source and $sRGB$ target color space is to measure a set of color patches with known properties in the target $sRGB$ space using an optimally set up imaging system, and to try to deduce or construct a general transform from the RGB to $sRGB$ mapping of these patches. It is obvious that the number and distribution of the patches used will greatly influence the accuracy of this mapping, and consequently of the imaging system. On the other hand, a large number of patches like in the industry standard IT8.7/2 chart, see fig. 5.3, will make the calibration procedure cumbersome and time consuming. The MacBeth color checker chart[1] (MBCCC) with its 24 large patches, see fig. 5.4, seems ideal from this point of view. Determination of the $sRGB$ tristimulus value of a MBCCC patch i was done by measuring its D65 CIE XYZ tristimulus value $(\langle X_{SPM,i}\rangle, \langle Y_{SPM,i}\rangle, \langle Z_{SPM,i}\rangle)$ with a Gretag[2] SPM50 spectrophotometer and transforming it to $sRGB$ using eq. (4.4). This device makes a spatially averaged measurement over a circular area of 5 mm diameter, hence the $\langle\rangle$ notation.

$$\begin{pmatrix}\langle \mathcal{R}_{SPM,i}\rangle\\ \langle \mathcal{G}_{SPM,i}\rangle\\ \langle \mathcal{B}_{SPM,i}\rangle\end{pmatrix} = \Phi_{XYZ\rightarrow sRGB}\begin{pmatrix}\langle X_{SPM,i}\rangle\\ \langle Y_{SPM,i}\rangle\\ \langle Z_{SPM,i}\rangle\end{pmatrix}. \tag{5.4}$$

If the camera sensor spectral sensitivities are equal to or a linear combination of the spectral sensitivities of the HVS, and consequently the $sRGB$ primaries by eq. (4.4), then the relationship between the RGB and the $sRGB$ color space under the same lighting would simply be linear. In that case the camera is said to be colorimetric.

However, this rarely holds and consequently the mapping between the source and the target color space is generally locally highly nonlinear, and may also be undefined or have one-to-many and many-to-one relations for some tristimuli. Tristumuli have an undefined mapping, i.e. no mapping, when the colors corresponding with those tristimuli in the source color space are out of gamut in the target color space. The effect of this phenomenon can be minimized by using so-called 'gamut remapping' techniques, as is often done in the printing world. Tristumuli have one-to-many and many-to-one relations when so-called human-machine metamerism occurs, i.e. when two colors look the same when imaged

---

[1] Macbeth, 405 Little Britain rd, New Windsor, NY 12553-6148, USA.

[2] GretagMacbeth Ag, Althardstrasse 70, CH-8105, Regensdorf, Switserland.

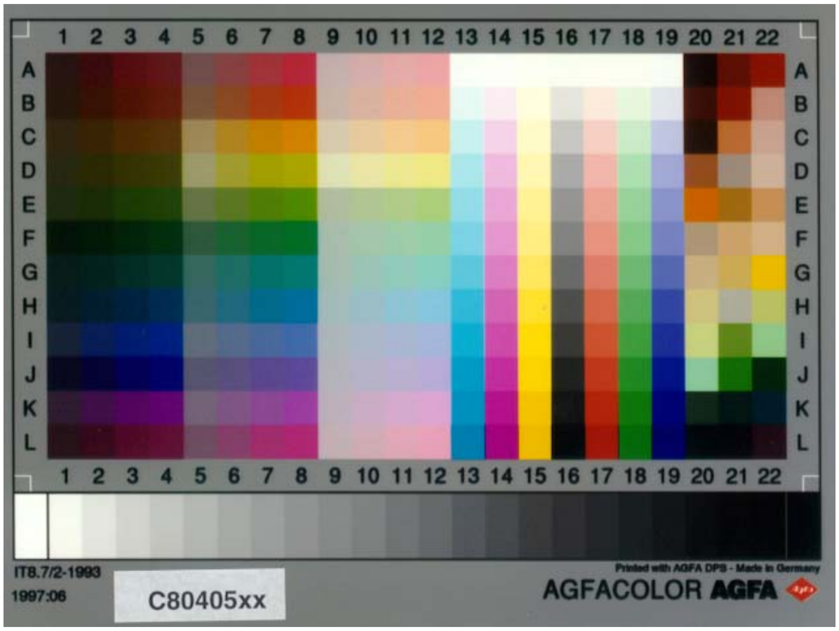

Figure 5.3: The IT8.7/2 reflection calibration target set.

Figure 5.4: The MacBeth color checker chart.

with a non-colorimetric camera, but different when seen by a human observer, or inversely. It is clear that it is impossible to compensate for this effect. Keeping this in mind some of the methods used to relate source and target color spaces include 3D lookup tables, neural networks and polynomial regression, see [42]. Lookup tables (LUTs) are relatively fast and good at modeling local non-linearities, but tend to require a lot of storage and a dense grid of source colors with a known mapping to the target color space. Neural networks can be highly non-linear while still retaining good generalizing properties. They are computationally expensive in use due to a high number of processing nodes, and may take minutes or even hours to train. As the emphasis is on a simple scheme with a limited set of calibration color patches, polynomial regression is the method of choice here.

In what follows we will use matrices to try to create a clear and compact notation that allows us to write down both the linear and non-linear relationships between the imaging system color spaces. Obviously this requires the introduction of some non-linear operators. These will act on a matrix, result in an possibly differently dimensioned matrix or submatrix, but cannot be represented by a matrix. Within this notation tristimulus values or other color triplets will always be notated as column vectors in equations.

A general polynomial transform $\Phi_{RGB\to sRGB,m}$ with m terms between RGB tristimulus values (R, G, B) and $sRGB$ tristimulus values $(\mathcal{R}, \mathcal{G}, \mathcal{B})$ can be written as:

$$\begin{aligned}
\begin{pmatrix} \mathcal{R} \\ \mathcal{G} \\ \mathcal{B} \end{pmatrix} &= \Phi_{RGB\to sRGB,m} \begin{pmatrix} R \\ G \\ B \end{pmatrix} \\
&= \begin{pmatrix} a_{\mathcal{R},1} & \dots & a_{\mathcal{R},m} \\ a_{\mathcal{G},1} & \dots & a_{\mathcal{G},m} \\ a_{\mathcal{B},1} & \dots & a_{\mathcal{B},m} \end{pmatrix} \left[\Theta_m \begin{pmatrix} R \\ G \\ B \end{pmatrix} \right].
\end{aligned} \tag{5.5}$$

The 'delinearizing' operator Θ_m transforms a 3 element column vector to an m element row vector representing a set of plausible polynomial transforms [42]:

$$
\begin{aligned}
\Theta_3\begin{pmatrix}R\\G\\B\end{pmatrix} &= \begin{pmatrix}R & G & B\end{pmatrix}^t\\
\Theta_6\begin{pmatrix}R\\G\\B\end{pmatrix} &= \begin{pmatrix}R & G & B & RG & GB & BR\end{pmatrix}^t\\
\Theta_8\begin{pmatrix}R\\G\\B\end{pmatrix} &= \begin{pmatrix}1 & R & G & B & RG & GB & BR & RGB\end{pmatrix}^t \qquad (5.6)\\
\Theta_9\begin{pmatrix}R\\G\\B\end{pmatrix} &= \begin{pmatrix}R & G & B & RG & GB & BR & R^2 & G^2 & B^2\end{pmatrix}^t\\
\Theta_{11}\begin{pmatrix}R\\G\\B\end{pmatrix} &= \begin{pmatrix}1 & R & G & B & RG & GB & BR & R^2 & G^2 & B^2 & RGB\end{pmatrix}^t .
\end{aligned}
$$

The coefficients of the transform $\Phi_{RGB\rightarrow sRGB,m}$ can be determined by substituting the SPM measurements of the 24 MBCCC patches $(\langle\mathcal{R}_{SPM,i}\rangle, \langle\mathcal{G}_{SPM,i}\rangle, \langle\mathcal{B}_{SPM,i}\rangle), i = 1, \ldots, 24$ on the left in eq. (5.5). These patches are then also measured by the imaging system, and the resulting spatially averaged RGB tristimulus values $(\langle R_i\rangle, \langle G_i\rangle, \langle B_i\rangle), i = 1, \ldots, 24$ are substituted on the right in eq. (5.5), see also fig. 5.5 for an overview. This results in one set of overdetermined linear equations for each color channel $\mathcal{P} = \mathcal{R}, \mathcal{G}, \mathcal{B}$ of the $sRGB$ color space:

$$
\begin{aligned}
&\begin{pmatrix}\langle\mathcal{P}_{SPM,1}\rangle & \ldots & \langle\mathcal{P}_{SPM,24}\rangle\end{pmatrix} = \\
&\qquad \begin{pmatrix}a_{\mathcal{P},1} & \ldots & a_{\mathcal{P},m}\end{pmatrix}\begin{pmatrix}\Theta_m\begin{pmatrix}\langle R_1\rangle\\ \langle G_1\rangle\\ \langle B_1\rangle\end{pmatrix} & \ldots & \Theta_m\begin{pmatrix}\langle R_{24}\rangle\\ \langle G_{24}\rangle\\ \langle B_{24}\rangle\end{pmatrix}\end{pmatrix} . \qquad (5.7)
\end{aligned}
$$

These equations can easily be solved in a least-squares sense using e.g. singular-value decomposition (SVD). The resulting transform $\Phi^{LLSQ}_{RGB\rightarrow sRGB,m}$ is called the linear least-squares (LLSQ) solution. Unfortunately, this solution is only optimal in the mathematical sense, as the sum of squares criterion in the $sRGB$ color space is hardly representative for the human perception of the mapping error associated with $\Phi^{LLSQ}_{RGB\rightarrow sRGB,m}$. This could be achieved by minimizing the mapping error in the CIE $L^*a^*b^*$ color space. For this we introduce the non-linear operator $\Phi_{sRGB\rightarrow L^*a^*b^*}$ which represents the known transform from $sRGB$

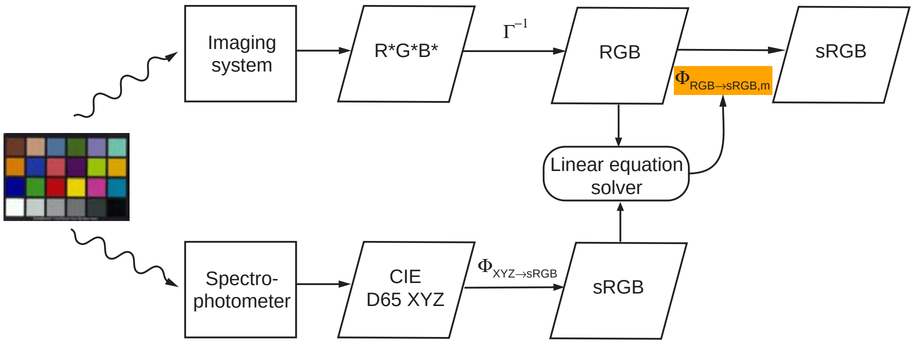

Figure 5.5: Determination of the RGB to $sRGB$ transform $\Phi_{RGB \rightarrow sRGB,m}$ using a set of overdetermined linear equations in $sRGB$ space obtained by comparing measurements of the MBCCC color patches made with a SPM with those made by the imaging system.

tristimulus values to CIE $L^*a^*b^*$ color triplets (L^*, a^*, b^*) via the CIE XYZ color space:

$$\begin{aligned} \begin{pmatrix} L^* \\ a^* \\ b^* \end{pmatrix} &= \Phi_{sRGB \rightarrow L^*a^*b^*} \begin{pmatrix} \mathcal{R} \\ \mathcal{G} \\ \mathcal{B} \end{pmatrix} \\ &= \Phi_{XYZ \rightarrow L^*a^*b^*} \; \Phi_{sRGB \rightarrow XYZ} \begin{pmatrix} \mathcal{R} \\ \mathcal{G} \\ \mathcal{B} \end{pmatrix} , \end{aligned} \tag{5.8}$$

with the linear operator $\Phi_{sRGB \rightarrow XYZ}$ defined in eq. (4.3). $\Phi_{XZY \rightarrow L^*a^*b^*}$ represents a non-linear operator implementation of the equations in (3.10), the precise form of which is not important here. Consequently, the CIE $L^*a^*b^*$ color triplets spatial averages $(\langle L_i^* \rangle, \langle a_i^* \rangle, \langle b_i^* \rangle)$ of the MBCCC patches as measured by the imaging system can be written down as:

$$\begin{pmatrix} \langle L_i^* \rangle \\ \langle a_i^* \rangle \\ \langle b_i^* \rangle \end{pmatrix} = \Phi_{sRGB \rightarrow L^*a^*b^*} \; \Phi_{RGB \rightarrow sRGB,m} \begin{pmatrix} \langle R_i \rangle \\ \langle G_i \rangle \\ \langle B_i \rangle \end{pmatrix} . \tag{5.9}$$

The CIE $L^*a^*b^*$ color triplets $(\langle L^*_{SPM,i} \rangle, \langle a^*_{SPM,i} \rangle, \langle b^*_{SPM,i} \rangle)$ of the MBCCC patches as measured by the SPM can be computed from their measured CIE XYZ tristimulus values $(\langle X_{SPM,i} \rangle, \langle Y_{SPM,i} \rangle, \langle Z_{SPM,i} \rangle)$ as:

$$\begin{pmatrix} \langle L^*_{SPM,i} \rangle \\ \langle a^*_{SPM,i} \rangle \\ \langle b^*_{SPM,i} \rangle \end{pmatrix} = \Phi_{XYZ \rightarrow L^*a^*b^*} \begin{pmatrix} \langle X_{SPM,i} \rangle \\ \langle Y_{SPM,i} \rangle \\ \langle Z_{SPM,i} \rangle \end{pmatrix} . \tag{5.10}$$

This allows us to define the perceptual mapping error in ΔE^*_{ab} units of one color patch i under a certain transform $\Phi_{RGB\to sRGB,m}$:

$$\Delta E^*_{ab}(\Phi_{RGB\to sRGB,m}, i) = \sqrt{(\langle L^*_i\rangle - \langle L^*_{SPM,i}\rangle)^2 + (\langle a^*_i\rangle - \langle a^*_{SPM,i}\rangle)^2 + (\langle b^*_i\rangle - \langle b^*_{SPM,i}\rangle)^2}. \quad (5.11)$$

This still doesn't provide us with a total mapping error of $\Phi_{RGB\to sRGB,m}$, but two feasible candidates are the average ΔE^*_{ab} error per MBCCC patch:

$$\langle\Delta E^*_{ab}(\Phi_{RGB\to sRGB,m})\rangle = \frac{1}{24}\sum_{i=1}^{24}\Delta E^*_{ab}(\Phi_{RGB\to sRGB,m}, i), \quad (5.12)$$

and the maximal ΔE^*_{ab} error over all the 24 MBCCC patches, $\max(\Delta E^*_{ab}(\Phi_{RGB\to sRGB,m}))$. The transforms obtained by minimizing these two forms of the total mapping errors will be denoted as $\Phi^{avg}_{RGB\to sRGB,m}$ and $\Phi^{\max}_{RGB\to sRGB,m}$ respectively. The non-linear minimization itself is performed by the Nelder-Mead simplex algorithm [43], using the linear least-squares solution $\Phi^{LLSQ}_{RGB\to sRGB,m}$ as an initial guess. The simplex algorithm is an iterative method and therefore much slower than the singular-value decomposition used to solve eq. (5.7). This is especially true for the higher-order transforms and when minimizing the highly non-linear $\max(\Delta E^*_{ab}(\Phi_{RGB\to sRGB,m}))$ function. Fig. 5.6 gives an overview of the iterative scheme.

5.1.4 The calibration procedure

We will now describe the steps which are needed to calibrate the imaging system. This consists of proper focus and zoom setting to obtain the FOV, determination of a set of 'optimal' imaging system settings and finally the computation of the RGB to $sRGB$ transform using the MBCCC patches. With 'optimal' we mean the settings that make best use of the imaging system in terms of dynamic range and signal-to-noise ratio, and this for each color channel independently. It is also important to avoid any non-linear behavior, mainly in the form of clipping of very 'weak' or very 'strong' signals. In simple terms this means ensuring that a perfect 'black' is mapped to the lowest RGB tristimulus value $(0, 0, 0)$ and a perfect 'white' is mapped to the highest RGB tristimulus value $(1, 1, 1)$. In order to ensure a perfect linear response of the imaging system to luminance within that range a LUT will also be

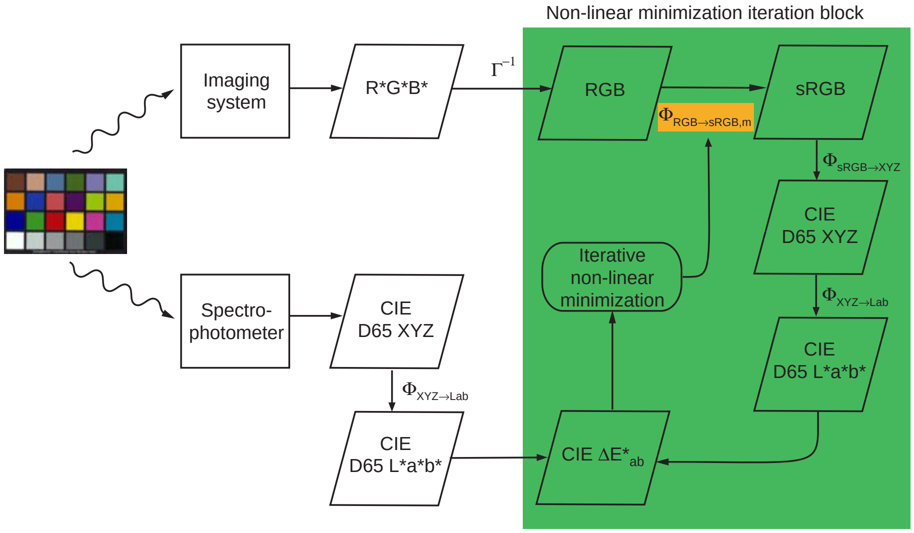

Figure 5.6: Determination of the *RGB* to *sRGB* transform $\Phi_{RGB\rightarrow sRGB,m}$ using iterative non-linear minimization of the transform mapping error based on ΔE^*_{ab} values between measurements of the MBCCC color patches made with a SPM and those made by the imaging system.

constructed using gray (achromatic) patches between perfect black and perfect white. Note that the order in which the settings are determined is crucial, although other sequences may be possible!

The whole calibration procedure takes about 5 to 10 minutes, and all the resulting settings, LUT's and the *RGB* to *sRGB* transform are stored on the computer in a so-called *calibration profile* which will be read when images needs to be acquired, see fig. 5.7. Such a profile remains valid for many hours of operation of the imaging system, and typically only needs to be redetermined after e.g. the light bulb of the light source is changed.

Field of view setting

Before anything else the manual zoom and focus of the camera lens must be set to obtain the desired FOV. This is simply achieved by imaging a small logo with dimensions equal to the desired FOV, i.e. 1.6 cm by 1.2 cm. The zoom is then adjusted so that it just fits in the displayed image, see fig. 5.8. This logo also contains some stripe patterns and letters so that precise focus can be achieved.

Once set, the zoom and focus rings of the lens are taped up so they

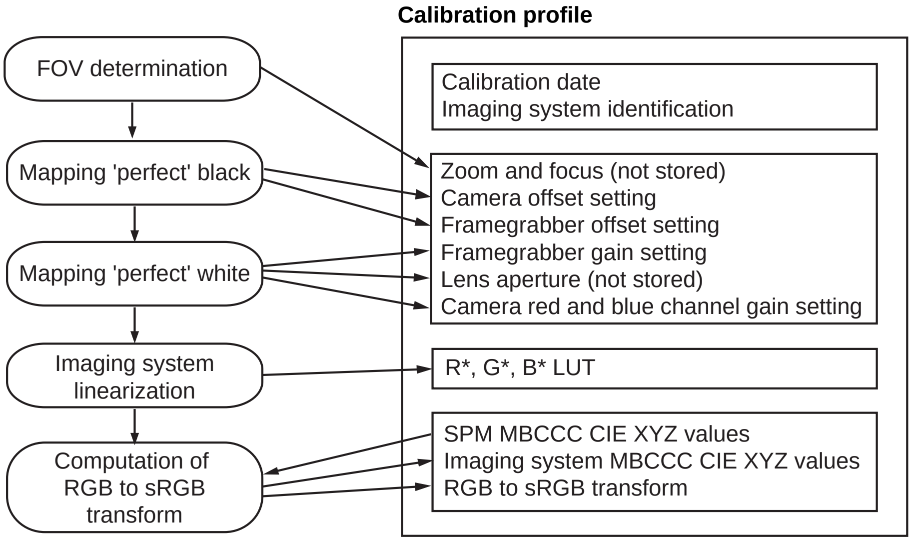

Figure 5.7: Calibration steps and the corresponding settings in the calibration profile.

Figure 5.8: The logo used to set the camera FOV and focus (real size).

cannot be changed inadvertently. Obviously these settings cannot be stored in the calibration profile, although with a motorized lens the whole procedure could probably be performed automatically, and the settings also stored.

Mapping ‘perfect’ black

The aim is to make sure that a perfect ‘black’ , i.e. an object with reflective luminance $Y = 0$ and thus $V_P^{CCD} = 0, P = R, G, B$, results in RGB tristimulus value $(0, 0, 0)$. A patch representing such an object is not included on the MBCCC, but can be simulated by turning the light source off, closing the lens diaphragm and putting the lens cap on. Measurements of patches, real or simulated, are always spatially averaged in the $R^*G^*B^*$ space over a few thousand pixels in the center of the image. Spatial averaging in $R^*G^*B^*$ space is much faster than spatial averaging in CIE $L^*a^*b^*$, and almost as good from the point of view of human vision. A SPM, on the other hand will perform spatial averaging in its spectral sensors, which is equivalent to spatial averaging in the linear-light domain. Restricting spatial averaging to the center of the image speeds things up compared to computing the average over the whole image. It also avoids problems due to a possibly inhomogeneous spatial response of the imaging system, a problem which we will return to later.

The first step in achieving the optimal mapping of perfect black is making sure that it leads to a zero camera output signal $V_P^{cam} = 0$ by properly setting the camera offset V_{offset}^{cam}. A look at eq. (5.1) shows us that the optimal setting for V_{offset}^{cam} will depend on the camera color channel gains g_P^{cam}. Because there is only one camera offset acting on all three color channels it is usually impossible to find an optimal setting for all color channels at the same time. Remembering that the green channel has a fixed camera gain $g_G^{cam} = 1$, that channel will be used to determine V_{offset}^{cam}. As no other parameters of the imaging system have been properly set so far we cannot determine a target pixel green component value $G_{Y=0}^*$ or $G_{Y=0}$ corresponding with the condition that $V_G^{CCD} = 0$, and therefore adopt the following scheme:

1. Make sure perfect black produces a green component $G_{Y=0} > 0$ by setting a high frame grabber gain g^{fg} and offset V_{offset}^{fg}.
2. Measure the spatially averaged $\langle G_{Y=0} \rangle$ for all the possible settings of camera offset voltage V_{offset}^{cam}.

It can be seen using eqs. (5.1) and (5.3) that this will result in a curve consisting of two straight lines: one horizontal line as long as $V_{offset}^{cam} + V_{offset}^{CCD} < 0$, and one sloping line once clipping no longer occurs and $V_{offset}^{cam} + V_{offset}^{CCD} \geq 0$ (see fig. 5.9). At the setting at which the two lines join the camera offset voltage exactly compensates for the CCD offset voltage. To determine this point reliably and independently of the frame grabber settings we fit a horizontal and a sloping straight line intersecting at each of the camera offset voltage settings through the data, and compute the total fitting error for each setting. The optimal setting is the one with the lowest error (see fig. 5.9). We will refer to this operation as the 'two-line intersection method'.

Fig. 5.10 shows the results for all the color channels. The fact that the optimal camera offset settings are different for the red and blue channel at the same color channel gain would lead us to the conclusion that V_{offset}^{cam} is in fact slightly color channel dependent, or, more unlikely,

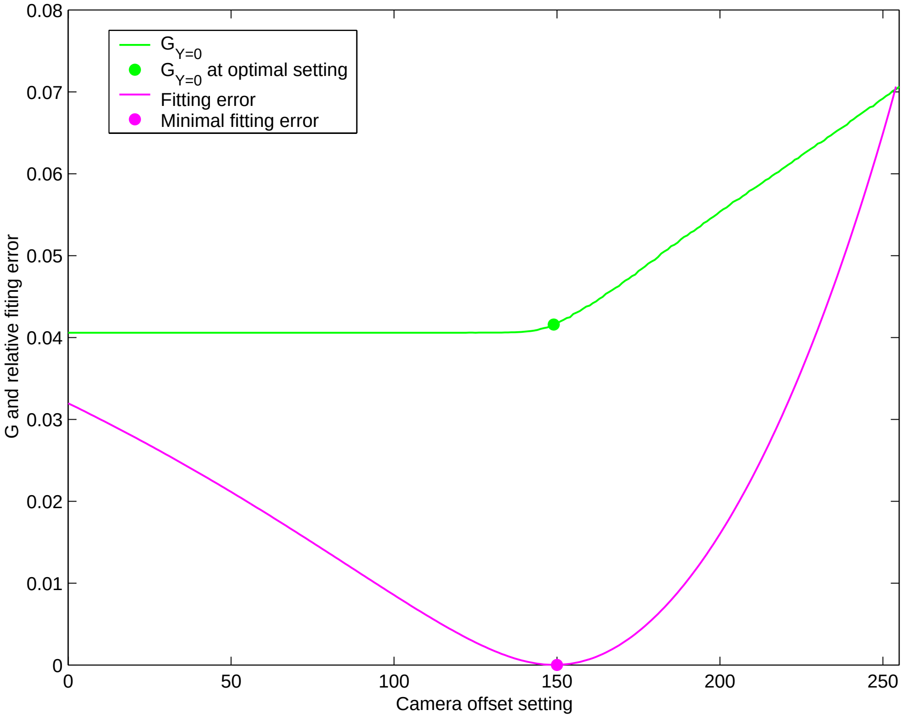

Figure 5.9: $\langle G_{Y=0} \rangle$ in function of the camera offset V^{cam}_{offset} setting, and the corresponding fitting errors of the two-line intersection method. The optimal setting is the one with the lowest error.

that the camera offset settings do not correspond to the same electronic gains on different color channels. This channel dependency was voluntarily excluded from the model because nothing could be done about it. Fig 5.11 shows the results for the red channel with different red channel gain settings $g^{cam}_{R} \sim 129, 196, 255$. This shows the increase of the optimal camera offset setting of the red channel with the red channel gain, and is in agreement with the camera model in eq. (5.1).

Now that the camera offset voltage V^{cam}_{offset} is properly set for the green channel, we can do the same for the frame grabber offset voltage V^{fg}_{offset}. This means finding the setting so that $\langle G^{*}_{Y=0} \rangle = \langle G_{Y=0} \rangle = 0$. Because $V^{cam}_{G} = 0$ for perfect black, $G^{*}_{Y=0}$ is independent of the frame grabber gain g^{fg}. This means theoretically we only have to find the highest frame grabber offset setting at which $\langle G^{*}_{Y=0} \rangle = 0$. However, we still favor the two-line intersection method as being more robust. It is important to note that because the camera signal V^{cam}_{G} doesn't change

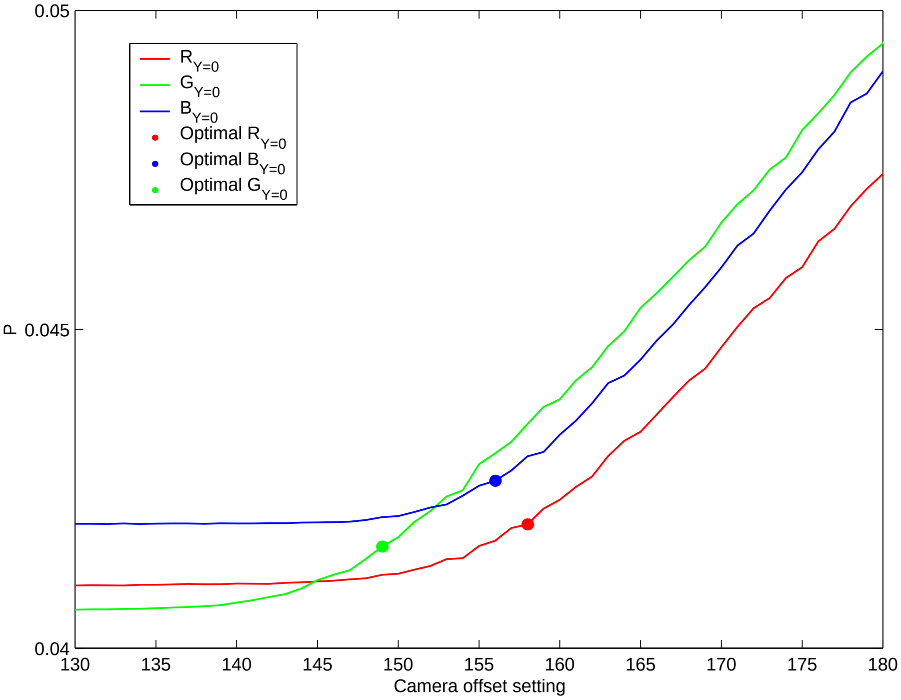

Figure 5.10: RGB tristimulus values $(\langle R_{Y=0}\rangle, \langle G_{Y=0}\rangle, \langle B_{Y=0}\rangle)$ of perfect black in function of the camera offset V^{cam}_{offset} setting, together with the corresponding optimal camera offset settings. This shows a slight dependence of the optimal camera offset setting on the color channel.

but is digitized with another offset voltage only $G^*_{Y=0}$ has a piecewise linear relationship with the offset voltage, and not $G_{Y=0}$!

Mapping 'perfect' white

So far an optimal response was obtained for a perfect black object, and now the same must be done for a perfect white (perfect diffuse reflector), i.e. an object of reflective luminance $Y = 100$. Objects with higher reflective luminances exist, e.g. objects with mirror-like properties. Although the horny layer of the skin may under certain circumstances exhibit such properties, we assume $Y = 100$ is the most luminous object we will encounter and consequently we will try to map it to RGB tristimulus value $(1, 1, 1)$, given the light source.

Firstly, we need to set the frame grabber gain g^{fg} in such a way that the theoretical camera response corresponding with perfect white,

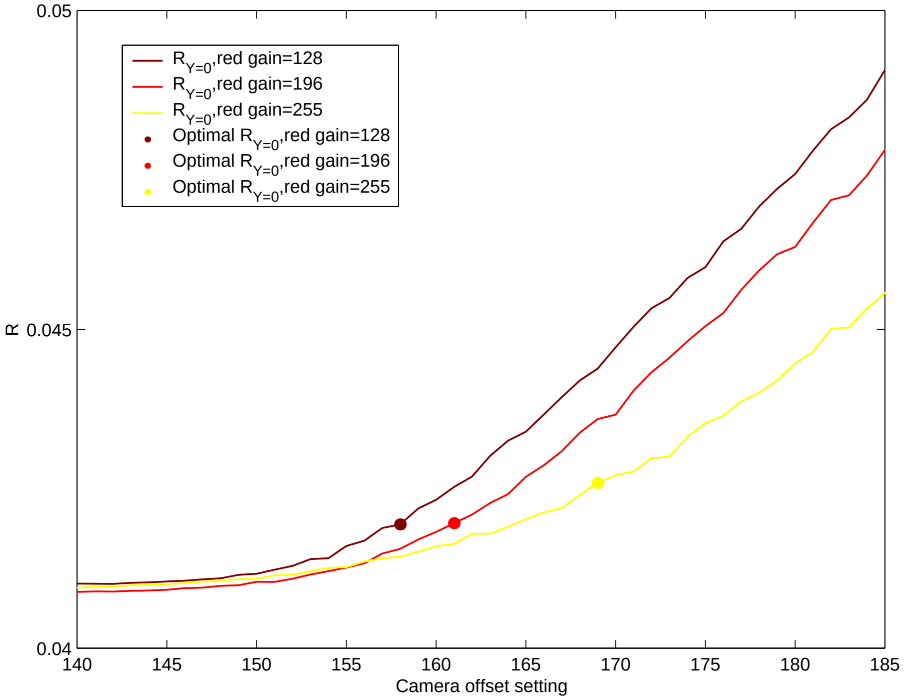

Figure 5.11: $\langle R_{Y=0} \rangle$ of perfect black in function of the camera offset V_{offset}^{cam} setting for different red channel gain settings, together with the corresponding optimal camera offset settings. This clearly shows the dependence of the optimal camera offset setting on the color channel gain as predicted by the camera model in eq. (5.1).

i.e. the maximal camera output voltage $V_P^{cam} = V_{max}^{cam}, P = R, G, B$, is mapped to tristimulus $(1, 1, 1)$. Because the maximal camera output voltage V_{max}^{cam} is the same for the three color channels, it is clear that if the frame grabber gain setting is optimal for one color channel it is also optimal for the other two channels. As the camera gain is already set for the green channel, we will use that channel to proceed. The maximal output voltage for the green channel $V_G^{cam} = V_{max}^{cam}$ is obtained by saturating the camera CCD's by fully opening the lens aperture, and measuring the highly reflecting MBCCC 'white' patch. Then $\langle G \rangle$ is measured in function of g^{fg} and the two-line intersection method is again used to determine the optimal frame grabber gain setting.

Next we need determine the lens aperture setting where saturation of the CCD's is just avoided for our chosen luminance dynamic range of $Y = 100$. As this needs to be done manually we cannot use the two-line intersection method, but instead compute a green channel target value for the MBCCC 'white' patch based on its D65 luminance value and assuming a linear response of the imaging system: $G^*_{white,target} = 255\Gamma(Y_{white}/100)$. The MBCCC 'white' patch is not a perfect diffuse reflector and has a slightly lower luminance value. This means the resulting target value $G^* < 255$, which allows for visual feedback during manual lens aperture adjustment both for when the lens is too much closed and for when it is too much open. The user is prompted to stop adjusting the lens aperture when the continually measured green component value of the imaging system $\langle G^*_{white}\rangle$ remains within a relative error of 0.002 of $G^*_{white,target}$ for a few consecutive measurements.

Once the proper lens aperture is determined we can obtain the same response to the MBCCC white patch from the red and blue channels, i.e. $\langle R^*_{white}\rangle = \langle B^*_{white}\rangle = \langle G^*_{white}\rangle = G^*_{white,target}$, by adjusting the camera color dependent gain factors g_R^{cam} and g_B^{cam} using a simple bisection root finding method. This optimizes the dynamic range of each color channel separately for a given light source, and makes linearization, see next paragraph, feasible.

Linearizing imaging system response

The aim of this operation is to make sure the imaging system has a linear behavior with regards to luminance over its entire dynamic range. This assumption is implicit when using linear-light tristimulus spaces like RGB, $sRGB$ and CIE XYZ, and small deviations of this assumption may be corrected using one or several LUTs. A possible culprit for non-linear behavior is the anti-blooming drain of the CCD camera, but there may be others.

In our case three LUTs are used, one for every color channel. They operate in the $R^*G^*B^*$ color space before the inverse gamma correction, even though they linearize linear-light response:

$$P^*_{LUT} = LUT_P(P^*),\ P = R, G, B \tag{5.13}$$

The LUTs have the full 8-bit resolution of 256 elements so no interpolation is necessary. They are based on the series of 6 'neutral' MBCCC achromatic patches which have the same or almost the same chromaticity coordinates but different luminances ranging from $Y \approx 3$ to $Y \approx 90$. Each LUT is determined such that for these 6 patches the LUT corrected RGB tristimulus values are proportional to their luminance, i.e. $\langle R\rangle = \langle G\rangle = \langle B\rangle = Y_{patch}/100$. This is also called 'gray balancing' , and represents a kind of normalization with regard to the light source or white point. Fig. 5.12 shows an example of the LUTs for the three color channels obtained for the imaging system. It shows a pretty good overall linear behavior of the imaging system. The biggest correction is for the darkest patch on the MBCCC, and this is probably due to the fact that the color channel independent camera and frame grabber offset settings are only optimal for the green channel. For the moment the LUTs always map $R^*G^*B^*$ color triplet $(0, 0, 0)$ to $(0, 0, 0)$ and $(255, 255, 255)$ to $(255, 255, 255)$, and this could clearly be improved to allow correction for the suboptimal offset correction by V_{offset}^{cam} and V_{offset}^{fg} for the red and blue channels.

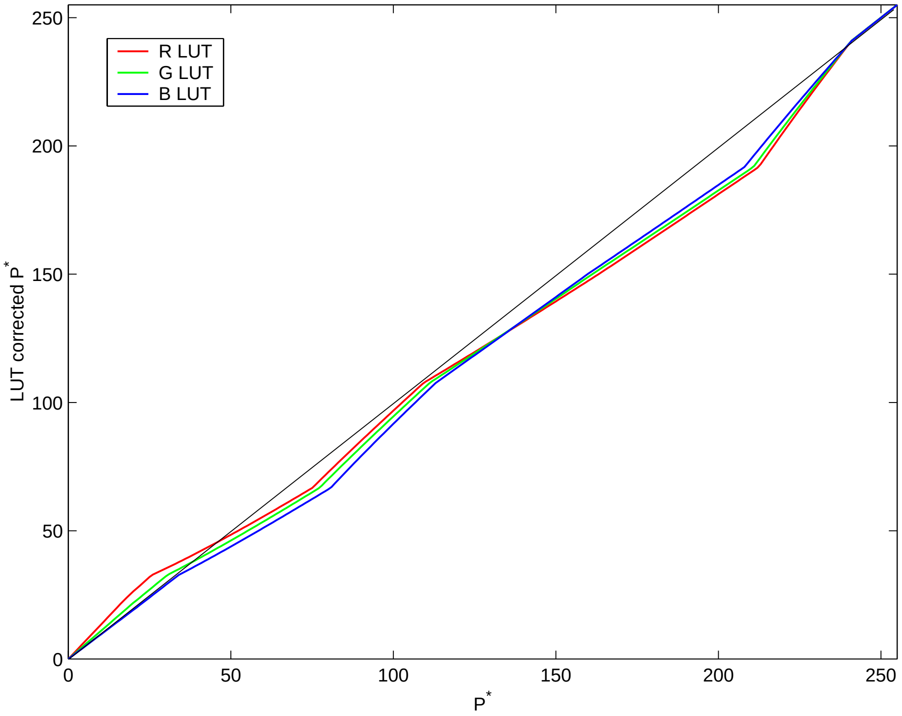

Figure 5.12: An example of the three color channel LUTs obtained for the imaging system.

Determining the RGB to sRGB transform

Now the imaging system is properly set up, the *RGB* to *sRGB* transform $\Phi_{RGB \rightarrow sRGB}$ can be computed by comparing measurements of the

24 MBCCC patches by the imaging system and their corresponding spectrophotometric measurements. The newly computed transform is then used to transform the measurements of the MBCCC patches by the imaging system to the CIE XYZ color space. These are then stored on file as representing the state of the imaging system during calibration and will be used to test the validity of the calibration profile prior to image acquisition.

5.2 Acquisition

To be of any use in a clinical context the image acquisition must be as simple and as quick as possible. On the other hand, in order to acquire calibrated images a number of checks and adjustments of the imaging system and the imaging system calibration profile may need to be performed. Moreover, as the lighting is not completely spatially homogeneous over the FOV it would be desirable to correct for this too. This is called shading correction, and one of the simplest ways to achieve this employs an image of a uniform object. Consequently the MBCCC 'white' patch will be used to perform both the calibration profile checks and adjustments and the shading correction. For easy positioning a copy of this patch is fixed on the inside of the cardboard lens cap. Clearly, more thorough checks and adjustments of the calibration profile would be possible by using more patches, but they would require more user interaction and thus defy the purpose of being simple and quick. To further minimize user interaction a valid, i.e. checked and adjusted, calibration profile remains valid for 15 minutes, and during this period images can be acquired freely without any extra interaction than acquisition of the desired image itself.

5.2.1 Short term imaging system drift

As mentioned above, once a calibration profile is determined it can be used as long as the imaging system does not change too much. This may occur e.g. when the light bulb of the light source is replaced or after a long time due to slow changes in CCD sensors spectral sensitivities. The imaging system does, however, also exhibit a short term drift when turned on. This drift greatly diminishes in amplitude after 30 to 40 minutes warmup time, but nevertheless remains present even after more than 2 hours of continued operation (see fig. 5.13). It is possible to compensate for this drift by adjusting some of the imaging system

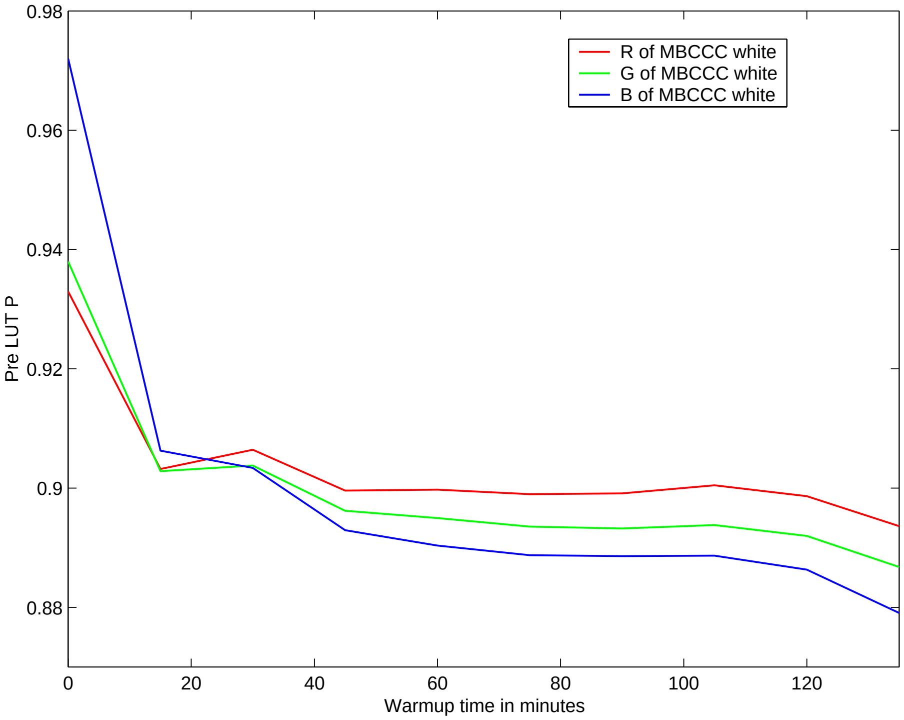

Figure 5.13: Short term drift of pre-LUT RGB tristimulus values of the MBCCC 'white' patch in function of warmup time of the imaging system.

settings, namely the frame grabber gain g^{fg} and the camera red and blue channel gains, g_R^{cam} and g_B^{cam}. This is easily achieved by comparing pre-LUT RGB tristimulus value of the MBCCC 'white' patch measured by the imaging system with its tristimulus value at calibration, which by definition is $R^*_{white} = B^*_{white} = G^*_{white} = 255\Gamma(Y_{white}/100)$. Note that calibration was performed with a well warmed up system.

Fig. 5.14 shows the result of the calibration profile adjustment on the MBCCC 'white' patch obtained by computing the color difference $\Delta E^*_{ab}(white)$ between its tristimulus value at calibration with those measured by the imaging system during warmup, both with and without profile adjustment. It can clearly be seen that, for MBCCC 'white' at least, the adjustment procedure is able to compensate even the large deviations existing right after the imaging system is switched on. However, a look at figures 5.15 and 5.14 show that the color differences for some of the other MBCCC patches can be quite high if the color difference of the MBCCC 'white' patch was large prior to the profile adjustment. This is

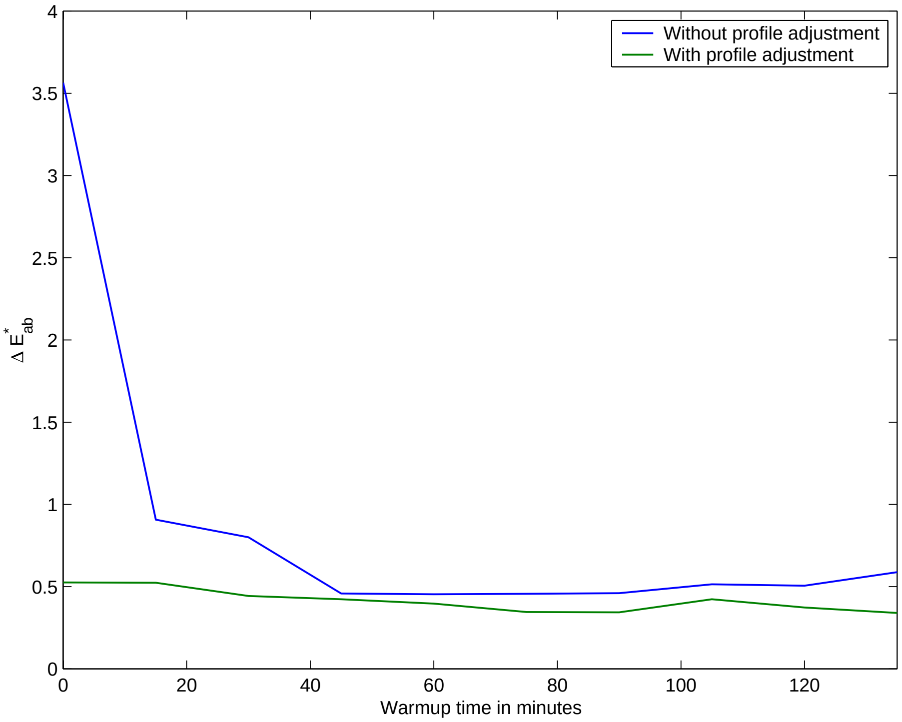

Figure 5.14: The ΔE^*_{ab} color differences of the MBCCC 'white' patch with its tristimulus value at calibration in function of the warmup time of the imaging system, both with and without calibration profile adjustment. Measurements originate from the same warmup cycle as in fig. 5.13.

quite logical as normally the linearizing LUTs and the RGB to $sRGB$ transform should be recomputed if one or more of the imaging system settings is changed. Nevertheless, those same two figures also show us that if the adjustment of the settings is small we may assume that the LUTs and the transform remain valid and the color differences of the MBCCC patches with their values at calibration remain smaller than 2 ΔE^*_{ab} units. This is usually the case after about 15 to 20 minutes of warmup time. Note that the apparent contradiction between the color differences of the MBCCC 'white' patch of the same warmup cycle in fig. 5.14 and 5.15 is because they are the result of separate measurements. Indeed, the measurements shown in fig. 5.14 are taken right after the profile adjustment, while the lens cap with the MBCCC 'white' patch is still on. After this, the whole MBCCC, including the 'white' patch, is measured, leading to the results shown in fig. 5.15. While this is not a problem when the imaging is properly warmed up, it is for a system that is just switched on and is drifting strongly. In that case the profile adjustment will only be correct for a very brief period, resulting in larger errors when the MBCCC ‘white’ patch is remeasured shortly afterwards. This can clearly be seen in figs. 5.14 and 5.15 for the MBCCC ‘white’ patch at 0 minutes warmup time, going from a color difference of $0.5\Delta E^*_{ab}$ units right after profile adjustment to about $1.7\Delta E^*_{ab}$ units a minute or so later when the MBCCC is measured.

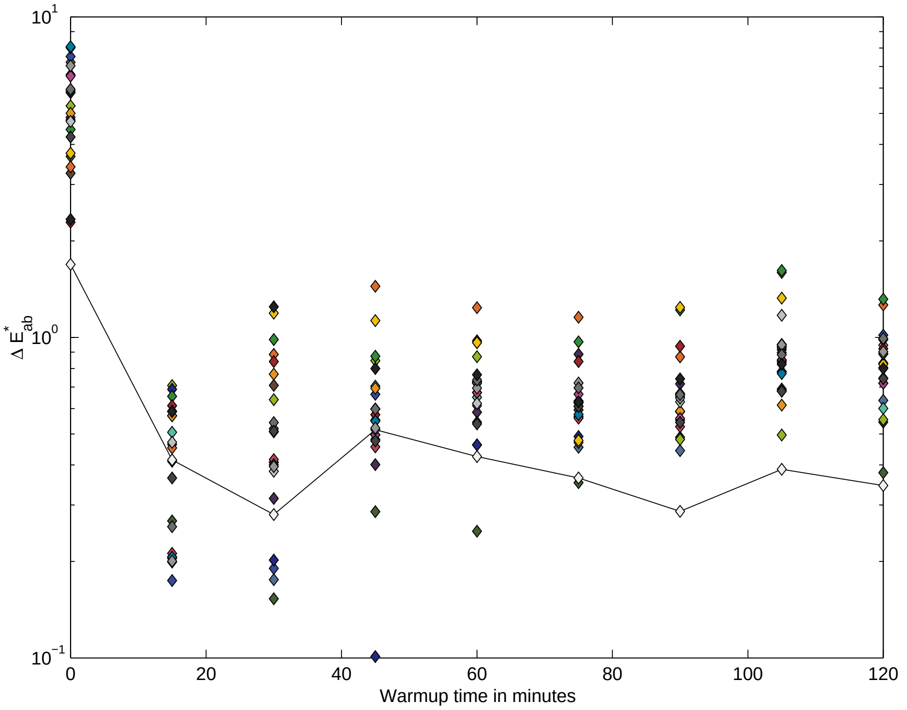

Figure 5.15: The ΔE^*_{ab} color differences of all the MBCCC patches with their tristimulus values at calibration in function of the warmup time of the imaging system, with profile adjustment. The measurements of the ‘white’ patch are connected by a solid line. Note that the y-axis is on a logarithmic scale. Measurements originate from the same warmup cycle as in figs. 5.13 and 5.14.

We now define a calibration profile quality factor Q based on the color difference $\Delta E^*_{ab}(white)$ of the MBCCC ‘white’ patch with its value at calibration as:

$$Q = \begin{cases} 100 - 20 * \Delta E^*_{ab}(white) & \text{if} \quad \Delta E^*_{ab}(white) < 5 \\ 0 & \text{if} \quad \Delta E^*_{ab}(white) \geq 5. \end{cases} \tag{5.14}$$

This quality factor becomes 100 for a perfect match, 0 for any color difference of $5\Delta E^*_{ab}$ units or larger, and will be used when deciding on the validity of a profile or adjusted profile.

5.2.2 Shading correction

Shading correction tries to correct for any spatial inhomogeneity in the imaging system. Those are mainly the result from inhomogeneous lighting, but the camera lenses and CCD arrays may also introduce some spatial inhomogeneities. The simplest way to perform shading correction is by acquiring an image of a homogeneous surface, the MBCCC 'white' patch in our case, and use it to determine a multiplicative pixel-by-pixel correction for any subsequently acquired image:

$$P_i' = P_i \frac{\langle \hat{P} \rangle}{\hat{P}_i}. \tag{5.15}$$

In this equation P_i is a RGB color triplet component of pixel i of an acquired image, with P_i' its shading corrected counterpart. $\hat{P}_i$ is a tristimulus value component of pixel i of the shading correction image of the MBCCC 'white' patch, while $\langle \hat{P} \rangle$ is a spatially averaged tristimulus value of the central region of that same image. The central region used to compute $\langle \hat{P} \rangle$ has the same size as the one used throughout the calibration procedure. Notice that the shading correction image is smoothed prior to use with a 3 by 3 pixel averaging filter. Ideally this filter should be bigger, as can be seen from the noise in fig. 5.16, but bigger filters take too much time.

5.2.3 Acquisition procedure

The different steps needed to acquire a calibrated image are outlined in the flow-chart in fig. 5.17. The imaging system needs to be turned on for about 15 to 20 minutes before acquiring any images. The sequence of events for image acquisition is as follows:

1. Check if a calibration profile is present on the PC. If not end acquisition with an error.

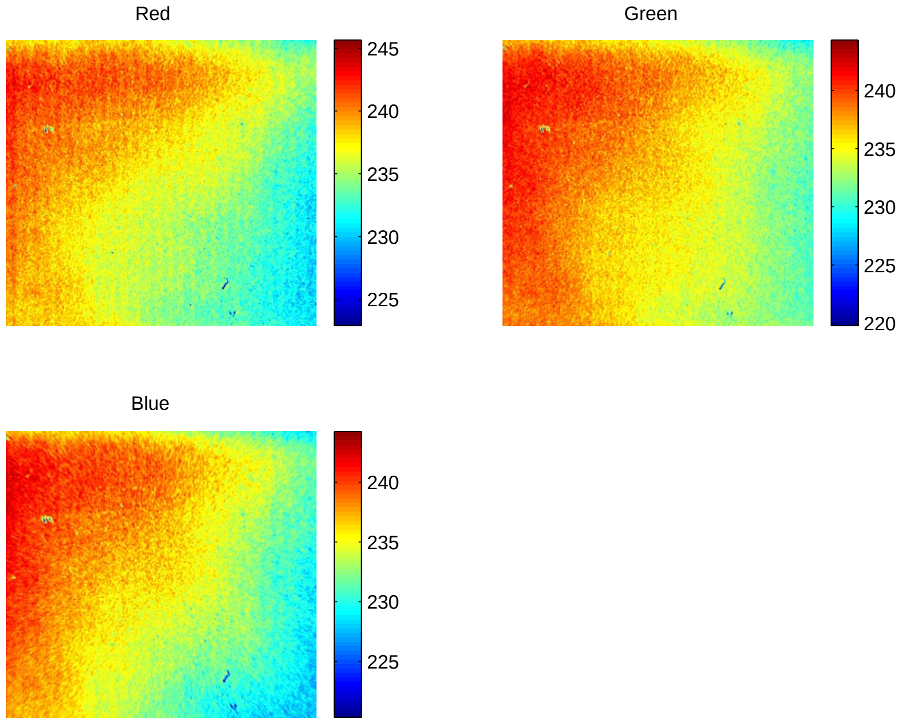

Figure 5.16: The three color channels of the shading correction image, displayed with a color map adapted to the image content in order to enhance contrast.

2. Check if the elapsed time since the last successful profile adjustment is higher than some predefined limit, typically 15 minutes. If not go tot step 7.
3. Check if profile is valid by computing the quality factor Q of the MBCCC 'white' patch in the lens cap. If $Q < 60$, then post a warning saying that either the imaging system isn't warmed up properly, or it needs recalibration. The user may choose to continue with the risk of poor image quality, or return to the calling application with an error.
4. Adjust the calibration profile using the same MBCCC 'white' patch in the lens cap.
5. Check if adjusted profile is valid by recomputing the quality factor Q of the MBCCC 'white' patch in the lens cap. If $Q < 80$, end

acquisition with an error..

6. Acquire the shading correction image based on the MBCCC 'white' patch and smooth it using a 3 by 3 averaging filter. No extra user interaction is needed as the lens cap is still on.
7. Acquire the desired image, apply shading correction and transform to $sR^*G^*B^*$ color space. This step takes about 20 seconds. Return to calling application.

No decisions are made during acquisition concerning the need to recalibrate, that responsibility is left to the calling application when an error is returned to it. When no error is reported the acquired image resides in a buffer and can be copied to the windows clipboard or saved to file at the calling application's discretion.

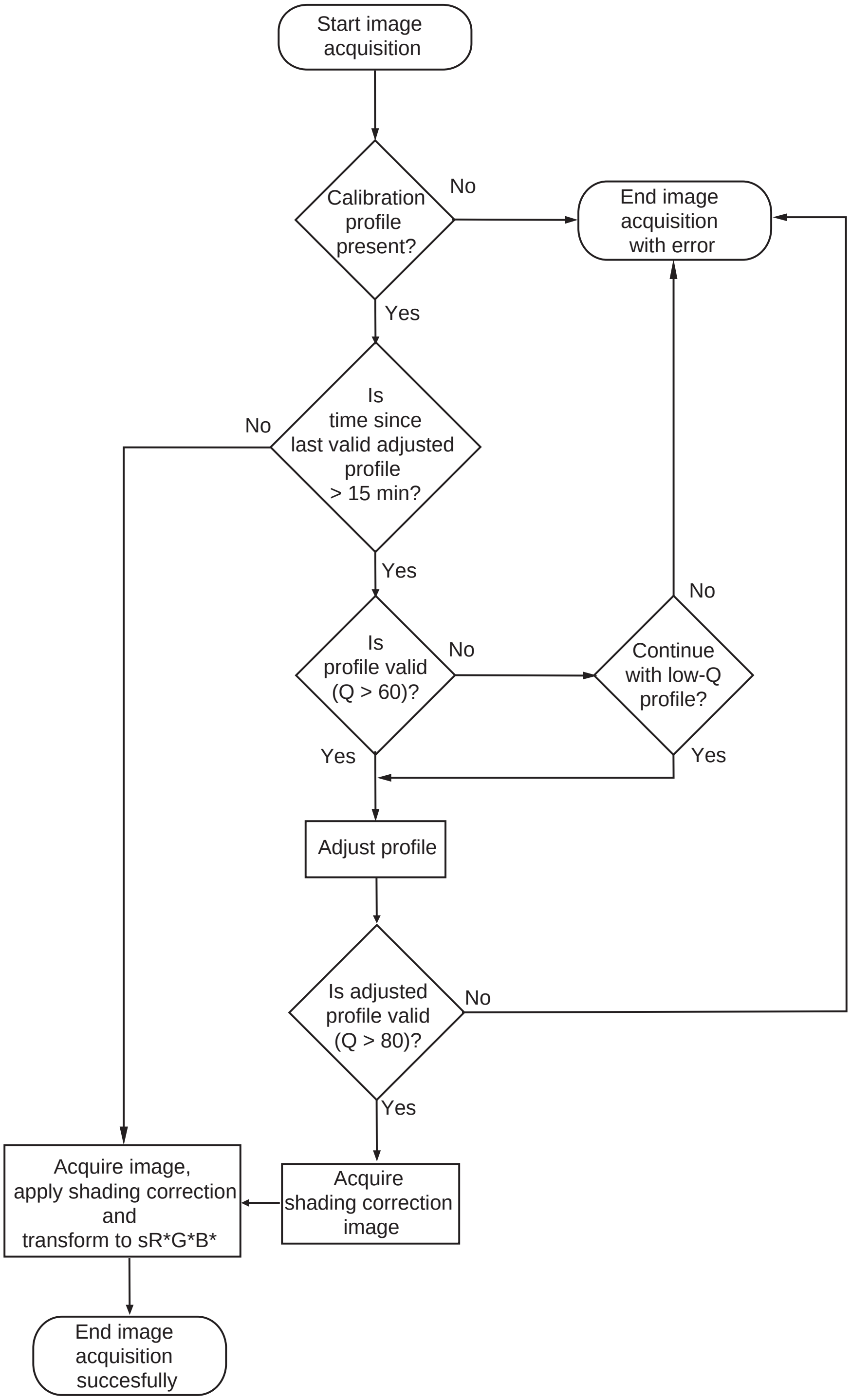

Figure 5.17: The flow-chart for the image acquisition procedure.

5.3 Experiments and results

The first thing to assess was the usability of the images as a visual record. This is mostly a question of image resolution and sharpness, which must be good enough to distinguish certain diagnostic features. Some papers have been published on this subject, [44, 45], but these did not allow general conclusions. Consequently, a simple subjective comparison was made with the images seen through a dermatoscope, and the images were found to be satisfactory, with the remark that the spatial resolution could be a little higher in order to see structures like a pigmented network on dermatoscopic images well. Spatial resolution can easily be increased, but at the cost of reducing the FOV. Keeping in mind that imaging the whole lesion is important for subsequent image segmentation and in assessing certain lesion properties like area, the current spatial resolution of 47.5 pixels per mm was maintained. Instead, a mental note was made for the next generation of the imaging system, if ever. The colors were found to be of good quality, and figures 5.18 and 5.19 shows some examples of clinical and dermatoscopic images obtained with the imaging system.

However, before further applications and tools are to be developed that would result in a dermatological workstation that could be used in daily clinical practice, we have to answer two fundamental questions: what is the *precision* and what is the *accuracy* of the colorimetric measurements obtained from images made by it? The answer to those two questions will greatly influence general applicability of the imaging system, and will now be investigated thoroughly.

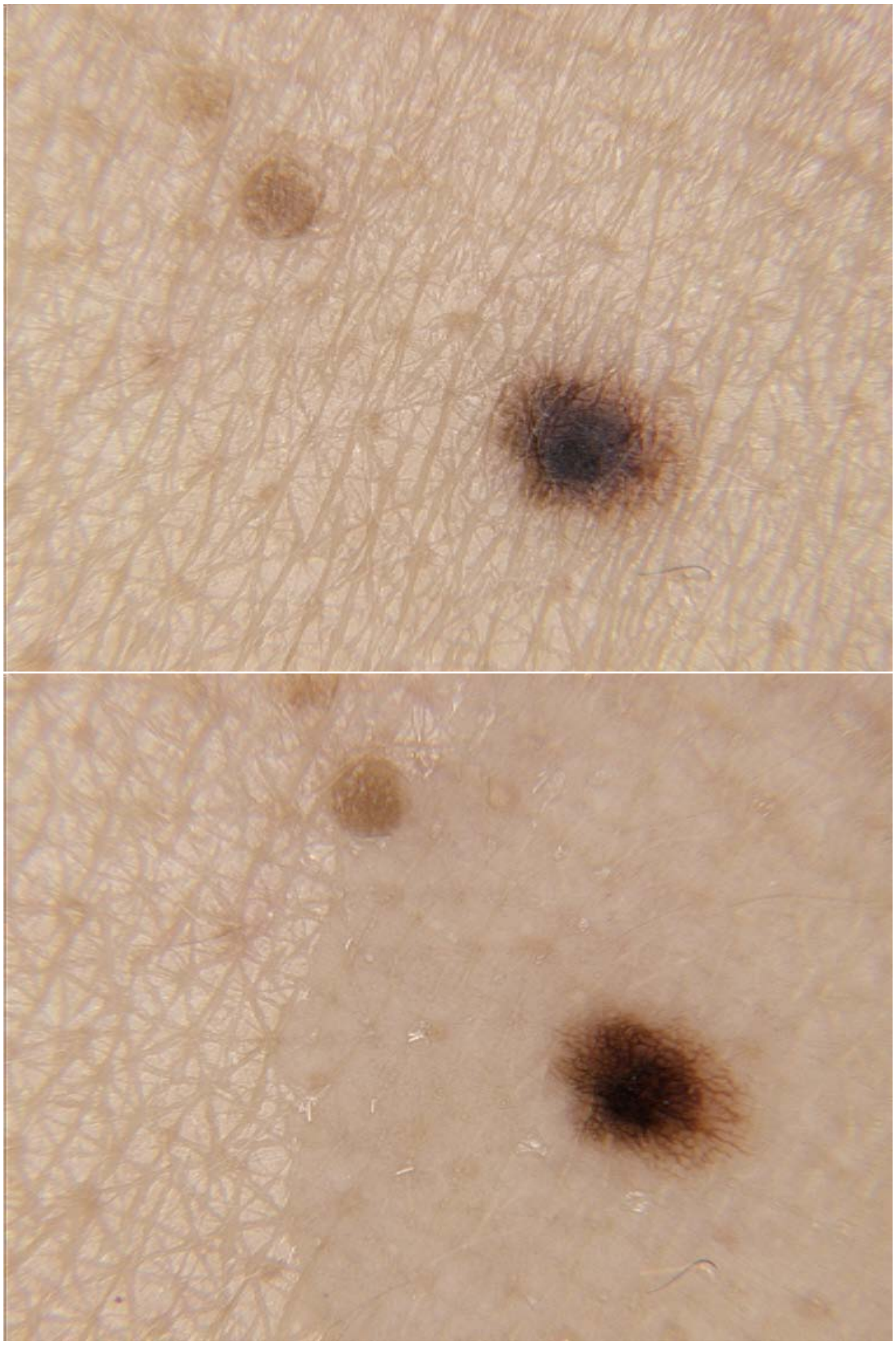

Figure 5.18: A junction naevus shot with the imaging system, both clinically (top) and dermatoscopically (bottom). Notice, how on the bottom image the oil used for dermatoscopy did not spread properly.

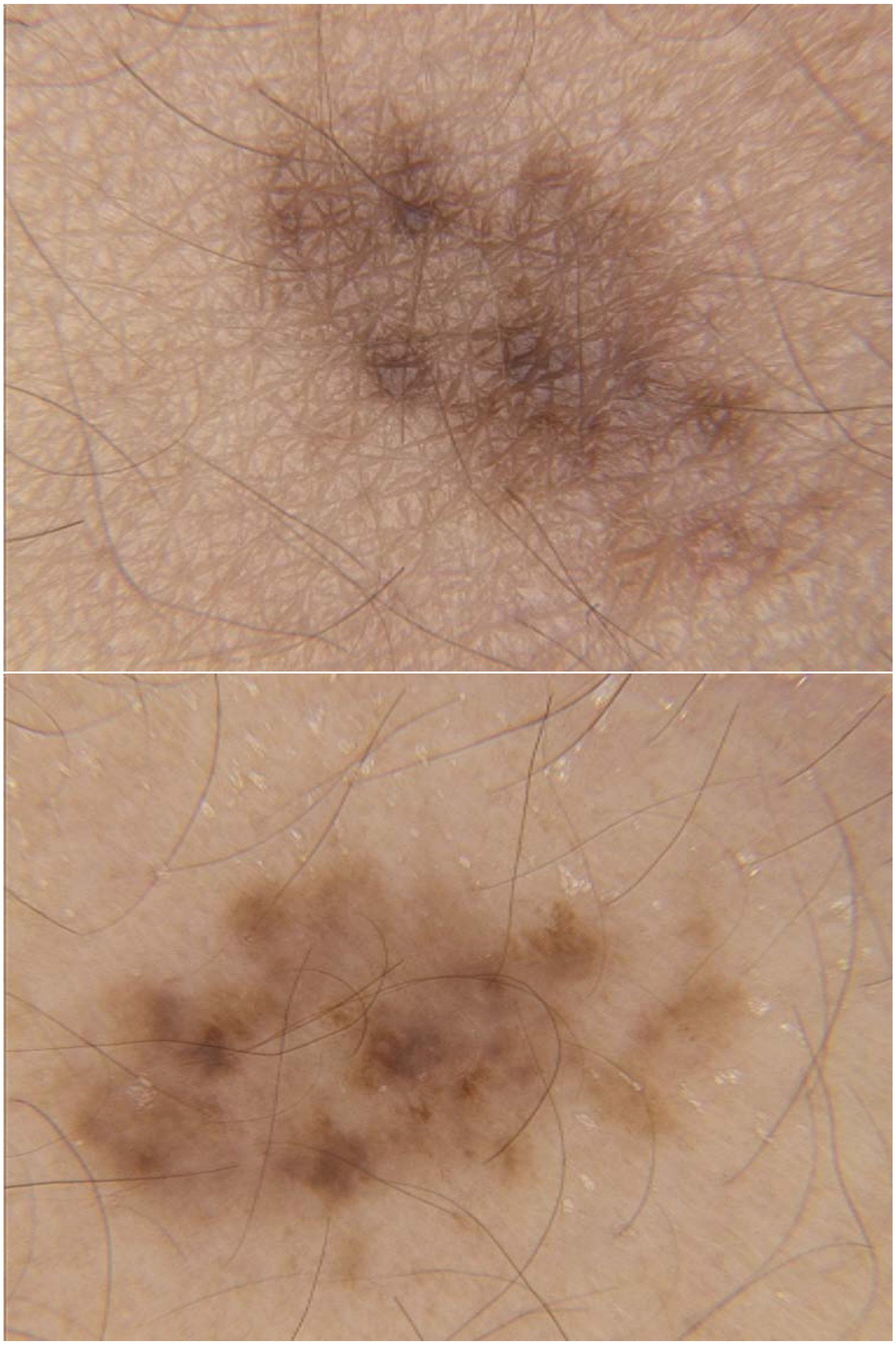

Figure 5.19: An atypical naevus shot with the imaging system, both clinically (top) and dermatoscopically (bottom).

5.3.1 Precision

The precision or reproducibility of a measurement process is a measure of the way repeated measurements of the same sample are spread around the average of those measurements. High precision results in tightly packed 'clusters' of measurements, as opposed to loose clusters in the case of low precision. Notice that precision does not say anything about how 'correct' the measurements are, see fig. 5.20 for a shooting range analogy. The precision of the imaging system says something about the (electronic) stability of its components, the appropriateness of the settings determined during calibration, and the ability of the profile adjustment algorithm to counteract some of the inevitable small response fluctuations of the imaging system. It is independent of the RGB to $sRGB$ transform $\Phi_{RGB \rightarrow sRGB,m}$ for $m = 3$, but higher order transforms may have a small influence. For this reason a linear transform $\Phi_{RGB \rightarrow sRGB,3}$ was always used in the evaluation of the precision.

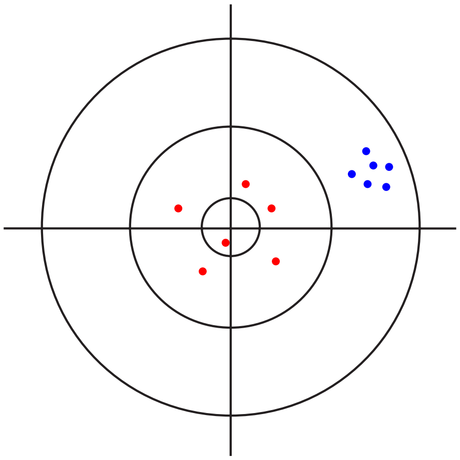

Figure 5.20: Illustration of concepts of precision and accuracy for a shooting range target. The shots indicated by the blue dots form a tightly packed cluster, meaning they are very reproducible. The shooter thus has a high precision, although he consequently misses the center of the target and thus has low accuracy. The red dots, on the other hand, represent a shooter with low precision because his shots form a rather loose cluster. He is, however, always close to the center of the target which means he is quite accurate.

Precision will be important for any quantitative measurement of image color characteristics. We can distinguish between several types of precision: short-term precision when making several consecutive measurements of the same object, medium-term or profile precision when comparing measurements made under one calibration profile, and long-term or inter-profile precision when talking about the agreement between measurements made under different calibration profiles. The reported errors are color differences in ΔE^*_{ab} units of the measurements with regard to the averages of those measurements in CIE $L^*a^*b^*$ space. Consequently, the maximal color difference between two single *spatially averaged* measurements of a color might be as bad as *twice* the reported maximal error! Errors between measurements of individual pixels might of course be even larger than that and experiments show that at least a few hundred pixels are needed to obtain a stable measurement of color, see fig. 5.21.

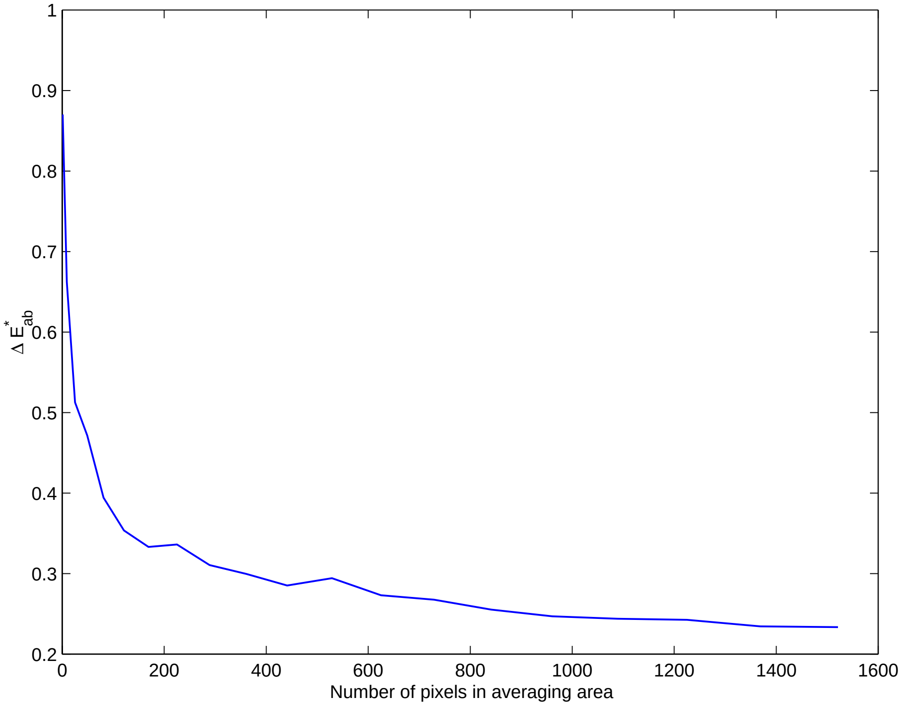

Figure 5.21: ΔE^*_{ab} error in function of increasing number of averaging area pixels obtained by comparing the square averaging area $sR^*G^*B^*$ spatial average value to the whole image $sR^*G^*B^*$ spatial average. The image used was 570 by 760 pixels and was a picture of the MBCCC 'white' patch.

The short term precision based on 20 consecutive measurements of the MBCCC 'white' patch is very good: $\langle \Delta E^*_{ab} \rangle = 0.04$, with $\Delta E^*_{ab} \leq 0.1$.

The medium-term precision is determined using 10 measurements of all the MBCCC patches. These were performed during different warmup cycles and at different stages of warmup of the imaging system, but always using the same calibration profile. The measurements themselves can be seen in fig. 5.22, while the corresponding average and maximal errors per patch can be seen in fig. 5.23. The overall error, i.e. over all MBCCC patches, is $\langle \Delta E^*_{ab} \rangle = 0.34$, with $\Delta E^*_{ab} \leq 1.2$.

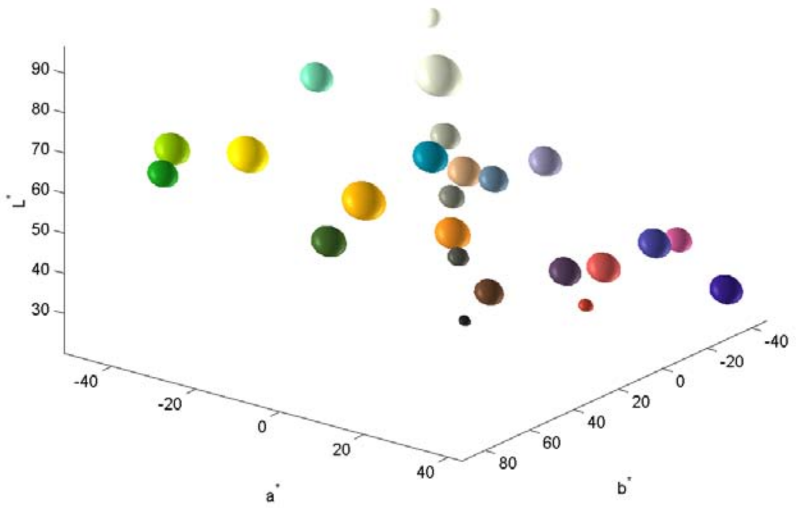

Figure 5.22: Locations of the averages of the measurements of the MBCCC patches in CIE $L^*a^*b^*$ space made under one calibration profile. Each sphere is colored according to the MBCCC patch it represents, and has a radius corresponding to 10 times the average medium-term error of that patch.

The long-term precision is determined using 9 measurements of all the MBCCC patches, each under a different calibration profile determined just before the measurement. To simulate possible long-term changes in the imaging system, the light source voltage was modified for half of the profiles. This resulted in a clearly visible change in color temperature of the light source, although how much precisely was not measured. There was no noticeable difference in precision between measurements made using the profiles of the imaging system with the light

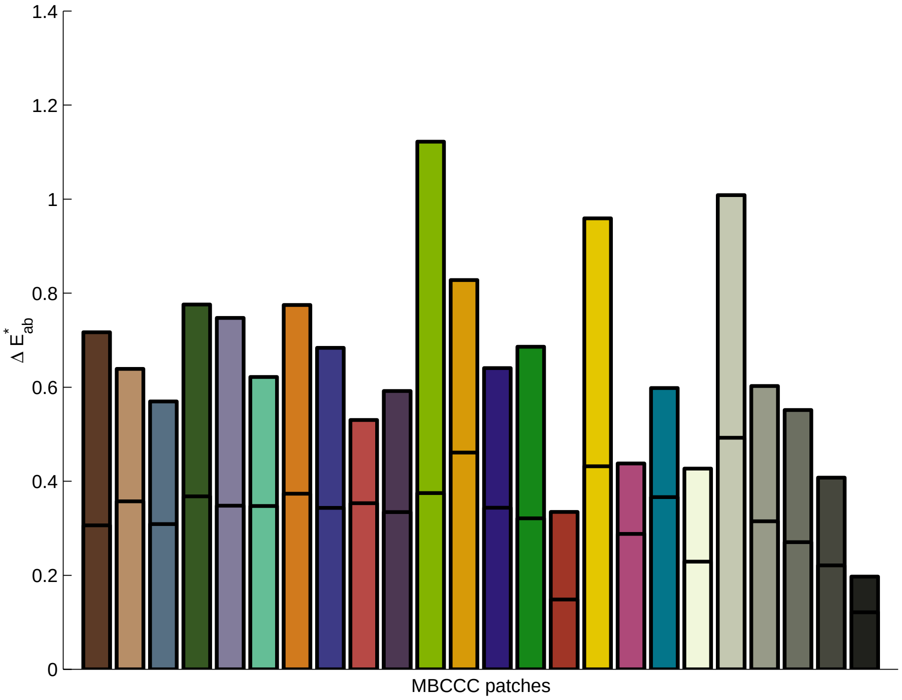

Figure 5.23: Average and maximal ΔE^*_{ab} error of each MBCCC patch over 10 measurements under one calibration profile, with regards to their measurement average determined in CIE $L^*a^*b^*$ space. The color of each bar corresponds to the color of the MBCCC patch it represents.

source at the standard setting and those with the light source at the modified settings. The actual measurements can be seen in fig. 5.24, while the corresponding average and maximal errors per patch can be seen in fig. 5.25. The resulting average and maximal errors over all the MBCCC patches are $\langle \Delta E^*_{ab} \rangle = 0.30$ with $\Delta E^*_{ab} < 1.2$ respectively. The fact that the long-term precision is slightly better than the medium-term precision might be explained by the fact that any measurements for the long-term precision were made directly after the profile was determined, thereby avoiding the drift problems outlined earlier.

5.3.2 Accuracy

The accuracy of a measurement process is a measure of the way measurements of an object are close to the measurement of the same object made by a reference instrument, a spectrophotometer in this case (see

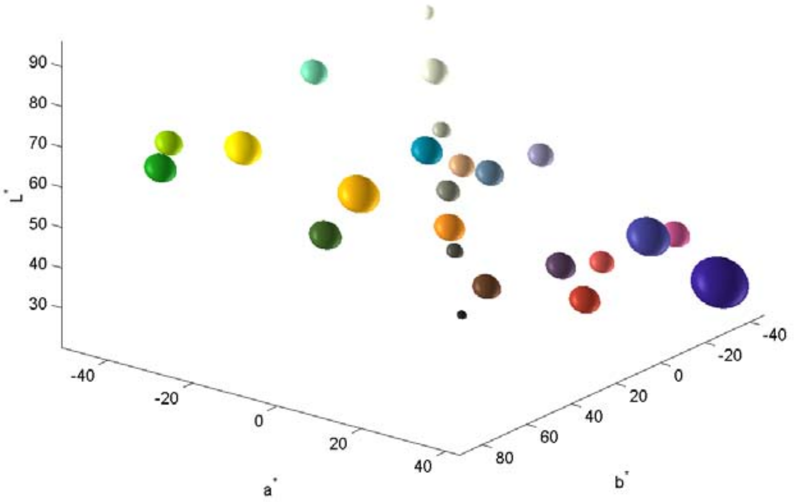

Figure 5.24: Locations of the averages of the measurements of the MBCCC patches in CIE $L^*a^*b^*$ space made under different calibration profiles. Each sphere is colored according to the MBCCC patch it represents, and has a radius corresponding to 10 times the average long-term error of that patch.

fig. 5.20 again for a shooting range analogy). The most important factor in the imaging system accuracy is the RGB to $sRGB$ transform $\Phi_{RGB \rightarrow sRGB,m}$. The accuracy cannot be evaluated using the same objects, i.e. the MBCCC patches, used to calibrate the system. Instead, we need to determine how the transform $\Phi_{RGB \rightarrow sRGB,m}$ performs for different colors spread out over the gamut of the HVS. Keeping the context of dermatology in mind a test set of 27 objects consisting of 15 plastic and paper patches, and 12 in vivo skin areas (normal Caucasian and Asian skin, moles, pimples, etc. ...) will be used. All these objects have been measured using the SPM, and then imaged with the imaging system. Hereafter, spatial averages over areas roughly equal to the SPM measurement area are computed in the $R^*G^*B^*$ space and transformed to CIE $L^*a^*b^*$ via $sRGB$ using the transform $\Phi_{RGB \rightarrow sRGB,m}$. A total of 15 polynomial transforms have been tested: 5 transforms with 3, 6, 8, 9 and 11 terms respectively, each computed using 3 different methods.

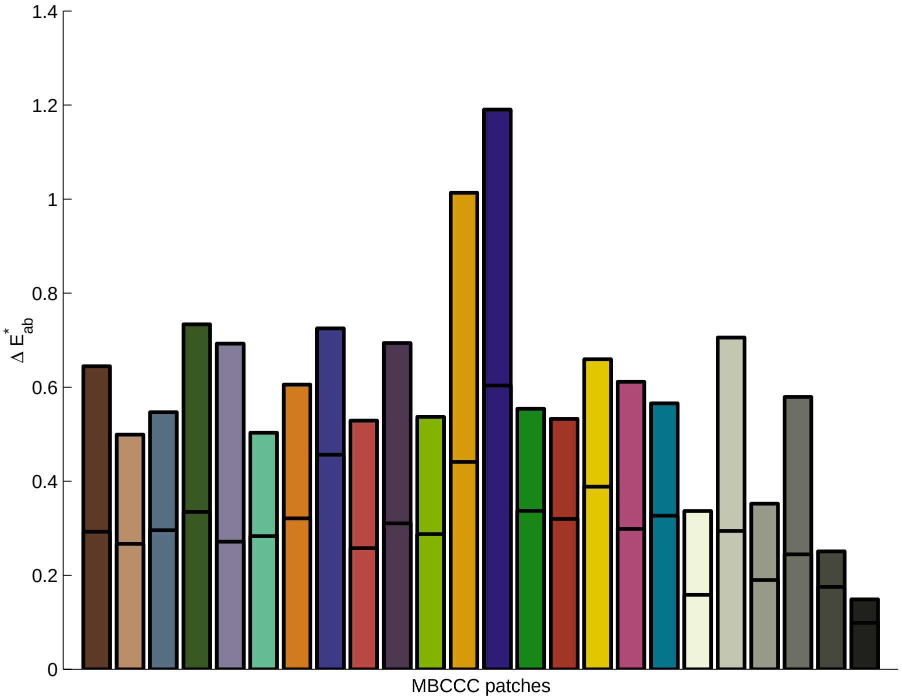

Figure 5.25: Average and maximal ΔE^*_{ab} error of each MBCCC patch over 9 measurements made under several different calibration profiles, with regards to their measurement average determined in CIE $L^*a^*b^*$ space. The color of each bar corresponds to the color of the MBCCC patch it represents.

These methods are: LLSQ, and non-linear minimization of the average and maximal ΔE^*_{ab} error, see also paragraph 5.1.4. Theoretically, each object should be imaged and measured several times to resolve the precision of the imaging system. However, we assume the accuracy will be much lower than the precision, and consequently each object in the test set is only imaged once.

Fig. 5.26 shows the performance of the transforms on the MBCCC patches, i.e. the objects used in computing the transforms. This is not very relevant and is simply used to check proper computation of the transforms by the notoriously tricky non-linear optimization. As expected, performance increases with the number of terms, although the performance of $\Phi_{RGB \to sRGB,11}$ is rather disappointing compared to some of the simpler transforms. One can also remark the hefty price paid by the maximal ΔE^*_{ab} error optimized transforms $\Phi^{max}_{RGB \to sRGB,m}$, $m = 3, 6, 8, 9, 11$ on the average ΔE^*_{ab} error, even if they succeed in strongly reducing the maximal ΔE^*_{ab} error. These transforms also take much longer to compute than the others, probably due to the highly non-linear relation between the transform coefficients and the associated maximal error.

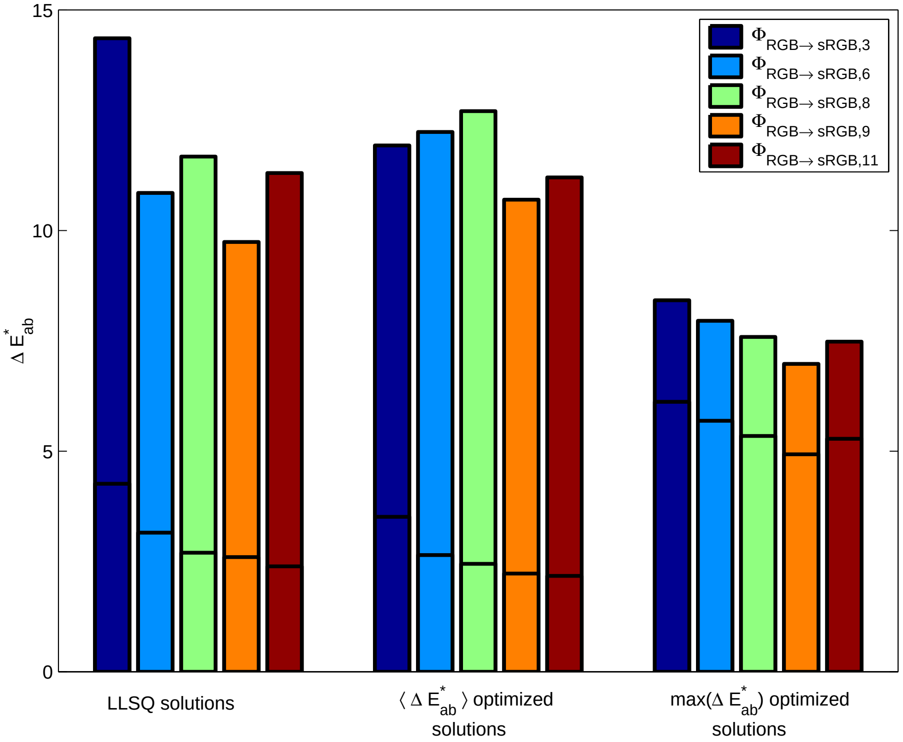

Figure 5.26: Average and maximal ΔE^*_{ab} error of the MBCCC patches with their SPM measurements, for all the LLSQ, average and maximal ΔE^*_{ab} optimized transforms $\Phi_{RGB\rightarrow sRGB,m}, m = 3, 6, 8, 9, 11$.

Fig. 5.27 shows the much more relevant performance of the transforms on the test set of 15 plastic and paper patches and 12 in vivo skin areas. Surprisingly, the non-linear transforms $\Phi_{RGB\rightarrow sRGB,m}, m = 6, 8, 9, 11$, however computed, perform rather poorly. The linear LLSQ and average ΔE^*_{ab} optimized transforms $\Phi^{LLSQ}_{RGB\rightarrow sRGB,3}$ and $\Phi^{avg}_{RGB\rightarrow sRGB,3}$ are clearly the best performers, with $\langle \Delta E^*_{ab} \rangle = 6.21$ and 6.77, and $\max(\Delta E^*_{ab}) = 13.31$ and 13.12 respectively. Considering its low computational complexity, the linear LLSQ transform becomes therefore the transform of choice. This surprising result is very probably due to the limited number of patches used in computing the transforms, leading to a very sparse sampling of the RGB and $sRGB$ color spaces. This hardly affects the linear transforms which have very good generalizing properties and which are already very 'overdetermined', but may lead to uncontrolled, oscillating behavior between the sample points for higher-order transforms. This sparse sampling is probably also the reason why even the linear maximal ΔE^*_{ab} optimized transform $\Phi^{max}_{RGB \rightarrow sRGB,3}$ isn't any good: for this transform to work it needs to have a good idea were the color with a potentially high mapping error is actually located...

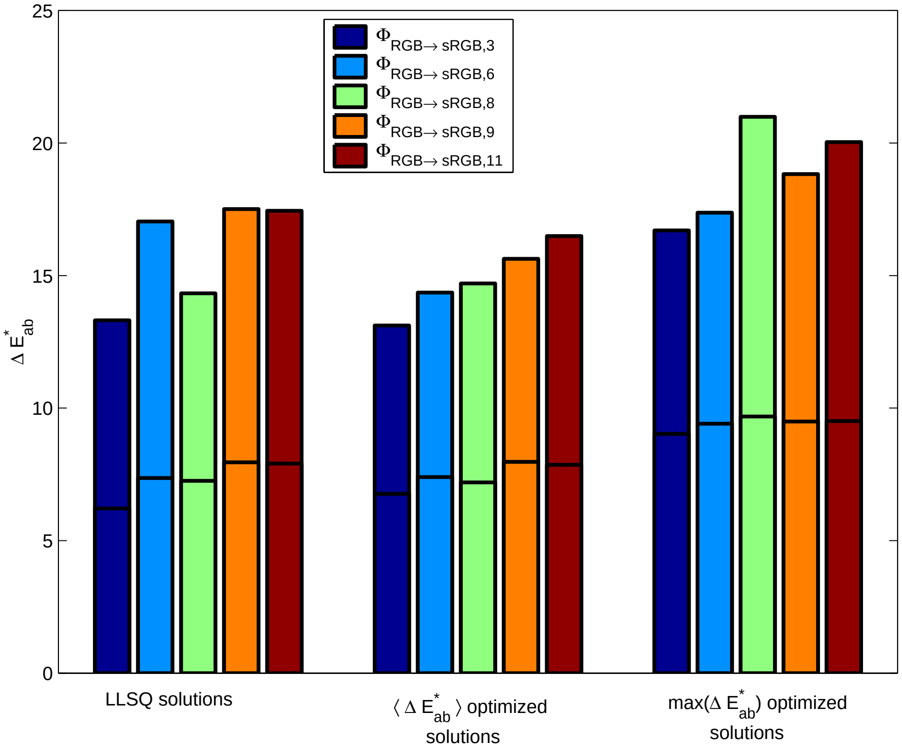

Figure 5.27: Average and maximal ΔE^*_{ab} error of the test set of 15 plastic and paper patches and 12 in vivo skin areas with their SPM measurements, for all the LLSQ, average and maximal ΔE^*_{ab} optimized transforms $\Phi_{RGB \rightarrow sRGB,m}, m = 3, 6, 8, 9, 11$.

Fig. 5.28 shows a comparison of the CIE $L^*a^*b^*$ values of the test set objects as measured by the imaging system with the chosen linear LLSQ transform and the SPM measurements, with the resulting ΔE^*_{ab} errors in fig. 5.29. Although the variety of color of the in vivo skin measurements of the test set was a bit disappointing, the corresponding errors are of the same order or lower than those of the plastic and paper patches. This could easily have been otherwise because the actual spectra of the skin samples may be completely different from those of the skin colored MBCCC patches used to calibrate the system (MBCCC skin patches have been designed to have both spectral and colorimetric properties that are similar to an *average* skin, [46]). This means that, as the camera is not colorimetric, two skin colored objects with the same color as perceived by a human but actually different spectra might result in different tristimulus values as measured by the imaging system. This machine-human metamerism can not be corrected, but is thus probably not in issue for skin imaging.

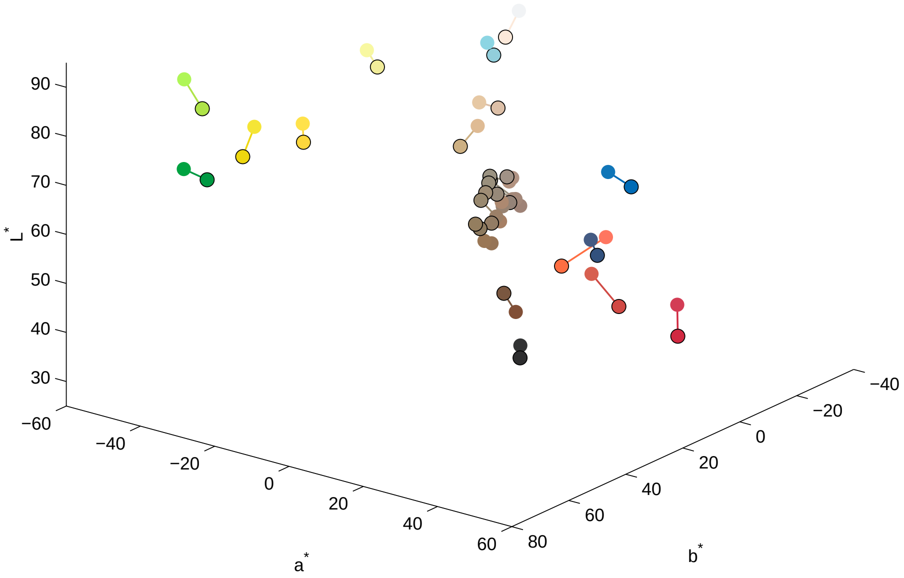

Figure 5.28: The CIE $L^*a^*b^*$ values of the test set of 15 plastic and paper patches and 12 in vivo skin areas, as measured by SPM and by the imaging system using the LLSQ linear transform $\Phi^{LLSQ}_{RGB\rightarrow sRGB,3}$. The markers are colored according to their position in CIE $L^*a^*b^*$ space, and the SPM measurements have black circles around them while the imaging system measurements have not.

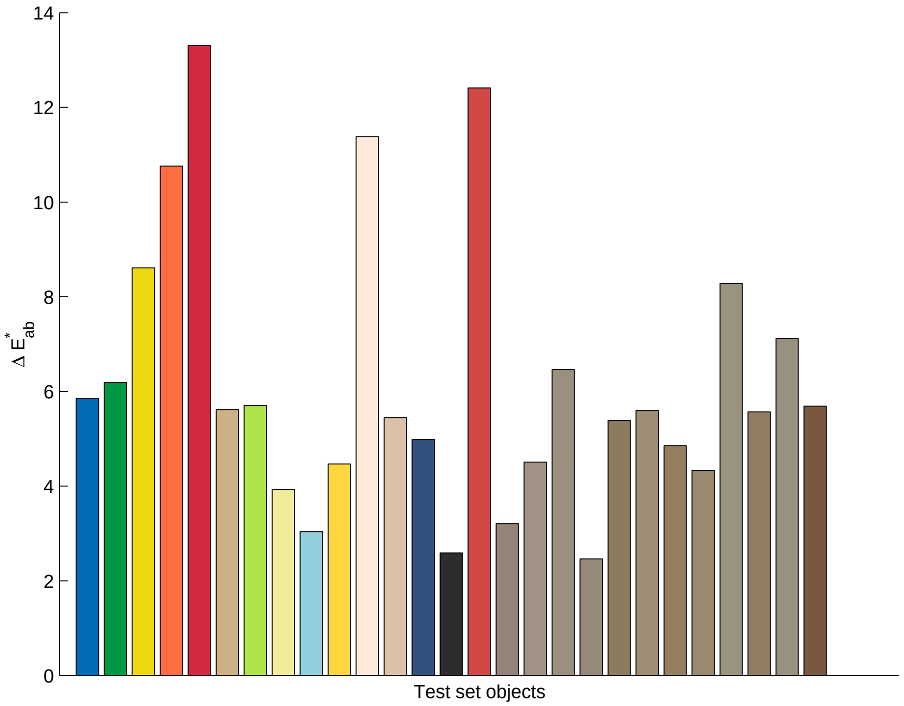

Figure 5.29: The ΔE^*_{ab} errors of the test set of 15 plastic and paper patches (bars on the left) and 12 in vivo skin areas (bars on the right) between the SPM and the imaging system measurements using the LLSQ linear transform $\Phi^{LLSQ}_{RGB \rightarrow sRGB,3}$. The color of each bar corresponds to the color of the test object it represents.

5.4 Conclusions

The calibration and operation of the dermatological imaging was thoroughly reviewed during the course of this chapter. Calibration involves the determination of a number of optimal imaging system settings called a calibration profile, and this should not take more than 10 minutes. Once determined a profile remains valid for tens of hours of operation of the imaging system. Operating the imaging system starts with a check and adjustment of the current calibration profile using a white patch. An image of this patch will also be used to perform a shading correction on acquired images. Images may then be acquired freely for about 15 minutes, and are subsequently transformed to the native color space of the imaging system, i.e. $sR^*G^*B^*$. This standard color space allows meaningful exchange of images, as well as realistic viewing on

CRT monitors without the need for conversion to another color space. Its known relation with human vision related color spaces provides a colorimetric framework for the development of image processing algorithms, which should in turn result in wider applicability and possibility of cross-validation of these algorithms.

Central to the discussion of this imaging system are the precision and accuracy of colorimetric measurements performed on acquired images. The precision of the imaging system is very good, with a series of measurements of the same color all lying within $\Delta E^*_{ab} = 1.2$ of the measurement average. The average color difference of the measurements with regard to the measurement average is much lower though, usually less than $\Delta E^*_{ab} = 0.34$. The accuracy of a colorimetric measurement compared to a SPM was determined using a set of 27 targets, including 12 in vivo skin areas. It is mainly dependent on the transform used between the RGB source and the $sRGB$ calibration target color space of the imaging system. Several types of polynomial transforms were tested, both optimized in the target color space and in the perceptually uniform CIE $L^*a^*b^*$ color space. The unexpected result is that 'simpler is better', with the simple linear transform optimized in the target color space turning in a respectable average error of $\Delta E^*_{ab} = 6.21$, with no error exceeding $\Delta E^*_{ab} = 13.31$. It has to be said that the exact implications of these errors for the diagnose of dermatological afflications is unknown, and must definitvely be addressed in the future.

The work detailed in this chapter is the subject of several congress papers and abstracts, [47, 48, 49, 50]. It is also the subject of an article published in a international peer-reviewed journal, [51]. Furthermore, there has been interest from a private company to incorporate some of the technology behind our imaging system into a multi-modal dermatological imaging system, and negotiations are currently underway.

Chapter 6

The dermatological workstation

With the imaging system operational and completely characterized we can shift our attention to the creation of the dermatological workstation, which hopefully turns what is still a complicated and unwieldy system into a useful clinical tool. On a basic level this dermatological workstation adds three new components to the imaging system: a patient and image database, an application to manage this database, and a software 'object' for the processing of the acquired images. In its most simple form this object allows for image viewing and simple manipulation, e.g. zooming, but it can readily be extended to include more complex functions such as segmentation and feature extraction (see fig. 6.1). The creation of these three components involves many different aspects from both the technological and the scientific domain: GUI design, patient and image database design, software design, image processing, etc. .... Some of these facets turned out to be quite complex and time consuming, and involved a very close and constant cooperation with the intended final users, i.e. the dermatologists. The work presented in this chapter needs to be further refined and extended to be widely applicable. This lies outside the scope of a phd, and is consequently best left to interested commercial third parties, if any. Instead, the work in this chapter must be seen as a demonstration of some of the capabilities of the imaging system, i.e. a 'proof of concept'.

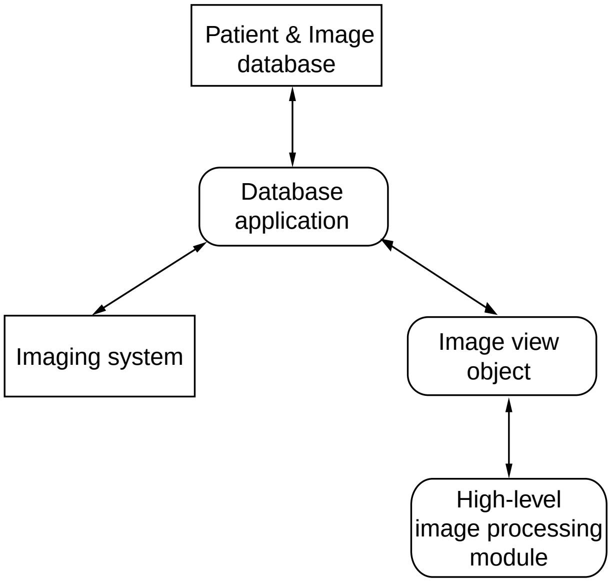

Figure 6.1: The parts constituting the dermatological workstation.

6.1 The patient and image database

Both the patient and image database structure and GUI design of the database application should reflect the work-flow of a dermatologist when performing the follow-up of patients with an increased risk of melanoma. To this end a kind of 'entity tree' was constructed in cooperation with the dermatologists, see fig. 6.2. This hierarchy of entities shows how a patient can have several consultations. For each consultation several regions-of-interest (ROIs) can be defined, and each of these ROIS can be examined. During such a ROI examination one or more images of that ROI can be acquired. As intended, this very 'vertical' model forces the user in a well-defined work flow, hereby reducing the room for mistakes.

The patient and image database contains many database tables and records which are exact representations of the entities in fig. 6.2, see fig. 6.3. However, for practical and efficiency reasons the database structure also shows some significant departures from the entity tree, especially regarding the relationships between the database tables-entities. An example of this is the tables of ROIs: it is not known beforehand during how many consultations a ROI has to be examined, just as it is not known how many ROIs a consultation will have. Short of having

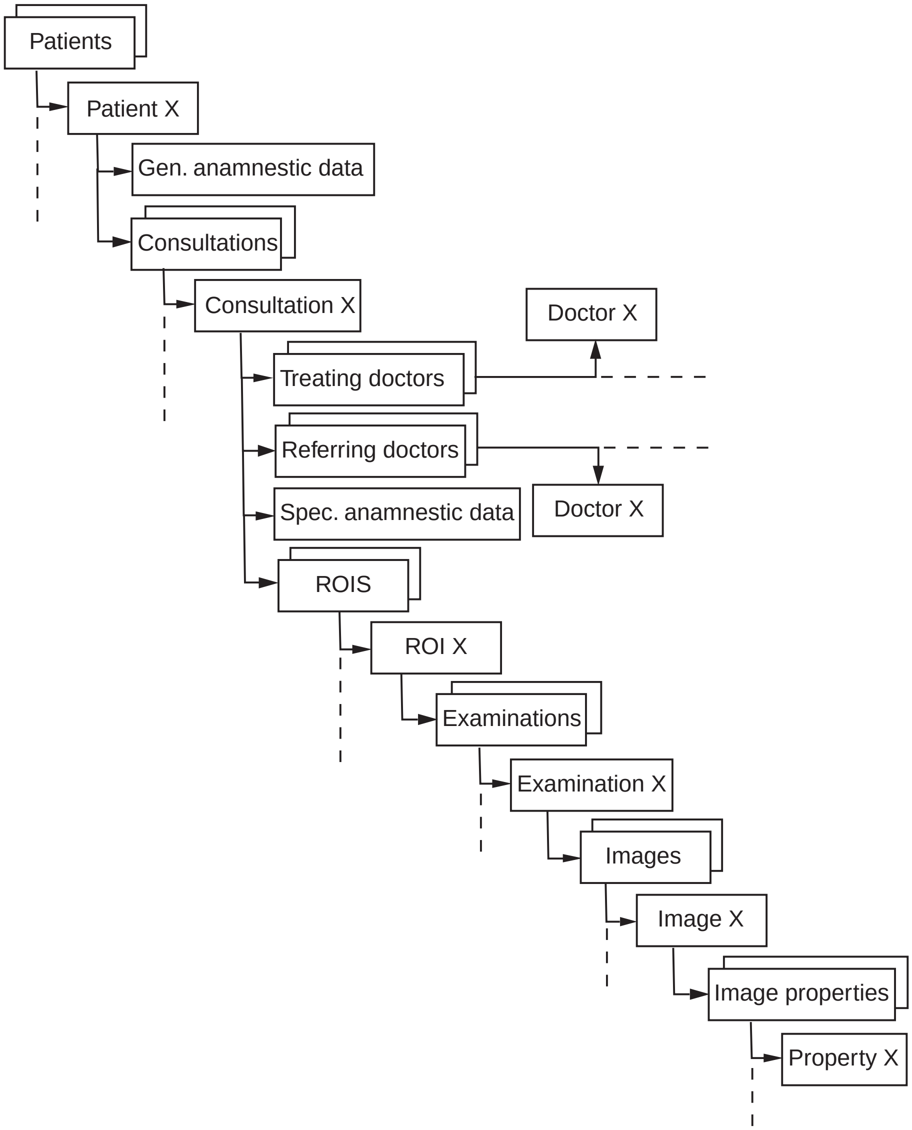

Figure 6.2: Overview of the entity tree on which both the database structure and the GUI of the database application are based.

a quickly growing intermediary table in the database, the following solution is used: ROI records are only linked to the record representing the consultation during which they were created. The ROI examination records, on the other hand, are linked to the ROI record to which they belong and to the record representing the current consultation. Consequently, the first link allows retrieval of information on the ROI and the consultation during which the ROI was first created, while the second link provides information on the current consultation.

An attempt was made to take a lot of possibilities and contingencies into account when creating the database structure, resulting in a very consistent database on which retrospective studies (data mining), e.g. for epidemiological purposes, are relatively easy to perform. Free text fields are exceptional in the database, and almost all the field entries, especially medical terms, are taken from exhaustive lists in order to avoid ambiguities.

The database has been developed in MS Access, but it should be easy to convert to any database management system (DBMS). Fig. 6.3 shows the tables, record fields and their relationships in the database. The field and table names are in Dutch, but this is not important as the figure is purely demonstrative and we will not go into a detailed discussion of all the tables and fields. Images are not saved in the database as so-called 'binary large objects' (BLOBs), instead they are given a unique filename that is stored in the database. The image itself is saved in two special directories, once as a full-sized image and once as a thumbnail for fast preview.

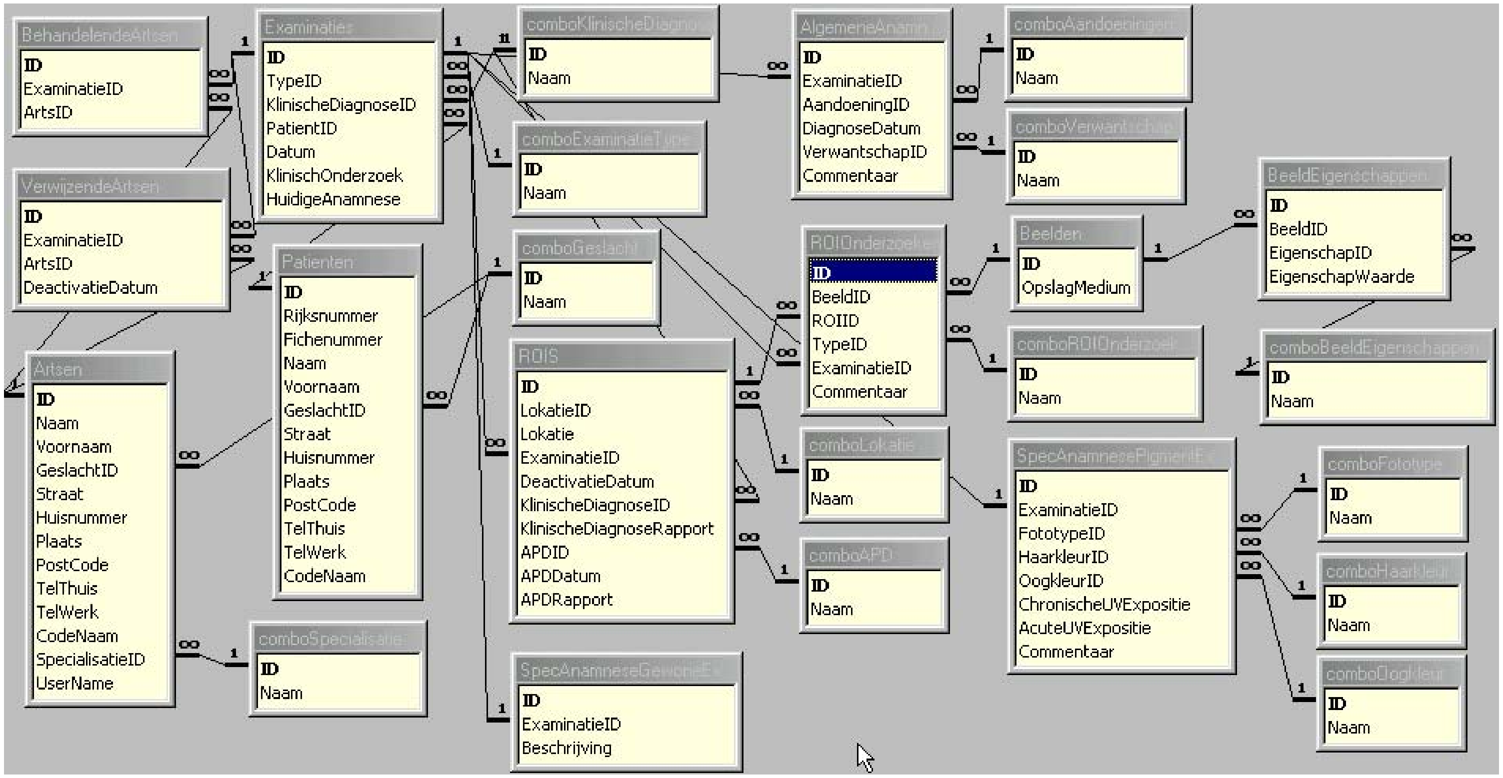

Figure 6.3: The tables, fields and relationships of the dermatological database. The table and field names are in Dutch.

6.2 The database application

The database application is developed in VB using ActiveX data objects (ADO). This object model provides a standard interface to any data provider that has an OLE DB driver. As such it can access not only Jet databases (MS Access), but also e.g. several types of SQL (structured query language) DBMS running on different platforms. All database queries are written using SQL.

The database application is closely modeled on the database structure of fig. 6.2, which means that it has a rather 'static' GUI. Consequently, if the database structure changes the application has to be adapted to those changes. Note that this would indicate a fault or omission in the design phase of the database, and should therefore not occur.

In order to make the creation or modification of data forms, i.e. windows used for the manipulation of data, as easy as possible generalized event handlers were developed. These event handlers take care of most of the actions initiated from the data forms by the user, e.g. searching, adding and editing of records. Certain data form controls are bound to a database field during the design phase, and the generalized event handlers will then automatically handle all traffic between the 'bound' control and its database field. This is similar in concept to the data bound controls provided by VB, but tailored to our specific needs and without some annoying bugs and hefty overhead. The generalized event handlers also manage the visibility and availability of controls, e.g. buttons, in a data form according to the current context. The use of general event handlers, besides resulting in increased code reusability, also ensures consistent operation of the data forms throughout the application.

The database application also enforces a simple security model based on the login name of the user. Because the database contains a list of doctors and their login names the application is able to recognize them. Only a doctor can create a new consultation, and he or she is then automatically added as a treating doctor to that consultation. Once created, only a treating doctor can modify any field from a consultation or any object derived from an consultation, e.g. a ROI or a (ROI) examination. If more than one doctor needs to be able to modify a consultation, the 'creating' doctor can simply add a colleague to the list of treating doctors for that consultation.

The database application does not allow the removal of records. Moreover, modification of records, on top of personal user permissions, is restricted to the most recent consultation of a patient, i.e. a consultation remains ‘open’ as long as no new consultation is created for that patient. This avoids illegal modifications of prior consultations, which may have been involved in a medical decision making process. On top of that, records are generally time stamped either explicitly using a date field, or implicitly by being linked to another explicitly time stamped record. This allows the database application to report all the information concerning a consultation *as it was known at the time that consultation was performed*, eventually disregarding more recent information. In so doing the exact context of a medical decision may be recreated, so that it can be reviewed and discussed. Time stamping also allows some database records to be ‘persistent’ , i.e. to appear linked to more records than they actually are. An example of this are ROI records which are linked to a certain consultation when they are created, but which are assumed present in any consultation of later date until explicitly deactivated using a termination time stamp. This would not be possible using normal one-to-many relations in the database without an evergrowing intermediary table because the number of ROIs per consultation is unknown and variable.

The database application has a so-called ‘multiple document interface’ (MDI), whereby the main application form acts as a container managing a series of child forms. Some of these child forms will now be reviewed, without going into too much detail. The application is also able to generate printable reports in the hypertext markup language (HTML) so they can be viewed in a web browser, or to create a MS Word document.

6.2.1 The main database view

The main database view form is always present and provides the user with an overview of the information of one or more patients in the database, see fig. 6.4. For this it uses a so-called ‘tree-view’ similar to the one used in many file managers. The hierarchy of the nodes in this tree-view is a representation of the entity tree in fig. 6.2. Such a tree-view provides a number of methods for navigation where individual nodes are identified and can be retrieved using unique so-called ‘keys’ . These keys play an important role because they are constructed in such a way that from a key we can retrieve the type, e.g. a patient, patients, a consultation, etc. . . . , as well as the ID of the corresponding record in the database, if applicable. Context sensitive menus are available for most nodes, allowing viewing and editing for nodes representing single records (singular name), e.g. a patient, an examination, etc. .... For nodes representing a table (plural name), e.g. patients, examinations, etc. ..., these menus allow searching or the addition of a new record. Availability of these actions is of course subject to individual user permissions. There are one or two types of nodes that depart from this principle, most notably the 'medical antecedents' node type which uses a spread sheet type data form that allows both viewing and editing of individual records as well as addition of a record at the same time.

6.2.2 The data forms

In order for a data form to use the generalized event handlers to search, modify or create database records it must contain some predefined controls, as well as some special routines in its associated code module. These are supplemented at design time by the necessary data bound controls to show some or all of the fields of a record, see fig. 6.5. The generalized event handlers are usually triggered from the data form code module upon any user interaction resulting in a form control event, e.g. pushing a button, changing a text field, ... Before and after processing by the general event routines control is temporarily passed back to the form module using some predefined callback methods. These callbacks can be used to perform some special processing or control management not foreseen in the generalized event handlers, but most of the time they do not contain any code. Fig. 6.6 gives an overview of the operation of the generalized event handlers. Besides some frames and labels, the predefined controls include buttons to change the operational mode of the form, to end an operational mode, and to dispatch the form. The normal passive operational mode is 'view', which is used to view one or more records. The possible active operational modes are 'search', 'edit' and 'new ' which are used to search for a record, edit a record or add a new record respectively. An active operational mode can only be accessed from the passive view mode, and must be terminated properly using the 'Ok' or 'Cancel ' button before any other operation can be initiated, including dispatching the form. Enforcement of these simple rules is done by hiding or disabling buttons that start inappropriate actions. The behavior of a data form, e.g. the availability of the active operational modes, can be modified at run time when the form is created. Fig. 6.7 gives an example of the use of a data form to search a patient.

The acquisition of calibrated color images can be initiated from the data form used to add a new ROI examination using a context sensitive

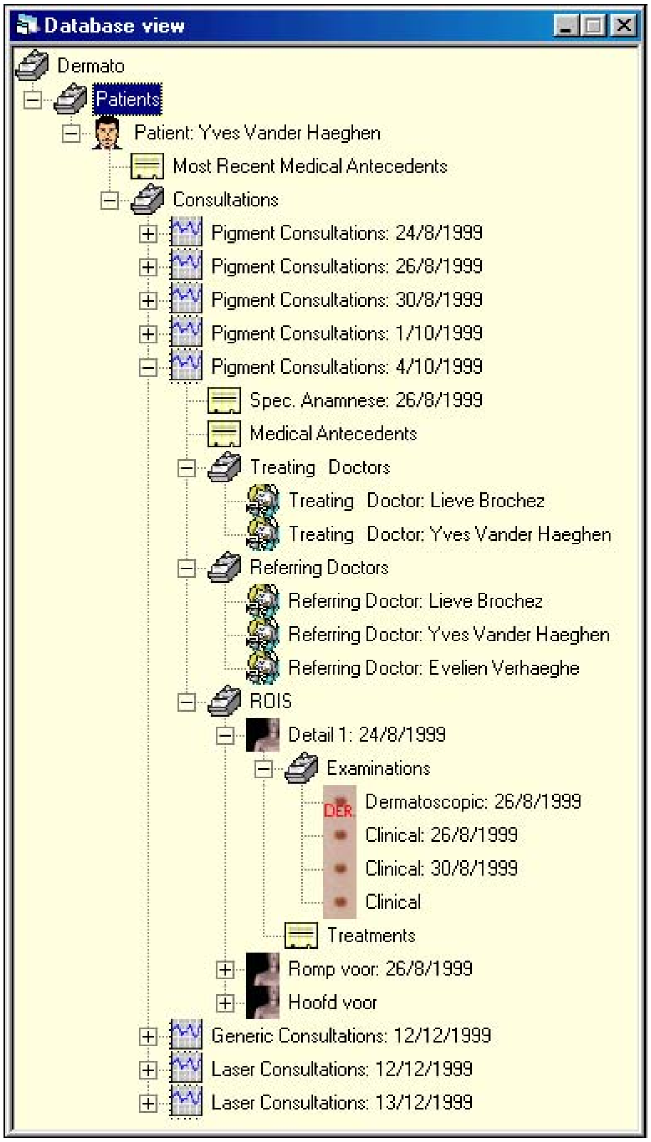

- Dermato
  - Patients
    - Patient: Yves Vander Haeghen
      - Most Recent Medical Antecedents
      - Consultations
        - Pigment Consultations: 24/8/1999
        - Pigment Consultations: 26/8/1999
        - Pigment Consultations: 30/8/1999
        - Pigment Consultations: 1/10/1999
        - Pigment Consultations: 4/10/1999
          - Spec. Anamnese: 26/8/1999
          - Medical Antecedents
          - Treating Doctors
            - Treating Doctor: Lieve Brochez
            - Treating Doctor: Yves Vander Haeghen
          - Referring Doctors
            - Referring Doctor: Lieve Brochez
            - Referring Doctor: Yves Vander Haeghen
            - Referring Doctor: Evelien Verhaeghe
          - ROIS
            - Detail 1: 24/8/1999
              - Examinations
                - Dermatoscopic: 26/8/1999
                - Clinical: 26/8/1999
                - Clinical: 30/8/1999
                - Clinical
              - Treatments
            - Romp voor: 26/8/1999
            - Hoofd voor
        - Generic Consultations: 12/12/1999
        - Laser Consultations: 12/12/1999
        - Laser Consultations: 13/12/1999

Figure 6.4: The main database view for one patient, using a tree-view. Different types of nodes, corresponding with different objects in the database, usually have their own icon for easy overview.

menu, see fig. 6.8. This instantiates a software object that represents the imaging system and guides the user through the acquisition process as described in the previous chapter. Upon successful completion the acquired calibrated color image is left on the clipboard where it can be

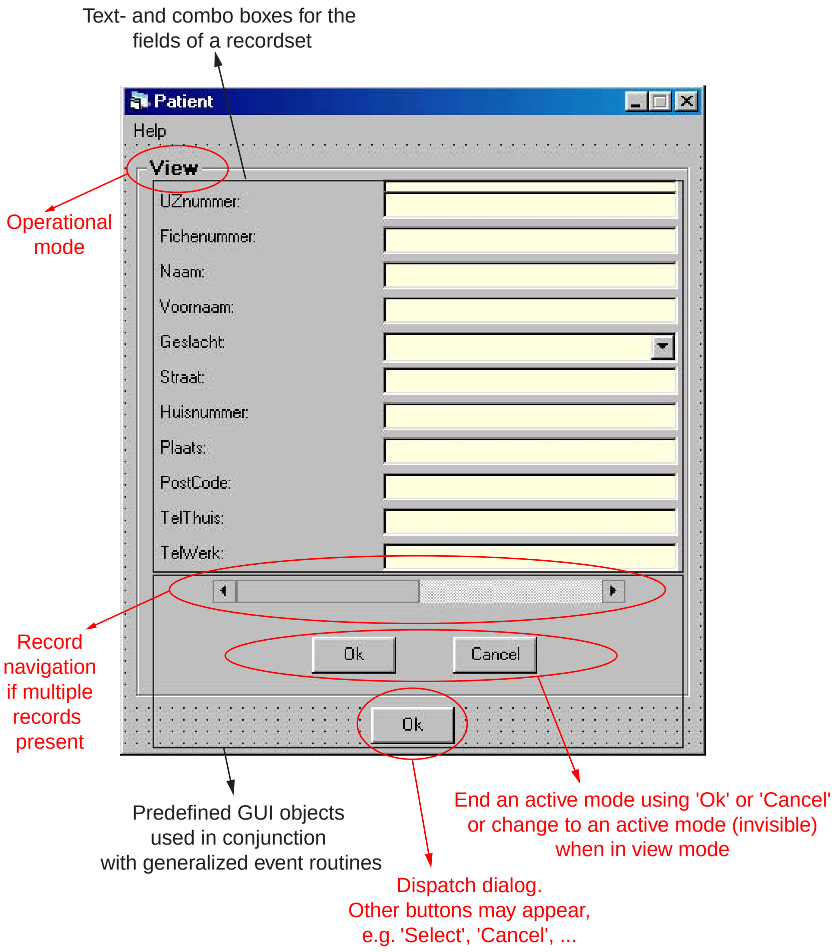

Figure 6.5: Layout and use of the controls of a data form using the generalized event handlers. Note that not all predefined controls are visible, and that button labels may change.

retrieved by the workstation application for further processing. This processing consists of the creation of a thumbnail and the saving of the original and thumbnail images in the proper directories using the proper filenames.

6.2.3 The 3D localization and quick view form

There are two types of ROIs: ‘overview’ ROIs which represent a named body part, e.g. arm, back, etc. . . . , and ‘detail’ ROIs which represents

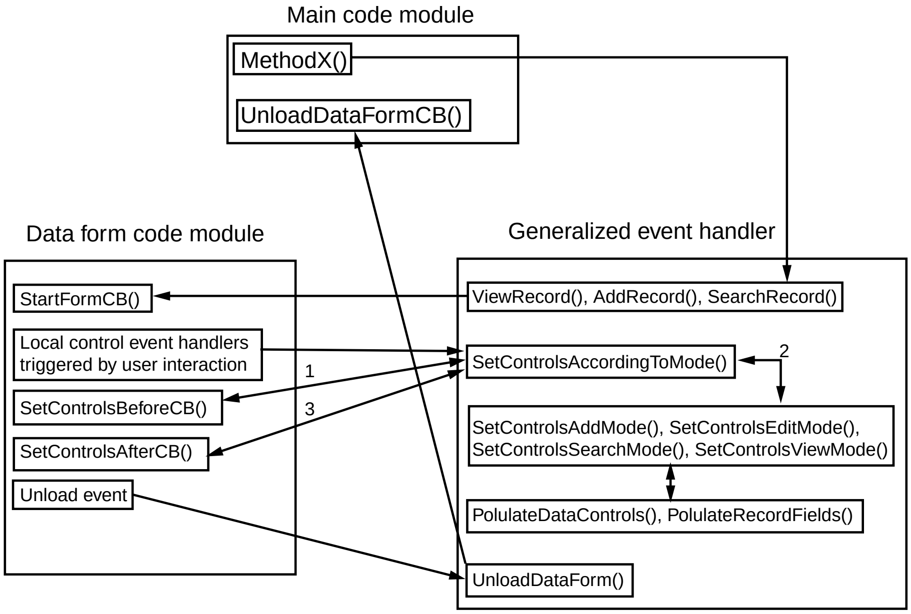

Figure 6.6: Overview of the interaction between a form and the generalized event module.

a very small area consistent with the FOV of the calibrated color images. Consequently, calibrated color images can only be added to detail ROIs, and not to overview ROIs which are used to link uncalibrated low resolution imagery. All active ROIs of a patient are instantly accessible when a new consultation is created, and their history of 'ROI examinations' can be reviewed. If required, a new ROI examination can be added, with or without an image. These examinations can be of 2 types for the moment: 'clinical' or 'dermatoscopic' . This could be extended with e.g. histological examinations in the future.

Consequently, reviewing existing ROIs and examinations, and adding new examinations are the main tasks during a patient consultation. To aid in this task two special forms can be permanently displayed: the 3D localization form which displays markings corresponding to the location of detail ROIs on a 3D puppet, and the quick view form which shows thumbnail previews of images associated with ROI examinations, see fig. 6.9. Both these forms work in unison with the main database view and display information according to the selected node there:

A node of type 'ROIs' is selected The 3D localization form displays all the active ROIs of the consultation. The quick view shows

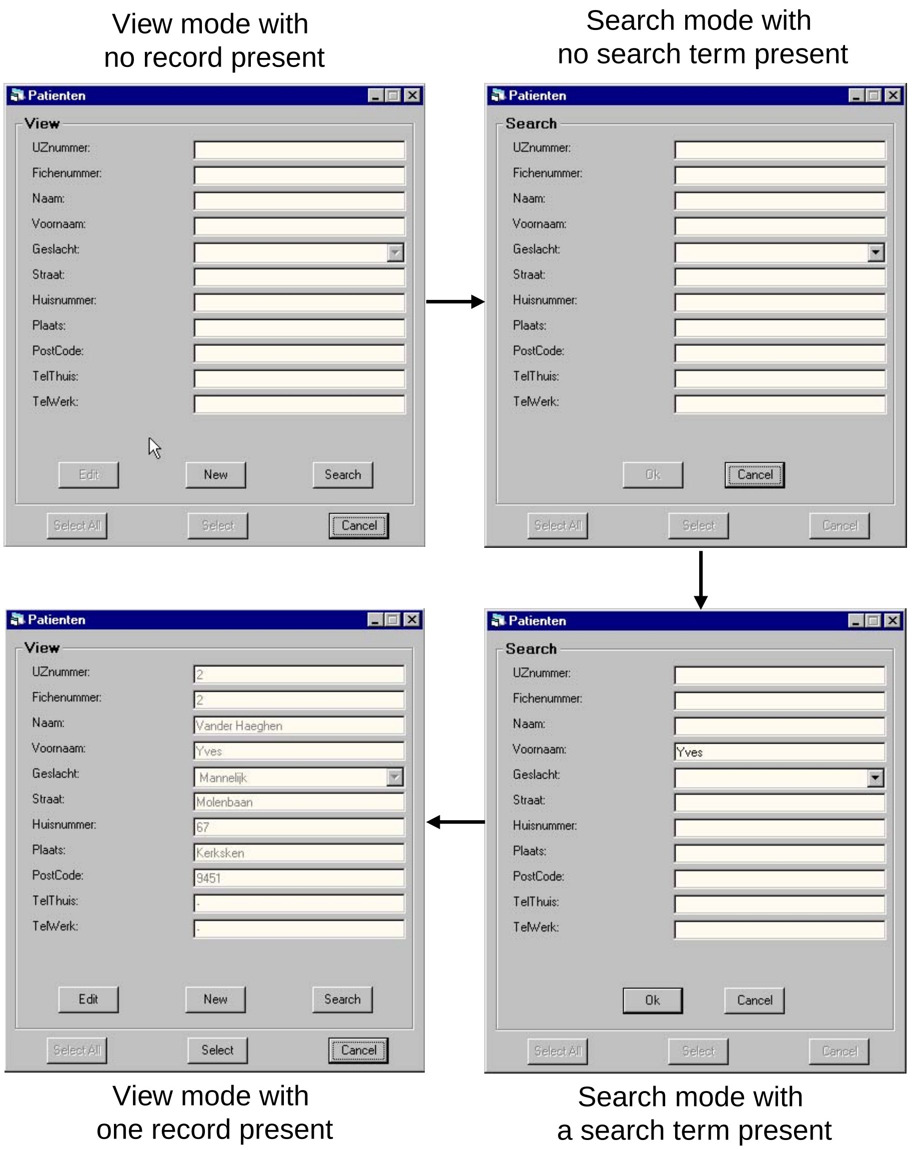

View mode with no record present

Search mode with no search term present

Search mode with a search term present

View mode with one record present

Search mode with a search term present:

Voornaam: Yves

View mode with one record present:

UZnummer: 2
Fichenummer: 2
Naam: Vander Haeghen
Voornaam: Yves
Geslacht: Mannelijk
Straat: Molenbaan
Huisnummer: 67
Plaats: Kerksken
PostCode: 9451
TelThuis: -
TelWerk: -

Figure 6.7: Operation of a data form when searching for a patient. Notice how controls that represent inappropriate actions are either disabled (grayed out) or invisible.

the thumbnails of the most recent image of each ROI examination type and for each active ROI;

A node of type 'ROI' or 'ROI examinations' is selected The

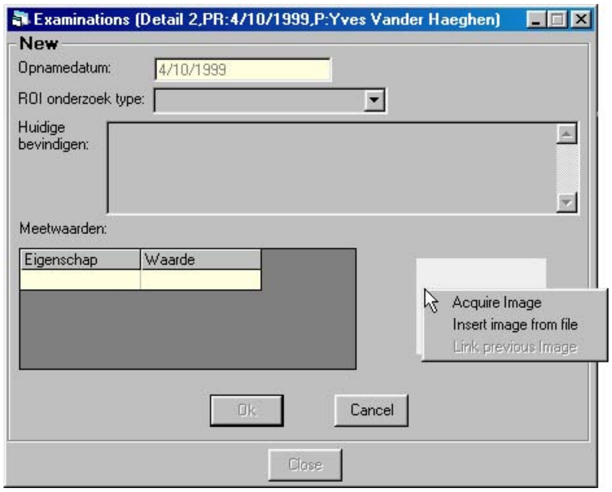

Examinations (Detail 2,PR:4/10/1999,P:Yves Vander Haeghen)

Opnamedatum: 4/10/1999

Figure 6.8: Initiation of calibrated color image acquisition from the data form used to add a new ROI examination.

3D localization form displays all the active ROIs of the consultation, but the current ROI is encircled. The quick view shows the thumbnails of the images associated with all the ROI examinations of that ROI, see fig. 6.9;

A node of type 'ROI examination' is selected The 3D localization form displays all the active ROIs of the consultation, but the current ROI is encircled. The quick view shows the thumbnails of the images associated with all the ROI examinations of the same type as the selected ROI examination, and belonging to that ROI.

The 3D localization form is also used when adding a new ROI during a consultation, but in that case a top-down view of the puppet is also displayed so that a full 3D location can be deduced. When showing 3D locations those on the front of the puppet are in green, those on the back are in red. The puppet can be rotated in steps of 45 degrees. Full-size view of any image is performed by the view high-level image processing module described in the next paragraph, and is accessed by clicking on any thumbnail.

6.2.4 Report generation

The database application can also generate single document printable reports of patients, see fig. 6.10. At first the idea was to provide a docu-

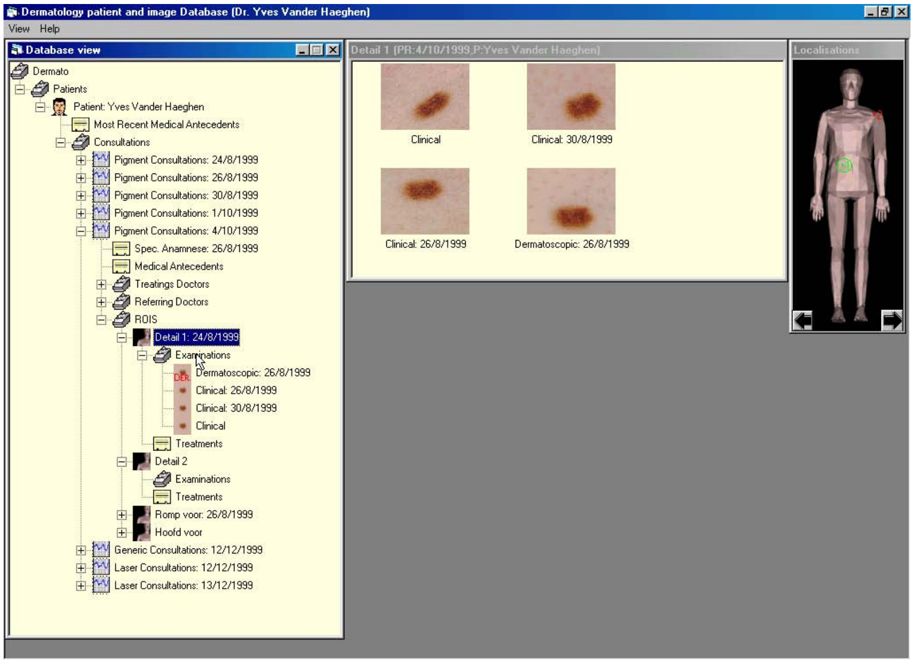

Figure 6.9: Example of synchronous operation between the main database form and both the 3D localization and the quick view form.

ment similar to the paper patient files compatible with the current filing system, and avoid loss of data if the introduction of the dermatological workstation did not work out. With this in mind reports where generated in MS Word. However, if in the future patient information is to be accessible from any generic workstation in the dermatology department, the hypertext markup language (HTML) is much more interesting. Consequently, the report generator software module was rewritten to create dynamic HTML pages which could easily be published on the intranet. In such a setup the database application would be used for imaging and data input, while read-only access of the patient database and images would be done through an intranet webserver and the report generator module. New technologies like the extensible markup language (XML) and its companions make this kind of setup more and more powerful and easier to create.

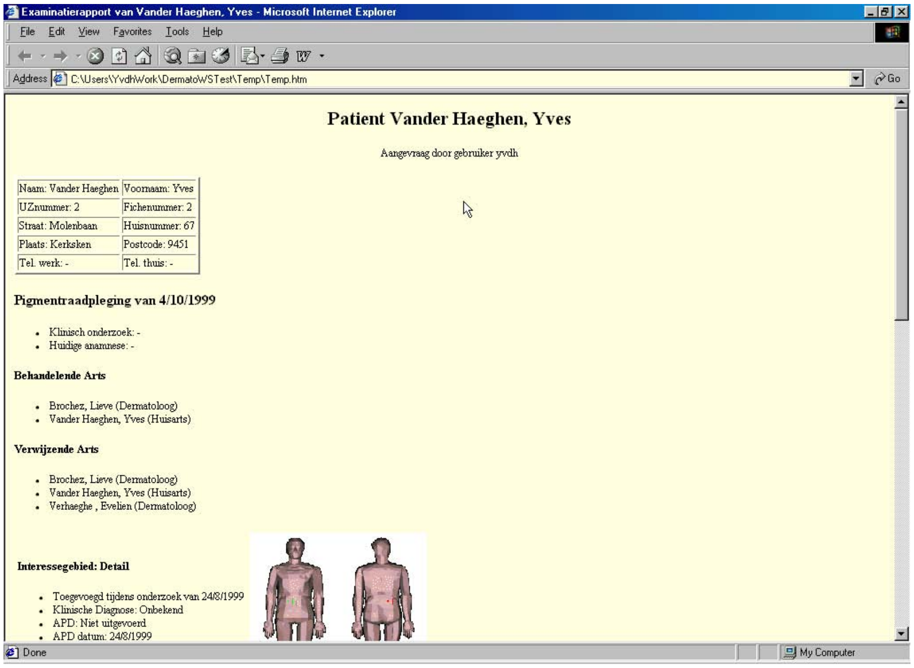

Patient Vander Haeghen, Yves

Aangevraag door gebruiker yvdh

Naam: Vander Haeghen	Voornaam: Yves
UZnummer: 2	Fichenummer: 2
Straat: Molenbaan	Huisnummer: 67
Plaats: Kerksken	Postcode: 9451
Tel. werk: -	Tel. thuis: -

Pigmentraadpleging van 4/10/1999

- Klinisch onderzoek: -
- Huidige anamnese: -

Behandelende Arts

- Brochez, Lieve (Dermatoloog)
- Vander Haeghen, Yves (Huisarts)

Verwijzende Arts

- Brochez, Lieve (Dermatoloog)
- Vander Haeghen, Yves (Huisarts)
- Verhaeghe , Evelien (Dermatoloog)

Interessegebied: Detail

- Toegevoegd tijdens onderzoek van 24/8/1999
- Klinische Diagnose: Onbekend
- APD: Niet uitgevoerd
- APD datum: 24/8/1999

Figure 6.10: Part of a report of a patient created using HTML.

6.3 The view object

The view object is responsible for simple manipulation of images, e.g. viewing and zooming, and file input and output. It is implemented as a software class object with its own display form and menus, and must be instantiated from other applications. It uses the Leadtools Medical Express Imaging Toolkit[1]. Some of the simple functionality from the view object and which is accessible by the user includes:

Zooming Zoom up or down whereby the zoom factor is multiplied or divided by 2 respectively. The zoom method can also be selected: nearest neighbor, linear or bicubic interpolation when zooming in or nearest neighbor and averaging when zooming out. There is also a freehand zoom.

Display of pixel values Assuming a 24-bit $sR^*G^*B^*$ image, the view object can display $sR^*G^*B^*$,$sRGB$, CIE XYZ, CIE xyY and CIE $L^*a^*b^*$ color triplets of an averaging window at the location of the

---

[1] LEAD Technologies, Inc., 900 Baxter Street, Charlotte, NC 28204.

mouse pointer. The size of the averaging window can be set using the '-' and '+' keys.

Visibility of annotations and region Annotations are graphical objects like text, rectangles, polygons, etc. ... which are drawn in overlay on the image. A region is made up of sets of rectangles. Both polygonal annotations and regions can be used for image processing.

sR*G*B* histogram Generates an histogram.

On top of these interactive functions, the view class allows both the interactive and programmatic creation, manipulation and retrieve of annotations. Together with the possibility of adding entries in the 'Action Menu' , called 'action modes' , and the propagation of events related to the selection and ending of these action modes to the calling application, it is easy to extend the basic functionality of the view class. This is precisely how the high-level image processing routines, e.g. segmentation and subsequent feature extraction, will be implemented.

6.4 Image processing

When trying to extend the basic workstation applications and tools with more sophisticated applications, e.g. to allow measurement and comparison of diagnostic lesion features and even classify lesions based on these features, image processing will play an important role. As mentioned several times already, one of the great interests for image processing of having images in well-defined colorimetric or colorimetry related color spaces, is the availability of color difference metrics and a wider applicability of any developed image processing algorithm. This last point is a natural consequence of the more precise knowledge of the nature of the image data. To demonstrate the first point we will propose a simple semi-automatic segmentation algorithm for skin lesions based on the CIE ΔE^*_{ab} color difference metric, and compare it with manual delineation by dermatologists.

6.4.1 Segmentation of a skin lesion

Before any skin lesion feature extraction and classification is possible, the skin lesion must be separated from the rest of the image, i.e. it must be segmented. Images of skin lesions show surprising variability in shape and color, see fig. 6.11. Together with the presence of hairs this makes the robust detection of a lesion border very difficult without some human intervention. Several papers have been published on this subject, e.g. [52, 13, 53, 54, 55, 56], claiming good segmentation results. These publications present many different methods: radial search starting from a central point, principal component transform (PCT) followed by histogram based techniques, adaptive thresholding, fuzzy C-means clustering, watershed segmentation followed by a region classifier, etc. .... Some of the presented methods also used the CIE $L^*a^*b^*$ color space, but again it was unclear how proper CIE $L^*a^*b^*$ color triplets could be obtained if the RGB primaries of the acquisition color space are unknown. Another potentially very interesting technique is so-called 'live-wire' segmentation [57]. This reproducible interactive technique computes locally optimal paths according to some criterion between a start point and the current cursor position, and thus allows segmentation in a fraction of the time needed to perform a manual segmentation. Anyway, here we do not aspire to solve the segmentation problem of skin lesions as this would be a thesis of its own right; nevertheless it is our strong belief that many of these algorithms would benefit from a more precise knowledge of the nature of the image data and the availability of a proper color difference metric that comes with the use of colorimetric color spaces.

The segmentation algorithm

One idea of the proposed semi-automatic segmentation method is to use the dermatologist for what he is very good at, namely the detection of the rough lesion border, but to relieve him of the laborious process of determining a detailed lesion contour. Although this may introduce some unwanted user-dependency, it is believed the benefits, especially an increased robustness versus the variety in shape and color of lesions, will outweigh this.

The contour that will be used to segment the skin lesion from the normal surrounding skin consists of a set of vertices spaced by a predetermined distance called the vertex resolution. The vertices can move radially inward or outward based on image properties in one or more areas around the vertex. If during such a move the distance between two vertices becomes less than half the vertex resolution that vertex is removed. If, on the other hand, the distance between two vertices becomes larger than 2 times the vertex resolution, a new vertex is inserted in the middle, see fig. 6.12. This resample scheme is based on [58].

Figure 6.11: Some examples of skin lesions which are hard to segment, e.g. due to the presence of hairs, a very diffuse border or the presence of erythema (red irritated skin).

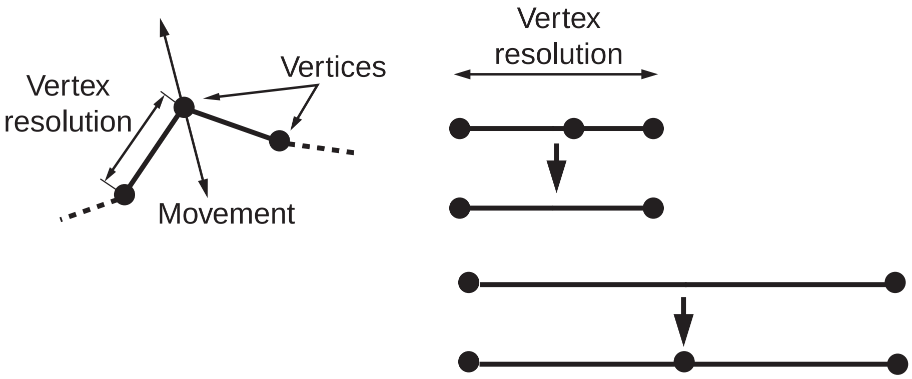

Figure 6.12: Contour consisting of vertices, and resample scheme.

The basic premise of the algorithm is that a skin lesion is surrounded by a band of 'normal' skin. To start the algorithm the user draws a rough outer contour of the lesion, making sure the vertices mark representative areas of normal skin. Next, the average color is computed around each vertex to obtain a local measure of the normal skin color. Hereafter, the contour is resampled based on the vertex resolution. Notice that if during resampling a vertex is added its local skin color will become the average of the local skin colors of the two neighboring vertices. This is opposed to first resampling the contour and then computing the local normal skin color, which denies the user the choice of some of the reference areas for normal skin and poses problems, e.g. when a skin lesion touches the border of the image. These local normal skin colors are then used to conditionally shrink the vertices radially inwards, based on their color difference with the current local color average. As long as this difference is within a predefined shrinking tolerance in ΔE^*_{ab} units, shrinking goes on, until all vertices come to a standstill. Recapitulating, we get:

1. Draw a rough outer contour of the skin lesion, marking the representative areas of normal skin;
2. Compute and store the average color around each vertex as a measure of the local normal skin color;
3. Resample the contour according to the vertex resolution;
4. Compute and store the color difference in ΔE^*_{ab} units between the average color around each vertex and the corresponding local normal skin color;
5. Move the vertex radially inwards if the vertex color difference is below a certain threshold called the shrinking tolerance;
6. Stop if no vertex has moved, else repeat from step 3.

The only two parameters of this algorithm are the vertex resolution which is set to 12 pixels, and the shrinking tolerance which is set to 8 ΔE^*_{ab} units. The averaging areas around the vertices are squares the size of the vertex resolution. More complex shapes, e.g. based on the local shape of the contour, could easily be implemented but would conceivably be slower.

The segmentation algorithm is implemented as an action mode in the view class, using VB. The core routines were written in C, for obvious speed reasons. Upon activating the segmentation action routine a CIE $L^*a^*b^*$ image is computed using the displayed $sR^*G^*B^*$ image, which allows fast calculation of color averages around the vertices. Again for speed reasons this CIE $L^*a^*b^*$ is subsampled, but this makes little or no difference as long as the vertex resolution is higher than the subsample factor, typically 2.

Testing the segmentation algorithm

As in general there is no consensus between dermatologists about a lesion contour, i.e. there is no golden standard, testing the segmentation algorithm is primarily concerned with its reproducibility versus that of a manually drawn contour.

In order to test the segmentation method a test set of 30 *images* of skin lesions is put to 4 dermatologists, called *observers* from now on. Each image is presented twice in a random sequence, and is segmented both manually and using the proposed semi-automatic segmentation method. By referring to each pairing of an observer and an image as a *case*, the above can be restated by saying that each case is segmented twice for each segmentation method. This brings the total number of segmentations to $30 * 4 * 2 * 2 = 480$. Next, two features which conceivably play a role when diagnosing skin lesions are computed for each segmentation: the area inside the contour in pixels, and the average $CIEL^*a^*b^*$ value inside the contour. These features are notated respectively as A_{ijkl} and $(L^*_{ijkl}, a^*_{ijkl}, b^*_{ijkl})$, with i the segmentation method, j the image, k the observer and l the presentation (see also table 6.1).

What	**Indices**
Segmentation methods	$i = 1(\text{manual}), 2(\text{semi-automatic})$
Images	$j = 1, \ldots, 30$
Observers	$k = 1, \ldots, 4$
Cases	$j = 1, \ldots, 30 : k = 1, \ldots, 4$, total 120
Presentations	$l = 1, 2$
Total number of segmentations	$i = 1, 2 : j = 1; \ldots, 30 : k = 1, \ldots, 4 : l = 1, 2$ total 480

Table 6.1: Some numeric details about the segmentation experiment

In order to assess the reproducibility of a segmentation method i for the contour area A and for a certain case jk, the standard deviations s_{ijk} could be used, obtained by compairing the measurements of the area over its two presentations A_{ijk1} and A_{ijk2}:

$$\begin{aligned}\langle A_{ijk}\rangle =&\frac{\sum_{l=1}^{2} A_{ijkl}}{2},\\ s_{ijk} =&\sqrt{\frac{\sum_{l=1}^{2}(A_{ijkl}-\langle A_{ijk}\rangle)^2}{2}}.\end{aligned} \tag{6.1}$$

However, due to the great variety in lesion areas it can be argued that this makes comparison of the reproducibility measure *between* cases with different images impossible, and we therefore propose to divide the standard deviation by the average area to obtain a better measure of reproducibility r_{ijk} for :

$$r_{ijk} = \frac{s_{ijk}}{\langle A_{ijk}\rangle}. \tag{6.2}$$

Note that the sample standard deviation was divided by 2 and not by 1 as usual for an unbiased estimator for the population standard deviation.

For the average CIE $L^*a^*b^*$ color of a contour we propose following formulas to obtain a measure of reproducibility of the segmentation method i for a case jk:

$$\begin{aligned}(\langle L^*_{ijk}\rangle, \langle a^*_{ijk}\rangle, \langle b^*_{ijk}\rangle) =& \frac{\sum_{l=1}^{2}(L^*_{ijkl}, a^*_{ijkl}, b^*_{ijkl})}{2},\\ \Delta E^*_{ab,ijkl} =&\Big((L^*_{ijkl}-\langle L^*_{ijk}\rangle)^2+(a^*_{ijkl}-\langle a^*_{ijk}\rangle)^2\\ &+(b^*_{ijkl}-\langle b^*_{ijk}\rangle)^2\Big)^{1/2},\\ \langle \Delta E^*_{ab,ijk}\rangle =& \sum_{l=1}^{2}\frac{\Delta E^*_{ab,ijkl}}{2}.\end{aligned} \tag{6.3}$$

Equations (6.2) and (6.3) can be used to compare the reproducibility of both segmentation methods per case, i.e. *for one observer performing the segmentation on one image.* These can then be averaged over all cases, in other words: over the set of observers and images, in order to remove some of the variability introduced by those two factors outside our experimental control. It is assumed that these reproducibility measures are also representative for one observer segmenting and measuring *different* images of the *same* skin lesion, e.g. when performing a lesion follow-up over time. Within this context we can speak of an intra-observer reproducibility. In reality it will not always be the same person who segments and measures a skin lesion, and so we also need to determine the total reproducibility of the manual and semi-automatic segmentation, which includes a part due to inter-observer variations. For this eqs. (6.2) and (6.3) need to be extended by computing the feature averages per segmentation method i, not over the two presentations $l = 1, 2$ of an image j to an observer k, but over all presentations $l = 1, 2$ of an image j to all observers $k = 1, \ldots, 4$:

$$\begin{aligned}
\langle A_{ij} \rangle &= \frac{\sum_{k=1}^{4} \sum_{l=1}^{2} A_{ijkl}}{8}, \\
s_{ij} &= \sqrt{\frac{\sum_{k=1}^{4} \sum_{l=1}^{2} (A_{ijkl} - \langle A_{ij} \rangle)^2}{8}}, \\
r_{ij} &= \frac{s_{ij}}{\langle A_{ij} \rangle},
\end{aligned} \tag{6.4}$$

and

$$\begin{aligned}
(\langle L^*_{ij} \rangle, \langle a^*_{ij} \rangle, \langle b^*_{ij} \rangle) &= \frac{\sum_{k=1}^{4} \sum_{l=1}^{2} (L^*_{ijkl}, a^*_{ijkl}, b^*_{ijkl})}{8}, \\
\Delta E^*_{ab,ijkl} &= \Big((L^*_{ijkl} - \langle L^*_{ij} \rangle)^2 + (a^*_{ijkl} - \langle a^*_{ij} \rangle)^2 \\
&\qquad + (b^*_{ijkl} - \langle b^*_{ij} \rangle)^2 \Big)^{1/2}, \\
\langle \Delta E^*_{ab,ij} \rangle &= \sum_{k=1}^{4} \sum_{l=1}^{2} \frac{\Delta E^*_{ab,ijkl}}{8}.
\end{aligned} \tag{6.5}$$

Finally, the difficulty of the manual segmentation and the quality of the semi-automatic contour are also both scored by the observers using the criteria in table 6.2.

Results and discussion

Although testing the semi-automatic segmentation algorithm was primarily concerned with the reproducibility of the segmentation method versus that of a manually drawn contour, the histograms of the scored values can be seen in fig. 6.13. These are very subjective measures, but the low number of poorly segmented images versus the number of difficult to segment images is nevertheless a clue as to the good performance of the algorithm. See fig. 6.14 and table 6.3 for some examples of though lesions. Notice how hairs do not seem to be a problem for human observers and result in 'easy' or 'average' difficulty scores, even though

Score	Difficulty of segmenting	Quality of contour
1	very hard, uncertain where the border is	bad, completely wrong
2	hard, contains parts where border is uncertain	poor, many errors
3	average, diffuse but defined	average, some errors
4	easy, partly crisp and partly diffuse but defined	good, a few errors
5	very easy, crisp border	perfect

Table 6.2: Subjective scores for difficulty of segmentation and contour quality of the result of the semi-automatic segmentation.

the semi-automatic segmentation method has quite some problems with it and consequently gets a relatively low quality score. This is opposed to the image in the top left of fig. 6.14 where the lesion has quite diffuse borders and gets a 'hard' difficulty score, while the semi-automatic segmentation has absolutely no problem ('good' quality score).

Image	Avg. difficulty 1=very hard 5=very easy	Avg. quality 1=bad 5=perfect
top left	2.625	4.125
top right	4.000	3.000
bottom left	2.875	2.750
bottom right	1.625	2.875

Table 6.3: The average difficulty of segmentation and quality of the contour using the semi-automatic segmentation method for the images in fig. 6.14. See table 6.2 for more info on the subjective scores.

A quick look at fig. 6.15 shows us that the intra-observer reproducibilities contain some outliers and are far from being normally distributed. However, with 120 cases per segmentation method and by virtue of the central limit theorem of statistics[2] we may safely state that the average reproducibility measure *over de cases* for one segmentation

---

[2] Whatever the distribution from which samples are drawn, the sample mean is normally distributed around the mean of the distribution, provided enough samples are drawn

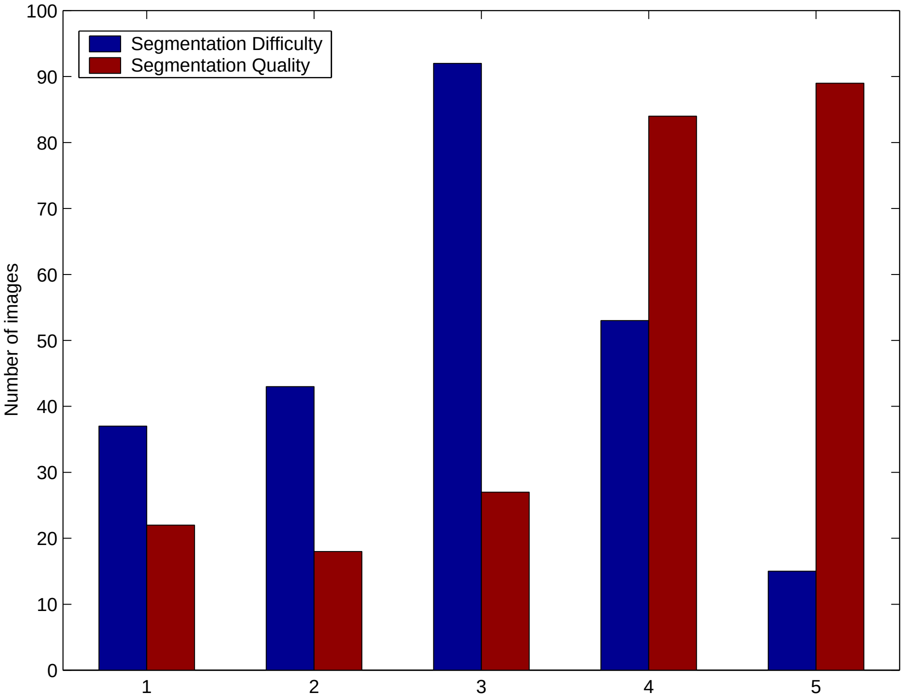

Figure 6.13: The subjective scores of the segmentation. See table 6.2 for an explanation of the labels.

method is normally distributed. In that case we may use a t-test to test if the two segmentation methods have a different mean. An alternative which doesn't require normality of the underlying distributions is the non-parametric Wilcoxon matched pairs signed-ranks test [59], which is almost as powerful as the t-test. This test relies on the ability to rank the differences in reproducibility between the segmentation methods for each case according to their magnitude. If the assumption that the reproducibility measures can be compared across cases is not valid, we must fall back on the much less powerful matched pairs sign test [59]. This test does not use the magnitude of the differences in reproducibility between the segmentation methods for each case but instead assign a label per case according to which segmentation method has the lower (or higher) reproducibility measure. If both segmentation methods perform equally well both types of labels should occur about the same number of times, i.e. the number of cases divided by 2. This test is not very powerful for large samples, i.e. it needs a lot of evidence before it can conclude

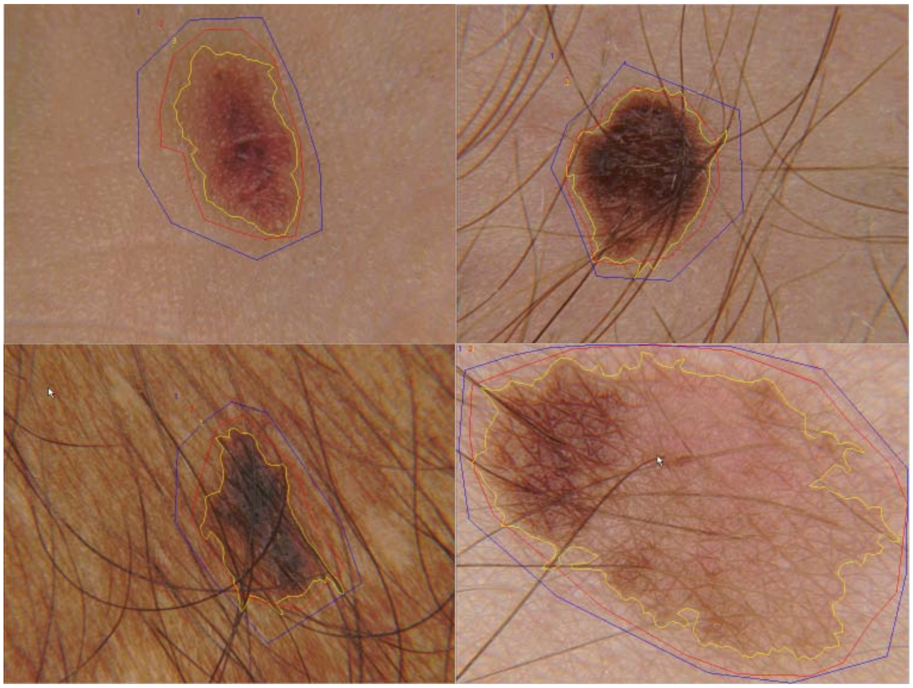

Figure 6.14: Segmentation results of the though images in 6.11. The manual contours are in red, the rough start contours for the semi-automatic segmentation are in blue and the semi-automatic contours are in yellow. Notice the problems with the dark hairs.

that both segmentation methods have different reproducibility. Notice that the statistical opposite of the prior conclusion is not ‘both methods have the same reproducibility’, but rather ‘we do not have enough evidence to conclude that both methods have different reproducibility’. In that sense statistical tests are much more conclusive when they reject the basic hypothesis of a test, than when they do not reject it.

The results of the t-test can be found in table 6.4, and as could be guessed from the histograms in fig. 6.15, no significant improvement was found for the semi-automatic segmentation method.

Fig. 6.16 shows the histograms of the total reproducibilities r_{ij} and $\langle \Delta E^*_{ab,ij} \rangle$. There are some indications of differences in distributions, but the overall picture is still unclear due to the low number of samples. To be sure we will use the weakest statistical test, the matched pairs sign test, to demonstrate a significant improvement for the semi-automatic versus manual segmentation. This test poses minimal requirements on

Feature	**Average reproducibility**		**Significant difference?**
	man.	**semi-aut.**	**t-test, p=0.05**
Area	0.26	0.25	No
Color	3.2	3.1	No

Table 6.4: Average intra-observer reproducibility for the manual and semi-automatic segmentation per case, and statistical significance of the t-test at the $p = 0.05$ level. Results are obtained by averaging over 120 cases (30 images and 4 observers).

the data, and its results can be seen in table 6.5. This time a statistically significant improvement was found for both image features, although in absolute value the reproducibilities can hardly be called exceptional.

Feature	**Average reproducibility**		**Number of improved images**	**Significant difference? sign-test, p=0.05**
	man.	**semi-aut.**		
Area	0.42	0.34	24/30	Yes
Color	7.6	6.3	26/30	Yes

Table 6.5: Average total reproducibility for the manual and semi-automatic segmentation per image, and statistical significance of the matched pairs sign-test at the $p = 0.05$ level. Results are obtained by averaging over 30 images.

Inspection of some of the contours, e.g. as in fig. 6.14, showed that the main problem for proper segmentation was the presence of hairs. This could possibly be remedied by giving the user the opportunity to interactively modify the resulting contour if deemed necessary. This was tried, but turned out to be laborious due to the high contour resolution which meant that many points had to be moved. A possible solution is the use of so-called 'rational Gaussian' curves [60] or similar method, which allow easy interactive repositioning of parts of contours.

The segmentation algorithm also still exhibits a reproducibility which may be too low for practical purposes, but this could possibly be improved by using information from the first segmented image of a lesion to guide segmentation of subsequent images of that same lesion. Of course, combinations of one or more other, more complex, algorithms also warrant future investigation, especially watersheds and clustering. A technique that would be interesting to investigate is the combination of a watershed segmentation followed by fuzzy clustering of the, usually oversegmented, regions. The resulting region borders could then be used to restrict possible paths of a manual contour. Subsequent images of the same lesion could then be quasi automatically segmented based on the regions included in the original segmented lesion image. The problem with clustering, however, is their sensitivity, e.g. to the initial clusters centroids or to the order in which the objects are presented to the algorithm. Some of these problems can be circumvented, but usually at huge computational cost.

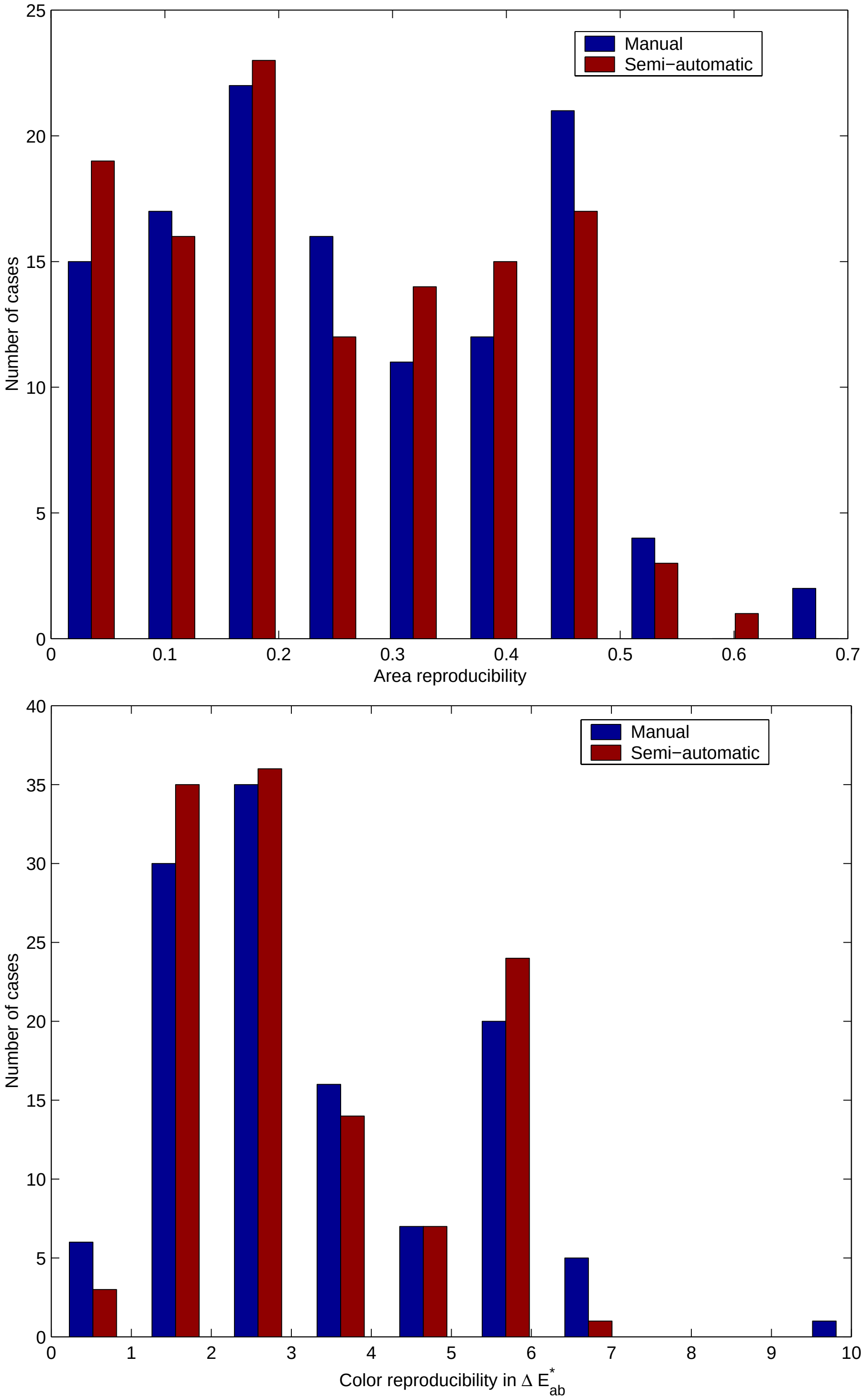

Figure 6.15: Comparison of histograms of the intra-observer reproducibility measures r_{ijk} (top) and $\langle \Delta E^*_{ab,ijk} \rangle$ (bottom) for the manual and semi-automatic segmentation methods.

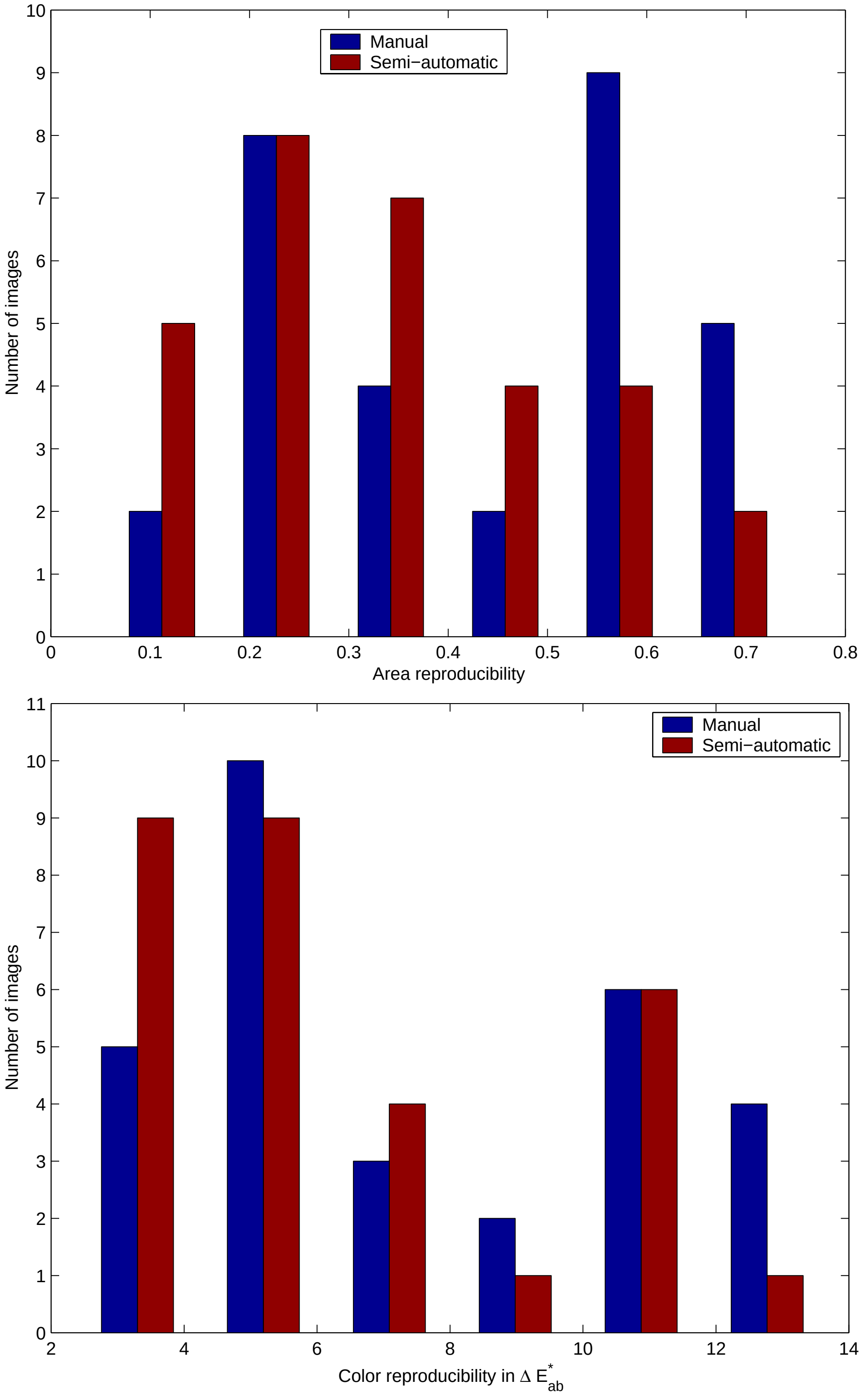

Figure 6.16: Comparison of the histograms of the total reproducibility measures r_{ij} (top) and $\langle \Delta E^{*}_{ab,ij} \rangle$ (bottom) for the manual and semi-automatic segmentation methods.

6.5 Discussion and conclusions

The dermatological workstation was tested in clinical practice at the university hospital for the follow-up of patients with an increased risk of developing melanoma. During this period about a 100 images of skin lesions were acquired and stored in the database. Segmentation of the images was not performed at that time, so functionality was limited to the presentation of a consistent skin lesion history in images. Despite the constant exchange of information and criticisms with the dermatologists resulting in constant refinement of the workstation, several problems hampered its usefulness. Besides the odd software bug, and although the dermatologists still have some problems in using the workstation and find it a bit complicated, we believe the main problems are more structural in nature. Indeed, the introduction of the workstation in a hospital service, where until a few years ago the use of computers was marginal, means information technology (IT) resources and knowledge are quite restricted, although vast improvements have been made. Moreover, the constantly high workload means there is sometimes little time to try to improve this situation, e.g. by providing IT training for the personnel. On top of that the hospital itself is developing a 'hospital information service' (HIS), of which nobody seems to know precisely what it will or will not provide, be it in hardware, software or information. The HIS system is also marred by constant delays, and consequently many plans for structural improvements emanating from the dermatology service, e.g. computer networks, computers, training, etc. …, are on halt until things become clearer. We can illustrate this with one of the main complaints of the dermatologists regarding the workstation: 'It takes too much time to enter the patient data in the computer during a consultation'. Most of this data, e.g. administrative data, could easily be entered by the technical staff during the registration of the patient at the reception of the dermatology service, were it not for some of the problems mentioned above. It is therefore our firm belief that if the dermatological workstation or any similar system is to have a chance of success in a clinical setting the technology gap with its supporting environment must first be reduced to a minimum. This is a major undertaking which does not happen overnight, and it may therefore be better in the near future to try to develop and validate the workstation outside the setting of the day clinic, e.g. by using small-scale research projects with volunteer patients.

Regarding skin lesion segmentation, we may state that some good results were obtained with a very simple algorithm by making use of the colorimetric properties of the image data. The method is quick and easy to use, but could definitely be improved. Alternatively, some existing methods could be modified to make use of the presence of the colorimetric image data. The resulting contours can then be used for further image feature extraction, e.g. area, contour length, shape descriptors, average color properties, number of colors, etc. .... These features could then conceivably form the input of a classification system, but for this a diagnostically much wider range of skin lesion images must first be acquired. This will take some time hence, due to the rarity of some types of skin lesion.

Chapter 7

Conclusion

In the course of this final chapter some of the main subjects and results of the current work will be reiterated. In addition, personal contributions, resulting scientific publications and possible future endeavors will be highlighted.

The first 3 chapters consisted of an introduction to this work and some background information on the fields of dermatology and colorimetry. They explored the motives and proposed some general goals for this work. Most of the information in these chapters was merely a rehashed version of information taken from several textbooks and articles, albeit with a structure tailored to the current work.

In chapter 4, the color imaging system components were discussed, as well as how these components cooperate and fit together. Some of these components could be used as is, others had to be modified, enhanced or created from scratch. Although a lot of the presented technical information originated from textbooks, articles and manuals, some of it also resulted from simple experiments. In any case we feel our main achievement in this chapter is not of a scientific, but rather of a technological nature: the seamless integration of several hardware and software components into a working color imaging system.

The operation and characterization of the imaging system was the subject of chapter 5. In order to achieve this, a simple, rather empirical model of the imaging system was proposed. Based on this model, calibration and acquisition procedures were developed using a set of color patches with known colorimetric properties. Several experiments were carried out to determine the precision and the accuracy of colorimetric measurements performed on images acquired with the system. Precision or reproducibility depends mainly on the stability of the imaging system as a whole and could be determined using the same color patches as those used during calibration, and was found to be quite good ($\langle \Delta E^*_{ab} \rangle = 0.34$, $\Delta E^*_{ab} \leq 1.2$). On the other hand, accuracy depends heavily on the transform from the device-dependent RGB source color space to the device-independent $sRGB$ target color space, and can only be determined by imaging a set of color patches or objects not used during calibration. Consequently, this set of test objects, which was about half made up of real skin samples, was used to determine the optimal transform between the source and target color space. Possible transforms included not only polynomial transforms of different order, but also computed in different ways. Indeed, besides normal linear-least-squares solutions in the target color space, the solutions of non-linear minimization of the average and maximal mapping error in $CIEL^*a^*b^*$ were also tried. As far as we could tell, such results had not been published at the time of the experiments. As it turns out, however, the higher-order polynomial transforms do not result in extra accuracy, mainly due to the limited set of color patches used for the calibration of the imaging system. This sparse sampling of both source and target color spaces was chosen out of practical considerations, i.e. a fast calibration process, but does not allow accurate determination of higher-order transforms. For the simple linear transform, the performance of the linear-least-squares solution is about the same as for the non-linearly optimized average mapping error transform, and consequently the linear-least-squares solution is preferred because of its low computational cost. The accuracy corresponding with this transform, as compared to spectrophotometric measurements, was fair ($\langle \Delta E^*_{ab} \rangle = 6.21$, $\Delta E^*_{ab} \leq 13.31$). The work presented in this chapter resulted in several congress papers and abstracts, [47, 48, 49, 50], as well as in an article in a peer-reviewed international journal, [51]. It has also raised interest from the private sector for the development of a multi-modal dermatological workstation.

Chapter 6 was devoted to some extensions to the imaging system which had as primary mission to turn a complex imaging system into a useful clinical tool, i.e. a real dermatological workstation for the follow-up of patients with an increased risk of developing melanoma. These extensions included a patient and image database and a tool for the manipulation and examination of the acquired calibrated images. An attempt was also made to demonstrate the usefulness of the colorimetric framework for image processing by developing a simple skin lesion segmentation algorithm. This algorithm was thoroughly evaluated and found to diminish inter-observer variability compared to a manual segmentation. The algorithm, which is the subject of a congress paper [61], can and needs to be improved before its results are to be used for further processing, e.g. for classification and computer-aided diagnose.

Although in general the extensions of the imaging system discussed in this chapter need a lot more development, it is important to note that other problems need to be addressed before the workstation can be further validated and used in the daily clinical practice. These problems are mainly structural in nature and stem from the realization that a dermatological workstation cannot properly function alone, rather it must integrate with existing systems and procedures in the day clinic of the dermatology department. As most of these systems and procedures need a major overhaul, this represents a unique challenge for the future whereby the workstation and its supporting environment can finally meet in a planified manner. This will not happen overnight, so we propose that meanwhile further clinical validation and development of the workstation should be undertaken on small-scale projects with well-determined goals.

Finally, we note that the cooperation with other researchers in the department of dermatology, especially in the image processing of electron microscope images and the statistical evaluation of measurements, has resulted in co-authorship of two publications in international peer-reviewed journals, [62, 63].

Appendix A

Mathematical symbols

λ	Wavelength.
$\langle\rangle$	An average.
Q	The calibration profile quality factor.
$\mathbf{Q}$	A visual stimulus.
$\mathbf{R}, \mathbf{G}, \mathbf{B}$	The primary stimuli of the CIE RGB color space.
$\overline{r}(\lambda), \overline{g}(\lambda), \overline{b}(\lambda)$	The CIE RGB 2° color matching functions.
$\overline{r}_{10}(\lambda), \overline{g}_{10}(\lambda), \overline{b}_{10}(\lambda)$	The CIE RGB 10° color matching functions.
(R, G, B)	A tristimulus value in a generic RGB color space, with red, green and blue components R, G and B respectively.
$P = R, G, B$	The red, green or blue component of a tristimulus value (R, G, B).
(R^*, G^*, B^*)	A color triplet in a generic gamma-corrected $R^*G^*B^*$ color space with red, green and blue components R^*, G^* and B^* respectively.
$P^* = R^*, G^*, B^*$	The red, green or blue component of a color triplet (R^*, G^*, B^*).
$(\mathcal{R}, \mathcal{G}, \mathcal{B})$	A tristimulus value in the $sRGB$ color space, with red, green and blue components $\mathcal{R}$, $\mathcal{G}$ and $\mathcal{B}$ respectively.

$\mathcal{P} = \mathcal{R}, \mathcal{G}, \mathcal{B}$	The red, green or blue component of a tristimulus value $(\mathcal{R}, \mathcal{G}, \mathcal{B})$.
$(\mathcal{R}^*, \mathcal{G}^*, \mathcal{B}^*)$	A tristimulus value in the gamma-corrected $sR^*G^*B^*$ color space, with red, green and blue components $\mathcal{R}^*$, $\mathcal{G}^*$ and $\mathcal{B}^*$ respectively.
$\mathcal{P}^* = \mathcal{R}^*, \mathcal{G}^*, \mathcal{B}^*$	The red, green or blue component of a tristimulus value $(\mathcal{R}^*, \mathcal{G}^*, \mathcal{B}^*)$.
$\mathbf{X}, \mathbf{Y}, \mathbf{Z}$	The primary stimuli of the CIE XYZ color space.
$\overline{x}(\lambda), \overline{y}(\lambda), \overline{z}(\lambda)$	The CIE XYZ 2° color matching functions.
$\overline{x}_{10}(\lambda), \overline{y}_{10}(\lambda), \overline{z}_{10}(\lambda)$	The CIE XYZ 10° color matching functions.
(X, Y, Z)	A tristimulus value in the CIE XYZ color space, with components X, Y and Z.
(L^*, a^*, b^*)	A color triplet in the CIE $L^*a^*b^*$ color space, with lightness, redness-greennes and yellowness-blueness components L^*, a^* and b^* respectively.
Γ, Γ^{-1}	The ITU-R BT.709 gamma correction function and its inverse.
$\Phi_{C1 \rightarrow C2}$	The transform from color space C1 to color space C2.
V_P^{cam}	The CCD camera output voltage for a certain pixel and component P.
V_{offset}^{cam}	The settable camera offset voltage.
V_P^{CCD}	The voltage proportional to the light incident on an element of the CCD array of color channel P.
V_{offset}^{CCD}	The CCD offset voltage.
g_P^{cam}	The camera gain for color channel P.
Ψ_0^V	The clipping function operating between 0 and V.
V_P^{fg}	The voltage inside the frame grabber before the ADC for color channel P.

V_{offset}^{fg}	The frame grabber offset voltage.
g^{fg}	The frame grabber gain.
$\Re$	The integer rounding operator.
A_{ijkl}	The area of a segmented region using method i, for measurement l, image j and observer k.
$(L^*_{ijkl}, a^*_{ijkl}, b^*_{ijkl})$	The average CIE $L^*a^*b^*$ color of a segmented region using method i, for measurement l, image j and observer k.
r_{ijk}	Area reproducibility measure for method i, image j and observer k.
$\langle \Delta E^*_{ab,ijk} \rangle$	Average color reproducibility measure in ΔE^*_{ab} units for method i, image j and observer k.
r_{ij}	Area reproducibility measure for method i, image j.
$\langle \Delta E^*_{ab,ij} \rangle$	Average color reproducibility measure in ΔE^*_{ab} units for method i, image j.

Index

Part II

Dutch Summary

Hoofdstuk 1

Inleiding

Traditionele fotografie wordt waarschijnlijk reeds sinds zijn uitvinding in de medische wereld gebruikt, meestal in een documenterende rol (in tegenstelling tot het gebruik ervan bij het stellen van een diagnose). Dit komt omdat het behalve enkele eenvoudige geometrische eigenschappen moeilijk is om metingen te verrichten op foto's. Kleur is een voorbeeld van zo'n moeilijk te meten eigenschap die belangrijke diagnostische informatie kan bevatten, zeker in het geval van foto's van de huid. Belangrijke obstakels voor het gebruik van kleurgegevens voor diagnostische toepassingen zijn het gebrek aan reproduceerbaarheid en nauwkeurigheid van de huidige kleurenbeeldvormingssystemen. Het hoofddoel van dit werk is dan ook de ontwikkeling van een dergelijk beeldvormingssysteem.

De medische context van dit werk, i.e. dermatologie, wordt nader toegelicht in het begin van hoofdstuk 2. Dit wordt gevolgd door de motivaties voor het dermatologisch werkstation, alsook enkele algemene doelstellingen bij de ontwikkeling ervan. Tijdens dit proces zullen concepten uit de colorimetrie een belangrijke rol spelen, en deze zullen uitgebreid aan bod komen in hoofdstuk 3. De discussie van alle componenten van het beeldvormingssysteem en hoe ze samenwerken vormt de hoofdmoot van hoofdstuk 4. Hoofdstuk 5 handelt over de werking en de bediening van het beeldvormingssysteem. Dit omvat zowel de kalibratie als de opname van beelden met het toestel, en wordt gevolgd door een bespreking van verscheidene experimenten om de nauwkeurigheid en de reproduceerbaarheid van de beeldopname te bepalen en te optimaliseren. De uitbreiding van het beeldvormingssysteem tot een praktisch en gebruiksvriendelijk dermatologisch werkstation wordt beschreven in hoofdstuk 6. Dit omvat een beeldendatabank, een databanktoepassing en de mogelijkheid om opgenomen beelden te bekijken en op te meten. Het nut van een meer ‘colorimetrische’ aanpak voor beeldverwerking wordt uitgetest aan de hand van een eenvoudig algoritme voor de aflijning van huidletsels. We sluiten af met hoofdstuk 7, waarin de belangrijkste conclusies nog eens worden overlopen, alsook de persoonlijke contributies en de publicaties die uit dit werk voortvloeiden.

Hoofdstuk 2

Context en doelstellingen

In dit hoofdstuk wordt de medische context van dit werk geïntroduceerd, nl. dermatologie. De mogelijke voordelen die digitale beeldopname en -verwerking in de bestrijding van huidkanker kan hebben zullen opgesomd worden. Uiteindelijk zal dit leiden tot een aantal algemene doelstellingen voor de ontwikkeling van het dermatologisch werkstation.

2.1 Dermatologie

Dermatologie is de tak van de geneeskunde die zich toelegt op de huid. Hoewel digitale beeldopname en -verwerking hier van algemeen nut kunnen zijn, zullen we ons toespitsen op het verbeteren van de vroegtijdige detectie van melanoom, een dodelijke vorm van huidkanker.

2.1.1 De huid

De huid heeft als hoofdfunctie de bescherming van het lichaam tegen externe factoren, en bestaat uit verscheidene lagen: de epidermis, de dermis en de subcutis.

De epidermis is de buitenste huidlaag, en is meestal ongeveer 100 μm dik. Ze bestaat uit 4 sublagen die de verschillende stadia van rijping van de keratinocyt, het meest voorkomende celtype in deze huidlaag, voorstellen. Een ander belangrijk celtype is de melanocyt die verantwoordelijk is voor de productie van melanine, een pigment dat de huid zijn kleur geeft en in staat is een deel van het schadelijk ultraviolet (UV) licht te absorberen.

De dermis bestaat hoofdzakelijk uit bindweefsel en is meestal 600 μm tot 3 mm dik. Verder bevat het nog enkele structuren zoals zweetklieren, haarfollikels en bloedvaten. De subcutis bestaat uit los bindweefsel en vet, en kan tot 3 cm dik zijn.

2.1.2 Melanocytische naevi

Een naevus is een goedaardige proliferatie van één of meer celtypes van de huid. Meer specifiek spreekt men van een melanocytaire naevus (MN) indien het gaat om een proliferatie van cellen afgeleid van de melanocyten. Dit type naevus kan bij geboorte aanwezig zijn (congenitale naevus), maar ontwikkelt zich meestal gedurende de kindertijd en de puberteit. Er bestaan verscheidene types, en hiervan is de atypische of dysplastische naevus voor ons het meest relevant omdat die, net zoals sommige congenitale naevi, een verhoogd risico hebben om te veranderen in een kwaadaardig letsel. Met andere woorden: dit type naevi kan een precursor letsel voor een melanoom zijn. De aanwezigheid van deze naevi brengt ook een verhoogd risico voor de ontwikkeling van een melanoom *elders op de huid* met zich mee. Normaal gezien is het niet nodig een MN weg te nemen, behalve als er verhoogd risico op een kwaadaardige verandering is. Daarenboven is de differentieeldiagnose tussen een MN en de vroege stadia van een melanoom niet altijd gemakkelijk.

2.1.3 Melanomen

Een melanoom is een kwaadaardige tumor van de huid, meer precies van de melanocyten. Het is de dodelijkste vorm van huidkanker, en er bestaat een verband tussen zijn ontstaan en blootstelling aan zonlicht (UV licht).

Hoe ontwikkelt een melanoom zich?

Een groot deel van de melanomen blijft maanden tot jaren in een goedaardig stadium, ‘radiale groeifase’ genaamd. Tijdens deze fase blijft de tumor binnen de epidermis gelocaliseerd zodat hij meestal door excisie kan verwijderd worden. Hierna komt de tumor in de zogenaamde ‘verticale groeifase’, waarbij ook de dermis betrokken is. In dit stadium kan de tumor ook metastaseren en tot secundaire tumoren in andere organen leiden.

Toenemende incidentie

De incidentie van melanomen is wereldwijd in blanke bevolkingsgroepen de laatste tientallen jaren sterk gestegen. Zo is in de V.S. het risico om tijdens het leven een melanoom te ontwikkelen gestegen van 1/1500 in 1935 tot 1/87 in 1996. Melanoom stelt wereldwijd ongeveer 1.2 procent van alle kankers voor, met 70000 nieuwe gevallen per jaar. De mortaliteit tengevolge van melanoom kent een analoge, zij het minder uitgesproken, trend.

Vroegtijdige diagnose is belangrijk

Doordat de mortaliteit minder sterk is gestegen dan de incidentie is het duidelijk dat de mortaliteit per incidentiegeval gedaald is. Daar de behandeling van melanoom weinig of niet is veranderd over de jaren, moeten dus andere factoren een rol spelen. Het feit dat de gemiddelde dikte van de tumoren met de jaren gedaald is, samen met de gekende correlatie tussen de tumordikte en de overlevingskansen of prognose (zie tabel 2.1), leidt ons tot de conclusie dat vroegtijdige detectie heel belangrijk is in de strijd tegen melanoom.

Breslow dikte	Overlevingskans op 5 jaar in %
$\leq$ 0.76 mm	98
0.76 - 1.69 mm	86
1.70 - 3.60 mm	69
$\geq$ 3.60 mm	33

Tabel 2.1: Prognose over 5 jaar in functie van de zogenaamde 'Breslow dikte'.

Doordat de helft van de melanomen ontstaat in een precursor letsel, en er verder ook nog een aantal andere risicofactoren voor de ontwikkeling van een melanoom elders op de huid bekend zijn (zie tabel 2.2), is het mogelijk om patiënten te herkennen met een verhoogd risico voor melanoom. Het is duidelijk dat het uiterst belangrijk is deze patiënten nauwkeurig op te volgen, zowel wat betreft primaire preventie, b.v. raadgevingen over blootstelling aan de zon, als secundaire preventie, i.e. de vroegtijdige detectie van melanomen door periodieke screening.

2.1.4 Bestaande diagnostische hulpmiddelen

Zoals reeds vermeld is de levensbelangrijke differentieeldiagnose tussen MN en melanoom, vooral in een vroeg stadium, niet altijd gemakkelijk. Correcte diagnose vergt veel ervaring en daartoe is de klinische ABCD-regel ingevoerd [4]. Deze regel stelt dat een letsel verdacht is als het

Risicofactor	Relatief risico
Atypische naevi met familiegeschiedenis van melanomen	100 - 400
Meerdere ($\geq$ 100) melanocytische naevi	30
Congenitale naevus ($\geq$ 1.5 cm diameter)	20
Vroeger melanoom	9
Rood haar en blauwe ogen, bruint bijna niet en verbrandt	2

Tabel 2.2: De belangrijkste risicofactoren voor de ontwikkeling van een melanoom.

asymmetrisch van vorm is, een onregelmatige rand heeft (‘**b**order’), verschillende kleuren heeft (‘**c**olor’) of een **d**iameter van meer dan 6 mm heeft.

De nauwkeurigheid van deze klinische ABCD-regel is echter eerder beperkt, [5, 6], en om dit te verhelpen werd de dermatoscoop en later de dermatoscopische ABCD-regel uitgevonden [7]. De dermatoscoop is een klein toestelletje dat de arts in staat stelt de huid onder een vergroting van 10 maal te bekijken. Het maakt gebruik van een glasplaatje dat tegen de huid wordt gedrukt. Het glasplaatje werd hiervoor bevochtigd met olie of water, wat als doel heeft de hoornlaag van de huid lichtjes doorzichtig te maken en onderliggende structuren zichtbaar te maken. De dermatoscopische ABCD-regel is kwantitatief, in zoverre dat nu scores voor het al dan niet aanwezig zijn van bepaalde kenmerken worden toegekend. Van deze scores wordt een gewogen som gemaakt om tot de zogenaamde ‘final dermatoscopic score’ te komen.

Het consistent toepassen van deze dermatoscopische ABCD-regel is echter niet gemakkelijk en vergt herhaaldelijke opleidingen voor artsen en dermatologen die niet dagelijks met gepigmenteerde letsels in aanraking komen. De regel houdt ook geen rekening met de veranderingen in de tijd van kenmerken, nochtans een mogelijke aanduiding van kwaadaardige veranderingen in een letsel. Dit betekent dat de dermatoscopische ABCD-regel bij de opvolging van patiënten met verhoogd risico telkens opnieuw wordt toegepast, zonder veel rekening te houden met vorige resultaten. Meestal wordt ook een foto genomen voor latere kwalitatieve vergelijking. Zo is er een studie [10] die concludeert dat beelden de beste methode zijn om veranderingen op lange termijn te detecteren.

2.2 Beeldvorming in dermatologie

Het is nu duidelijk dat visuele informatie van primordiaal belang is in de dermatologie. Het is bijgevolg niet verbazend dat beelden reeds jaren intensief gebruikt worden in dit domein, meestal opgenomen met behulp van traditionele fotografie. Digitale beeldvorming werd voor het eerst in 1990 [11] geprobeerd, en heeft veel potentiële voordelen ten opzichte van traditionele fotografie.

2.2.1 Traditionele fotografie

Tot ongeveer 10 jaar terug werd beeldvorming in de dermatologie uitsluitend uitgevoerd met traditionele fotografie, meestal diapositieven. Deze werden hoofdzakelijk gebruikt voor kwalitatieve vergelijking tijdens de opvolging van een letsel, en als visuele documentatie bij de historiek van een patiënt. Door de beperkingen van traditionele fotografie, hoofdzakelijk variaties in film, ontwikkeling en belichting, was het moeilijk om op de opgenomen beelden reproduceerbare metingen te verrichten buiten enkele eenvoudige geometrische eigenschappen zoals afmetingen of oppervlakten. Digitalisatie van foto's of diapositieven, [12, 13], laat toe om complexere eigenschappen op te meten, maar verandert niets aan de reproduceerbaarheidsproblemen van traditionele fotografie.

2.2.2 Digitale beeldvorming

De mogelijkheden en het gebruik van digitale beeldvorming in de dermatologie is reeds verscheidene malen onderzocht sinds 1990, [11, 14, 15, 16, 17], en de laatste jaren zijn zelfs enkele commerciële toestellen op de markt verschenen. Al deze systemen betekenen een grote vooruitgang t.o.v. traditionele fotografie op de meeste domeinen, behalve misschien wat betreft beeldresolutie.

Het probleem met al deze systemen is hun gebrek aan standaardisatie wat betreft kleur. Hoewel sommige van deze systemen heel waarschijnlijk ook één of andere vorm van kleurenkalibratie gebruiken, is geen enkele van deze systemen in staat om kleur nauwkeurig te meten (nauwkeurig is hier strikt genomen, d.w.z. met betrekking tot dezelfde metingen verricht met een standaard meettoestel zoals b.v. een spectrofotometer (SPM)). Alhoewel dit niet uitsluit dat de verrichtte kleurmetingen precies, i.e. reproduceerbaar, zijn beperkt dit toch sterk het nut van een dergelijk systeem. Zo is het b.v. onmogelijk om op een zinvolle manier beelden uit te wisselen omdat er geen referentiekader is voor de kleuren in de uitgewisselde beelden. Verder zullen alle beeldverwerkingsalgoritmes, b.v. voor segmentatie, parameterextractie en classificatie, uitsluitend werken op het systeem waarvoor ze ontwikkeld zijn. Het zal bijgevolg heel moeilijk zijn ze aan te passen voor andere systemen en ze aldus te valideren en te verspreiden. Een ander voordeel van het gebruik van colorimetrie en kleurstandaardisatie is de mogelijkheid om beeldverwerking te baseren op eigenschappen van menselijke kleurenvisie, voornamelijk een perceptuele kleurverschilmetriek. Het moet gezegd worden dat [15, 17] gebruik maken van zo'n metriek, maar voor zover we kunnen opmaken was dit gebaseerd op een generieke RGB naar CIE $L^*a^*b^*$ transformatie. Het is echter heel onwaarschijnlijk dat de eigenschappen van de RGB bronkleurenruimte van een beeldvormingssysteem overeenstemmen met deze waarvoor bovenvernoemde transformatie bestemd was. Theoretisch zou dus eerst een transformatie moeten uitgevoerd worden van de RGB bronkleurenruimte naar de RGB ruimte waarop de generieke RGB naar CIE $L^*a^*b^*$ transformatie van toepassing is, maar dit is nergens vermeld.

2.3 Algemene doelstellingen

Aan de hand van vorige paragrafen is het nu reeds mogelijk enkele algemene doelstellingen voor de ontwikkeling van het dermatologisch werkstation te formuleren. Dit werkstation zal niet alleen een beeldvormingssysteem omvatten, maar ook toepassingen en databanken om de opgenomen beelden te beheren en te verwerken.

- Hoge kwaliteit van de opgenomen beelden: hoge resolutie en ontbreken van artefacten, ruis, geometrische vervormingen, etc. ....

- Goede reproduceerbaarheid (precisie) van de beeldopname zodat beelden kunnen vergeleken worden, zowel kwalitatief, i.e. visueel, als kwantitatief, i.e. door opgemeten beeldeigenschappen.

- Gebruik van een gestandaardiseerde kleurenbeschrijving verbonden met colorimetrie. Dit laat toe om de nauwkeurigheid van kleurmetingen verricht op beelden te bepalen. Dit laat ook realistische weergave op een monitor en zinvolle uitwisseling van beelden toe.

- Mogelijkheid om zowel klinische als dermatoscopische beelden op te nemen.

- Gebruiksvriendelijk beheer van beelden en patiëntgegevens, aangepast aan de noden van de dienst dermatologie.
- Mogelijkheid om diagnostisch relevante gegevens uit de beelden te extraheren. Indien genoeg diversiteit aan huidletsels is verzameld kunnen pogingen worden ondernomen voor de classificatie ervan.

Hoofdstuk 3

Kleur

Zoals reeds vermeld zijn de visuele aspecten van de huid heel belangrijk in dermatologie. Bijgevolg dienen deze gegevens met de grootste zorg behandeld te worden, zowel tijdens de opname als bij de verwerking en opslag ervan. De onderwerpen in dit hoofdstuk zullen ons daarbij helpen. Voor een meer gedetailleerde behandeling van deze onderwerpen wordt de lezer verwezen naar [19, 20, 21, 22, 23].

3.1 Enkele definities

We definiëren volgende twee belangrijke termen:

Visuele stimulus *'Een visuele stimulus is zichtbaar licht dat net gaat gemeten worden of net het oog van een waarnemer gaat bereiken.'*

Kleur *'Kleur is de interpretatie van het menselijk visueel systeem, i.e. de ogen, optische zenuw en hersenen, van een visuele stimulus. Dit betekent dat kleur altijd een reële of gesimuleerde menselijke waarnemer impliceert.'*

3.2 Visuele stimuli

Een visuele stimulus, in de grond niets dan elektromagnetische energie in het zichtbaar spectrum, kan volledig beschreven worden m.b.v. radiometrische grootheden zoals b.v. spectrale radiantie. Deze grootheden vormen een zeer volledige beschrijving van het fysisch fenomeen, maar zijn niet gemakkelijk op te meten en resulteren in massa's gegevens die niet direct interpreteerbaar zijn.

Een compactere voorstelling van visuele stimuli kan bekomen worden met meettoestellen uitgerust met een aantal breedbandsensoren. Elke sensor integreert dan het spectrum van de visuele stimulus aan de hand van zijn spectrale gevoeligheid tot één respons. Indien de spectrale gevoeligheden van de sensoren niets te maken hebben met het menselijk visueel systeem spreekt men van densitometrie, en de bekomen responsen zijn dan moeilijk te correleren met kleur zoals gedefinieerd in 3.1. Als de sensoren echter wel spectrale gevoeligheden hebben die afgeleid zijn van eigenschappen van het menselijk visueel systeem spreekt men van een colorimetrische meting en zijn de resulterende metingen te correleren met kleur en kleurverschil zoals waargenomen door een mens.

3.3 Colorimetrie

We vestigen nu onze aandacht op colorimetrie als de meest geschikte aanpak voor het beeldvormingssysteem. De meeste concepten en termen die in dit hoofdstuk uitgewerkt worden zijn afkomstig uit het werk van de ‘Commision International de l’Eclairage’ (CIE).

3.3.1 Definitie

Colorimetrie is het vakdomein dat poogt kleur en kleurverschillen numeriek te beschrijven, met als randvoorwaarde dat deze beschrijving een continue functie is van de radiometrische eigenschappen van de bestudeerde visuele stimulus.

3.3.2 Opwekken van visuele stimuli

Het opwekken van visuele stimuli begint met een lichtbron, die door haar spectraal vermogen kan beschreven worden. Door dit spectrum te vergelijken met dat van een zwarte straler, en gebruik makend van de wet van Planck kan men deze spectrale distributie karakteriseren door een temperatuur, de kleurtemperatuur genaamd. Indien het spectrum teveel afwijkt van dat van een zwarte straler kan men er toch een kleurtemperatuur aan toekennen, nl. dat van een zwarte straler die dezelfde kleurindruk geeft voor een waarnemer. In dit geval spreekt men van gecorreleerde kleurtemperatuur (CCT voor ‘correlated color temperature’). Merk op dat dit impliceert dat twee verschillende spectra tot dezelfde kleur kunnen aanleiding geven!

Een illuminant is een abstractie van een typische lichtbron, en is gedefinieerd door een spectraal vermogen. Voor ons is vooral de CIE

D65 illuminant, een daglichtsimulatie met een CCT van 6504 K, van belang.

Het licht van een lichtbron wordt in ons geval meestal gereflecteerd door een voorwerp, v.b. de huid, voor het naar het oog van de waarnemer of een meettoestel gaat. Het spectrum van dat licht, de visuele stimulus, is dan eenvoudigweg het product van het spectraal vermogen van de lichtbron met de spectrale reflectantie van dat voorwerp.

3.3.3 'Color-matching' experimenten

Het trichromatisch principe stelt dat bijna alle kleuren kunnen nagebootst worden door een combinatie van drie geschikte vaste kleuren, primaire stimuli genaamd. Dit vormde de basis van de 'color-matching' experimenten uitgevoerd door de CIE in 1931, en daaruit voortvloeiend de CIE colorimetrie. Hierin moest een waarnemer een onbekende visuele stimulus nabootsen door de intensiteiten van drie primaire stimuli aan te passen (zie fig. 3.1). Deze primaire stimuli waren rode, groene en blauwe monochromatische visuele stimuli, vandaar de naam RGB.

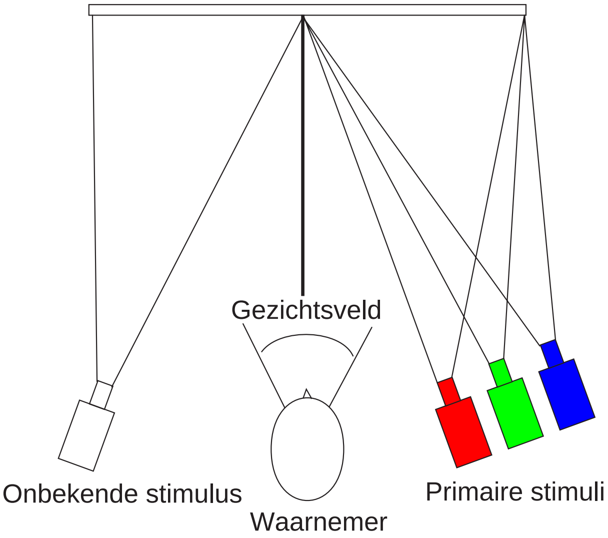

Figuur 3.1: Opstelling van de 'color-matching' experimenten waarin een waarnemer een onbekende visuele stimulus moet nabootsen door de intensiteiten van drie primaire stimuli aan te passen.

Dit experiment kan beschreven worden door:

$$\mathbf{Q} \equiv R_Q\mathbf{R} + G_Q\mathbf{G} + B_Q\mathbf{B}, \tag{3.1}$$

met $\mathbf{Q}$ een visuele stimulus, en $\mathbf{R}$, $\mathbf{G}$ en $\mathbf{B}$ de vaste primaire stimuli. (R_Q, G_Q, B_Q) is de tristimuluswaarde van $\mathbf{Q}$. Het $\equiv$ symbool wordt gebruikt om aan te duiden dat de gelijkheid niet fysisch of radiometrisch is, maar perceptueel of colorimetrisch. Bovenstaande vergelijking is niet erg praktisch daar ze inhoudt dat voor elke onbekende kleur een experiment moet opgezet worden. Bijgevolg werd gepoogd alle eigenschappen van het menselijk visueel systeem te bevatten in een compacte representatie door 'color-matching' experimenten uit te voeren voor monochromatische stimuli over het gehele visuele spectrum:

$$\mathbf{E}_\lambda \equiv R_\lambda \mathbf{R} + G_\lambda \mathbf{G} + B_\lambda \mathbf{B}, \quad \text{met } \lambda \in [360nm - 830nm], \tag{3.2}$$

met $\mathbf{E}_\lambda$ een monochromatische visuele stimulus met golflengte λ en één eenheid vermogen. $(R_\lambda, G_\lambda, B_\lambda)$ worden spectrale tristimuluswaarden genoemd. Deze operatie werd uitgemiddeld over verscheidene waarnemers om tot de $\overline{r}(\lambda)$, $\overline{g}(\lambda)$ en $\overline{b}(\lambda)$ 'color-matching' functies te komen voor een gezichtsveld van 2 graden, zie fig. 3.2

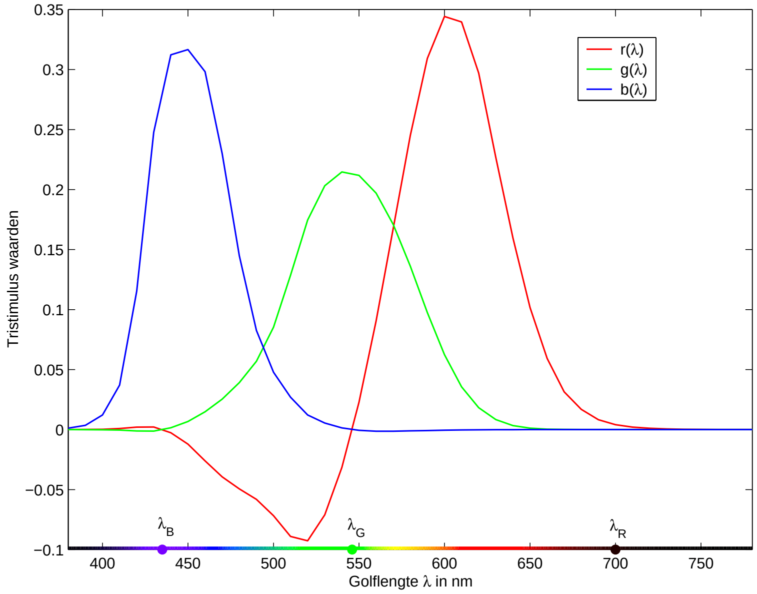

Figuur 3.2: De $\overline{r}(\lambda)$, $\overline{g}(\lambda)$ en $\overline{b}(\lambda)$ 'color-matching functions' en de golflengtes λ_R, λ_G en λ_B van de overeenkomstige primaire stimuli.

Een visuele stimulus $\mathbf{Q}$ met als spectraal vermogen $Q(\lambda)$ kan geïnterpreteerd worden als een som van monochromatische stimuli:

$$\mathbf{Q} = \int Q(\lambda)\mathbf{E}(\lambda) d\lambda. \tag{3.3}$$

Vervangen we deze monochromatische stimuli door hun tristimuluswaarden volgens vgl. (3.2), dan krijgen we volgende perceptuele gelijkheid:

$$\mathbf{Q} \equiv \int Q(\lambda)(\overline{r}(\lambda)\mathbf{R} + \overline{g}(\lambda)\mathbf{G} + \overline{b}(\lambda)\mathbf{B})d\lambda. \tag{3.4}$$

Door deze formule te vergelijken met (3.1) verkrijgen we een nuttige uitdrukking voor de CIE RGB tristimuluswaarden van $\mathbf{Q}$:

$$\begin{aligned} R_Q &= \int Q(\lambda)\overline{r}(\lambda)d\lambda, \\ G_Q &= \int Q(\lambda)\overline{g}(\lambda)d\lambda, \\ B_Q &= \int Q(\lambda)\overline{b}(\lambda)d\lambda. \end{aligned} \tag{3.5}$$

3.3.4 De CIE XYZ tristimulusruimte

De bepaling van tristimuluswaarden met behulp van vgl. (3.5) was praktisch moeilijk in 1931 door het negatieve gedeelte in de functie $\overline{r}(\lambda)$. Bijgevolg werd een nieuwe tristimulusruimte, CIE XYZ genaamd, afgeleid van de bestaande CIE RGB ruimte zodat de overeenkomstige $\overline{x}(\lambda)$, $\overline{y}(\lambda)$ en $\overline{z}(\lambda)$ 'color-matching' functies overal positief zijn. Deze ruimte is opgespannen door 3 nieuwe primaire stimuli $\mathbf{X}$, $\mathbf{Y}$ en $\mathbf{Z}$. Deze stimuli zijn niet fysisch realiserbaar, men spreekt van virtuele primaire stimuli. Doordat vgl. (3.1) ook geldt voor primaire stimuli en stimuli additief zijn is het duidelijk dat de nieuwe XYZ tristimuluswaarden (X_Q, Y_Q, Z_Q) van een visuele stimulus $\mathbf{Q}$ verbonden zijn met zijn RGB tristimuluswaarden (R_Q, G_Q, B_Q) door een lineaire transformatie. De resulterende $\overline{x}(\lambda)$, $\overline{y}(\lambda)$ en $\overline{z}(\lambda)$ 'color-matching' functies zijn te zien in fig. 3.3.

De (X_Q, Y_Q, Z_Q) tristimuluswaarden van een visuele stimulus $\mathbf{Q}$ kunnen dus neergeschreven worden als:

$$\begin{aligned} X_Q =& k \int Q(\lambda)\overline{x}(\lambda)d\lambda, \\ Y_Q =& k \int Q(\lambda)\overline{y}(\lambda)d\lambda, \\ Z_Q =& k \int Q(\lambda)\overline{z}(\lambda)d\lambda. \end{aligned} \tag{3.6}$$

k is een normalisatieconstante die normaal zo wordt gekozen dat voor een perfecte witte diffuse reflector de luminantie $Y = 100$.

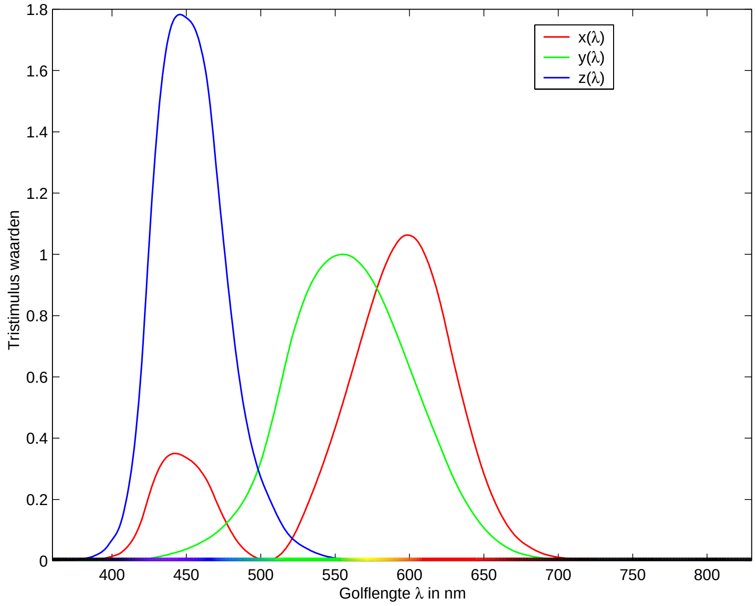

Figuur 3.3: De $\overline{x}(\lambda)$, $\overline{y}(\lambda)$ en $\overline{z}(\lambda)$ 'color-matching' functies.

Een veel gebruikte twee-dimensionele voorstelling voor XYZ tristimuluswaarden maakt gebruik van een projectieve transformatie:

$$\begin{aligned} x =& \frac{X}{X+Y+Z}, \\ y =& \frac{Y}{X+Y+Z}, \\ z =& \frac{Z}{X+Y+Z}. \end{aligned} \tag{3.7}$$

De resulterende (x, y, z) coördinaten worden chromaticiteitscoördinaten genoemd, en meestal gebruikt men x en y als twee-dimensionele voorstelling voor een kleurenruimte. Fig. 3.4 geeft het gamut van het menselijk visueel systeem, d.i. de verzameling van kleuren die het menselijk visueel systeem kan zien, weer in een chromaticiteitsdiagram.

3.3.5 De CIE L*a*b* kleurenruimte

De CIE XYZ tristimulus ruimte is uitermate geschikt voor het definiëren van kleuren, maar faalt bij het uitdrukken van kleurverschillen. Inderdaad, aan de hand van experimenten heeft men ontdekt dat de kleuren die net onderscheiden kunnen worden van een gegeven kleur (de

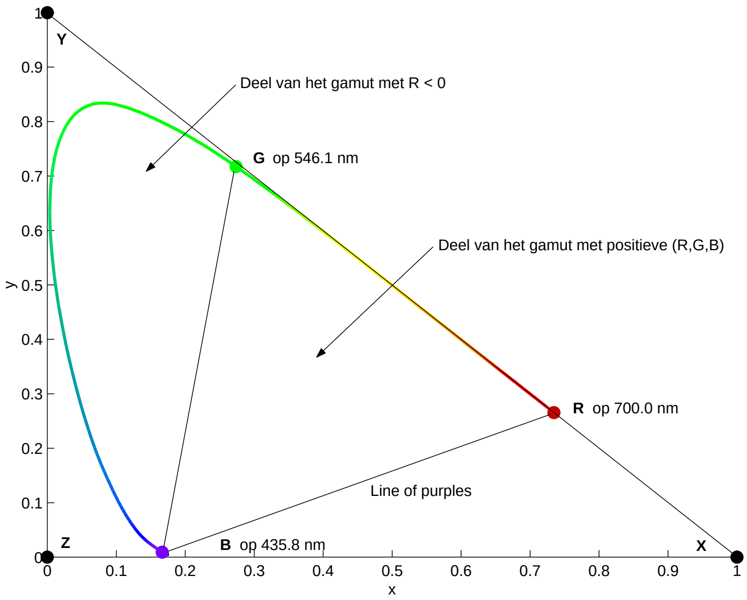

Figuur 3.4: Chromaticiteitsdiagram met het gamut van het menselijk visueel systeem, begrensd door de chromaticiteitscoördinaten van de color-matching functies en de zogenaamde 'line of purples'. De **X**, **Y** en **Z** en de **R**, **G** en **B** primaire stimuli zijn ook aangeduid.

'just noticeable difference' of JND) op een ellips rond die kleur liggen in een chromaticiteitsdiagram. Het probleem is nu echter dat de vorm en grootte van die ellips sterk varieert over het gamut van het menselijk visueel systeem, zodat het moeilijk is om een kleurverschillen te gaan kwantificeren in de XYZ ruimte. Om dit op te lossen werd door de CIE in 1976 de CIE $L^*a^*b^*$ ruimte als een niet-lineaire transformatie van de XYZ tristimulusruimte voorgesteld:

$$\begin{aligned} L^* =& 116 f(Y/Y_w) - 16, \\ a^* =& 500(f(X/X_w) - f(Y/Y_w)), \\ b^* =& 200(f(Y/Y_w) - f(Z/Z_w)), \\ f(t) =& \begin{cases} 7.787t + \frac{16}{116} & \text{als } t < 0.008856, \\ t^{1/3} & \text{als } 0.008856 \leq t \leq 1. \end{cases} \end{aligned} \tag{3.8}$$

L^* wordt 'lightness' genoemd, en is een maat voor de mate waarin een voorwerp licht schijnt uit te zenden. a^* is een maat voor het aanwezig zijn van rood of groen, en b^* is een maat voor het aanwezig zijn van geel of blauw. De tristimuluswaarde (X_w, Y_w, Z_w) noemt men het witpunt en is een referentie voor wit in het gezichtsveld. Het witpunt wordt hier gebruikt om een eigenschap van het menselijk visueel systeem te modelleren waarbij de meest heldere kleur in het gezichtsveld na een tijdje wit lijkt (chromatische adaptatie).

In de CIE $L^*a^*b^*$ ruimte is de gewone Euclidische metriek tussen twee kleuren een maat voor het waargenomen kleurverschil, en bovenvermelde ellipsen van net waar te nemen kleurverschillen zijn dus allemaal cirkels van gelijke grootte. Deze metriek wordt genoteerd als ΔE^*_{ab}, en wordt dus voor twee kleuren (L^*_1, a^*_1, b^*_1) en (L^*_2, a^*_2, b^*_2):

$$\begin{aligned} \Delta L^* &= L^*_1 - L^*_2, \\ \Delta a^* &= a^*_1 - a^*_2, \\ \Delta b^* &= b^*_1 - b^*_2, \\ \Delta E^*_{ab} &= \sqrt{(\Delta L^*)^2 + (\Delta a^*)^2 + (\Delta b^*)^2}. \end{aligned} \tag{3.9}$$

Om een gevoel te geven voor ΔE^*_{ab} waarden kunnen we vertellen dat de JND tussen twee kleuren $\Delta E^*_{ab} = 1$. Verschillen onder $\Delta E^*_{ab} = 3$ worden bij een vluchtige observatie meestal niet opgemerkt, verschillen van $\Delta E^*_{ab} \geq 5$ zijn meestal duidelijk zichtbaar.

3.3.6 Colorimetrische meettoestellen

Er zijn hoofdzakelijk twee types toestellen om kleur te meten: colorimeters en spectrofotometers. Deze toestellen zijn heel precies en nauwkeurig, maar ongeschikt voor onze toepassing omdat ze meestal metingen verrichten die uitgemiddeld zijn over een vast oppervlak, terwijl huidletsels een zeer grillige vorm kunnen hebben. Zulke toestellen nemen natuurlijk ook geen beelden op. Ze zijn daarentegen wel nuttig als referentietoestellen om de nauwkeurigheid van kleurmetingen met andere toestellen of methodes na te gaan.

Hoofdstuk 4

De opbouw van het kleurenbeeldvormingssysteem

Beelden kunnen gezien worden als verzamelingen van visuele stimuli, en zodoende gaan we nu over tot het opnemen, verwerken en weergeven van zulke beelden door het beeldvormingssysteem. Elk van bovenstaande taken kan min of meer geassocieerd worden met een subsysteem van het beeldvormingssysteem, elk bestaande uit verscheidene hard- en softwarecomponenten. In dit hoofdstuk zal de nadruk op de werking van de verschillende subsystemen liggen, terwijl de werking van het beeldvormingssysteem als een geheel besproken zal worden in hoofdstuk 5. Het dermatologisch werkstation, i.e. het beeldvormingssysteem met de nodige gebruiksvriendelijke programmatuur voor dagelijks gebruik in de polikliniek, zal besproken worden in hoofdstuk 6.

4.1 De computer en de programmatuur

De kern van het beeldvormingssysteem en het dermatologisch werkstation is een personal computer (PC) met Microsoft Windows NT 4.0. De meeste programmatuur werd ontwikkeld met Microsoft Visual Basic (VB) [28, 29, 30, 31]. Tijdkritische routines werden in C [32] ontwikkeld en gebundeld in bibliotheken die vanuit VB konden worden aangeroepen.

4.2 Kleurenbeeldweergave

Eén van de functies van het dermatologisch werkstation zal het rechtstreeks bekijken en vergelijken van beelden van huidletsels zijn. Tegenwoordig worden zowel klassieke beeldschermen (CRT voor 'cathode ray tube') alsook zogenaamde vlakke beeldschermen gebruikt als computermonitor. Deze laatste vertonen buiten een aantal voordelen zoals lager energieverbruik en het innemen van minder plaats, ook nadelen zoals een hogere prijs en een beperktere kijkhoek en kleurengamut. Bijgevolg werd de CRT gekozen voor de weergave van kleurenbeelden in ons beeldvormingssysteem.

4.2.1 De primaire stimuli van een CRT en zijn RGB ruimte

De rode, groene en blauwe fosfors in een CRT kunnen aanzien worden als de primaire stimuli van een RGB tristimulusruimte, net zoals de monochromatische primaire stimuli bij de CIE RGB ruimte. Deze RGB tristimulusruimte is eigen aan de CRT, en wordt daarom 'toestelafhankelijk' genoemd. Een CRT heeft een beperkt gamut t.o.v. het menselijk visueel systeem. Door het additief karakter van de CRT vormt zijn gamut een driehoek opgespannen door de CRT primaire stimuli in een chromaticiteitsdiagram, zie fig. 4.1. Een belangrijk punt in deze RGB ruimte is het witpunt. Het wordt verkregen door de maximale intensiteiten van de primaire stimuli te combineren. Het is *onmogelijk* om een beeld gedefinieerd in een bepaalde RGB ruimte nauwkeurig weer te geven als de primaire stimuli en het witpunt niet gekend zijn.

4.2.2 CRT gamma

De hoeveelheid licht (luminantie Y) geproduceerd door het beeldscherm van een CRT is geen lineaire functie van de spanning V van de aan de CRT aangelegde controlesignalen, en wordt gegeven door:

$$Y = kV^{\gamma}, \tag{4.1}$$

met γ de gammafactor met als typische waarden 2 tot 3.

Om deze niet-lineariteit te compenseren wordt de zogenaamde *gammacorrectie* op de CRT controlesignalen of op de digitale waarden die tot die controlesignalen leiden, uitgevoerd. Voor een N-bit digitale RGB tristimuluscomponent $P = R, G, B$ neemt de transformatie tot een gammagecorrigeerde $R^*G^*B^*$ component $P^* = R^*, G^*, B^*$ de volgende vorm aan:

$$P^* = (2^N - 1)(\frac{P}{2^N - 1})^{\frac{1}{\gamma}}. \tag{4.2}$$

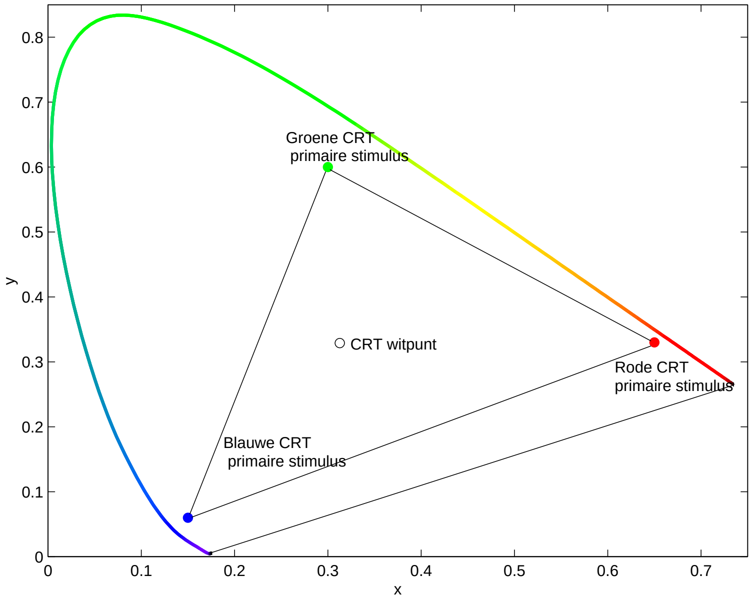

Figuur 4.1: Het driehoekige gamut van een CRT met als primaire stimuli rood (R), groen (G) en blauw (B), en het witpunt (W).

Merk de gelijkenis op tussen het niet-lineair gedrag van het menselijk visueel systeem, zie o.a. vergelijking (3.8), en de gammacorrectie in vergelijking (4.2). Door dit toeval is het zo dat gammagecorrigeerde digitale of analoge signalen perceptueel veel uniformer zijn dan de lineair-licht signalen waarvan ze afkomstig zijn. Dit heeft belangrijke gevolgen wanneer RGB componenten worden gekwantiseerd. Zo'n kwantisatie gebeurt b.v. tijdens de digitalisatie van analoge signalen of tijdens de conversie in de computer van tristimuluscomponenten met een vlottendekommarepresentatie naar een discrete representate met een kleiner aantal bits. Om dit effect te demonstreren werden de kwantisatiefouten bepaald door in een typische RGB kleurenruimte het perceptueel kleurverschil te berekenen tussen alle mogelijke tristimuluswaarden (R, G, B) en $(R + \Delta Q, G + \Delta Q, B + \Delta Q)$, met ΔQ de helft van een kwantisatiestap. Deze kleurverschillen in ΔE^*_{ab} eenheden werden dan vergeleken met analoge berekeningen in de corresponderende $R^*G^*B^*$ ruimte, zie fig. 4.2. Om het effect duidelijker te maken en de berekeningen te beperken werd een kwantisatie tot slechts 5 bit per component uitgevoerd, i.p.v. de meer gebruikelijke 8 bits per component. Men kan berekenen dat om duidelijk zichtbare fouten te vermijden men eigenlijk 12 tot 14

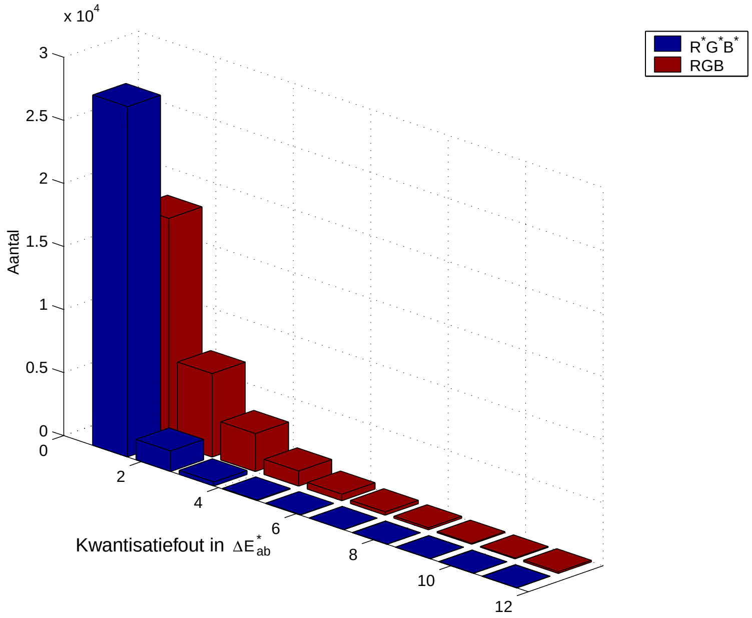

Figuur 4.2: Histogram van de ΔE^*_{ab} fouten tengevolge van kwantisatie tot 5 bit per component voor een typische RGB en geassocieerde $R^*G^*B^*$ kleurenruimte. Het kleurverschil bedroeg gemiddeld $\langle \Delta E^*_{ab} \rangle = 2.0$, met $\Delta E^*_{ab} \leq 23.0$ in de RGB ruimte, en gemiddeld $\langle \Delta E^*_{ab} \rangle = 1.5$, met $\Delta E^*_{ab} \leq 6.6$ in de $R^*G^*B^*$ ruimte.

bits resolutie per component nodig heeft in een RGB ruimte, terwijl in een $R^*G^*B^*$ ruimte 8 tot 9 bits voldoen.

4.2.3 De sRGB kleurenruimte

De *sRGB* kleurenruimte is een gestandaardiseerde RGB kleurenruimte, i.e. ze heeft welbepaalde primaire stimuli en een witpunt dat overeenkomt met CIE illuminant D65, zie tabel 4.1. Deze primaire stimuli zijn representatief voor moderne computermonitors zodat beelden gedefinieerd in deze ruimte realistisch kunnen weergegeven worden zonder extra transformaties. Deze ruimte is afgeleid uit de hoge-definitie televisiestandaard ITU-R BT.709.

De CIE XYZ en *sRGB* kleurenruimtes zijn verbonden door een lineaire transformatie, die er met een kolomvectornotatie als volgt uitziet

	Rood	**Groen**	**Blauw**	**Witpunt**
x	0.640	0.300	0.150	0.3127
y	0.330	0.600	0.060	0.3291
z	0.030	0.100	0.790	0.3583

Tabel 4.1: Chromaticiteiten van de *sRGB* primaire stimuli en het witpunt.

voor respectievelijke tristimuluswaarden $(\mathcal{R}, \mathcal{G}, \mathcal{B})$ en (X, Y, Z):

$$\begin{aligned}\begin{pmatrix} X \\ Y \\ Z \end{pmatrix} &= \Phi_{sRGB \rightarrow XYZ} \begin{pmatrix} \mathcal{R} \\ \mathcal{G} \\ \mathcal{B} \end{pmatrix} \\ &= 100 \begin{pmatrix} 0.412453 & 0.357580 & 0.180432 \\ 0.212671 & 0.715160 & 0.072169 \\ 0.019334 & 0.119193 & 0.950227 \end{pmatrix} \begin{pmatrix} \mathcal{R} \\ \mathcal{G} \\ \mathcal{B} \end{pmatrix}, \end{aligned} \tag{4.3}$$

en

$$\begin{aligned}\begin{pmatrix} \mathcal{R} \\ \mathcal{G} \\ \mathcal{B} \end{pmatrix} &= \Phi_{XYZ \rightarrow sRGB} \begin{pmatrix} X \\ Y \\ Z \end{pmatrix} = \Phi^{-1}_{sRGB \rightarrow XYZ} \begin{pmatrix} X \\ Y \\ Z \end{pmatrix} \\ &= 1/100 \begin{pmatrix} 3.240479 & -1.537150 & -0.498535 \\ -0.969256 & 1.875992 & 0.041556 \\ 0.055648 & -0.204043 & 1.057311 \end{pmatrix} \begin{pmatrix} X \\ Y \\ Z \end{pmatrix}. \end{aligned} \tag{4.4}$$

De *sRGB* tristimuluscomponenten zijn begrepen tussen 0 en 1, terwijl voor de XYZ componenten $Y = 100$ overeenkomt met een perfecte diffuse witte reflector.

De ITU-R BT.709 gammacorrectiefunctie voor tristimuluscomponenten $\mathcal{P} = \mathcal{R}, \mathcal{G}, \mathcal{B} \in [0,1]$ geeft aanleiding tot waarden $\mathcal{P}^* = \mathcal{R}^*, \mathcal{G}^*, \mathcal{B}^* \in [0,1]$, en is gedefinieerd als:

$$\mathcal{P}^*_{ITU} = \Gamma_{ITU}(\mathcal{P}) = \begin{cases} 4.5\mathcal{P} & 0 \leq \mathcal{P} \leq 0.018 \\ 1.099(\mathcal{P})^{0.45} - 0.099 & 0.018 < \mathcal{P} \leq 1.0. \end{cases} \tag{4.5}$$

De inverse gammacorrectie kan gemakkelijk afgeleid worden als:

$$\mathcal{P}_{ITU} = \Gamma^{-1}_{ITU}(\mathcal{P}^*) = \begin{cases} \mathcal{P}^*/4.5 & 0 \leq \mathcal{P}^* \leq 0.081 \\ \Big((\mathcal{P}^* + 0.099)/1.099\Big)^{(1/0.45)} & 0.081 < \mathcal{P}^* \leq 1.0. \end{cases} \tag{4.6}$$

Merk op dat de echte gammacorrectie van de $sRGB$ kleurenruimte lichtjes afwijkt van de ITU-R BT.709 versie, maar we hebben altijd deze laatste gebruikt. De 8 bit kwantisatiefout in de $sR^*G^*B^*$ ruimte bedraagt gemiddeld $\langle \Delta E^*_{ab} \rangle = 0.18$, met $\Delta E^*_{ab} \leq 0.93$.

4.3 Kleurenbeeldopname

De kleurenbeeldopname van het beeldvormingssysteem zal gebeuren met een zgn. CCD (‘charge coupled device’), en gedigitaliseerd worden door een ‘frame grabber’. Het is de bedoeling om beide toestellen zo in te stellen dat hun dynamisch bereik zo optimaal mogelijk gebruikt wordt en reproduceerbare opnames mogelijk zijn. Hiertoe zullen beide toestellen snel besproken worden. Voor een vollediger bespreking wordt de lezer verwezen naar [23].

4.3.1 De CCD camera

Algemene werking

Het hart van een CCD camera is natuurlijk de CCD-chip die het invallend licht omzet naar elektrische signalen. Om kleur te kunnen opnemen moeten drie signalen opgenomen worden volgens het trichromatisch principe. Goedkopere camera’s gebruiken hiervoor één CCD-chip met een masker met verschillende kleurenfilters voor verschillende pixels. Duurdere camera’s gebruiken 3 CCD-chips. In zo’n architectuur wordt invallend licht door een prisma gesplitst, waarna het gefilterd wordt en naar 3 verschillende CCD’s wordt geleid, één voor elke primaire kleur, zie fig. 4.3. Hierdoor is de beeldresolutie en de kwaliteit van de opgenomen kleuren veel hoger dan bij een camera met één CCD-chip.

Twee belangrijke fenomenen verdienen onze aandacht omdat ze de optimale werking van de camera kunnen verstoren: de donkerstroom en ‘blooming’. De donkerstroom is de stroom die vloeit zelfs wanneer geen licht op de CCD-chip valt, en is heel temperatuurgevoelig. Hoewel er methoden bestaan om dit effect te verminderen zullen we merken dat dit nog aanwezig is en het bijgevolg in ons model incorporeren. Blooming is een soort saturatiefenomeen; het treedt op wanneer heel fel licht op een individuele pixel in de CCD-chip invalt. Het gevolg is dat deze pixel als het ware ‘overstroomt’ in de naburige pixels. Ook dit effect kan voor een stuk teniet gedaan worden door een zogenaamde ‘anti-blooming drain’, maar deze kan leiden tot een niet-lineaire werking van de CCD die zonodig moet worden gecompenseerd.

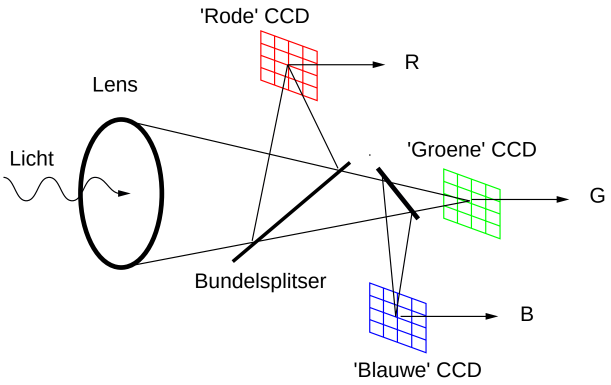

Figuur 4.3: 3 CCD architectuur.

Buiten de eigenlijke CCD-chip(s), bevat een CCD camera ook elektronica voor beeldverwerking, gammacorrectie en videocodering. Het kan ook zowel ADCs als DACs bevatten. De gammacorrectie kan meestal aan- of afgezet worden, en wordt normaal enkel aangezet om een CRT rechtstreeks aan te sturen. Merk op dat, zoals vermeld in sectie 4.2.2, de resolutievereisten voor digitalisatie lager zijn voor gammagecorrigeerde dan voor lineair-licht signalen.

Het videocoderingsgedeelte van de camera zorgt ervoor dat de beeldinformatie in een standaard analoog videoformaat wordt omgezet. Voorbeelden van zulke standaarden zijn PAL, NTSC en SECAM. Meestal worden met bovenstaande standaarden zogenaamde composiet signalen doorgestuurd. Een composiet videosignaal bevat zowel luminantie- als chrominantie-informatie in één signaal, met bijgevolg een lagere kwaliteit door een lagere bandbreedte en mogelijk overspraak. Het is echter ook mogelijk deze problemen te vermijden door de informatie van de 3 kleurkanalen apart door te sturen, zogenaamd ‘component analog video’.

De eigenschappen van de gebruikte CCD camera

De camera in ons beeldvormingssysteem is een JVC KY-F55B[1] 3 CCD met een resolutie van 580 bij 760 pixels. Deze camera heeft een ganse reeks eigenschappen die via de seriële poort van de PC ingesteld kunnen worden, zie tabel 4.2. Daarenboven bezit de camera nog automatische regelsystemen voor een aantal van die eigenschappen, b.v. voor de belichting en de witbalans. Het spreekt vanzelf dat deze automatische

---

[1] JVC: Victor Company of Japan, limited.

regelsystemen voor onze toepassing werden afgezet. De softwaremodule die de camera via de seriële poort bestuurt werd volledig zelf geschreven aan de hand van de communicatieprotocollen geleverd door de fabrikant.

Eigenschap	Mode	Waarde	Betekenis
WHITE BALANCE	**MANUAL**	N.T.	Handmatige instelling van de kleurenbalans
	FAW	N.T.	Automatische kleurenbalans
GAIN	**0dB**	N.T.	Totale versterking van 0 dB
	6,9,12,18dB	N.T.	Totale versterking van 6,9,12,18 dB
	ALC+EEI	N.T.	Automatische versterking en sluiter
	ALC	N.T.	Automatische versterking
GAMMA	**ON**	N.T.	Gammacorrectie
	OFF	N.T.	
MANUAL PAINT	RED	0-255	Handmatige instelling van versterking van rood kanaal
	BLUE	0-255	Handmatige instelling van versterking van blauw kanaal
MASTER BLACK	N.A.	0-255	Handmatige instelling van de basislijn van kleurkanalen

Tabel 4.2: Enkele relevante eigenschappen van de JVC camera met sommige van hun instellingen. Vetgedrukte tekst duidt een eigenschap aan die vast ingesteld wordt.

Camera-accessoires

Omdat het de bedoeling is om de beelden van de huid van dichtbij te nemen, is de camera uitgerust met een zoomlens [2]. Het gezichtsveld is 1.6 cm op 1.2 cm, zodat de spatiale resolutie ongeveer 47.5 pixels per mm bedraagt. De belichting van de huid gebeurt met behulp van een continu ringlicht[3] dat via een optische vezel verbonden is met een 150 Watt halogeen lichtbron. De kleurtemperatuur van deze lichtbron werd op 6500K gebracht d.m.v. een blauwfilter, wat bij benadering gelijk is

---

[2] Pentax Benelux B.V., Weiveldlaan 3-5, 1930 Zaventem, Belgium.

[3] Shott Glaswerke, Hagenauer strasze 38, D-65203 Wiesbaden.

aan de CIE D65 illuminant en het witpunt van de *sRGB* kleurenruimte.

Om te vermijden dat strooilicht in de lens terechtkomt is een kartonnen cilinder aan het ringlicht vastgemaakt. Deze cilinder mondt uit in een glazen plaat die overeenkomt met het focaalvlak en tegen de huid gedrukt kan worden. Dit laat toe om dermatoscopische beelden op te nemen, mits het aanbrengen van olie tussen de huid en de glasplaat. De camera is verder ook uitgerust met een pistoolgreep en trekker om de opnames te vergemakkelijken, zie fig. 4.4.

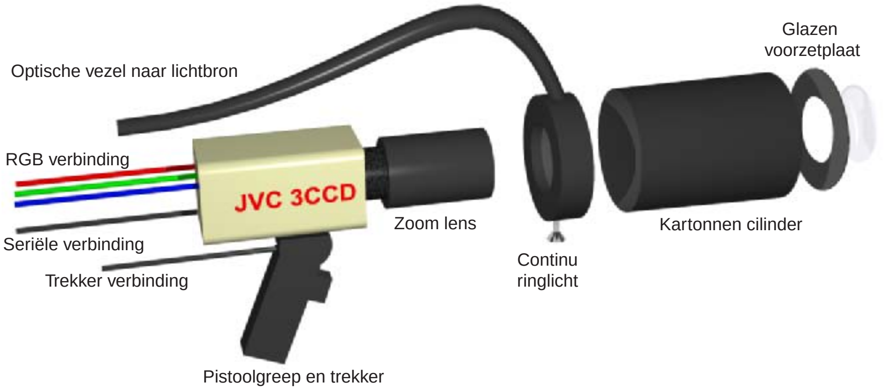

Figuur 4.4: Schema van de camera en zijn accessoires, op schaal.

4.3.2 De 'framegrabber'

De zogenaamde 'framegrabber' is verantwoordelijk voor het digitaliseren van de videosignalen van de camera. Hij bestaat hoofdzakelijk uit een videodecoder, een aantal ADCs, een stuureenheid en geheugen voor het bufferen van de beelden. Sommige framegrabbers vervullen terzelfdertijd de rol van schermkaart, wat het snel op scherm weergeven van opgenomen beelden vergemakkelijkt. De FlashPoint 128 Integral Technologies[4] framegrabber die hier gebruikt wordt is van dit type. Hij kan maximaal beelden van 570 op 760 pixels en 24 bit verwerken in PAL formaat. Net zoals de camera bezit de framegrabber een aantal eigenschappen die zijn werking controleren, zie tabel 4.3.

De framegrabbersoftwaremodule die de framegrabber stuurt en toelaat om 'live' video weer te geven en op te nemen is geschreven m.b.v.

---

[4] Integral Technologies, Inc. 9855 Crosspoint Blvd., Suite 140. Indianapolis, IN 46256 USA.

Eigenschap	**Waarde**	**Betekenis**
VIDEO STANDARD	**PAL** NTSC	De videostandaard
VIDEO TYPE	**RGB** COMPOSITE S-VIDEO	Het type videosignaal
VIDEO RECTANGLE	**570 bij 760** ...	De grootte van het opnamevenster
BRIGHTNESS	0-63	De versterking
CONTRAST	0-63	De basislijninstelling

Tabel 4.3: Enkele relevante eigenschappen van de framegrabber met sommige van hun instellingen. Vetgedrukte tekst duidt een eigenschap aan die vast ingesteld wordt.

een 'software development toolkit' van de fabrikant.

4.4 Kleurenbeeldverwerking

Binnen de context van het beeldvormingssysteem wordt met kleurenbeeldverwerking enkel die operaties bedoeld die ons in staat stellen dat systeem te kalibreren en op een reproduceerbare manier beelden op te nemen. Het gaat hier hoofdzakelijk om zeer eenvoudige operaties zoals het nemen van een spatiaal gemiddelde van pixels of het transformeren van alle pixels van een beeld met een lineaire of niet-lineaire transformatie. Deze routines vormen een onderdeel van de softwaremodule van het beeldvormingssysteem.

4.5 Uiteindelijk ...

De assemblage van de verschillende subsystemen in een kleurenbeeldvormingssysteem is schematisch weergegeven in fig. 4.5. De figuur toont ook de softwaremodule van het beeldvormingssysteem die het systeem als een geheel voorstelt en diengevolge de routines bevat waarmee een externe toepassing het beeldvormingssysteem kan aanspreken. Logischerwijs bevat deze module dus ook alle routines om het beeldvormingssysteem te gebruiken en te kalibreren, en deze maken uitvoerig gebruik van de hierboven vermelde kleurenbeeldverwerkingsroutines. De kalibratie en het gebruik van het beeldvormingssysteem zijn de hoofdonderwerpen van het volgende hoofdstuk.

Verdere uitbreidingen van het beeldvormingssysteem naar een volwaardig dermatologisch werkstation zijn vervat in de softwaremodules van het werkstation. Dit zal besproken worden in hoofdstuk 6.

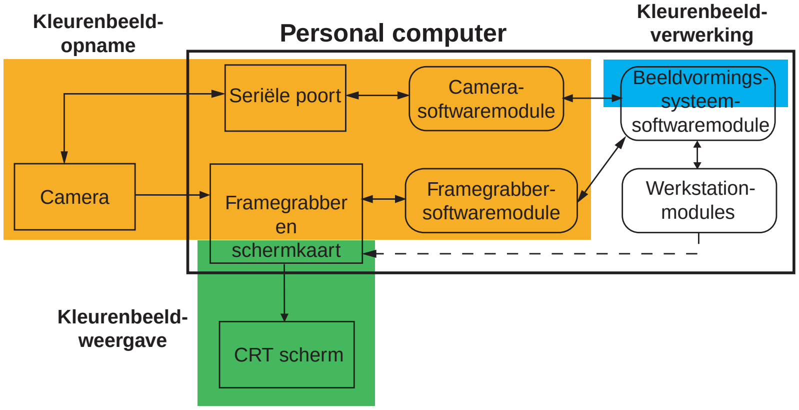

Figuur 4.5: Schema van het beeldvormingssysteem.

Het werkelijke uitzicht van het volledige geassembleerde kleurenbeeldvormingssysteem is te zien in fig. 4.6.

Figuur 4.6: Het volledige geassembleerde kleurenbeeldvormingssysteem.

Hoofdstuk 5

De werking van het kleurenbeeldvormingssysteem

We gaan nu over tot de bespreking van de werking van het beeldvormingssysteem als een geheel, i.e. de kalibratie en de opname van beelden. Dit wordt gevolgd door een aantal experimenten waarbij o.a. de nauwkeurigheid en reproduceerbaarheid van de opgenomen beelden zal bepaald worden. Een aantal conclusies sluiten vervolgens dit hoofdstuk af.

5.1 Kalibratie

Zoals reeds vermeld worden kleurenbeelden in de dermatologie meestal nog opgenomen d.m.v. traditionele fotografie. De beperkte reproduceerbaarheid van deze aanpak maakt echter dat kwantitatieve kleurmetingen niet alleen praktisch moeilijk te verwezenlijken maar ook onbetrouwbaar zijn. De exacte betekenis van de resultaten van deze metingen is bovendien onduidelijk zolang het verband van de bronkleurenruimte met b.v. de CIE colorimetrische ruimtes niet gekend is.

Digitale beeldvorming lost dit probleem echter niet op [34, 35]: ook hier heeft men meestal te maken met een niet-reproduceerbare, tijdsafhankelijke en toestelafhankelijke kleurenrepresentatie tengevolge van allerlei factoren zoals spectrale gevoeligheden, temperatuur, instellingen, etc. .... Kalibratie valt dus uiteen in het oplossen van twee distincte problemen: het verkrijgen van een constante respons van het beeldvormingssysteem, en het vinden van het verband tussen de toestelafhankelijke bronkleurenruimte en een toestelonafhankelijke kleurenruimte, v.b.

CIE XYZ. Dit laatste punt zorgt voor een stevige basis voor het ontwikkelen van ‘toestelonafhankelijke’ beeldverwerkingsalgoritmes gebaseerd op menselijke visie. Het maakt ook een zinvolle uitwisseling van beelden mogelijk, b.v. voor toepassingen in de tele-dermatologie. Voor zover ons bekend bestaan er nog geen commerciële dermatologische beeldvormingssystemen die op een gefundeerde manier in gestandaardiseerde en colorimetrische kleurenruimtes werken.

Het probleem van de kalibratie van beeldvormingssystemen is reeds verscheidene malen besproken in de literatuur, [36, 37, 35, 38, 39, 40, 41, 42]. In ons geval ligt de nadruk echter op een simpele en praktische procedure voor een beeldvormingssysteem ontwikkeld voor een welbepaalde taak. We zullen bovendien een stapje verder gaan dan de methodes beschreven in de literatuur.

5.1.1 De kleurenruimtes van het beeldvormingssysteem

Zoals reeds vermeld bestaat kalibratie o.a. uit het bepalen van de relatie tussen een toestelafhankelijke bronkleurenruimte en een nog te kiezen toestelonafhankelijke doelkleurenruimte. Verder moeten we ook een kleurenruimte kiezen voor de interne representatie van de beelden, i.e. de beelden in het geheugen van de PC. De meeste berekeningen op gekalibreerde beelden zullen van deze interne representatie vertrekken.

De keuze van deze interne kleurenruimte wordt vooral ingegeven door de vereiste van beperkt geheugengebruik en snelle en gemakkelijke weergave op het scherm. Hierdoor zijn kleurenruimtes zoals CIE XYZ en CIE $L^*a^*b^*$ uitgesloten. De $sR^*G^*B^*$ ruimte daarentegen is ideaal: ze laat onmiddellijke weergave op het scherm toe, en neemt slechts 24 bits per pixel in voor een redelijke nauwkeurige opslag. Een $sR^*G^*B^*$ beeld kan ook zonder extra bewerkingen in verscheidene populaire grafische bestandsformaten opgeslagen worden, en desgevallend in een externe toepassing op een realistische wijze bekeken worden. Het beperkt gamut van de $sR^*G^*B^*$ kleurenruimte t.o.v. de CIE colorimetrische ruimtes, zal in het geval van opnames van de huid niet zo belangrijk zijn door het ontbreken van de felle gesatureerde kleuren waarbij dit probleem zich kan stellen. Een nadeel van de $sR^*G^*B^*$ kleurenruimte is het groot aantal berekeningen die nodig zijn om kleurverschillen te berekenen. Om dit te verhelpen kan het bij complexe beeldverwerkingstaken nodig zijn om een tijdelijke CIE $L^*a^*b^*$ kopij van een beeld te berekenen en op te slaan, gebruik makend van een speciaal 32-bit formaat (zie tabel 5.1).

Nu de keuze van de interne kleurenruimte op $sR^*G^*B^*$ is gevallen is het logisch om als doelkleurenruimte van de kalibratie de $sRGB$ ruimte te nemen i.p.v. de meer gebruikelijke CIE XYZ ruimte. Dit beperkt het aantal berekeningen tijdens de beeldopname doordat de lineaire transformatie tussen CIE XYZ en $sRGB$ niet langer nodig is, zie ook fig. 5.1. Tabel 5.1 geeft een overzicht van de numerieke formaten en het gebruik van de kleurenruimtes van het beeldvormingssysteem.

Kleuren-ruimte	**Component waarde**	$\mathbf{\Delta E^*_{ab}}$	**Gebruik**
$R^*G^*B^*$	$\{0, \ldots, 255\}$	≈ 0.18	24-bit tijdelijke beeldopslag
RGB	$[0, 1]$	≈ 0	Tijdens berekeningen Geen beeldopslag
$sR^*G^*B^*$	$\{0, \ldots, 255\}$	0.18 ≤ 0.93	24-bit beeldopslag Bestandsopslag
$sRGB$	$[0, 1]$	≈ 0	Tijdens berekeningen Geen beeldopslag
CIE XYZ	$[0, +\infty[$	≈ 0	Tijdens berekeningen Geen beeldopslag
CIE $L^*a^*b^*$	$L^* \in [0, 100]$ $a^* \in [-100, 100]$ $b^* \in [-100, 100]$	≈ 0	Tijdens berekeningen Geen beeldopslag
CIE $L^*a^*b^*$ (opslag)	$L^* \in \{0, \ldots, 1023\}$ $a^* \in \{0, \ldots, 2047\}$ $b^* \in \{0, \ldots, 2047\}$	$= 0.08$	32-bit tijdelijke beeldopslag

Tabel 5.1: Overzicht van de numerieke formaten en het gebruik van de kleurenruimtes van het beeldvormingssysteem, alsook de geassocieerde kwantisatiefout.

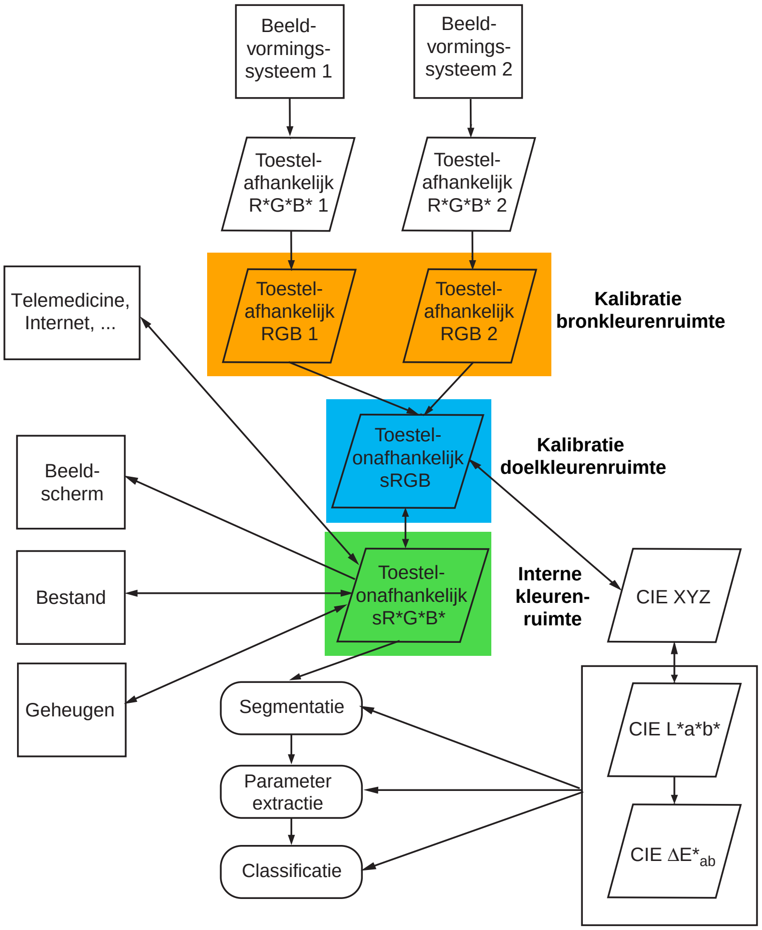

Figuur 5.1: Overzicht van de kleurenruimtes van het beeldvormingssysteem en hun onderlinge relaties.

5.1.2 Het model van het beeldvormingssysteem

Om een constante respons van het beeldvormingssysteem te verkrijgen is het nodig een set van 'optimale' instellingen van het systeem te bepalen, en deze eventueel aan te passen tijdens de werking. Hiervoor zal het eenvoudig model in fig. 5.2 gebruikt worden. In wat volgt zal het symbool $P = R, G, B$ in de RGB kleurenruimte gebruikt worden om zowel een tristimuluscomponent als een kleurkanaal wanneer in subscript aan te duiden. Hetzelfde geldt voor $\mathcal{P} = \mathcal{R}, \mathcal{G}, \mathcal{B}$ in de $sRGB$ kleurenruimte.

Het uitgangssignaal V_P^{cam} van de CCD camera voor een zekere pixel

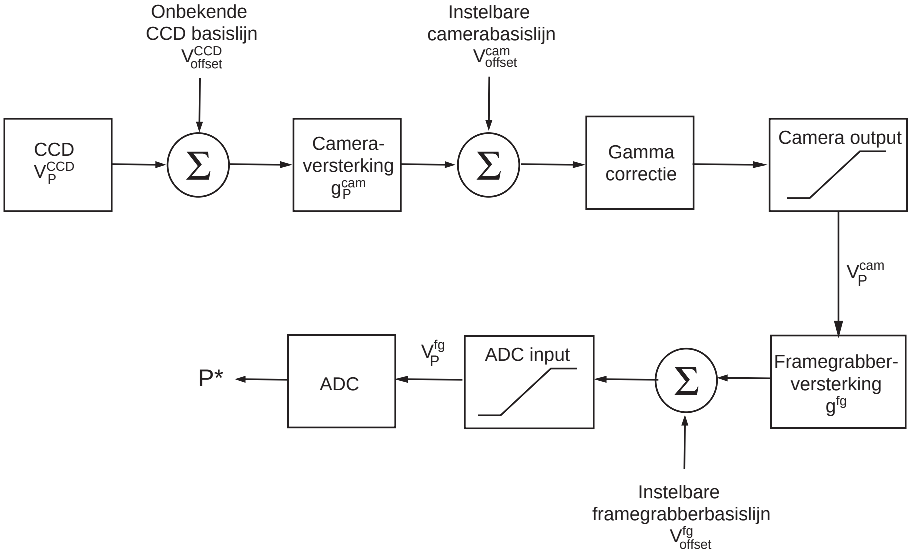

Figuur 5.2: Het model voor het beeldvormingssysteem voor één kleurkanaal $P = R, G, B$.

en component $P = R, G, B$ wordt gegeven door:

$$V_P^{cam} = \Psi_0^{V_{\max}^{cam}} \left(\Gamma(V_{offset}^{cam} + g_P^{cam}(V_P^{CCD} + V_{offset}^{CCD}))\right), \tag{5.1}$$

met V_{offset}^{cam} de basislijn van de camera ('MASTER BLACK' in tabel 4.2), en V_P^{CCD} een signaal evenredig met het licht invallend op de bedoelde pixel van de CCD van kleurkanaal P. V_{offset}^{CCD} is een onbekende basislijn, o.a. afkomstig van de donkerstroom van de CCD. g_P^{cam} is een variabele versterking specifiek voor kleurkanaal P ('MANUAL PAINT' in tabel 4.2). Merk op dat deze waarde fysisch vastligt op 1 voor het groene kanaal. De functie $\Psi_0^{V_{\max}^{cam}}$ stelt de begrenzing van een signaal voor:

$$\Psi_0^{V_{\max}}(V) = \begin{cases} 0 & \text{als } V < 0 \\ V & \text{als } 0 \leq V \leq V_{\max} \\ V_{\max} & \text{als } V > V_{\max}. \end{cases} \tag{5.2}$$

De functie Γ is de gammacorrectie zoals gedefinieerd in vgl. (4.5). Het signaal in de framegrabber voor de ADC V_P^{fg} en de overeenkomstige 8-bit $R^*G^*B^*$ en RGB component waarden P^* en P kunnen dus geschreven worden als:

$$\begin{aligned} V_P^{fg} =& \Psi_0^{V_{\max}^{fg}}(V_{offset}^{fg} + g^{fg} V_P^{cam}) \\ P^* =& \Re\left(255 \frac{V_P^{fg}}{V_{\max}^{fg}}\right),\ P^* \in \{0, \ldots, 255\}. \\ P =& \Gamma^{-1}(\frac{P^*}{255}),\ P \in [0, 1]. \end{aligned} \tag{5.3}$$

waarbij V_{offset}^{fg} de instelbare basislijn van de framegrabber voorstelt ('BRIGHTNESS' in tabel 4.3). g^{fg} is de instelbare maar kleurkanaalonafhankelijke versterkingsfactor van de framegrabber ('CONTRAST' in tabel 4.3), terwijl $\Re$ de afronding naar een natuurlijk getal voorstelt.

5.1.3 De transformatie tussen RGB en sRGB

Eén van de manieren om de relatie tussen de *RGB* bronkleurenruimte en de *sRGB* doelkleurenruimte te bepalen is d.m.v. een set van kleurplaatjes met bekende colorimetrische eigenschappen. Het opmeten van deze plaatjes met het beeldvormingssysteem kan dan gebruikt worden om een transformatie tussen bron- en doelkleurenruimte op te stellen. Het is duidelijk dat de hoeveelheid en distributie van deze plaatjes over het gamut in grote mate de nauwkeurigheid van deze transformatie, en bijgevolg het beeldvormingssysteem, zullen bepalen. Anderzijds mag de kalibratieprocedure ook geen eeuwigheid duren (de standaard industrie kleurenkaart, de IT8.7/2, bevat 288 plaatjes), en bijgevolg werd gekozen voor de MacBeth color checker chart[1] met zijn 24 kleuren, zie fig. 5.3. De colorimetrische eigenschappen van de plaatjes van de MBCCC werden opgemeten met een Gretag[2] SPM50 spectrofotometer. Dit toestel meet gemiddelde D65 CIE XYZ waarden over een cirkel van 5 mm, vandaar de $\langle\rangle$ notatie. Deze metingen kunnen gemakkelijk getransformeerd worden naar de *sRGB* ruimte:

$$\begin{pmatrix} \langle \mathcal{R}_{SPM,i} \rangle \\ \langle \mathcal{G}_{SPM,i} \rangle \\ \langle \mathcal{B}_{SPM,i} \rangle \end{pmatrix} = \Phi_{XYZ \to sRGB} \begin{pmatrix} \langle X_{SPM,i} \rangle \\ \langle Y_{SPM,i} \rangle \\ \langle Z_{SPM,i} \rangle \end{pmatrix} \tag{5.4}$$

Een beeldvormingssysteem wordt colorimetrisch genoemd als zijn spectrale gevoeligheden een lineair verband vertonen met de color-matching functies. Dit is echter over het algemeen niet het geval, en

---

[1] Macbeth, 405 Little Britain rd, New Windsor, NY 12553-6148, USA.

[2] GretagMacbeth Ag, Althardstrasse 70, CH-8105, Regensdorf, Zwitserland.

Figuur 5.3: De MacBeth ‘color checker chart’.

bijgevolg worden dikwijls complexe methodes gebruikt om bron- en doelkleurenruimte met elkaar te relateren, [42]. We beperken ons hier tot het gebruik van polynomen van verschillende ordes. We zullen matrices gebruiken om een duidelijke en vooral compacte notatie te creëren die ons in staat stelt zowel lineaire als niet-lineaire relaties neer te schrijven. Dit vergt het invoeren van een aantal niet-lineaire operatoren die inwerken op een matrix en resulteren in een andere matrix, maar zelf niet als een matrix kunnen genoteerd worden. Binnen deze notatie worden tristimuluswaarden en andere kleurtripletten altijd als een kolomvector genoteerd.

Een algemene polynomiale transformatie $\Phi_{RGB \to sRGB,m}$ tussen RGB tristimuluswaarden (R, G, B) en $sRGB$ tristimuluswaarden $(\mathcal{R}, \mathcal{G}, \mathcal{B})$, en die m termen bevat kan genoteerd worden als:

$$\begin{aligned} \begin{pmatrix} \mathcal{R} \\ \mathcal{G} \\ \mathcal{B} \end{pmatrix} &= \Phi_{RGB \to sRGB,m} \begin{pmatrix} R \\ G \\ B \end{pmatrix} \\ &= \begin{pmatrix} a_{\mathcal{R},1} & \dots & a_{\mathcal{R},m} \\ a_{\mathcal{G},1} & \dots & a_{\mathcal{G},m} \\ a_{\mathcal{B},1} & \dots & a_{\mathcal{B},m} \end{pmatrix} \left[\Theta_m \begin{pmatrix} R \\ G \\ B \end{pmatrix} \right] \end{aligned} \tag{5.5}$$

De ‘delinearisatie’ operator Θ_m verandert een kolomvector met 3 elementen in een kolomvector met m elementen en representeert een set van plausibele polynomiale transformaties [42]:

$$
\begin{aligned}
\Theta_3 \begin{pmatrix} R \\ G \\ B \end{pmatrix} &= \begin{pmatrix} R & G & B \end{pmatrix}^t \\
\Theta_6 \begin{pmatrix} R \\ G \\ B \end{pmatrix} &= \begin{pmatrix} R & G & B & RG & GB & BR \end{pmatrix}^t \\
\Theta_8 \begin{pmatrix} R \\ G \\ B \end{pmatrix} &= \begin{pmatrix} 1 & R & G & B & RG & GB & BR & RGB \end{pmatrix}^t \qquad (5.6) \\
\Theta_9 \begin{pmatrix} R \\ G \\ B \end{pmatrix} &= \begin{pmatrix} R & G & B & RG & GB & BR & R^2 & G^2 & B^2 \end{pmatrix}^t \\
\Theta_{11} \begin{pmatrix} R \\ G \\ B \end{pmatrix} &= \begin{pmatrix} 1 & R & G & B & RG & GB & BR & R^2 & G^2 & B^2 & RGB \end{pmatrix}^t
\end{aligned}
$$

De coëfficiënten van $\Phi_{RGB \rightarrow sRGB,m}$ kunnen bepaald worden door de 24 SPM metingen van de MBCCC plaatjes $(\langle \mathcal{R}_{SPM,i} \rangle, \langle \mathcal{G}_{SPM,i} \rangle, \langle \mathcal{B}_{SPM,i} \rangle), i = 1, \ldots, 24$ te substitueren in het linkerlid van vgl. (5.5). Diezelfde plaatjes kunnen ook gemeten worden met het beeldvormingssysteem, en de resulterende spatiaal uitgemiddelde RGB tristimulus waarden $(\langle R_i \rangle, \langle G_i \rangle, \langle B_i \rangle), i = 1, \ldots, 24$ vervolgens gesubstitueerd in het rechterlid van vgl. (5.5) (zie fig. 5.4 voor een overzicht). Dit levert ons 3 overgedetermineerde lineaire stelsels, één per kleurkanaal $\mathcal{P} = \mathcal{R}, \mathcal{G}, \mathcal{B}$ van de $sRGB$ ruimte:

$$
\begin{aligned}
&\begin{pmatrix} \langle \mathcal{P}_{SPM,1} \rangle & \ldots & \langle \mathcal{P}_{SPM,24} \rangle \end{pmatrix} = \\
&\qquad \begin{pmatrix} a_{\mathcal{P},1} & \ldots & a_{\mathcal{P},m} \end{pmatrix} \left(\Theta_m \begin{pmatrix} \langle R_1 \rangle \\ \langle G_1 \rangle \\ \langle B_1 \rangle \end{pmatrix} \quad \ldots \quad \Theta_m \begin{pmatrix} \langle R_{24} \rangle \\ \langle G_{24} \rangle \\ \langle B_{24} \rangle \end{pmatrix} \right). \qquad (5.7)
\end{aligned}
$$

Deze vergelijkingen kunnen gemakkelijk opgelost worden in de kleinste-kwadraten zin door gebruik te maken van singulierewaardenontbinding. Het resultaat $\Phi^{LLSQ}_{RGB \rightarrow sRGB,m}$ wordt de lineaire kleinste-kwadratenoplossing genoemd (LLSQ voor 'linear least-squares'). Deze oplossing mag dan wel wiskundig optimaal zijn, voor een menselijke waarnemer is dit zeker niet het geval omdat de som van kwadraten in de $sRGB$ ruimte geen goede maat is voor de visuele fout

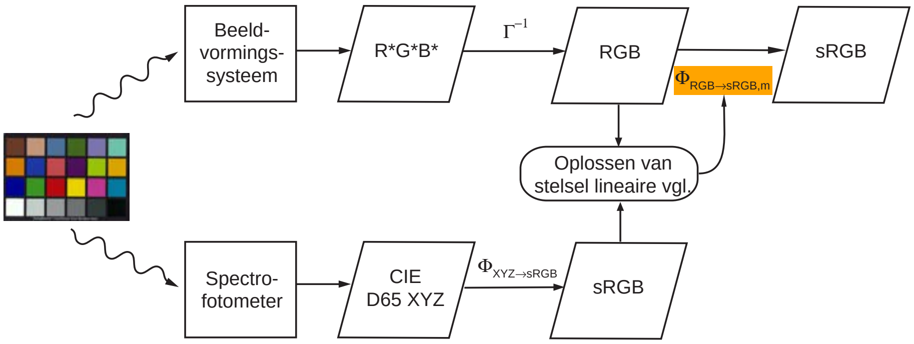

Figuur 5.4: Overzicht van de bepaling van de RGB naar $sRGB$ transformatie $\Phi^{LLSQ}_{RGB\rightarrow sRGB,m}$.

geassocieerd met $\Phi^{LLSQ}_{RGB\rightarrow sRGB,m}$. Een betere transformatie zou men dus kunnen bekomen door b.v. de fout geassocieerd met een transformatie in de CIE $L^*a^*b^*$ kleurenruimte te minimaliseren. Hiertoe voeren we de niet-lineaire operator $\Phi_{sRGB\rightarrow L^*a^*b^*}$ in die de gekende transformatie van $sRGB$ tristimuli naar CIE $L^*a^*b^*$ tripletten via CIE XYZ voorstelt (zie ook vgl. (4.3) en vgl. (3.8)):

$$\begin{aligned}\begin{pmatrix} L^* \\ a^* \\ b^* \end{pmatrix} &= \Phi_{sRGB\rightarrow L^*a^*b^*} \begin{pmatrix} \mathcal{R} \\ \mathcal{G} \\ \mathcal{B} \end{pmatrix} \\ &= \Phi_{XZY\rightarrow L^*a^*b^*}\ \Phi_{sRGB\rightarrow XYZ} \begin{pmatrix} \mathcal{R} \\ \mathcal{G} \\ \mathcal{B} \end{pmatrix}, \end{aligned} \tag{5.8}$$

Bijgevolg kunnen de CIE $L^*a^*b^*$ tripletten $(\langle L^*_i\rangle, \langle a^*_i\rangle, \langle b^*_i\rangle)$ van de MBCCC plaatjes zoals gemeten door het beeldvormingssysteem neergeschreven worden als:

$$\begin{pmatrix} \langle L^*_i\rangle \\ \langle a^*_i\rangle \\ \langle b^*_i\rangle \end{pmatrix} = \Phi_{sRGB\rightarrow L^*a^*b^*}\ \Phi_{RGB\rightarrow sRGB,m} \begin{pmatrix} \langle R_i\rangle \\ \langle G_i\rangle \\ \langle B_i\rangle \end{pmatrix} \tag{5.9}$$

De CIE $L^*a^*b^*$ tripletten $(\langle L^*_{SPM,i}\rangle, \langle a^*_{SPM,i}\rangle, \langle b^*_{SPM,i}\rangle)$ van de MBCCC plaatjes, zoals gemeten door de SPM, worden gemakkelijk berekend via:

$$\begin{pmatrix} \langle L^*_{SPM,i}\rangle \\ \langle a^*_{SPM,i}\rangle \\ \langle b^*_{SPM,i}\rangle \end{pmatrix} = \Phi_{XYZ\rightarrow L^*a^*b^*} \begin{pmatrix} \langle X_{SPM,i}\rangle \\ \langle Y_{SPM,i}\rangle \\ \langle Z_{SPM,i}\rangle \end{pmatrix} \tag{5.10}$$

Dit laat ons toe om de fout in ΔE^*_{ab} eenheden van een MBCCC plaatje i geassocieerd met $\Phi_{RGB\to sRGB,m}$ te definiëren als:

$$\Delta E^*_{ab}(\Phi_{RGB\to sRGB,m}, i) = \sqrt{(\langle L^*_i\rangle - \langle L^*_{SPM,i}\rangle)^2 + (\langle a^*_i\rangle - \langle a^*_{SPM,i}\rangle)^2 + (\langle b^*_i\rangle - \langle b^*_{SPM,i}\rangle)^2} \quad (5.11)$$

Dit is nog altijd geen maat voor de *volledige* fout van een transformatie $\Phi_{RGB\to sRGB,m}$. Twee logische kandidaten voor deze volledige fout zijn de gemiddelde ΔE^*_{ab} fout per MBCCC plaatje:

$$\langle \Delta E^*_{ab}(\Phi_{RGB\to sRGB,m})\rangle = \frac{1}{24}\sum_{i=1}^{24} \Delta E^*_{ab}(\Phi_{RGB\to sRGB,m}, i), \quad (5.12)$$

en de maximale ΔE^*_{ab} fout over de set van MBCCC plaatjes $\max(\Delta E^*_{ab}(\Phi_{RGB\to sRGB,m}))$. De transformaties die verkregen worden door gebruik te maken van deze twee verschillende volledige fouten worden genoteerd als $\Phi^{avg}_{RGB\to sRGB,m}$ en $\Phi^{\max}_{RGB\to sRGB,m}$ respectievelijk. De minimalisatie gebeurt d.m.v. het iteratieve Nelder-Mead simplex algoritme [43], met de LLSQ oplossing als initiële gissing. Zie fig. 5.5 voor een overzicht.

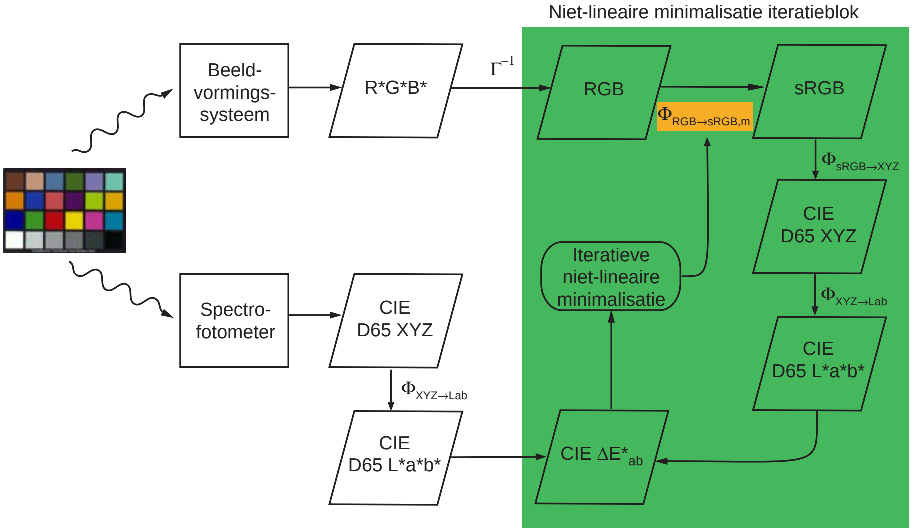

Figuur 5.5: Overzicht van de bepaling van de *RGB* naar *sRGB* transformaties $\Phi^{avg}_{RGB\to sRGB,m}$ en $\Phi^{\max}_{RGB\to sRGB,m}$.

5.1.4 De kalibratieprocedure

We gaan nu over tot de beschrijving van de nodige stappen om het beeldvormingssysteem te kalibreren. Dit omvat onder meer de instelling van het gezichtsveld van de camera (FOV voor ‘field of view’), het bepalen van de optimale (maximaal dynamisch bereik) instellingen en het berekenen van de transformatie van de RGB bronkleurenruimte naar de $sRGB$ doelkleurenruimte. De volgorde waarin de verschillende operaties besproken worden is ook de volgorde waarin ze moeten uitgevoerd worden. De ganse procedure neemt 5 tot 10 minuten in beslag, en alle resulterende instellingen worden in een zogenaamd ‘kalibratieprofiel’ opgeslagen. Dit profiel blijft vrij lang geldig, en moet typisch slechts opnieuw bepaald worden wanneer b.v. de lamp van de lichtbron vervangen wordt.

Instelling van het gezichtsveld van de camera

Hiertoe wordt gebruik gemaakt van een klein logo dat de gewenste afmetingen heeft, nl. 1.6 cm bij 1.2 cm voor een resolutie van 48 pixels per mm. De zoomlens wordt simpelweg zo ingesteld dat het logo net volledig in beeld is. Het logo bevat tevens letters, wat toelaat om ook de focussering nauwkeurig in te stellen.

Instellingen voor ‘perfect’ zwart

Het doel van deze stappen is ervoor te zorgen dat ‘perfect’ zwart, i.e. een voorwerp met reflectieve luminantie $Y = 0$ en dus ook $V_P^{CCD} = 0, P = R, G, B$, resulteert in RGB tristimuluswaarde $(0, 0, 0)$. Zo’n voorwerp kan gemakkelijk gesimuleerd worden door de lenskap op te zetten, het diafragma te sluiten en de lichtbron af te zetten. Metingen van de RGB waarden tijdens de kalibratie gebeuren altijd door het uitmiddelen van enkele duizenden pixels afkomstig uit het midden van het beeld in de $R^*G^*B^*$ ruimte. Dit versnelt de berekeningen en vermijdt problemen met inhomogene belichting of respons van het beeldvormingssysteem.

Vooreerst zorgen we dat ‘perfect’ zwart leidt tot een camera uitgangssignaal $V_P^{cam} = 0$ door de basislijn van de camera V_{offset}^{cam} correct in te stellen. Vgl. (5.1) toont ons echter dat de optimale instelling van V_{offset}^{cam} zal afhangen van de versterkingen van de kleurkanalen van de camera g_P^{cam}. Het is dus vrij onwaarschijnlijk om een optimale instelling voor de drie kleurkanalen tegelijkertijd te vinden. Daar de versterking van het groene kanaal vast staat $g_G^{cam} = 1$, kiezen we dat kanaal om V_{offset}^{cam} in te stellen. Daar de instellingen van de framegrabber nog niet bepaald zijn is het echter niet mogelijk om een doelwaarde voor de groene component $G^*_{Y=0}$ of $G_{Y=0}$ voor te stellen die overeenkomt met de eis dat $V_G^{CCD} = 0$. We stellen daarvoor volgende procedure voor:

1. Zorg ervoor dat perfect zwart resulteert in een groene component $G_{Y=0} > 0$ door de versterking g^{fg} en basislijn V^{fg}_{offset} van de framegrabber hoog in te stellen.

2. Meet de spatiaal gemiddelde $\langle G_{Y=0}\rangle$ voor alle mogelijk instellingen van de basislijn van de camera V^{cam}_{offset}.

Met behulp van vgl. (5.1) en (5.3) kan men inzien dat dit zal leiden tot een curve die bestaat uit twee lijnstukken: een horizontaal stuk zolang $V^{cam}_{offset} + V^{CCD}_{offset} < 0$, een schuin stuk als $V^{cam}_{offset} + V^{CCD}_{offset} \geq 0$, zie fig. 5.6. De optimale instelling, i.e. deze waarvoor $V^{cam}_{offset} + V^{CCD}_{offset} = 0$, bevindt zich op het snijpunt van deze lijnstukken. Om dit punt op een betrouwbare manier te vinden stellen we volgende methode voor: fit voor elke mogelijke instelling van de camerabasislijn twee lijnstukken door de data, en bereken telkens de residuele fout tussen de data en de gefitte lijnstukken. De optimale instelling is dan deze met de laagste residuele fout, zie opnieuw fig. 5.6. We zullen naar deze methode refereren als de ‘twee-lijn-intersectiemethode’.

We kunnen nu zoeken naar de instelling voor de basislijn van de framegrabber V^{fg}_{offset} waarvoor perfect zwart $\langle G^*_{Y=0}\rangle = \langle G_{Y=0}\rangle = 0$. Doordat we er reeds voor gezorgd hebben dat $V_G^{cam} = 0$ voor perfect zwart hoeven we eigenlijk enkel de laagste instelling voor de basislijn van de framegrabber V^{fg}_{offset} te vinden waarvoor $\langle G^*_{Y=0}\rangle = 0$. We verkiezen echter opnieuw de twee-lijn-intersectiemethode te gebruiken omdat die robuuster is. Merk op dat enkel $G^*_{Y=0}$ een stuksgewijze lineaire relatie met V^{fg}_{offset} heeft, en niet $G_{Y=0}$.

Instellingen voor ‘perfect’ wit

We moeten er nu voor zorgen dat ‘perfect wit’, i.e. een perfecte diffuse reflector met luminantie $Y = 100$, resulteert in een tristimuluswaarde $(1, 1, 1)$.

Hiertoe bepalen we eerst de versterking van de framegrabber g^{fg} (deze is dezelfde voor alle kleurkanalen). We wensen g^{fg} zo in te stellen dat het maximale uitgangssignaal van de camera $V_P^{cam} = V_{max}^{cam}, P = R, G, B$ resulteert in een tristimuluswaarde van $(1, 1, 1)$. Doordat dat maximale uitgangssignaal V_{max}^{cam} hetzelfde is voor alle kleurkanalen is het

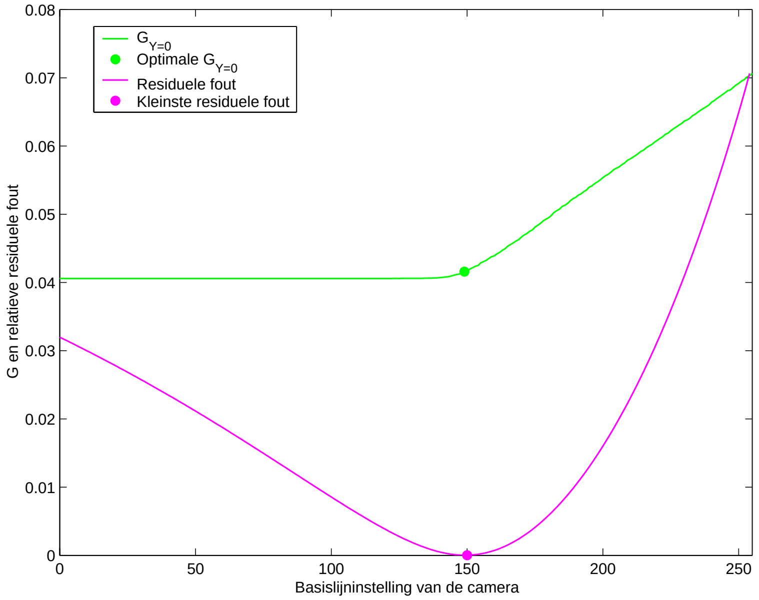

Figuur 5.6: $\langle G_{Y=0} \rangle$ in functie van de instelling van de basislijn van de camera V^{cam}_{offset}, en de corresponderende residuele fouten met de twee-lijn-intersectiemethode.

duidelijk dat als de versterking van de framegrabber optimaal is voor één kleurkanaal ze dat ook automatisch is voor de andere twee kleurkanalen. Omdat de versterking van de camera reeds ingesteld is voor het groene kanaal is het gemakkelijker om hiermee verder te werken. Het maximale uitgangssignaal voor het groene kanaal wordt bekomen door de CCD te satureren door het diafragma volledig te openen en het hoog-reflectieve witte MBCCC plaatje te meten. Hierna wordt $\langle G \rangle$ gemeten voor alle mogelijke instellingen van g^{fg}, en de optimale instelling bepaald met de twee-lijn-intersectiemethode.

Vervolgens moeten we de stand van het diafragma bepalen waarvoor saturatie van de CCD's juist vermeden wordt bij een luminantie van $Y = 100$. We zijn niet in het bezit van zo'n plaatje, en gebruiken het witte MBCCC plaatje in de plaats ervan. Gebruik makend van de gekende D65 luminantie van dit plaatje Y_{wit} en door de lineariteit van het beeldvormingssysteem is het mogelijk de theoretische groene component te berekenen voor dit plaatje, nl. $G^*_{wit,th} = 255\,\Gamma(Y_{wit}/100)$. Er rest ons dan enkel het diafragma manueel aan te passen totdat de gemeten waarde $\langle G^*_{wit} \rangle$ voor het witte MBCCC plaatje overeenkomt met die theoretische waarde. Eens dit gebeurd is kunnen ook de versterkingsfactoren voor het rode en blauwe kleurkanaal van de camera op analoge wijze ingesteld worden: $\langle R^*_{wit} \rangle = \langle B^*_{wit} \rangle = \langle G^*_{wit} \rangle = G^*_{wit,th}$.

Linearisatie

Het doel van deze operatie is het lineair gedrag van het beeldvormingssysteem in functie van de luminantie over het gehele dynamische bereik te verzekeren. Deze assumptie is eigenlijk impliciet wanneer gebruik wordt gemaakt van CIE en andere tristimulusruimtes, en kleine afwijkingen hiervan kunnen bijgestuurd worden door één of meerdere opzoektabellen (LUT voor 'lookup table').

Hier worden drie LUTs gebruikt, één voor elk kleurkanaal. Ze worden opgesteld in de RGB tristimulusruimte, maar zijn werkzaam in de $R^*G^*B^*$ kleurenruimte omdat die gediscretiseerd is:

$$P^*_{LUT} = LUT_P(P^*),\ P = R, G, B. \tag{5.13}$$

Elke LUT heeft 256 elementen, zodat er geen nood is aan interpolatie wat de snelheid verbetert. De LUTs zijn gebaseerd op de 6 achromatische (grijze) MBCCC plaatjes die allemaal ongeveer dezelfde chromaticiteitscoördinaten hebben, maar verschillende luminantie, gaande van $Y \approx 3$ tot $Y \approx 90$. Elke LUT wordt zo opgesteld dat voor elk van de 6 plaatjes i de LUT-gecorrigeerde gemeten RGB waarden proportioneel zijn met de luminantie van het plaatje, i.e. $\langle R_i \rangle = \langle G_i \rangle = \langle B_i \rangle = Y_i/100$. Dit noemt men 'gray balancing'.

Het bepalen van de transformatie van RGB naar sRGB

Eens het beeldvormingssysteem volledig optimaal is ingesteld kan de RGB naar $sRGB$ transformatie $\Phi_{RGB \to SRGB}$ berekend worden door metingen van de 24 MBCCC plaatjes met het beeldvormingssysteem te vergelijken met eerder uitgevoerde metingen met een SPM. De resultaten van de MBCCC metingen met het beeldvormingssysteem bekomen met de berekende transformatie $\Phi_{RGB \to SRGB}$ worden in een bestand opgeslagen om later de validiteit van het kalibratieprofiel te kunnen nagaan.

5.2 Beeldopname

Om bruikbaar te zijn in een klinische context moet de beeldopnameprocedure zo simpel en snel mogelijk zijn. Langs de andere kant kan het wenselijk zijn om toch een aantal controles en aanpassingen aan het beeldvormingssysteem, of beter gezegd het kalibratieprofiel, te kunnen uitvoeren om de kwaliteit van de opgenomen beelden te kunnen garanderen. Als compromis werd gekozen voor het gebruik van één MBCCC plaatje, gemonteerd in de lenskap, om alle bovenstaande taken uit te voeren. Zodoende is de gebruikersinteractie minimaal, te meer daar men gedurende een kwartier vrij gekalibreerde beelden kan opnemen eens het systeem met zijn kalibratieprofiel doorheen de controleprocedure gelopen is.

5.2.1 Korte-termijn drift

Zoals reeds voorheen gezegd blijft een kalibratieprofiel lange tijd geldig. Het beeldvormingssysteem vertoont echter een korte-termijn drift wanneer het voor het eerst aangezet wordt, i.e. opwarmt. Deze drift vermindert sterk in amplitude na 30 of 40 minuten, zonder echter ooit echt te verdwijnen. Het is mogelijk voor deze drift te compenseren door een aantal instellingen aan te passen, voornamelijk de versterking van de framegrabber g^{fg} en de versterking van de camera voor het rode en blauwe kleurkanaal, g_R^{cam} en g_B^{cam}. Dit kan bekomen worden door de huidige pre-LUT RGB tristimulus waarden van het witte MBCCC plaatje te vergelijken met de waarden van datzelfde plaatje tijdens de kalibratie, per definitie gelijk aan $R^*_{wit} = B^*_{wit} = G^*_{wit} = 255\,\Gamma(Y_{wit}/100)$.

Fig. 5.7 toont het resultaat van het aanpassen van een kalibratieprofiel door het kleurverschil ΔE^*_{ab} uit te zetten tussen de meetwaarden van het witte MBCCC plaatje tijdens kalibratie en op verschillende tijdstippen tijdens het opwarmen van het beeldvormingssysteem, zonder en met aanpassing van het kalibratieprofiel. Merk op dat men er op het eerste zicht zelfs in slaagt de grote verschillen net na het aanzetten van het beeldvormingssysteem te compenseren. Dit is echter slechts schijn, want de fouten op de andere MBCCC plaatjes blijken onaanvaardbaar hoog als de aanpassingen van het kalibratieprofiel te belangrijk zijn. Verdere metingen bevestigen dat dit het geval is als het initieel kleurverschil voor het witte MBCCC plaatje groter is dan 2 Δ^*_{ab} eenheden, wat overeenkomt met een opwarmtijd van ongeveer 20 minuten. Om de zaken te vergemakkelijken wordt er een kwaliteitsfactor voor het kalibratieprofiel ingevoerd, gebaseerd op het hierboven vermelde kleurverschil ΔE^*_{ab} van het witte MBCCC plaatje:

$$Q = \begin{cases} 100 - 20 * \Delta E^*_{ab} & \text{als} \quad \Delta E^*_{ab} < 5 \\ 0 & \text{als} \quad \Delta E^*_{ab} \geq 5. \end{cases} \tag{5.14}$$

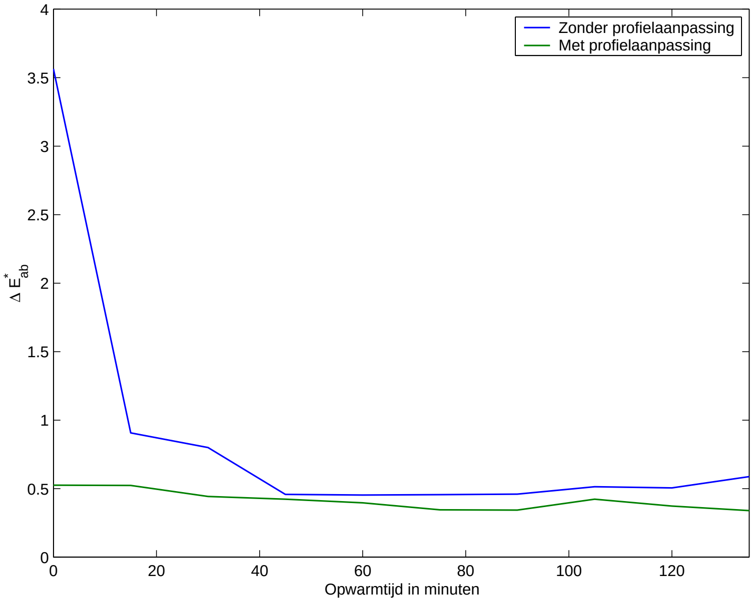

Figuur 5.7: Kleurverschil ΔE^*_{ab} van het witte MBCCC plaatje tussen meetwaarden tijdens de kalibratie en op verschillende tijdstippen tijdens het opwarmen van het beeldvormingssysteem, zonder en met aanpassing van het kalibratieprofiel.

Een kwaliteitsfactor van 100 is perfect, een waarde van 0 duidt een verschil van meer dan $5\Delta E^*_{ab}$ eenheden aan.

5.2.2 Correctie voor spatiale inhomogeniteiten

Spatiale inhomogeniteiten in het beeldvormingssysteem zijn hoofdzakelijk het gevolg van inhomogene belichting, en in mindere mate van de CCDs en de optica. Men kan hiervoor gemakkelijk corrigeren door een beeld op te nemen van een homogeen oppervlak (zie fig. 5.8), en dit correctiebeeld te gebruiken om opgenomen beelden pixel per pixel multiplicatief aan te passen:

$$P_i' = P_i \frac{\langle \hat{P} \rangle}{\hat{P}_i}. \tag{5.15}$$

In deze vergelijking stellen P_i' en P_i een gecorrigeerde, respectievelijk ongecorrigeerde tristimuluscomponent van een pixel i van een opgenomen beeld voor. $\hat{P}_i$ is de tristimuluscomponent van pixel i van het correctiebeeld, terwijl $\langle \hat{P} \rangle$ de spatiaal gemiddelde tristimuluscomponent van het centrum van het correctiebeeld is. In de praktijk wordt het correctiebeeld door een 3 bij 3 pixel filter uitgemiddeld vóór gebruik.

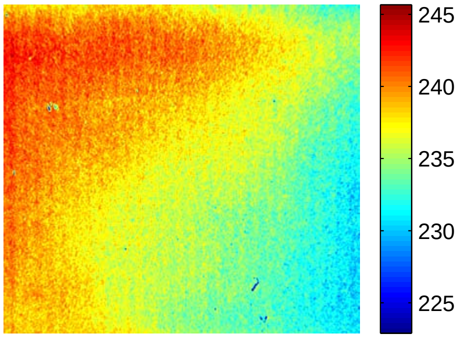

Figuur 5.8: De rode tristimuluscomponent van het correctiebeeld met een aangepaste kleurenmap om het contrast te vergroten.

5.2.3 De beeldopnameprocedure

De verschillende stappen voor het opnemen van een beeld zijn:

1. Kijk na of er een kalibratieprofiel aanwezig is op de PC. Stop indien dit niet zo is.

2. Kijk na of de tijd verstreken sinds de laatste succesvolle aanpassing van het profiel hoger is dan een vooropgezette drempel, typisch 15 minuten. Indien niet ga naar stap 7.

3. Kijk na of het profiel geldig is, gebruik makend van de initiële, i.e. onaangepaste instellingen, en het witte MBCCC plaatje in de lenskap. Indien de kwaliteitsfactor $Q < 60$ wordt een waarschuwing aan de gebruiker doorgegeven, met de optie te stoppen met de beeldopname.

4. Pas het profiel aan d.m.v. het witte MBCCC plaatje in de lenskap.

5. Kijk na of het aangepaste profiel geldig is. Indien de kwaliteitsfactor $Q < 80$ wordt gestopt met de beeldopname.

6. Neem het correctiebeeld voor spatiale inhomogeniteiten op (weerom het witte MBCCC plaatje in de lenskap), en filter het met een 3 bij 3 pixel laagdoorlaatfilter.

7. Neem het beeld op, voer de correctie voor spatiale inhomogeniteiten uit en transformeer het resultaat naar de $sR^*G^*B^*$ kleurenruimte. Keer terug naar de aanroepende routine of toepassing.

Als de beeldopname succesvol verloopt kan het beeld naar het windows klembord worden getransfereerd of worden opgeslagen in een bestand.

5.3 Experimenten en resultaten

Als visueel document werden de opgenomen beelden over het algemeen goed bevonden door de dermatologen. Dit is hoofdzakelijk een kwestie van scherpte en resolutie, die hoog genoeg moeten zijn om bepaalde diagnostische kenmerken te kunnen zien. Fig. 5.9 geeft een klinisch en dermatoscopisch voorbeeld opgenomen met het beeldvormingssysteem.

Voordat we verder gaan met het uitbouwen van het beeldvormingssysteem tot een dermatologisch werkstation moeten we ons twee fundamentele vragen stellen: wat is de *precisie* en wat is de *nauwkeurigheid* van colorimetrische metingen verricht op beelden opgenomen met het beeldvormingssysteem? Het antwoord op deze twee vragen zal in grote mate de bruikbaarheid van het systeem bepalen, en zal nu in detail onderzocht worden

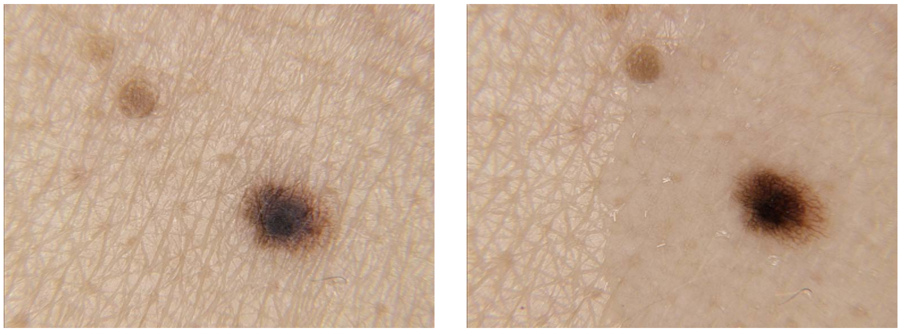

Figuur 5.9: Een junctienaevus opgenomen met het beeldvormingssysteem, zowel klinisch (links) als dermatoscopisch (rechts). Merk op dat de olie zich niet volledig verspreid heeft bij de dermatoscopische opname.

5.3.1 Precisie

De precisie of reproduceerbaarheid van een meetproces is de mate waarin herhaalde metingen van hetzelfde onderwerp verspreid zijn rond het gemiddelde van die metingen. In ons geval zegt het iets over de geschiktheid van de instellingen van het beeldvormingssysteem en de bekwaamheid van het algoritme dat het kalibratieprofiel net vóór de beeldopname aanpast om kleine fluctuaties in de respons van het beeldvormingssysteem tegen te gaan.

Precisie is belangrijk voor het uitvoeren van kwantitatieve kleurmetingen op de beelden. We maken onderscheid tussen verschillende types precisie: korte-termijnprecisie voor consecutieve metingen van éénzelfde onderwerp, middellange-termijnprecisie voor metingen van éénzelfde onderwerp op verschillende tijdstippen maar onder hetzelfde kalibratieprofiel, en lange-termijnprecisie voor metingen van éénzelfde onderwerp onder verschillende kalibratieprofielen. De fouten zijn uitgedrukt in ΔE^*_{ab} eenheden tot het gemiddelde van de metingen in de CIE $L^*a^*b^*$ kleurenruimte.

De korte-termijnprecisie is gebaseerd op 20 consecutieve metingen van het witte MBCCC plaatje: $\langle \Delta E^*_{ab} \rangle = 0.04$, met $\Delta E^*_{ab} \leq 0.1$. Dit is even goed als een typische spectrofotometer.

De middellange-termijnprecisie werd berekend aan de hand van 10 metingen van al de MBCCC plaatjes, op verschillende tijdstippen in de opwarmcyclus en tijdens verschillende opwarmcycli van het beeldvormingssysteem, maar altijd gebruik makend van hetzelfde kalibratieprofiel. De gemiddelde en maximale fout voor elk MBCCC kleurplaatje is te zien in fig. 5.10. Over alle MBCCC plaatjes krijgen we $\langle \Delta E^*_{ab} \rangle = 0.34$, met $\Delta E^*_{ab} \leq 1.2$.

De lange-termijnprecisie werd berekend aan de hand van 9 metingen van al de MBCCC plaatjes, telkens onder een nieuw kalibratieprofiel dat net voor de meting bepaald werd. Om mogelijke lange-termijn veranderingen in het beeldvormingssysteem te simuleren werd de spanning van de lichtbron in de helft van de metingen gewijzigd. Dit resulteerde in een duidelijk zichtbare wijziging in de kleurtemperatuur van de lichtbron, maar niet in nadelige gevolgen voor de precisie van de betrokken metingen. De gemiddelde en maximale fout voor elk MBCCC kleurplaatje is te zien in fig. 5.11. Over alle MBCCC plaatjes krijgen we $\langle \Delta E^*_{ab} \rangle = 0.30$, met $\Delta E^*_{ab} \leq 1.2$.

5.3.2 Nauwkeurigheid

De nauwkeurigheid van een meetproces is een maat voor hoe dicht metingen in de buurt liggen van een meting met een referentie-instrument, b.v. een SPM. De belangrijkste factor voor de nauwkeurigheid van

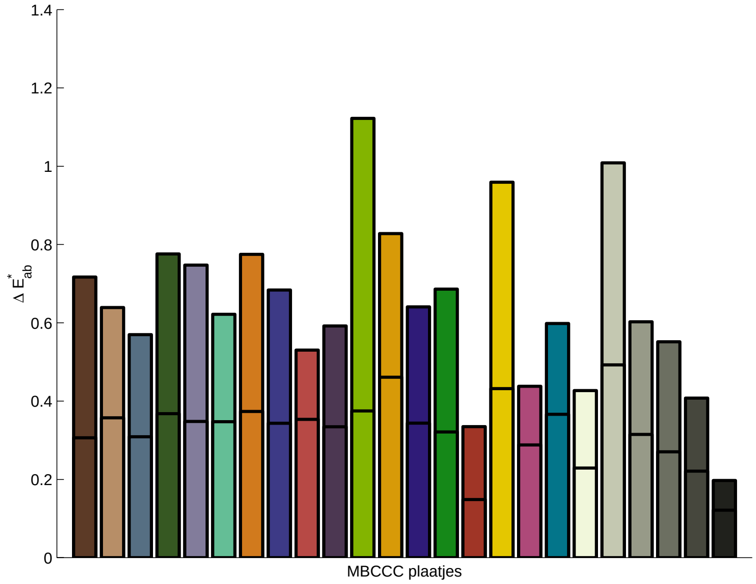

Figuur 5.10: De gemiddelde en maximale ΔE^*_{ab} fout voor elk MBCCC kleurplaatje over 10 metingen uitgevoerd onder hetzelfde kalibratieprofiel. De kleuren van de balken van deze en volgende figuren komen min of meer overeen met de kleuren van de plaatjes of voorwerpen die ze representeren.

het beeldvormingssysteem is de transformatie van RGB naar $sRGB$ $\Phi_{RGB\rightarrow sRGB,m}$. De nauwkeurigheid kan niet bepaald worden met dezelfde kleuren als deze gebruikt tijdens de kalibratie, i.e. de MBCCC plaatjes. In de plaats daarvan werd een testset van 27 voorwerpen gekozen: 15 plastieken en papieren plaatjes van allerlei kleuren, en 12 in vivo huidgebieden (blanke huid, bruine huid, naevi, etc. ...). Al deze voorwerpen werden zowel met de SPM als met het beeldvormingssysteem opgemeten. In het geval van het beeldvormingssysteem werden de meetwaarden bepaald door het spatiaal gemiddelde in de $R^*G^*B^*$ ruimte over een gebied ongeveer gelijk aan het meetgebied van de SPM te berekenen. Deze meetwaarden werden vervolgens getransformeerd naar de CIE $L^*a^*b^*$ kleurenruimte via de $sRGB$ kleurenruimte d.m.v. $\Phi_{RGB\rightarrow sRGB,m}$. In het totaal werden 15 polynomiale transformaties $\Phi_{RGB\rightarrow sRGB,m}$ getest: 5 met 3,6,8,9 en 11 termen, telkens op drie verschillende manieren berekend (LLSQ en niet-lineaire minimalisatie van de gemiddelde en maximale ΔE^*_{ab} fout), zie ook paragraaf 5.1.3. Omdat we veronderstellen dat de nauwkeurigheid veel lager zal liggen dan de precisie volstaat het om één meting van de testset uit te voeren.

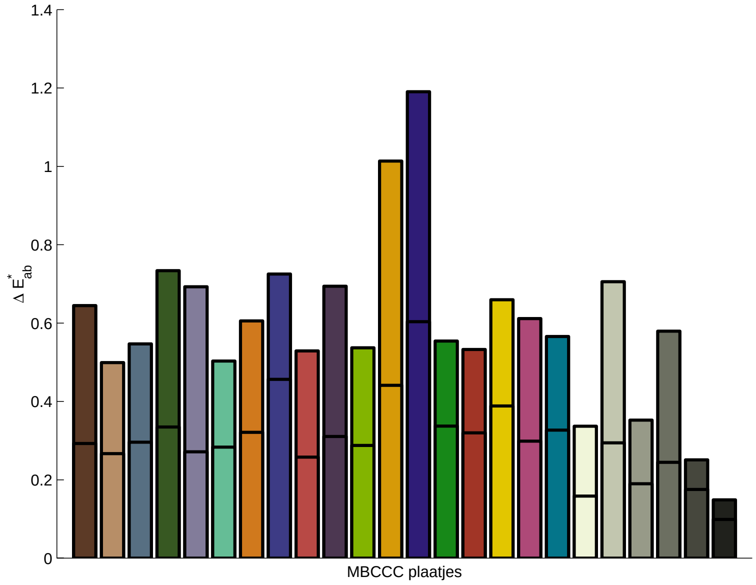

Figuur 5.11: De gemiddelde en maximale ΔE^*_{ab} fout voor elk MBCCC kleurplaatje over 9 metingen uitgevoerd onder verschillende kalibratieprofielen.

Fig. 5.12 toont de resultaten van de verschillende transformaties op de MBCCC plaatjes. Zoals verwacht worden de prestaties beter met het stijgend aantal termen van de polynomen, en doen de niet-lineair geoptimaliseerde transformaties het over het algemeen beter dan hun equivalente LLSQ versies. Deze resultaten hebben echter niets te maken met de werkelijke prestaties van de transformaties, ze dienen louter als controle voor hun correcte berekening.

Fig. 5.13 toont de resultaten van de verschillende transformaties op de testset van 15 plastieken en papieren plaatjes en 15 in vivo huidgebieden. Hieruit blijkt dat de eenvoudige lineaire LLSQ en gemiddelde ΔE^*_{ab} fout geoptimaliseerde transformaties de beste resultaten geven, met $\langle \Delta E^*_{ab} \rangle = 6.21$ en 6.77, en $\max(\Delta E^*_{ab}) = 13.31$ en 13.12 respectievelijk. Uiteindelijk wordt de LLSQ oplossing verkozen boven zijn niet-lineair geoptimaliseerde soortgenoot gezien zijn veel eenvoudigere en snellere berekening. Dit opmerkelijk resultaat is heel waarschijnlijk het gevolg van het beperkt aantal plaatjes die gebruikt werden om de transformaties te berekenen, zodat de bron- en doelkleurenruimtes eigenlijk zeer ijl bemonsterd worden. Dit heeft weinig consequenties voor de lineaire transformaties omdat die zeer goede veralgemenende eigenschappen hebben, maar kan leiden tot oscillerend gedrag in de ruimte

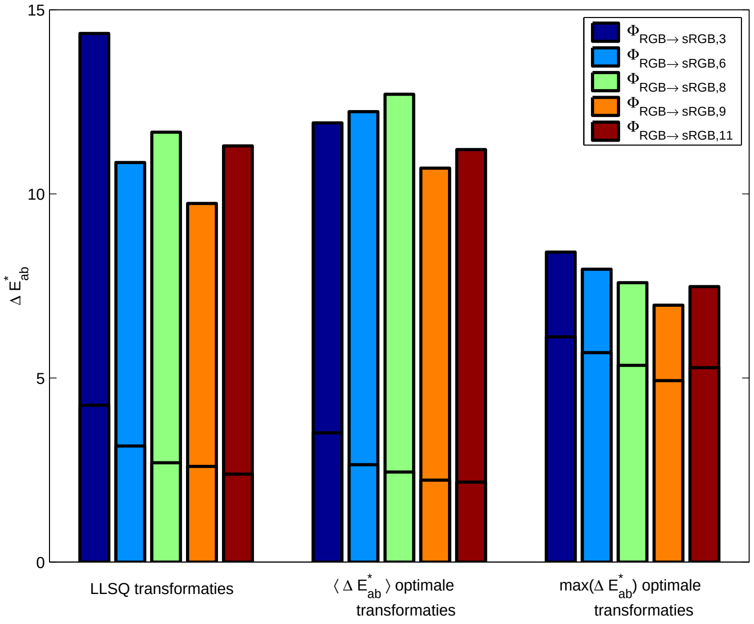

Figuur 5.12: De gemiddelde en maximale ΔE^*_{ab} fout van al de MBCCC plaatjes t.o.v. SPM metingen, voor alle LLSQ, gemiddelde en maximale ΔE^*_{ab} geoptimaliseerde transformaties $\Phi_{RGB \to sRGB,m}, m = 3, 6, 8, 9, 11$.

tussen de monsters voor de hogere-orde transformaties. Een belangrijke conclusie is ook dat de fouten voor de 12 in vivo huidgebieden van dezelfde orde zijn als voor de 15 ‘synthetische’ plaatjes, zie fig 5.14.

5.4 Conclusies

De kalibratie en de beeldopname van het beeldvormingssysteem, werden in detail doorgenomen. De kalibratie bestaat uit twee onderdelen: het bepalen van een set van optimale instellingen van het beeldvormingssysteem en het bepalen van de transformatie van de RGB bronkleurenruimte naar de $sRGB$ doelkleurenruimte. Al deze informatie wordt in een zogenaamd kalibratieprofiel opgeslagen, en zo’n profiel blijft lange tijd geldig. Om een beeld op te nemen moet het profiel eerst nagekeken worden, en eventueel lichtjes aangepast. Hierna kan men voor een beperkte periode, typisch 15 minuten, vrij gekalibreerde beelden opnemen. Opgenomen beelden worden getransformeerd naar de $sR^*G^*B^*$ ruimte, wat toelaat om ze direct weer te geven op het scherm of ze in een be-

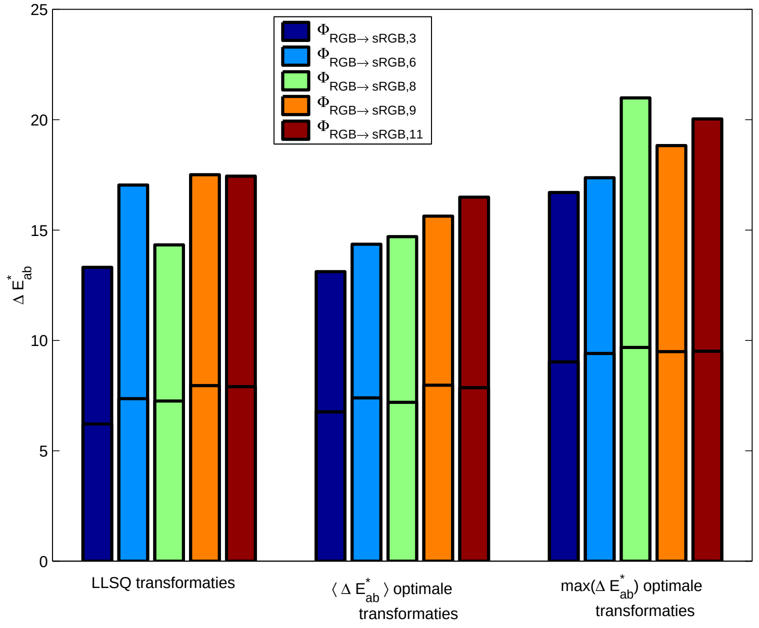

Figuur 5.13: De gemiddelde en maximale ΔE^*_{ab} fout van de testset van 15 plastieken en papieren plaatjes (links) en 12 in vivo huidgebieden (rechts) t.o.v. hun SPM metingen, voor alle LLSQ, gemiddelde en maximale ΔE^*_{ab} geoptimaliseerde transformaties $\Phi_{RGB \rightarrow sRGB,m}, m = 3, 6, 8, 9, 11$.

stand op te slaan. Doordat de *sRGB* ruimte een gekende relatie heeft met de CIE colorimetrische ruimtes beschikt men ook direct over een raamwerk voor beeldverwerking gebaseerd op menselijke visie. Het gebruik van gestandaardiseerde kleurenruimtes zou moeten leiden tot een breder toepassingsgebied voor ontwikkelde beeldverwerkingsalgoritmes, alsook tot de mogelijkheid voor externe validatie ervan.

De precisie en de nauwkeurigheid van het beeldvormingssysteem werden bepaald. De precisie bleek zeer goed, met het verschil tussen een individuele meting en het gemiddelde van een set van metingen maximaal 1.2 ΔE^*_{ab} eenheden. Het gemiddeld verschil is echter veel kleiner, 0.34 ΔE^*_{ab} eenheden. De nauwkeurigheid van het beeldvormingssysteem hangt vooral af van de transformatie tussen de *RGB* en *sRGB* kleurenruimtes. Het werd bepaald aan de hand van een testset van zowel plastieken en papieren voorwerpen als in vivo huidgebieden. Verschillende polynomiale transformaties, 15 in totaal, werden uitgetest, en het resultaat is dat de simpele lineaire kleinste-kwadraten transformatie de beste resultaten geeft met $\langle \Delta E^*_{ab} \rangle = 6.21$ en $\Delta E^*_{ab} < 13.31$. De precieze

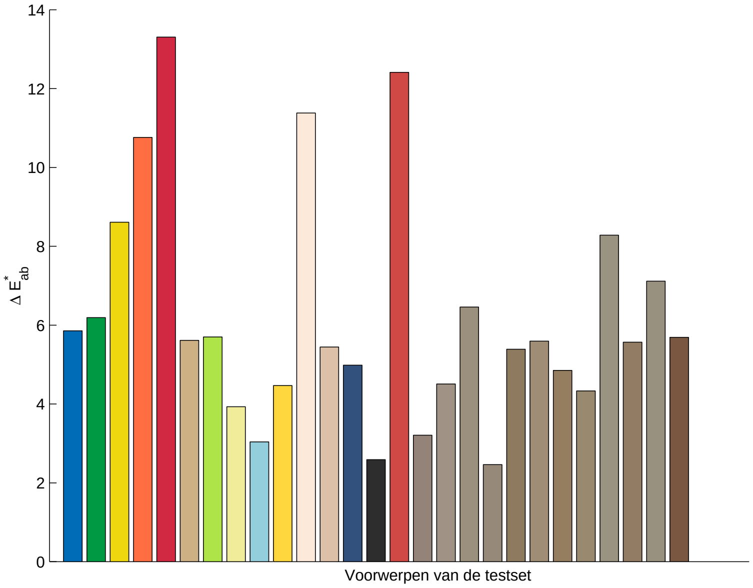

Figuur 5.14: De ΔE^*_{ab} fout van elk voorwerp van de testset van 15 plastieken en papieren plaatjes en 12 in vivo huidgebieden t.o.v. hun SPM metingen voor de lineaire LLSQ transformatie.

betekenis van deze resultaten voor het stellen van een dermatologische diagnose is echter niet bekend, en is dus iets wat in de toekomst moet onderzocht worden.

Het werk dat in dit hoofdstuk werd voorgesteld gaf aanleiding tot verscheidene artikels en abstracts, [47, 48, 49, 50]. Het vormt tevens het onderwerp van een artikel in een internationaal tijdschrift, [51], en wekte interesse op bij een privé-bedrijf.

Hoofdstuk 6

Het dermatologisch werkstation

Het dermatologisch werkstation voegt 3 componenten toe aan het beeldvormingssysteem teneinde het om te vormen tot een bruikbaar klinisch toestel: een patiënt- en beeldendatabank, een toepassing voor het gebruik van die databank, en een uitbreidbaar software-object dat toelaat om opgenomen beelden te bekijken en manipuleren. Het tot stand komen van de componenten was een tijdrovende bezigheid, en was slechts mogelijk d.m.v. een constante coöperatie met de eindgebruikers, i.e. de dermatologen. Het resultaat is verre van af, en moet eerder gezien worden als een demonstratie van de mogelijkheden van het beeldvormingssysteem, i.e. een 'proof of concept'.

6.1 De patiënten- en beeldendatabank

Zowel de grafische gebruikersomgeving (GUI) van de databanktoepassing als de structuur van de patïenten- en beeldendatabank weerspiegelen de manier waarop de dermatoloog werkt tijdens de opvolging van patïenten met een verhoogd risico op melanoom. We stellen hiervoor een soort entiteitenboomstructuur voor die werd opgesteld in samenwerking met de dermatologen, zie fig. 6.1. Dit vrij 'verticale' model laat weinig ruimte toe voor een alternatieve werkwijze, maar vermindert ook sterk de kans op fouten en inconsistenties. Merk op dat de databankstructuur, als *implementatie* van de entiteitenboomstructuur om praktische redenen, buiten vele overeenkomsten ook enkele afwijkingen van die structuur vertoont. Er werd ook rekening gehouden met de mogelijkheid om retrospectieve studies uit te voeren op de data ('data mining'), b.v. voor epidemiologische toepassingen. Hiertoe werd het gebruik van keuzelijsten veralgemeend, wat het aantal achteraf moeilijk te doorzoeken zogenaamde 'vrije tekstvelden' tot een minimum beperkt.

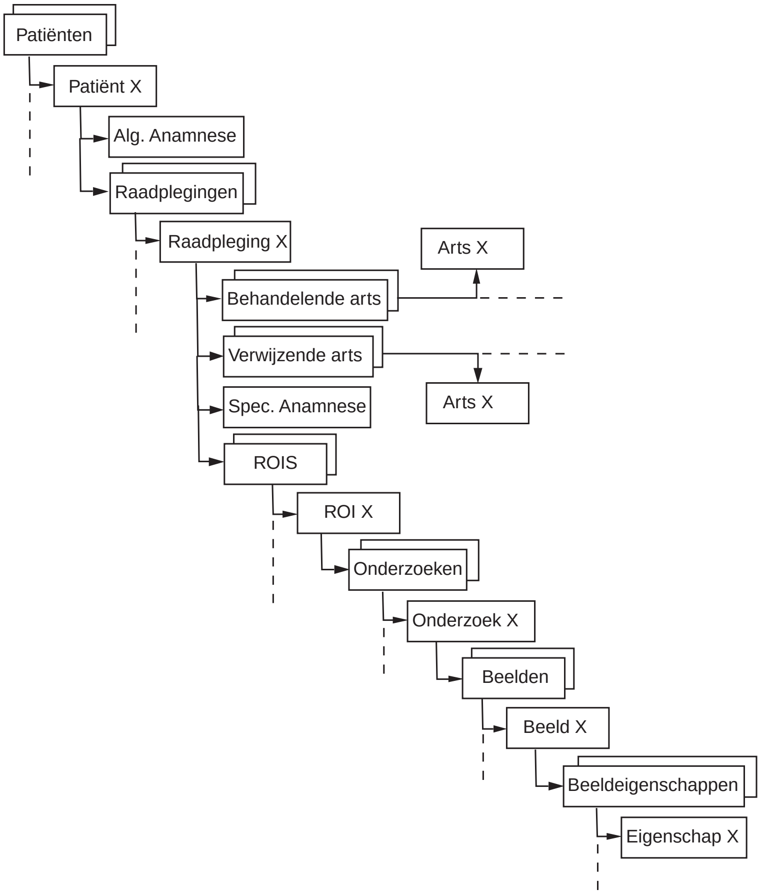

Figuur 6.1: Entiteitenboomstructuur waarop zowel de GUI van de databanktoepassing als de databankstructuur gebaseerd zijn.

6.2 De databanktoepassing

De databanktoepassing werd ontwikkeld in VB en maakt gebruik van 'ActiveX data objects' (ADO). Deze ADO bezitten een standaard objectenmodel, ongeacht het type van databank dat gebruikt wordt (deze moet wel een aangepast ‘OLE DB’ stuurprogramma bezitten). Alle zoekopdrachten zijn in SQL (‘structured query language’) geschreven. De toepassing maakt gebruik van een zogenaamde ‘multiple document interface’ (MDI), i.e. het fungeert als beheerder van een ganse reeks vensters, elk met hun specifieke rol.

Teneinde de hoeveelheid te schrijven code zoveel mogelijk te beperken werd een standaard datadialoogvenster ontworpen dat gebruik maakt van gemeenschappelijke ‘eventhandlers’. Deze eventhandlers zorgen voor het afwerken van al de acties die de gebruiker vanuit het datadialoogvenster kan starten, b.v. opzoeken, toevoegen en wijzigen van gegevens. Verder werd een eigen versie van de VB ‘data bound controls’ geschreven (zonder de vele bugs en de slechte performantie). Deze datagebonden GUI-elementen, e.g. tekstvensters, keuzelijsten, etc. . . . , kunnen aan een datadialoogvenster worden toegevoegd, waarna de gemeenschappelijke eventhandlers automatisch zorgen voor de overdracht van gegevens van en naar de databank. De eventhandlers zullen ook de zichtbaarheid en functionaliteit van de GUI-elementen, datagebonden of ongebonden, beheren in functie van de operationele mode waarin het datadialoogvenster zich bevindt: ‘bekijken’, ‘wijzigen’, ‘opzoeken’ of ‘toevoegen’.

De databanktoepassing herkent de gebruiker door zijn gebruikersnaam, en kan zodoende artsen en dermatologen herkennen. Enkel herkende personen kunnen raadplegingen aan de databank toevoegen, en eens toegevoegd kan alleen de persoon die een raadpleging heeft aangemaakt, i.e. de behandelende arts, gegevens van deze raadpleging nog wijzigen. De behandelende arts kan wel collega’s toevoegen aan de lijst van behandelende artsen, en zodoende deze ook de toelating geven om de gegevens van een raadpleging te wijzigen.

De databanktoepassing kan ook afdrukbare rapporten genereren, in MS Word of HTML (‘Hypertext Markup Laguage’) formaat. Zodoende is de compatibiliteit met de bestaande papieren patiëntenbestanden gegarandeerd. We lopen nu even snel door de belangrijkste vensters van de databanktoepassing.

6.2.1 Het hoofdvenster

Dit venster geeft een compacte weergave van de gegevens van één of meer patiënten weer d.m.v. van een boomstructuur gelijkaardig aan de entiteitenboomstructuur (zie fig. 6.2). Bijna alle mogelijke acties van de databanktoepassing, b.v. zoeken of toevoegen van gegevens, worden vanuit dit venster opgestart d.m.v. contextgevoelige menu's.

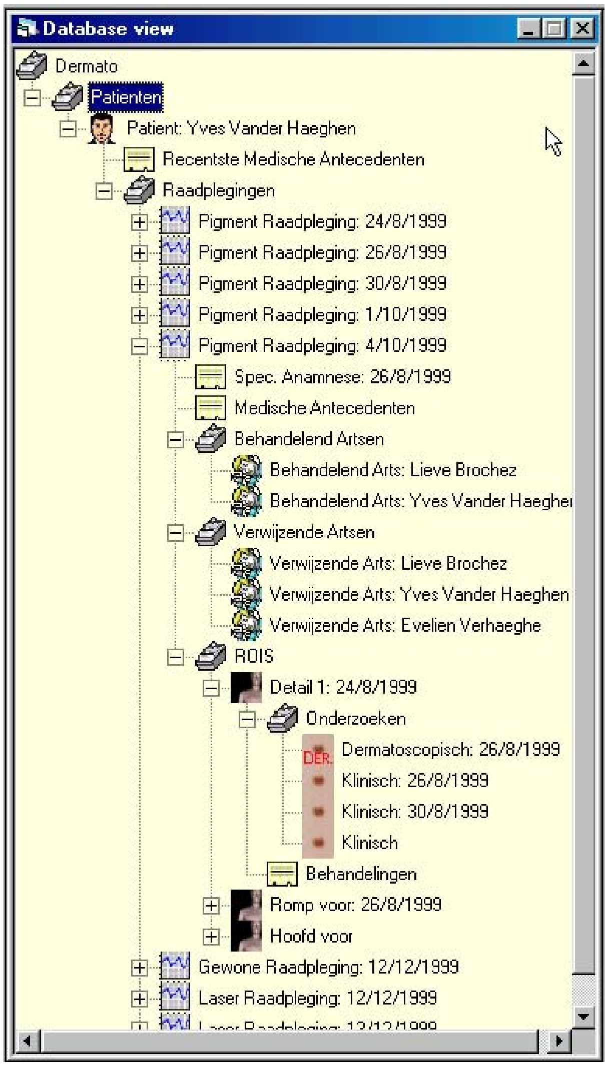

- Dermato
  - Patienten
    - Patient: Yves Vander Haeghen
      - Recentste Medische Antecedenten
      - Raadplegingen
        - Pigment Raadpleging: 24/8/1999
        - Pigment Raadpleging: 26/8/1999
        - Pigment Raadpleging: 30/8/1999
        - Pigment Raadpleging: 1/10/1999
        - Pigment Raadpleging: 4/10/1999
          - Spec. Anamnese: 26/8/1999
          - Medische Antecedenten
          - Behandelend Artsen
            - Behandelend Arts: Lieve Brochez
            - Behandelend Arts: Yves Vander Haeghe
          - Verwijzende Artsen
            - Verwijzende Arts: Lieve Brochez
            - Verwijzende Arts: Yves Vander Haeghen
            - Verwijzende Arts: Evelien Verhaeghe
          - ROIS
            - Detail 1: 24/8/1999
              - Onderzoeken
                - Dermatoscopisch: 26/8/1999
                - Klinisch: 26/8/1999
                - Klinisch: 30/8/1999
                - Klinisch
              - Behandelingen
            - Romp voor: 26/8/1999
            - Hoofd voor
        - Gewone Raadpleging: 12/12/1999
        - Laser Raadpleging: 12/12/1999

Figuur 6.2: Het hoofdvenster van de databanktoepassing.

6.2.2 De datadialoogvensters

Alle datadialoogvensters zijn afgeleid van hetzelfde basisvenster dat gebruik maakt van de gemeenschappelijke eventhandlers. Dit basisvenster bevat een reeks standaard GUI-elementen dat gesupplementeerd wordt met de nodige datagebonden GUI-elementen voor de weergave van gegevens uit de databank, zie fig. 6.3. Het gebruik van de gemeenschappelijke eventhandlers en het basisvenster zorgt voor een uniforme werking en een uniform uitzicht van de datadialoogvensters voor de gehele toepassing.

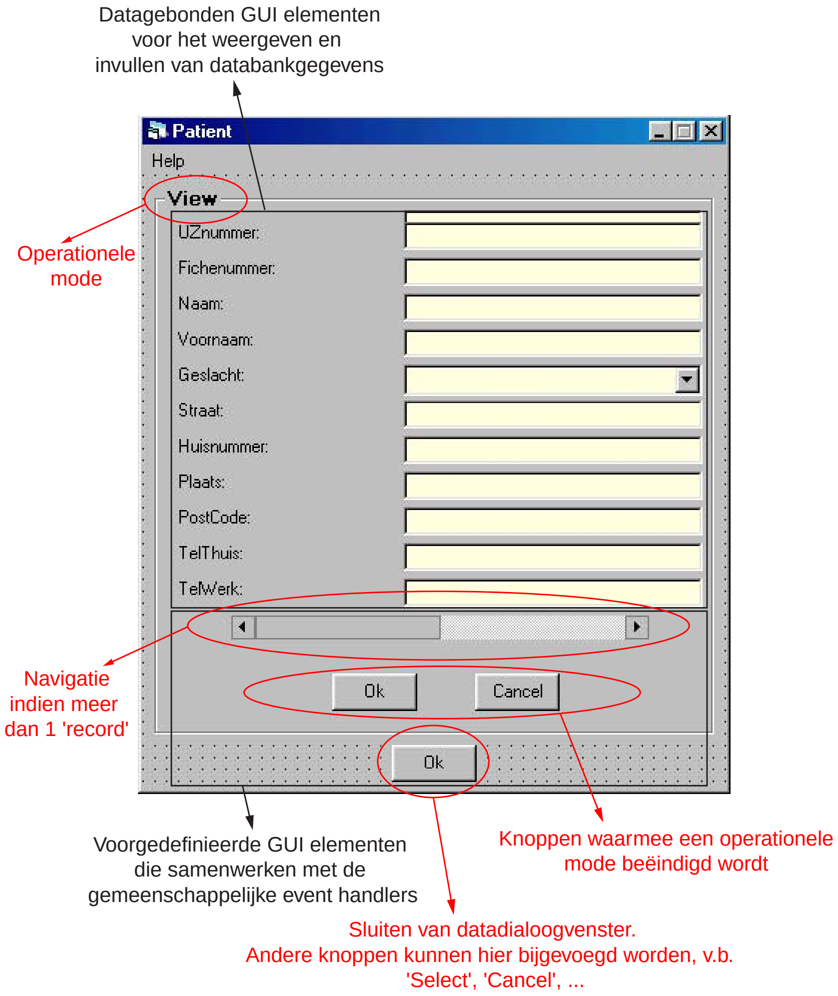

Datagebonden GUI elementen voor het weergeven en invullen van databankgegevens

Operationele mode

Navigatie indien meer dan 1 'record'

Voorgedefinieerde GUI elementen die samenwerken met de gemeenschappelijke event handlers

Knoppen waarmee een operationele mode beëindigd wordt

Sluiten van datadialoogvenster. Andere knoppen kunnen hier bijgevoegd worden, v.b. 'Select', 'Cancel', ...

Figuur 6.3: Voorbeeld van een datadialoogvenster. Merk op dat tijdens de werking bepaalde GUI-elementen onzichtbaar gemaakt worden, en dat hun labels kunnen veranderen.

De beeldopnameprocedure wordt indien nodig opgestart vanuit een datadialoogvenster tijdens het aanmaken van een nieuw onderzoek voor een bepaald interessegebied (ROI voor 'region of intrest').

6.2.3 Het 3D localisatievenster en het beeldoverzichtsvenster

Deze twee vensters zijn beide gesynchroniseerd met het hoofdvenster, en geven extra informatie over actieve ROI(s) weer. Het 3D localisatievenster geeft de exacte locatie van de ROI of ROIs op het lichaam weer d.m.v. een 3D pop die kan rondgedraaid worden in 8 stappen. Dit venster wordt tevens gebruikt bij de aanmaak van een ROI om zijn locatie aan te duiden. Hiertoe verschijnt dan ook een boven- of onderaanzicht van de pop. Het beeldoverzichtsvenster toont verkleinde versies van de reeds opgenomen beelden van de ROI of ROIs.

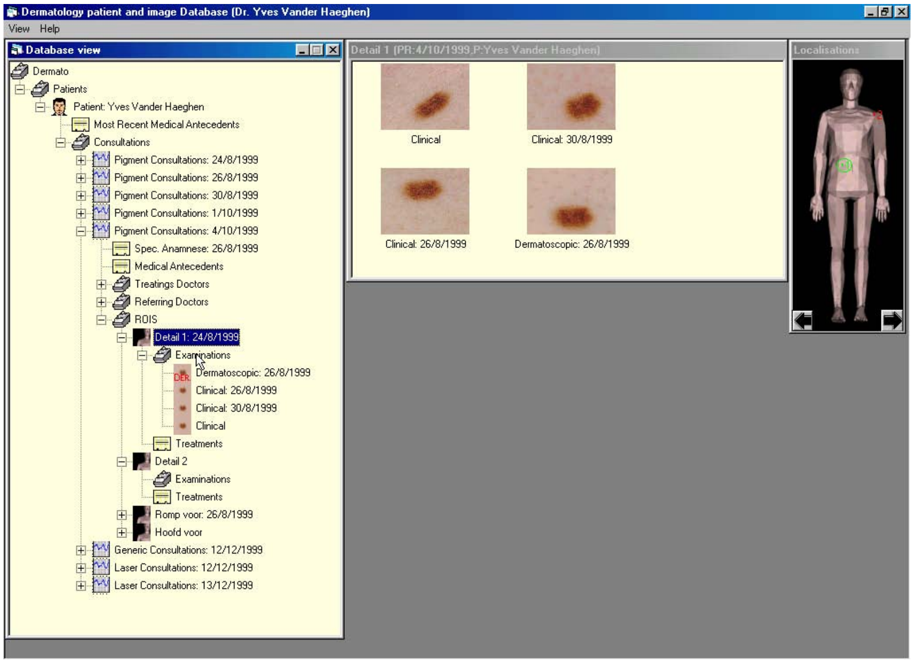

- Dermato
  - Patients
    - Patient: Yves Vander Haeghen
      - Most Recent Medical Antecedents
      - Consultations
        - Pigment Consultations: 24/8/1999
        - Pigment Consultations: 26/8/1999
        - Pigment Consultations: 30/8/1999
        - Pigment Consultations: 1/10/1999
        - Pigment Consultations: 4/10/1999
          - Spec. Anamnese: 26/8/1999
          - Medical Antecedents
          - Treatings Doctors
          - Referring Doctors
          - ROIS
            - Detail 1: 24/8/1999
              - Examinations
                - Dermatoscopic: 26/8/1999
                - Clinical: 26/8/1999
                - Clinical: 30/8/1999
                - Clinical
              - Treatments
            - Detail 2
              - Examinations
              - Treatments
            - Romp voor: 26/8/1999
            - Hoofd voor
        - Generic Consultations: 12/12/1999
        - Laser Consultations: 12/12/1999
        - Laser Consultations: 13/12/1999

Figuur 6.4: Voorbeeld van de synchronisatie tussen het hoofdvenster, het 3D localisatievenster en het beeldoverzichtsvenster.

6.3 Het beeldobject

Het beeldobject laat toe om eenvoudige manipulaties uit te voeren op de beelden, b.v. zoomen. Het is geïmplementeerd als een object dat moet gecreëerd worden vanuit andere applicaties, en is gemakkelijk uitbreidbaar, b.v. met beeldverwerkingsroutines. Het maakt gebruik van de Leadtools Medical Express Imaging Toolkit[1]. De standaard mogelijkheden van het beeldobject zijn:

Zoomen In- en uitzoomen met verschillende algoritmes: dichtste buur, lineaire en bikubische interpolatie.

Weergeven van pixelwaarden In de veronderstelling dat een 24-bit $sR^*G^*B^*$ beeld is ingeladen kan het beeldobject gemiddelde $sR^*G^*B^*$,$sRGB$, CIE XYZ, CIE xyY en CIE $L^*a^*b^*$ kleurtripletten weergeven over een $2n+1$ op $2n+1$ venster rond de muiscursor. n is een natuurlijk getal dat met de '-' en '+' toetsen kan ingesteld worden.

Annotaties Annotaties zijn grafische objecten zoals tekst, lijnen, rechthoeken, polygonen, etc. ...die bovenop het beeld worden getekend. Annotaties zullen intensief gebruikt worden voor beeldverwerking.

Histogram Berekent en geeft een $sR^*G^*B^*$ histogram van een beeld weer.

6.4 Beeldverwerking

Beeldverwerking zal een belangrijke rol spelen wanneer men het dermatologisch werkstation wil uitbreiden met meer gesofistikeerde toepassingen, v.b. om diagnostisch belangrijke eigenschappen van huidletsels op te meten en te gebruiken voor classificatie en automatische diagnose. Zoals reeds een paar keer vermeld kan men hiervoor steunen op de kennis van de kleurenruimte waarin de beelden gedefinieerd zijn en daaruit voortvloeiend de beschikbaarheid van een gefundeerde kleurenverschilmetriek. De toepasbaarheid van beeldverwerking gebaseerd op een standaardkleurenruimte is ook veel groter doordat men niet 'vastzit' aan een bepaald beeldvormingssysteem, men creëert als het ware toestel-onafhankelijke beeldverwerking. Om sommige van deze voordelen te demonstreren zullen we een eenvoudig segmentatiealgoritme voor huidletsels voorstellen en vergelijken met een manuele aflijning door dermatologen.

---

[1] LEAD Technologies, Inc., 900 Baxter Street, Charlotte, NC 28204

6.4.1 Segmentatie van huidletsels

Voordat het mogelijk is om gegevens uit een huidletsel te extraheren is het nodig dit letsel af te lijnen. Huidletsels vertonen echter een grote variatie in vorm en kleur, wat samen met de aanwezigheid van haar een robuuste automatische aflijning niet gemakkelijk maakt. Verscheidene publicaties, e.g. [52, 13, 53, 54, 55, 56], zijn reeds verschenen over dit onderwerp. Deze methodes werken meestal in een RGB kleurenruimte. Sommige maken gebruik van de CIE $L^*a^*b^*$ kleurenruimte, maar het is onduidelijk hoe een correcte transformatie naar deze ruimte kon opgesteld worden zonder de kennis van de primaire stimuli van de bronruimte. Een interessant algoritme is [57], een interactieve maar vrij reproduceerbare segmentatiemethode. Spijtig genoeg kan men bovenstaande algoritmes grosso modo als 'toestel-afhankelijk' bestempelen, en het is dan ook onze persoonlijk overtuiging dat nog betere en meer algemene resultaten zouden kunnen bekomen worden mits een meer 'colorimetrische' aanpak. In ieder geval is het hier niet de bedoeling om het probleem van huidletselsegmentatie op te lossen, maar enkel te demonstreren dat een eenvoudige methode inwerkend op colorimetrische data reeds behoorlijke resultaten kan opleveren.

Het segmentatiealgoritme

Het segmentatiealgoritme start met een ruwe manuele aflijning door de dermatoloog. Deze taak is zeer eenvoudig voor deze laatste, maar vrij ingewikkeld voor een segmentatiealgoritme. Hierna zal het algoritme overnemen en de gedetailleerde aflijning, die manueel langdradig zou zijn, uitvoeren.

De contour die gebruikt wordt om de aflijning van een huidletsel uit te voeren bestaat uit een set van vertices op een afstand, de vertexresolutie, van elkaar. De vertices kunnen zich enkel radiaal voortbewegen. Als tijdens die beweging de afstand tussen de vertices teveel afwijkt van de vertex resolutie zullen waar nodig vertices bijgevoegd of weggelaten worden, zie fig. 6.5. Dit herbemonsteringsschema van de contour is gelijkaardig aan dat beschreven in [58].

Het basisidee van het algoritme is dat een letsel omringd is door gewone huid. De opeenvolgende stappen zijn:

1. Vraag de gebruiker een ruwe contour van het huidletsel te tekenen door de representatieve gebieden van normale huid rond het letsel aan te klikken;

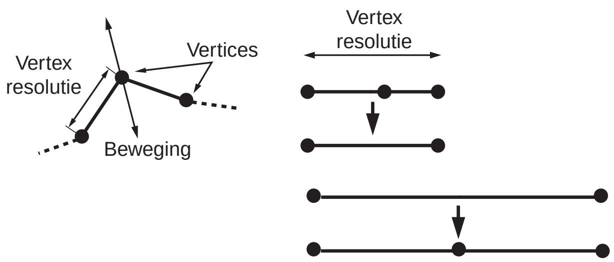

Figuur 6.5: Contour bestaande uit een set van vertices, en het herbemonsteringsschema.

2. Bereken de gemiddelde kleur rond elke vertex van de ruwe contour als maat voor de lokale normale huid, en sla die op;
3. Herbemonster de contour volgens de gevraagde vertexresolutie;
4. Bereken het kleurverschil in ΔE^*_{ab} eenheden van het gebied rond elke vertex met de eerder berekende lokale normale huid van die vertex;
5. Beweeg de vertex in de radiaal inwaartse richting indien het net berekende kleurverschil kleiner is dan een bepaalde bewegingsdrempel;
6. Stop indien geen enkele vertex bewogen heeft, herneem vanaf stap 3 indien dit wel zo is.

Dit semi-automatische algoritme is uiterst eenvoudig en heeft slechts 2 parameters: de vertexresolutie die op 12 pixels is ingesteld en de bewegingsdrempel die op 8 ΔE^*_{ab} eenheden is ingesteld.

Experimenten

Omdat er geen algemene consensus is tussen dermatologen over de ligging van een contour, zullen we ons beperken tot het bepalen van de reproduceerbaarheid van de semi-automatische segmentatie versus een manuele aflijning. Hiertoe werd een testset van 30 beelden van huidletsels voorgelegd aan 4 dermatologen (waarnemers). De combinatie van een waarnemer en een beeld wordt een geval genoemd. Elk beeld werd tweemaal voorgelegd aan elke waarnemer in een willekeurige volgorde, en telkens werd zowel een manuele als semi-automatische aflijning uitgevoerd. De moeilijkheidsgraad van de manuele segmentatie (1 = zeer moeilijk - 5 = zeer gemakkelijk) en de kwaliteit van de semi-automatische aflijning (1 = volledig verkeerd - 5 = perfect) werd telkens door de waarnemer gescoord. Twee beeldeigenschappen die potentieel een rol kunnen spelen in de diagnose van huidletsels werden berekend voor elk gesegmenteerd beeld: het oppervlak van het letsel in pixels, en de gemiddelde $CIEL^*a^*b^*$ kleur van het letsel. We noteren deze eigenschappen voor segmentatiemethode $i = 1(\text{manueel}), 2(\text{semi-automatisch})$, beeld $j = 1, \ldots, 30$ en waarnemer $k = 1, \ldots, 4$, meting $l = 1, 2$ respectievelijk als A_{ijkl} en $(L^*_{ijkl}, a^*_{ijkl}, b^*_{ijkl})$.

Als maat r_{ijk} voor de reproduceerbaarheid voor het bepalen van het letselopppervlak van methode i voor een beeld j en een waarnemer k stellen we de standaard deviatie gedeeld door het gemiddelde letseloppervlak voor:

$$\begin{aligned}\langle A_{ijk}\rangle =& \frac{\sum_{l=1}^{2} A_{ijkl}}{2},\\ r_{ijk} =& \frac{\sqrt{\frac{\sum_{l=1}^{2}(A_{ijkl}-\langle A_{ijk}\rangle)^2}{2}}}{\langle A_{ijk}\rangle}.\end{aligned} \tag{6.1}$$

Voor de gemiddelde $CIEL^*a^*b^*$ kleur van een letsel stellen we volgende formules voor als maat voor de reproduceerbaarheid $\langle \Delta E^*_{ab,ijk}\rangle$ van methode i voor een beeld j en een waarnemer k:

$$\begin{aligned}(\langle L^*_{ijk}\rangle, \langle a^*_{ijk}\rangle, \langle b^*_{ijk}\rangle) &= \frac{\sum_{l=1}^{2}(L^*_{ijkl}, a^*_{ijkl}, b^*_{ijkl})}{2},\\ \Delta E^*_{ab,ijkl} &= \Big((L^*_{ijkl} - \langle L^*_{ijk}\rangle)^2 + (a^*_{ijkl} - \langle a^*_{ijk}\rangle)^2\\ &\quad + (b^*_{ijkl} - \langle b^*_{ijk}\rangle)^2\Big)^{1/2},\\ \langle \Delta E^*_{ab,ijk}\rangle &= \sum_{l=1}^{2} \frac{\Delta E^*_{ab,ijkl}}{2}.\end{aligned} \tag{6.2}$$

Vergelijkingen (6.1) en (6.2) kunnen gebruikt worden om de reproduceerbaarheid van beide segmentatiemethodes te vergelijken *voor één waarnemer en één beeld*, i.e. per geval. Door uitmiddelen over alle gevallen kan men de invloed van zaken die aan onze experimente controle ontsnappen, de beelden en de waarnmeners, verminderen. Doordat het niet altijd dezelfde persoon zal zijn die de segmentatie zal uitvoeren is het echter ook nodig de totale reproduceerbaarheid voor het letseloppervlak r_{ij} en de letselkleur $\langle \Delta E^*_{ab,ij}\rangle$ van beide segmentatiemethodes te vergelijken. Hiervoor worden vergelijkingen (6.1) en (6.2) uitgebreid door tevens uit te middelen over de waarnemers:

$$\begin{aligned}\langle A_{ij}\rangle =&\frac{\sum_{k=1}^{4}\sum_{l=1}^{2}A_{ijkl}}{8},\\ r_{ij} =&\frac{\sqrt{\frac{\sum_{k=1}^{4}\sum_{l=1}^{2}(A_{ijkl}-\langle A_{ij}\rangle)^2}{8}}}{\langle A_{ij}\rangle},\end{aligned}\tag{6.3}$$

en

$$\begin{aligned}(\langle L^*_{ij}\rangle,\langle a^*_{ij}\rangle,\langle b^*_{ij}\rangle) =& \frac{\sum_{k=1}^{4}\sum_{l=1}^{2}(L^*_{ijkl},a^*_{ijkl},b^*_{ijkl})}{8},\\ \Delta E^*_{ab,ijkl} =&\Big((L^*_{ijkl}-\langle L^*_{ij}\rangle)^2+(a^*_{ijkl}-\langle a^*_{ij}\rangle)^2\\ &+(b^*_{ijkl}-\langle b^*_{ij}\rangle)^2\Big)^{1/2},\\ \langle\Delta E^*_{ab,ij}\rangle =& \sum_{k=1}^{4}\sum_{l=1}^{2}\frac{\Delta E^*_{ab,ijkl}}{8}.\end{aligned}\tag{6.4}$$

Resultaten en discussie

De histogrammen van de subjectieve scores van de segmentatie zijn te zien in fig. 6.6. Het lage aantal beelden waarvan de segmentatie als minder goed werd aanzien t.o.v. het aantal als moeilijk te segmenteren aanziene beelden toont aan dat de dermatologen relatief tevreden zijn over de resultaten. Een aantal van deze moeilijk te segmenteren beelden zijn te zien in fig. 6.7.

De resultaten voor de reproduceerbaarheid r_{ijk} en $\langle\Delta E^*_{ab,ijk}\rangle$ van methode i voor een beeld j en een waarnemer k vertonen een grote variabiliteit en zijn verre van normaal verdeeld. We beschikken echter over 120 gevallen (30 beelden en 4 waarnemers), zodat we kunnen stellen dat de gemiddelde reproduceerbaarheid per geval wel normaal verdeeld is (centrale limietstelling van statistische distributies). We kunnen bijgevolg gebruik maken van de t-test om te zien of de twee segmentatiemethodes een significant verschil in reproduceerbaarheid vertonen. De resultaten van de t-test zijn te zien in tabel 6.1, en geen enkele verbetering van de reproduceerbaarheid is dus te verwachten van de semi-automatische segmentatie t.o.v. een manuele segmentatie *als één en dezelfde waarnemer de segmentaties uitvoert op verschillende beelden van hetzelfde letsel.*

Ook de resultaten voor de totale reproduceerbaarheid r_{ij} en $\langle\Delta E^*_{ab,ij}\rangle$ van methode i voor een beeld j zijn verre van normaal verdeeld. Met

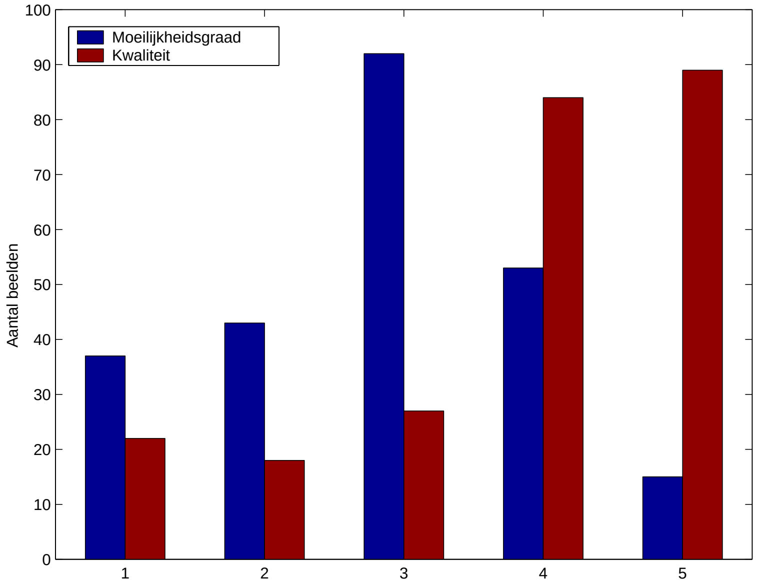

Figuur 6.6: Histogram van de subjectieve scores van alle beelden: moeilijkheidsgraad van de manuele segmentatie (1 = zeer moeilijk - 5 = zeer gemakkelijk) en de kwaliteit van de semi-automatische aflijning (1 = volledig verkeerd - 5 = perfect).

Beeld-eigenschap	**Gem. reprod.**		**Significant verschil? t-test, p=0.05**
	man.	**semi-aut.**	
Oppervlak	0.26	0.25	Nee
Kleur	3.2	3.1	Nee

Tabel 6.1: Gemiddelde reproduceerbaarheid per geval voor de manuele en semi-automatische segmentatie, en statistische significantie voor de t-test met $p = 0.05$.

slechts 30 verschillende beelden is het echter twijfelachtig of de centrale limietstelling toepasbaar is. We gebruiken dan ook de zogenaamde ‘matched pairs sign test’ , een vrij zwakke statistische test die minimale eisen aan de data stelt. Als een zwakke test een significant verschil vindt, dan is de kans dat deze echt aanwezig is echter zeer groot. De resultaten van de test zijn te vinden in tabel 6.2, en deze keer werd een significante verbetering van de totale reproduceerbaarheid voor de semi-automatische segmentatie gevonden. De semi-automatische segmentatie vermijdt dus voor een stuk de problemen die voorkomen wanneer verschillende waar-

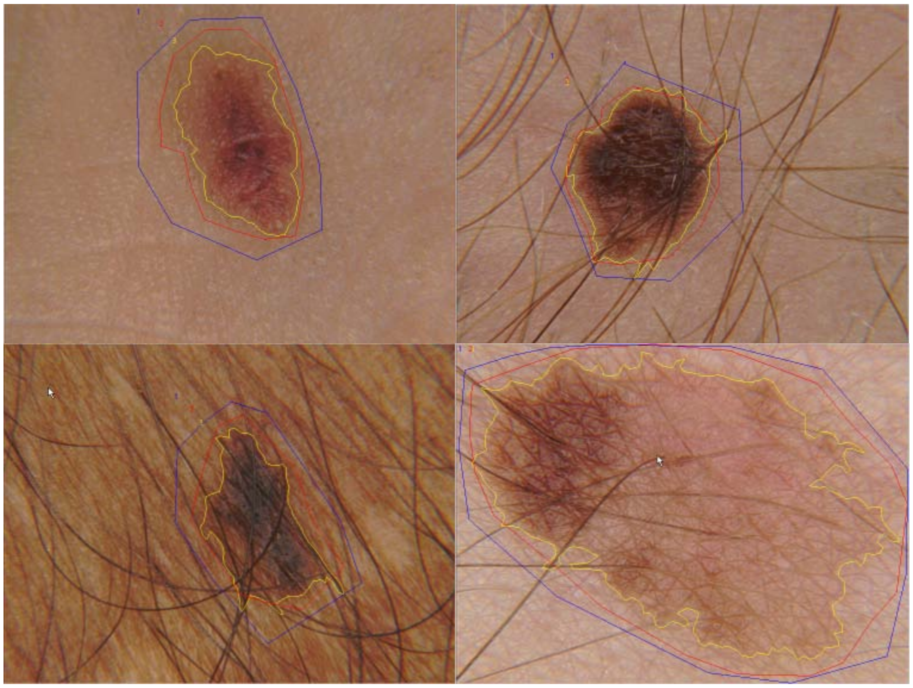

Figuur 6.7: Segmentatie van enkele moeilijke beelden. De manuele segmentatie is in rood, de ruwe startcontour in blauw en de semi-automatische segmentatie in geel. Merk op dat donkere haren nog steeds problemen geven.

nemers de aflijning uitvoeren.

Beeld-eigenschap	**Gem. reprod.**		**Aantal verbeterde beelden**	**Significant verschil? p=0.05**
	man.	**semi-aut.**		
Oppervlak	0.42	0.34	24/30	Ja
Kleur	7.6	6.3	26/30	Ja

Tabel 6.2: Gemiddelde totale reproduceerbaarheid per beeld voor de manuele en semi-automatische segmentatie, en statistische significantie voor de matched pairs sign-test met $p = 0.05$.

Een inspectie van de aflijningen, v.b. als in fig. 6.7, toont dat de meeste problemen het gevolg zijn van de aanwezigheid van donkere haren. Een mogelijke oplossing is de gebruiker de kans geven om de gevonden contour te verbeteren. Dit werd geprobeerd, maar was zeer arbeidsintensief door de vele vertices die soms moesten verplaatst worden. Het gebruik van zogenaamde ‘rational Gaussian curves’ als benadering voor een contour met veel minder controlepunten, [60], zou hierbij kunnen helpen.

6.5 Algemene discussie en conclusies

Het dermatologisch werkstation werd in de polikliniek van het universitair ziekenhuis getest voor het opvolgen van patiënten met een verhoogd risico op huidkanker. Ongeveer 100 beelden werden opgenomen en opgeslagen in de databank. Ondanks een constante verbetering van het werkstation tengevolge van suggesties van de dermatologen, blijft ons inziens een fundamenteel probleem het nut van het werkstation in de weg staan: een gebrek aan ondersteunende infrastructuur. Inderdaad, het invoeren van een volledig geïnformatiseerd systeem in een omgeving waar de meeste patiënteninformatie nog steeds op papieren fiches staat is gewoon niet realistisch. Dit is aan het veranderen, o.a. met het invoeren van het zogenaamde ‘order-communicatiesysteem’ in het ziekenhuis, maar de volledige omschakeling zal nog een hele poos op zich laten wachten. Het is bijgevolg beter het werkstation voorlopig verder te valideren aan de hand van kleinschalige projecten i.p.v. in de polikliniek.

Wat betreft de segmentatie van huidletsels kunnen we stellen dat behoorlijke resultaten werden behaald met een zeer eenvoudige methode door gebruik te maken van de colorimetrische aard van de beelden. De methode is tevens snel en eenvoudig in gebruik, maar is voor verbetering vatbaar.

Hoofdstuk 7

Conclusies

De eerste drie hoofdstukken van dit werk bestonden hoofdzakelijk uit achtergrondinformatie over dermatologie en colorimetrie. De meeste informatie was afkomstig uit externe bronnen, voorgesteld met een structuur aangepast aan het vervolg van het betoog.

In hoofdstuk 4 werd de opbouw van het beeldvormingssysteem besproken. Alhoewel veel informatie in dit hoofdstuk weerom uit externe bronnen afkomstig is, werden ook enkele kleine experimenten uitgevoerd. In ieder geval is het onze mening dat de verwezenlijkingen in dit hoofdstuk niet van wetenschappelijke maar eerder van technologische aard zijn: de integratie van heel verscheiden hard- en softwarecomponenten tot een volwaardig kleurenbeeldvormingssysteem.

De werking van het beeldvormingssysteem is het onderwerp van hoofdstuk 5. Hiertoe werd een eenvoudig empirisch model van het beeldvormingssysteem voorgesteld. Vertrekkend van dit model werden procedures voor zowel kalibratie als beeldopname uitgewerkt. Aan de hand van experimenten werden de precisie en nauwkeurigheid van colorimetrische metingen op opgenomen gekalibreerde beelden bepaald. De resultaten toonden aan dat de precisie van het beeldvormingssysteem vrij goed is, terwijl de nauwkeurigheid t.o.v. spectrofotometrische metingen matig is. Tevens werd de optimale polynomiale transformatie tussen de onbekende bronkleurenruimte en de gestandaardiseerde doelkleurenruimte bepaald. Het opmerkelijk resultaat hier was dat de eenvoudigste lineaire transformatie de beste resultaten geeft, gezien het beperkt aantal kleuren dat tijdens de kalibratie gebruikt wordt. Het werk dat in dit hoofdstuk werd voorgesteld gaf aanleiding tot verscheidene artikels en abstracts, [47, 48, 49, 50], alsook tot een artikel in een internationaal tijdschrift, [51]. Het wekte tevens interesse op bij een privé-bedrijf.

Hoofdstuk 6 was gewijd aan enkele extensies van het beeldvormingssysteem die tot doel hadden het om te vormen tot een praktisch bruikbaar dermatologisch werkstation voor de opvolging van patiënten met een verhoogde kans op huidkanker. Deze extensies bestonden uit een patiënten- en beeldendatabank, een databanktoepassing en een softwarecomponent om de opgenomen beelden te bekijken en te manipuleren. Verder werd gepoogd het nut van een colorimetrische aanpak van beeldverwerking te demonstreren door een eenvoudig algoritme voor de segmentatie van huidletsels voor te stellen en te testen. Dit werk is het onderwerp van een congresartikel [61].

Het invoeren van het werkstation in de polikliniek was voorlopig geen onverdeeld succes, mede door de grote technologische kloof met de bestaande infrastructuur. Deze situatie is snel aan het evolueren, maar voorlopig lijkt het beter het dermatologisch werkstation verder te valideren a.d.h. van kleinschalige projecten i.p.v. in de polikliniek.

Tenslotte merken we op dat de samenwerking met andere wetenschappers op de dienst dermatologie tevens geleid heeft tot het coauteurschap van een tweetal artikels in internationale tijdschriften, [62, 63].

Bibliography

[1] D. Gawkrodger, *Dermatology: An illustrated colour text.* Churchill Livingstone, second ed., 1997.

[2] L. Bleyen, D. D. Bacquer, K. Myny, L. Brochez, J. Naeyaert, and G. D. Backer, "Trends in mortality from cutaneous mailignant melanoma in Belgium," *International Journal of Epidemiology*, vol. 9, pp. 40–45, 1999.

[3] L. Brochez, J. Naeyaert, *et al.*, "Understanding the trends in melanoma incidence and mortality: where do we stand?," *European Journal on Cancer*, vol. 10, pp. 71–76, 2000.

[4] R. Friedman *et al.*, "Early detection of malignant melanoma: the role of physician examination and self-examination," *CA*, vol. 35, pp. 130–151, 1985.

[5] B. Cassileth *et al.*, "How well do physicians recognize melanoma and other problem lesions?," *J. Am. Acad. Dermatol.*, no. 14, pp. 555–560, 1986.

[6] C. Grin *et al.*, "Accuracy in the clinical diagnosis of malignant melanoma," *Arch. Dermatol.*, no. 126, pp. 763–766, 1990.

[7] W. Stolz *et al.*, "ABCD rule of dermatoscopy: a new practical method for early recognition of malignant melanoma," *European Journal of Dermatology*, vol. 4, no. 7, pp. 521–527, 1994.

[8] F. Nachbar *et al.*, "The ABCD rule of dermatoscopy," *Journal of the American Academy of Dermatology*, vol. 30, pp. 551–559, April 1994.

[9] A. Steiner, H. Pehamberger, and K. Wolff, "In vivo epiluminescence microscopy of pigmented skin lesions i. pattern analysis of

pigmented skin lesions," *Journal of the American Academy of Dermatology*, vol. 17, pp. 571–583, 1987.

[10] P. Hanrahan *et al.*, "Examination of the ability of people to identify early changes of melanoma in computer-altered pigmented skin lesions," *Arch. Dermatol.*, pp. 301–311, March 1997.

[11] J. L. Stone, R. L. Peterson, and J. E. Wolf, "Digital imaging techniques in dermatology," *Journal of the American Academy of Dermatology*, no. 5, part 1, pp. 913–917, 1990.

[12] N. Cascinelli *et al.*, "A possible tool for clinical diagnosis of melanoma: The computer," *Journal of the American Academy of Dermatology*, vol. 16, no. 2, Part 1, pp. 361–367, 1987.

[13] S. E. Umbaugh, *Computer vision in medicine: Color metrics and image segmentation methods for skin cancer diagnosis.* Ph.D., University of Missouri - Rolla, 1990.

[14] R. Kenet *et al.*, "Clinical diagnosis of pigmented lesions using digital epiluminescence microscopy," *Arch. of Dermatology*, vol. 129, pp. 157–174, february 1993.

[15] T. Schindewolf *et al.*, "Evaluation of different image acquisition techniques for a computer vision system in the diagnosis of malignant melanoma," *Journal of the American Academy of Dermatology*, vol. 31, no. 1, pp. 33–41, 1994.

[16] W. Stolz et al., "Improvement of monitoring of melanocytic skin lesions with the use of a computerized acquisition and surveillance with a skin surface microscopic television camera," *Journal of the American Academy of Dermatology*, vol. 35, no. 2, Part 1, pp. 202–207, 1996.

[17] M. Nischik *et al.*, "Analysis of skin erythema using true-color images," *IEEE Trans. On Medical Images*, vol. 16, no. 6, pp. 711–715, 1997.

[18] J. Taylor, "Color Imaging in Telemedicine," in *Color Imaging Conference: Color Science, Systems and Applications*, pp. 181–185, IS&T, SID,, 1995.

[19] R. Hunt, *The Reproduction of Colour.* Fountain Press, fifth edition ed., 1995.

[20] G. Wyszecki and W. Stiles, *Color Science: Concept and Methods, Quantitative Data and Formulae.* John Wiley & Sons, second edition ed., 1982.

[21] M. Fairchild, *Color Appearance models.* Addison-Wesley, 1998.

[22] E. Giorgianni and T. Madden, *Digital Color Management.* Addison-Wesley, 1998.

[23] G. Holst, *CCD arrays, Cameras and Displays.* SPIE Optical Engineering Press, 1996.

[24] F. Konig and W. Praefcke, *Color Imaging, Vision and Technology*, ch. 7. John Wiley & Sons, 1998.

[25] J. Y. Hardeberg *et al.*, *Color Imaging, Vision and Technology*, ch. 8. John Wiley & Sons, 1998.

[26] P. Herzog *et al.*, "Colorimetric characterization of novel multiple channel sensors for imaging and metrology," *Journal of electronic imaging*, vol. 8, pp. 342–353, October 1999.

[27] S. Tominaga, "Spectral imaging by a multichannel camera," *Journal of electronic imaging*, vol. 8, pp. 332–341, October 1999.

[28] J. Webb, M. McKelvy, *et al.*, *Using Visual Basic 4.* QUE, 1995.

[29] M. McKelvey, B. Siler, and J. Spotts, *Using Visual Basic 5.* QUE, 1997.

[30] M. Amundsen *et al.*, *Visual Basic 5 Fundamentals.* SAMS publishing, 1997.

[31] R. Thayer, *Visual Basic 6 Unleashed.* SAMS publishing, 1998.

[32] A. Kelley and I. Pohl, *A book on C.* Addison-Wesley, 3rd ed., 1998.

[33] IEC, "Colour management in Multimedia systems - Part2: Colour Management, Part2.1: Default RGB colour space-sRGB," tech. rep., International Electrotechnical Commision, 1998.

[34] G. E. Healey and R. Kondepudy, "Radiometric CCD camera calibration and noise estimation," *IEEE Transactions on Pattern Analysis and Machine Intelligence*, vol. 16, no. 3, pp. 267–276, 1994.

[35] Y.-C. Chang and J. F. Reid, "RGB calibration for color image analysis in machine vision," *IEEE Transactions on Image Processing*, vol. 5, no. 10, pp. 1414–1422, 1996.

[36] B. A. Wandell, "The synthesis and analysis of color images," *IEEE Transactions on Pattern Analysis and Machine Intelligence*, vol. PAMI-9, no. 1, pp. 2–13, 1987.

[37] D. Slater and G. Healey, "The illumination-invariant recognition of 3d objects using local color invariants," *IEEE Transactions on Pattern Analysis and Machine Intelligence*, vol. 18, no. 2, pp. 206–210, 1996.

[38] G. Finlayson, "Color in perspective," *IEEE Transactions on Pattern Analysis and Machine Intelligence*, vol. 18, no. 10, pp. 1034–1038, 1996.

[39] G. D. Finlayson and M. S. Drew, "White-point preserving color correction," in *Fifth Color Imaging Conference: Color Science, Systems and Applications*, pp. 258–261, IS&T, SID,, 1997.

[40] E. Boldrin, P. Campadelli, and R. Schettini, "Learning color appearance models," in *Fifth Color Imaging Conference: Color Science, Systems and Applications*, pp. 173–176, IS&T, SID,, 1997.

[41] P. M. Hubel, J. Holm, G. D. Finlayson, and M. S. Drew, "Matrix calculations for digital photography," in *Fifth Color Imaging Conference: Color Science, Systems and Applications*, pp. 105–111, IS&T, SID,, 1997.

[42] H. Kang, *Color Technology for Electronic Imaging Devices.* SPIE Optical Engineering Press, 1997.

[43] W. H. Press, *Numerical Recipes in C: The Art of Scientific Computing.* Cambridge Univ. Press, 1993.

[44] D. Perednia *et al.*, "Comparison of the clinical informativeness of photographs and digital imaging media with multiple-choice receiver operating characteristics analysis," *Arch. Dermatol.*, vol. 131, pp. 292–297, 1994.

[45] A. Bittdorf *et al.*, "Resolution requirements for digital images in dermatology," *Journal of the American Academy of Dermatology*, vol. 37, pp. 195–199, August 1997.

[46] C. McCamy, H. Marcus, and J. Davidson, “A color-rendition chart,” *Journal of Applied Photographic Engineering*, vol. 2, pp. 95–99, Summer 1976.

[47] Y. Vander Haeghen, J. Naeyaert, and I. Lemahieu, “Consistent digital color image acquisition of the skin,” in *20th Annual international conference of the IEEE Engineering in Medicine and Biology, Hong-Kong*, vol. 20, pp. 944–949, IEEE, 1998.

[48] Y. Vander Haeghen, J. Naeyaert, and I. Lemahieu, “Towards consistent color image acquisition in dermatology,” in *International congress on Imaging Science, Antwerp, Belgium*, pp. 377–381, ICPS, 1998.

[49] Y. Vander Haeghen, J. Naeyaert, L. Brochez, E. Verhaeghe, and I. Lemahieu, “A dermatological workstation with an electronic medical dossier, calibrated color image acquisition and semi-automatic lesion segmentation,” in *6th Congress of the International Society for Skin Imaging*, 1999.

[50] Y. Vander Haeghen, J. Naeyaert, and I. Lemahieu, “Consistent optical imaging and color measurement of the skin,” in *Proceedings of SPIE in San Diego, California, USA*, pp. 749–758, february 1999.

[51] Y. Vander Haeghen, J. Naeyaert, I. Lemahieu, and W. Philips, “An imaging system with calibrated color image acquisition for use in dermatology,” *IEEE Transactions on Medical Imaging*, vol. 19, pp. 722–730, july 2000.

[52] J. Golston *et al.*, “Boundary detection in skin tumor images: an overall approach and a radial search algorithm,” *Pattern Recognition*, vol. 23, no. 11, pp. 1235–1247, 1990.

[53] S. E. Umbaugh *et al.*, “An automatic color segmentation algorithm with application to identification of skin tumor borders,” *Computerized Medical Imaging and Graphics*, vol. 16, pp. 227–235, May-June 1992.

[54] S. E. Umbaugh *et al.*, “Automatic color segmentation algorithms,” *IEEE Engineering in Medicine and Biology*, pp. 75–82, September 1993.

[55] T. Lee *et al.*, “Describing the shape of melanocytic lesions,” in *SPIE 99 Medical Imaging*, SPIE, 1999.

[56] O. Debeir *et al.*, “Pigmented skin lesion cartography by supervised image segmentation: pixel vs region classification,” in *Proceedings In memoriam Pierre Devijver*, pp. 102–107, 1999.

[57] W. Barrett and E. Mortensen, “Fast, accurate, and reproducible live-wire boundary extraction,” in *Proc. Visualization in Biomedical Computing, Hamburg*, 1996.

[58] S. Lobregt and M. A. Viergever, “A discrete dynamic contour model,” *IEEE Transactions on Medical Imaging*, vol. 14, pp. 12–24, march 1995.

[59] A. D. Aczel, *Complete business statistics.* Irwin, 2nd ed., 1992.

[60] M. Jackowski, A. Goshtasby, and M. Satter, “Interactive tools for image segmentation,” 1999.

[61] Y. Vander Haeghen, J. Naeyaert, and I. Lemahieu, “Development of a dermatological workstation: Preliminary results on lesion segmentation in CIE $L^*a^*b^*$ color space,” in *Proceedings of the First International Conference on Color in Graphics and Image Processing*, October 2000.

[62] J.Lambert, J. Onderwater, Y. Vander Haeghen, G. Vancoillie, H. Koerten, A. Mommaas, and J. Naeyaert, “Myosin V colocalizes with melonosomes and subcortical actin bundles not associated with stress fibers in human epidermal melanocytes,” *The journal of investigative Dermatology*, vol. 111, pp. 835–840, november 1998.

[63] G. Vancoillie, J.Lambert, Y. Vander Haeghen, W. Uilbroek, A. Mommaas, H. Koerten, P. Van Oostveldt, and J. Naeyaert, “Colocalization of the dynactin subunit p150glued and p50 with melanosomes in human melanocytes,” *Pigment Cell Research*, 2000. In press.